Acoustic underwater target tracking methods using autonomous vehicles

Ivan Masmitjà Rusiñol

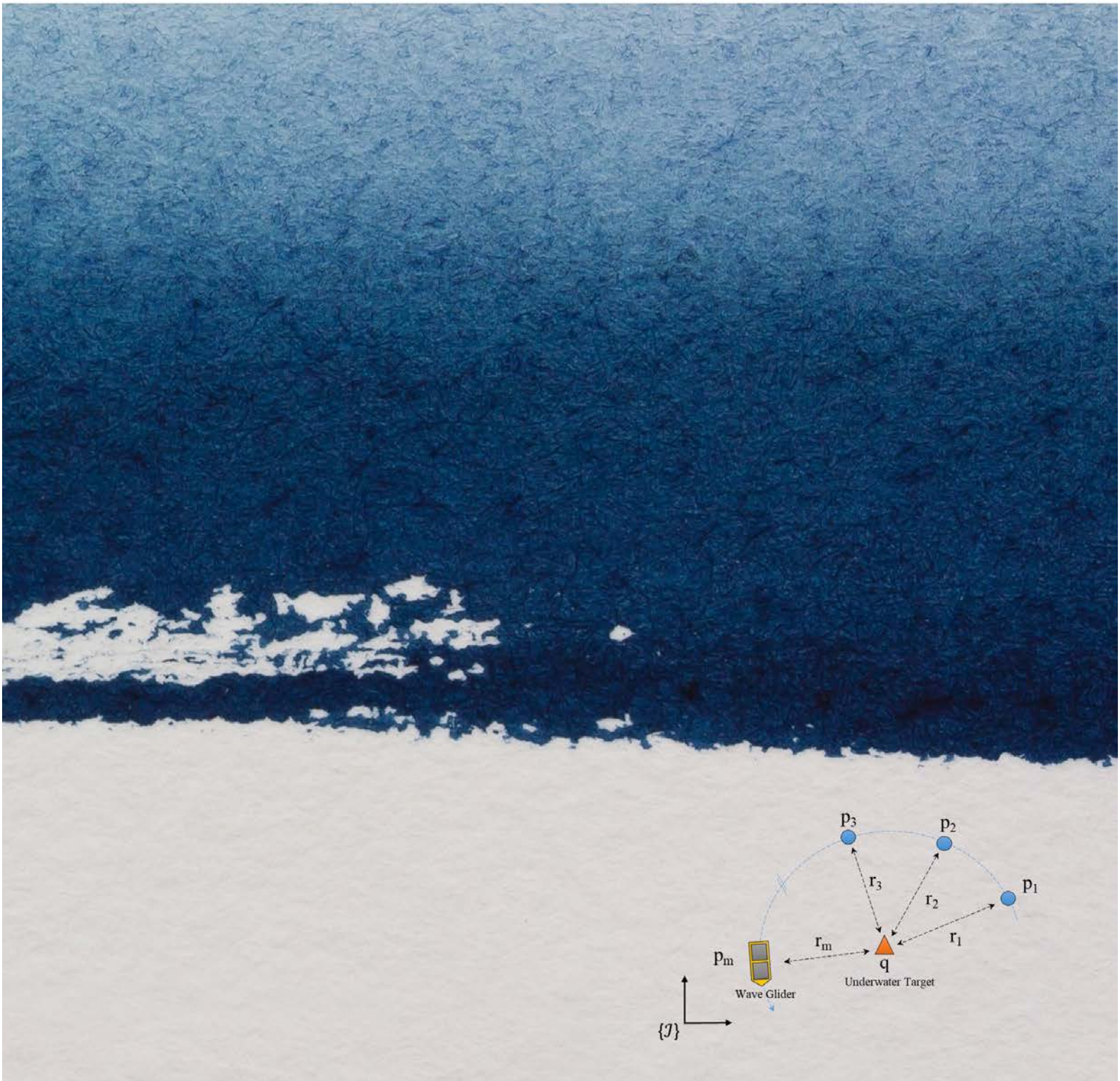

UNIVERSITAT POLITÈCNICA DE CATALUNYA
BARCELONATECH

Departament d'Enginyeria Electrònica

"Acoustic underwater target tracking methods using autonomous vehicles"

Thesis submitted in partial fulfillment of the requirement for the PhD Degree issued by the Universitat Politècnica de Catalunya, in its Electronic Engineering Program

Ivan Masmitjà Rusiñol

Supervisor:
Dr. Spartacus Gomáriz Castro

Co-Supervisors:
Dr. Jacopo Aguzzi

July 2019


Ivan Masmitjà Rusiñol, 2019

A copy of this PhD thesis can be downloaded from:
http://www.tdx.cat/
http://upcommons.upc.edu/

Date of defense: October 2019
Date of this version: July 16, 2019

Ivan Masmitjà Rusiñol
SARTI Research Group
Universitat Politècnica de Catalunya
Electronic Engineering Department
Rambla de l'Exposició 24 Edifici C, 08800
Vilanova i La Geltrú, Spain
<ivan.masmitja@upc.edu>

Abstract

Marine ecological research related to the increasing importance which the fisheries sector has reached so far, new methods and tools to study the biological components of our oceans are needed. The capacity to measure different population and environmental parameters of marine species allows a greater knowledge of the human impact, improving exploitation strategies of these resources. For example, the displacement capacity and mobility patterns are crucial to obtain the required knowledge for a sustainable management of fisheries.

However, underwater localisation is one of the main problems which must be addressed in subsea exploration, where no Global Positioning System (GPS) is available. In addition to the traditional underwater localisation systems, such as Long BaseLine (LBL) or Ultra-Short BaseLine (USBL), new methods have been developed to increase navigation performance, flexibility, and to reduce deployment costs. For example, the Range-Only and Single-Beacon (ROSB) is based on an autonomous vehicle which localises and tracks different underwater targets using slant range measurements conducted by acoustic modems. In a moving target tracking scenario, the ROSB target tracking method can be seen as a Hidden Markov Model (HMM) problem. Using Bayes' rule, the probability distribution function of the HMM states can be solved by using different filtering methods. Accordingly, this thesis presents different strategies to improve the ROSB localisation and tracking methods for static and moving targets. Determining the optimal parameters to minimize acoustic energy use and search time, and to maximize the localisation accuracy and precision, is therefore one of the discussed aspects of ROSB. Thus, we present and compare different methods under different scenarios, both evaluated in simulations and field tests. The main mathematical notation and performance of each algorithm are presented, where the best practice has been derived. From a methodology point of view, this work advances the understanding of accuracy that can be achieved by using ROSB target tracking methods with autonomous vehicles.

Moreover, whereas most of the work conducted during the last years has been focused on target tracking using acoustic modems, here we also present a novel

method called the Area-Only Target Tracking (AOTT). This method works with commercially available acoustic tags, thereby reducing the costs and complexity over other tracking systems. These tags do not have bidirectional communication capabilities, and therefore, the ROSB techniques are not applicable. However, this method can be used to track small targets such as jellyfish due to the reduced tag's size. The methodology behind the area-only technique is shown, and results from the first field tests conducted in Monterey Bay area, California, are also presented.

Keywords: Range-only, underwater target, tracking, autonomous underwater vehicle, autonomous surface vehicle, acoustics, acoustic modem, biologging, marine animal.

Acknowledgements

I would like to thank a large number of people who in many different ways have helped me in the accomplishment of this PhD thesis.

First of all, I would like to thank the valuable help and support that I have received from Prof. Spartacus Gomáriz, my supervisor. My relationship with Prof. Spartacus Gomáriz dates back to the first years of my telecommunications degree at EPSEVG, where we developed an AUV (called Guanay II). Since then, I have been captivated by marine technology and research. During those years, he has always advised and pushed me forward in order to achieve my goals.

Furthermore, I would like to thank the whole SARTI research group of the UPC, especially, Prof. Joaquin del Rio, who has always facilitated things for me and my research. My relationship with SARTI is also intense. Since I begun, I have learnt the key aspects to become a good engineer, for example, how to solve problems quickly, find projects, grants, scholarships, how to fillin large amounts of documents, justifications, time-sheets, etc. I have also lived lots of experiences and anecdotes, from having to repair a fiber optic cable damaged by rats in the sewage system of Vilanova on a hot summer Saturday, to many extraordinary immersions at the OBSEA observatory to install amazing new instruments. All of which, would not have been possible without all my colleagues who I have had at SARTI, in particular: Oriol Pallarés, David Sarriá, Marc Nogueras, Daniel Toma, Matias Carandell, Enoc Martinez, Javier Cadena, and Joaquim Olive.

On the other hand, I would like to thank especially my co-supervisor Dr. Jacopo Aguzzi of the ICM-CSIC. As a scientist, he has helped me to perceive things form another perspective. Many times, those people who have a predominant technological background, like myself, lose the reference of why the devices that we develop are important. He has always been there giving wise advice.

During my PhD, I have had the opportunity to travel around the world and meet extraordinary people. In the first place, I was able to conduct a stay and work with Prof. Pierre-Jean Bouvet of the ISEN-Yncrea university in Brest, France. He has been my second co-supervisor and has helped me form the beginning. There,

|

I also meet Prof. Yves Auffred, and Prof. Clément Aubry, all of them hosted me exquisitely, helping me in my research and in the developing of my algorithms.

Moreover, I have had the opportunity to perform my research and two stays at MBARI, one of the main oceanographic research institutes in the USA. They opened their doors for me, and there I was able to try and test all my algorithms using the amazing installations and equipment available. Those two years of collaboration have had a crucial role on my PhD thesis, which allowed a giant leap forward. I would like to thank many people at MBARI and the David and Lucile Packard foundation, especially, Tom O'Reilly who from the very start trusted me, I will always be in debt to him, and his office colleague Brian Kieft. Both of them helped me in everything and taught me many things, from piloting a Wave Glider to showing me the best sandwiches at Phil's Snack Shack. I would also like to thank George Matsumoto, the summer internship coordinator, Douglas Au, the director of engineering, and Christopher Wahl, Brent Jones, and Jared Figurski. Also, a special thank you to Dr. Kakani Katija, who opened a whole new world around the jellyfish to me, her motivation inspired me!

Finally, I would like to thank the support which at all times I have received from my parents, Medir Masmitjà and Fina Rusiñol, and my brother Gerard Masmitjà. They have always believed in me, even during complicated moments, because those moments also exist... Who could have imagined that a simple boy, who was born in a small farmhouse in the countryside, would be able to finish a PhD thesis related to underwater acoustic localisation, and conducted field tests in oceans on the other side of the planet? Not me, for sure! However, they did, and I am convinced that they are proud of me, but not as much as I am proud of my family, common people who have known how to face the adversities and give my brother and myself everything that we have required. Gràcies per tot!

Maria, this PhD thesis is also thanks to you. You have helped me in all moments, listening to me even though you did not understand what I was saying. In the case that I have bored you to death with my stories, I apologise! However, you have always had wise advice to give. Now, we face a new future full of hope. It is difficult to know everything, but if all three of us stay together, you, Marcel and I, life will be wonderful!

"Shoot for the moon. If you miss it, you will still land among the stars."

— Norman Vincent Peale

Contents

List of Figures

List of Tables

List of Acronyms

ADC Analog-to-Digital Converter.

AI Artificial Intelligence.

AOTT Area-Only Target Tracking.

ASV Autonomous Surface Vehicle.

AUV Autonomous Underwater Vehicle.

BIN Benthic Instrument Node.

BPF Band-Pass Filter.

CDF Cumulative Distribution Function.

CEKF Centralized Extended Kalman Filter.

CPF Coastal Profiling Float.

CRB Cramér-Rao Bound.

cRIO CompactRIO.

DAC Digital-to-Analog Converter.

DAT Directional Acoustic Transponder.

DLBL Distributed Long Baseline.

DOA Difference Of Arrival.

DP Dynamic positioning.

DRL Deep Reinforcement Learning.

DVL Doppler Velocity Log.

EKF Extended Kalman Filter.

FIFO First-In First-Out.

FIM Fisher Information Matrix.

FIR Finite Impulse Response.

FOG Fibre Optic Gyro Compass.

FPGA Field-Programmable Gate Array.

GA Geometric Algebra.

GA-BM Geometric Algebra Batch Methods.

GIB GPS Intelligent Buoy.

GPS Global Positioning System.

HMM Hidden Markov Model.

ICM *Institut de Ciències del Mar*.

ID Identifier.

IMU Inertial Measurement Unit.

INS Inertial Navigation System.

IoT Internet of Things.

ISEN *Institut Supérieur De L'electronique Et Du Numérique*.

KAUST King Abdullah University of Science and Technology.

LA Linear Algebra.

LA-BM Linear Algebra Batch Methods.

LA-OM Linear Algebra Online Methods.

LBL Long BaseLine.

LS Least Square.

LS-SVD Least Square Single Value Decomposition.

MAP Maximum A Posteriori.

MBARI Monterey Bay Aquarium Research Institute.

MCS Monte Carlo Simulation.

ML Maximum Likelihood.

MLE Maximum Likelihood Estimation.

MPR Maximum Particles Range.

MTR Maximum Transmission Range.

NLS Nonlinear Least Squares.

OS Operating System.

OTN Ocean Tracking Network.

PC Personal Computer.

PDF Probability Density Function.

PF Particle Filter.

PPS Pulse Per Second.

PTP Precision Time Protocol.

RMSE Root Mean Square Error.

ROSB Range-Only and Single-Beacon.

ROTT Range-Only Target Tracking.

ROV Remote Operated Vehicle.

SARTI *Sistemes d'Adquisició Remota i Tractament de la Informació.*

SASES *Sistemas Acusticos Submarinos para la monitorizacion del comportamiento especial de ESpecies.*

SBL Short BaseLine.

SF Survival Function.

SLAM Simultaneous Localisation and Mapping.

SNR Signal-to-Noise Ratio.

SOS Sensor Observation Service.

SR Successful Reception.

STD Standard Deviation.

SVD Single Value Decomposition.

SWE Sensor Web Enablement.

TCR Tracker Circumference Radius.

TDOA Time Difference Of Arrival.

TOA Time Of Arrival.

TOF Time Of Flight.

TT Total Transmissions.

UDP User Datagram Protocol.

UKF Unscented Kalman Filter.

ULS Unconstrained Least Square.

UPC *Universitat Politècnica de Catalunya*.

USBL Ultra-Short BaseLine.

UWAN Underwater Acoustic Networks.

WG Wave Glider.

WHOI Woods Hole Oceanographic Institution.

Chapter 1

Introduction

The oceans provide important ecosystem services for the human well-being, which includes supply services, cultural services, and environmental regulations [1]. However, the food supply is the main benefit that the human being obtains from the oceans. 15% of animal protein consumed worldwide is provided by the marine habitat, and furthermore, this ratio is expected to increas in the future. Therefore, a sustainable development of our marine resources in order to guarantee the availability and the access to sufficient food, innocuous and nutritive, is a key priority in the European H2020 programme, inside of what is known as Blue Growth [2].

Previously, the directive 2008/56/EC of the European Parliament and of the Council of 17 June 2008 established a framework for community action in the field of marine environmental policy, which states "*The marine environment is a precious heritage that must be protected, preserved and, where practicable, restored with the ultimate aim of maintaining biodiversity and providing diverse and dynamic oceans and seas which are clean, healthy and productive. In that respect, this Directive should, inter alia, promote the integration of environmental considerations into all relevant policy areas and deliver the environmental pillar of the future maritime policy for the European Union*". This directive also pinpointed an indicative list of characteristics which should be taken into consideration to analyse the marine habitat. This list can be seen in table 1 of annex III in the cited European directive, which indicates aspects such as physical and chemical features, habitat types, and biological features.

During the last century, the measurement of these marine and oceanographic indicators is under a constant development. It has been possible with technological advances to execute more observations with a greater detail and base. The main characteristics which are addressed with these new technologies are threefold: the frequency resolution, which allows a great number of measurements in a single point

under study; the spatial resolution, which guarantees small distances between measurement points; and the increase of the total observable area to obtain conclusions of studies conducted in a specific region.

In the middle of the XX century, exploration was characterised by the use of oceanographic buoys and vessels designed specifically for this purpose [3], [4], [5], [6] and [7]. This allowed the acquisition of a great temporal frequency measurements, as well as the increase of the duration of the missions, and consequently, it was possible to capture a great volume of information in specific zones.

At the same time, new technology emerges in space. The ocean's motorisation from space by satellites has allowed the increasing of the extension under observation [8], and [9], which has been used to study global phenomena such as *El Niño* [10]. Nonetheless, these methods are not useful to obtain measurements with great frequency resolution neither spatial resolution, and as a consequence, can not be used for detailed studies in specific regions (e.g. coast zones), to study infrequent events (e.g. oil spills), or to track benthic and pelagic marine species [11], and [12].

As a result of these necessities, since the 1950s new unmanned vehicles have been created, such as the Remote Operated Vehicles (ROVs), the Autonomous Underwater Vehicles (AUVs), and the AUV Gliders [13], [14], and [15]. Their main function is to decrease the cost of manned vehicles as well as increase the robustness of the operations. Nowadays, a great number of commercial vehicles can be found, which are used in a great number of applications (e.g. underwater surveillance, intervention or manipulation). Nevertheless, as the oceans become widely known, more and more specific needs arise. For example, the collaboration among multiple autonomous vehicles [16], [17], [18], and [19], which can be used to create 3D maps of complex underwater features [20]. In those circumstances new navigation control and localisation techniques need to be developed.

Another example of new applications arises in the area of marine biology related to the increasing importance which the fisheries sector has reached. The capacity to measure different population and environmental parameters of marine species allows a greater knowledge of the human impact [21], improving exploitation strategies of these resources [22], and [23]. For example, the displacement capacity and mobility patterns are crucial to obtain the required knowledge for a sustainable management of the involved fisheries [24] and [25]. For that purpose, electronic tags are commonly used, which provide information about the behaviour of marine species, and environmental measurements about their surroundings [26]. Many studies focused on great species (e.g. cetaceans, dolphins, and selachimorpha) can be found, which habitually rise to the sea surface [27] and [28]. This behaviour allows the possibility to use Global Positioning System (GPS) devices and satellite communication,

which are used to know their movements in real time. Currently, many commercial electronic tags can be found, such as: Desert Star System (www.desertstar.com), Argos (www.argos-system.org), and Spot (www.findmespot.com). The accuracy of the system, the satellite network used, and its weight, are aspects which must be taken into consideration to choose the appropriate device for each purpose. Weight is an important limitation in such cases, where the size of those tags should not exceed the commonly used tag-to-body-mass rule of 2% [29].

However, this methodology is not suitable for benthic and pelagic species, where electromagnetic waves suffer a high attenuation due to the water [30]. For this reason, acoustic positioning methods are the most common in underwater scenarios [31], [32], and [33]. Unfortunately, the acoustic underwater communication channel has some constraints, such as: propagation delay, multi-path behaviour, small bandwidth, the Doppler effect, or variations in phase and amplitude [34]. These characteristics mean that important technological challenges have to be faced in the development of acoustic devices, and still nowadays, a standard acoustic positioning method is not possible.

The study of marine animal movements, and their behaviour by acoustic tags is based on the implementation of acoustic transducers on them [28]. Then, using different receivers spread on a specific zone, the presence of the tagged animal inside the reception's range can be detected, or otherwise its absence derived. The reception's range varies as a function of the tag's size and its transmission power, typically a few hundred meters. Different companies have developed their own acoustic tags, for example the most common are Vemco (www.vemco.com), Lotek (www.Lotek.com), or HtiSonar (www.HtiSonar.com). The functionality of these tags is similar, which consists in the transmission of an acoustic signal periodically with a unique identification code. Nowadays, one of the smallest commercial tag is produced by Vemco (model V4), which is 5x12 mm in size, and can transmit a signal every 90 s for 100 days. The reception of these signals is conducted by compatible devices. In general, these receptors are used as data loggers and only after the experiment, when they are recovered, the information recorded can be studied [35]. This method allows the study of the presence of species in specific zones, or their migration between them. Nevertheless, small movements inside the zone can not be studied (i.e. only presence/absence studies related to daytime behaviour [36], or long migrations [26] are possible). In these cases an error of one hundred meter is assumable. Therefore, an optimal target localisation and tracking system for marine species, with great performance, can not be found [37].

Some high end methods allow the localisation of underwater tagged animals using triangulation techniques [38] and [39]. Recently, Vemco has introduced a new

asynchronous monitoring system which allows the localisation of an acoustic tag if it is received by at least three receivers [40]. Whereas Vemco offers this technology, its performance is still far from meeting the scientists' needs, especially in deep-sea studies, where the correct deployment of each receiver is increasingly difficult with the depth. Moreover, it is necessary to use specially designed synchronisation tags in order to keep synchronisation between each receiver, which increases the complexity of both deployment and post-process (which must be conducted by the company) [37].

For example, if the species under study is the Norway lobster (*Nephrops norvegicus*), the standard tags are not suitable. This species, small in size, can live deeper than 300 m, and in general its movements are limited around its burrow ~5 m (i.e. it is very territorial [25]). Hence, not only knowing its movements inside its territory, but also in the adjacent areas (spillover effect), is a key aspect to manage no take zones, which are used to establish methods for a sustainable fishery management [41]. On the other hand, soft-bodied marine invertebrates such as jellyfish play critical roles in many oceanic ecosystems [42]. Nonetheless, fine-scale behaviours (e.g. accelerations or swimming) are not discernible using the commercially available tools. Furthermore, environmental measures are often conducted in a broad area by satellites but not in the immediate surroundings of the animal, which can obscure potentially interactions with fine-scale conditions such as thermoclines.

Thus, it is necessary to develop new acoustic underwater systems to track and monitor the behaviour of different marine species. To accomplish this necessity, this thesis has focused on threefold: studying the limitations of the traditional acoustic localisation methods, improving and developing newer range-only tracking methods using autonomous vehicles, and proposing novel methods to track tagged animals using current commercially available tags and setting the basis for further improved acoustic tags.

1.1 Previous work

The *Sistemes d'Adquisició Remota i Tractament de la Informació* (SARTI) research group in the Electronics Department for the *Universitat Politècnica de Catalunya* (UPC) has been working on underwater communications over the past years. For example, the PhD thesis by Pallarés [43] was focused on the study and development of new acoustic synchronisation methods between acoustic modems. The thesis presented by Sarriá [44], who studied different methodologies to monitor marine species in both the laboratory and field must also be mentioned. Moreover, Sarriá developed an acoustic modem and tested many piezoelectric transducers.

On the other hand, SARTI has been developing an AUV called Guanay II. This project has also derived in many PhD thesis. For example, Gonzalez [45] determines the equations and parameters of the vehicle's mathematical model and studied different control techniques for path following and way-point following on the $x - y$ plane. A posterior PhD thesis, presented by Galarza [46], extended the navigation capabilities of Guanay II in the z dimension, and introduced an obstacle avoidance system using a sonar.

Furthermore, SARTI has a long experience in underwater technology, which has successfully developed, keeping in operation, an underwater cabled observatory since 2009 (`www.obsea.es`). In addition, SARTI has been collaborating with national and international oceanographic institutions such as *Institut de Ciències del Mar* (ICM) and Monterey Bay Aquarium Research Institute (MBARI). As a result, the UPC research group SARTI had the enough background related to underwater acoustics and autonomous vehicles to successfully accomplish the goals of this thesis, which is inside of the scope of interest of the group, and can be seen as another contribution to this line of research.

1.2 Motivation

The motivation of this thesis is twofold. Firstly, as stated in the introduction, the study of marine animal behaviour is an important aspect which has to be addressed in order to preserve the different species, which develops a key role in our society and environment. In this framework, studying their movements and being able to correlate them with different surrounding aspects, such as climate change or fisheries, are crucial to understand our world and the species that live in it. Here, acoustic tracking methodologies are essential due to the underwater environment, where no radio-frequency signals can be used (e.g. GPS or satellite communications).

On the other hand, due to the boom which consumer electronic devices have suffered over the last decades, many small devices, with low power consumption and relatively cheap in price, can be found everywhere (e.g. smartphones, wearable technology, or Internet of Things (IoT)). Those devices have pushed the limits of technology and have brought these to many applications. For example, nowadays different underwater or surface autonomous vehicles are used to explore our oceans. And moreover, fleets of them are normally used by researchers, which increase the coverage zone of study and allow more complex missions (e.g. thermal front tracking or complex seabed surface mapping). In this framework, the underwater localisation has a key role, where new methods with improved capabilities (e.g. more flexible, or less expensive) are required.

Regarding the first idea, this PhD thesis wants to address the study of different acoustic target localisation and tracking algorithms, which go from traditional Long BaseLine (LBL) systems to newer Range-Only and Single-Beacon (ROSB) methods, where the best practices have been derived, as well as the best accuracy achievable. Furthermore, we proposed a novel method to track acoustic tags implanted in marine species, which is the most common method used by scientists.

Regarding the second idea, this thesis has been conducted in its main part with the use of autonomous vehicles. Nowadays, both AUV and Autonomous Surface Vehicle (ASV) are used extensively in oceanographic research, which reduce the cost of expensive research vessels while increasing their capabilities. Here, as well as the analytical study of different methods and techniques, different real experiments have been conducted. For instance, the tracking of a benthic Rover with an ASV.

Finally, these target tracking methods using autonomous vehicles can be seen as an important part of a more general view of the growing interconnection between different platforms, for example AUV, and cabled observatories, which are used to study our oceans, Fig. 1.1.

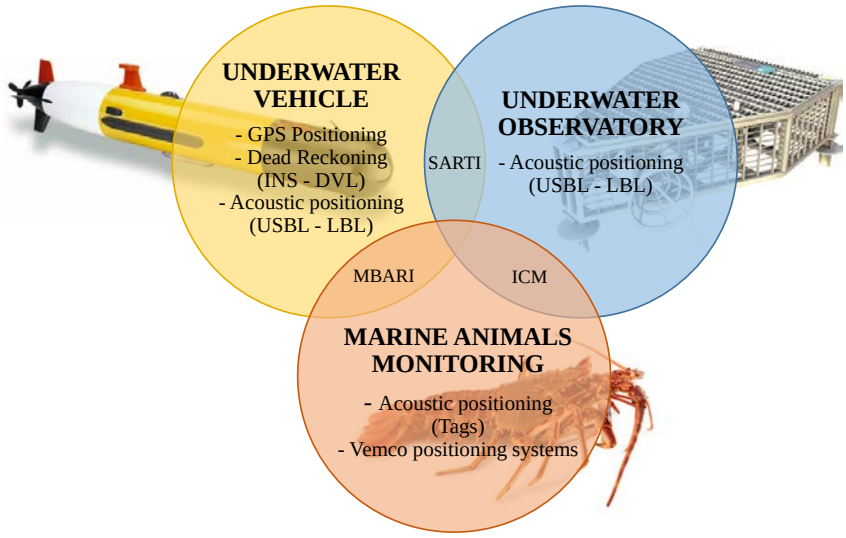

Figure 1.1: Block diagram of the background and the work conducted at SARTI with their collaborators (ICM and MBARI). The most important achievements have been performed in the ambit of underwater vehicles, cabled observatories, and marine animal monitoring.

1.3 Related work

One of the first acoustic underwater localisation methods was the LBL, which appears in the 1960s and 1970s [47]. Since then, different alternatives have been developed, such as the Short BaseLine (SBL), the Ultra-Short BaseLine (USBL), the GPS Intelligent Buoy (GIB) systems or the use of acoustic modems [48] and [49].

A The LBL and SBL systems

The LBL system employs a set of different transponders deployed on the seabed, which are called landmarks. The position of each of them must be known in advance with a high accuracy, and also their synchronisation is a key factor. Therefore, calibration procedures with vessels [50] and also helicopters [51] are commonly conducted [52]. Then, the target (e.g. an AUV) can interrogate each transponder and compute the Time Of Flight (TOF), which is used to know the distance between the target and each landmark. Another option is using the Time Difference Of Arrival (TDOA) of a signal transmitted by the target and received by two or more landmarks. Finally, using triangulation techniques, the target's position can be estimated. This kind of system has typical errors between 0.1 m and 10 m, using transmitting frequencies of 12 kHz, sampling rates of 20 s, and working ranges of up to 12 km [53]. These values can be improved using higher frequencies (300 kHz) and sampling rates (10 Hz) [54], these devices can achieve an accuracy below 1 cm.

The SBL system is similar to the LBL, where the main difference is the separation between landmarks. Usually, if the range between the target and each landmark is smaller than the distance between landmarks (inter-baseline), the system is called LBL, otherwise it is known as a SBL [38]. The accuracy achievable with the SBL systems increases proportionally with the inter-baseline of the landmarks, which theoretically can reach the same accuracy as the LBL method. However, as the size of the SBL system is smaller, its deployment is easier and cheaper. This system can also be mounted on a mobile platform such as oceanographic vessels.

B The USBL system

The operating principle of the USBL system is similar to the one explained above. Different transponders receive an acoustic signal with slight differences of time due to the inter-distance between them. Then triangulation techniques are used to compute the angle of arrival (elevation and bearing) of a signal transmitted by a target, which is used to estimate its position.

Yet, in a USBL system, all the transducers are placed together in a single device, where the inter-baseline is typically around ~10 cm, which allows the use of this

system on small platforms such as boats. Moreover, a USBL is commonly used with a GPS (to have a geodetic reference) and an Inertial Navigation System (INS) (to know the platform's attitude) [55].

Because of the use of the INS and small inter-baseline distances, the error of these systems is worse than the previous ones. Furthermore, calibration procedures must be conducted in order to adjust all the different systems involved in localising a target [56].

C The GIB system

The GIB method was developed to avoid the complexity and the costs derived from the LBL's deployment and calibration, and to increase the accuracy of the USBL systems. The main idea of the GIB system is to place the landmarks on buoys on the sea surface. With this simple idea, its deployment is simpler, and additionally, the GPS signal can be used to know the landmarks' position and adjust their synchronisation with high precision [57]. This system is commercialized by Alseamar-alcen (`www.alseamar-alcen.com`), model GIB-SAR.

D The single-beacon system

Finally, other methods have been developed to reduce even more the deployment's complexity of acoustic positioning systems, such as, the single-beacon methods. In this case, only one mobile landmark is used, which reduce the deployment complexity of the GIB method, whereas it can reach the same accuracy.

The main idea behind this architecture is to use an autonomous vehicle as a mobile landmark to compute the position of an underwater target, which, while moving in the area, takes some ranges between the target and itself to triangulate the target's position.

The interest in this methodology has been increased over the past years, as a consequence of the necessity to reduce localisation costs, and find new techniques to localise and track multiple nodes in Underwater Acoustic Networks (UWAN) [58], or in fleets of AUVs, where all the nodes have their own acoustic communication modem, and the crore,efan be used to know the ranges from other nodes on the gird. For instance, this methodology is used in the MORPH EC FP7 project [20] as explained in [59]. The authors present a system called Distributed Long Baseline (DLBL), where high synchronised modems from EvoLogics in 4-node network composed for AUVs were used.

In contrast, this technique is also used in single node architectures. For example, it is used in applications such as Simultaneous Localisation and Mapping (SLAM),

AUVs aid navigation, [60], [61], and [62], and in AUV homing as well, [63] and [64]. Finally, single-beacon localisation using autonomous vehicles as a moving landmark can also be used for target positioning and tracking in large areas without fixed beacon constraints. As an example, in [65] a tracking and following method of a tagged Leopard shark was presented.

1.4 Goal of the thesis

After the description of the research antecedents, motivation and related work, the goal of this thesis is stated. The general purpose is summarised as:

"The improvement of underwater target tracking methods using autonomous vehicles, with a close focus on underwater marine species tracking. Studying the best practices, and deriving the accuracy that can be achievable".

This main goal is divided into six related hypothesis:

1. Using smart hydrophones with signal processing, Ethernet connectivity, and synchronisation capabilities will allow an easy integration in an underwater cabled observatory network, which can be used to implement a short baseline target tracking system.

2. Using a USBL system in an ASV, such as a Wave Glider, which is smaller than standard oceanographic vessels, will introduce more uncertainty in the prediction of the target's position due to the sea state (e.g. waves and surface wind).

3. Range-only and single-beacon target localization using autonomous vehicles and acoustic modems will solve the limitations in the coverage zone and deployment costs presented by the LBL systems, and will solve the uncertainty presented by the USBL systems when working in complex scenarios such as shallow waters.

4. Range-only and single-beacon underwater target localisation methods using an autonomous vehicle and acoustic modems can also be used to track mobile targets. In such case, the previous target state and its propagation model must be taken into consideration.

5. The area-only underwater target localisation and tracking algorithm using acoustic tags will allow the study of the behaviour of small marine species and their movements in a way which has not been possible until the present day.

6. A new smart acoustic tag with bidirectional communications and range capabilities will allow the increase of the estimated target's position accuracy and will allow the transmission of important environmental measures. Both aspects could be used to increase the knowledge of biologging marine animals behaviour.

1.5 Thesis main contributions

This research has several objectives related to each hypothesis above:

- **Chapter 2** Studying an SBL system using smart hydrophones:
  - Calibration procedures for the SBL system
  - Accuracy achievable in the estimation of the target's position
- **Chapter 3** Studying the USBL system installed on an ASV:
  - Calibration procedures for the USBL system
  - Accuracy achievable in the estimation of the target's position
  - Derivation of the main source of errors
- **Chapter 4** Studying the ROSB methods for static targets
  - The study of the optimal path which must be conducted by an observer
  - Comparison among different target localization algorithms
  - Best practices derived to improve the target's estimation accuracy
- **Chapter 5** Studying the ROSB methods for moving targets:
  - The study of the optimal path which must be conducted by a tracker
  - Comparison among different target tracking algorithms
  - Best practices derived to improve the target's estimation accuracy
- **Chapter 6** Presentation of the Area-Only Target Tracking (AOTT) method:
  - The study of the optimal path which must be conducted by a tracker
  - Comparison among other target tracking methods
  - Best practices derived to improve the target's estimation accuracy
- **Chapter 7** Smart tag development:

  - Setting the basis of a new tag design with bidirectional communication capabilities
  - Tag implementation using the CompactRIO (cRIO) platform
  - Laboratory tests

1.6 Dissertation Structure

This chapter has provided a high-level introduction to acoustic underwater localisation methods and an explicit statement of the thesis. The following chapters present each individual contribution in detail, which has been structured in four main blocks:

- Firstly, Chapter 2 and 3 present the main limitations of the traditional acoustic localisation methods LBL/SBL and USBL
- Then, Chapter 4 and 5 compare different target localisation and tracking methods using the ROSB technique
- On the other hand, Chapter 6 presents a novel method for tagged target tracking called AOTT
- Finally, the basis of a new acoustic tag with bidirectional communication capabilities to improve current marine animal tracking methods has been derived in Chapter 7

Chapter 2

LBL/SBL systems using smart hydrophones

Using smart hydrophones with signal processing, Ethernet connectivity, and synchronisation capabilities will allow an easy integration in an underwater cabled observatory network. For example, these smart hydrophones could be used to implement a short baseline target tracking system.

2.1 Introduction

A cost-efficient, innovative and interoperable ocean passive acoustic sensor system has been developed within the European FP7 project called NeXOS (Next generation Low-Cost Multifunctional Web Enabled Ocean Sensor Systems Empowering Marine, Maritime and Fisheries Management), which can be deployed both on fixed and mobile platforms [66], [67] and [68]. Within this context, two passive acoustic sensors have been designed and developed called A1 and A2 [69].

2.1.1 Motivation

An important part of the effort of NeXOS project was focused on the development of a device with a great dynamic range, improved processing performance, and integration capabilities on autonomous platforms [70]. The A1 is a standalone small, compact, low power, and low consumption digital hydrophone with embedded pre-processing, which is suitable for mobile platforms with limited autonomy and communication capabilities. The A2 consists of four A1 digital hydrophones with Ethernet interface and one master unit for data processing, which enables real-time measurements of underwater noise and several soundscape sources.

Moreover, the A2 device can be used to localise and track different sound's

sources using its in situ processing and synchronization capabilities. However, after its deployment, a calibration process must be conducted to estimate the position of each A1 hydrophone, and to adjust the internal parameters. In this framework, the methodology used and the results obtained are presented in the following sections.

2.1.2 Contributions

A target localization method is presented in this chapter, which uses the capabilities of the new A1 hydrophones developed within the NeXOS project. This method is based on the Time Difference Of Arrival (TDOA) tecniques [71] and [72], which consist of computing the differences between the arrival time of a signal at different locations. Moreover, a complete study to calibrate the system is presented, and different field tests to validate the development have also been conducted.

2.2 NeXOS A2 system

The A2 system designed within the NeXOS project consists of an array of four A1 hydrophones and a master unit [73]. Each hydrophone have one transducer and two Analog-to-Digital Converters (ADCs), which are simultaneously sampling at different gains. These are used to detect acoustic source levels from 50 dB re 1μPa to 180 dB re 1μPa in the frequency range of 1 Hz to 50 kHz. The use of two amplifier stages with different gains is a cost efficient approach in order to obtain a wide dynamic range. Then, a micro-controller processes the sampled data and transmits the result through a EIA RS-232 serial port. Moreover, the A1 is equipped with a real time clock which is used to temporally tag the sampled data, and it is also equipped with a Pulse Per Second (PPS) input from a Global Positioning System (GPS) link.

The hardware designed to build each hydrophone is presented in Fig. 2.1, where the sensor internals and externals are shown.

(a) (b)

Figure 2.1: The sensor internal electronic circuit (a), and the external rubber cover (b).

The A2 master unit has been build with an ODROID-C2 (Hardkernel, South Korea). The ODROID-C2 is a 64-bit quad-core single board computer, which is one of the most cost-effective 64-bit development boards available in the ARM world. This embedded computer is used to process the signal of the four A1 hydrophones in real-time, which is used to implement the TDOA algorithm required to estimate the position of a source of sound. Here, the most important point when computing the TDOA is the accuracy and precision between each internal clock. The time synchronization of the master unit and the slave units (A1 hydrophones) is conducted by using the IEEE 1588 Precision Time Protocol (PTP) standard [74].

The NeXOS A2 system is briefly described below and presented in Fig. 2.2:

- The A2 sensor is a digital passive acoustic transducers array, and its output (raw signal) can be processed by a master unit.
- The acoustic array A2 is composed by four A1 acoustic devices, called the A2hyd, which provide the acoustic data output to the Master Unit through a serial digital port with Ethernet protocol.
- The master Unit manages the timing synchronization of the four A2hyd to get the proper simultaneous sampling.

(a) (b)

Figure 2.2: The NeXOS A2 system, (a) internal, and (b) external with the A1 hydrophones installed.

This system has been validated in the framework of NeXOS project. For example, a single smart hydrophone (A1) was installed on an Autonomous Underwater Vehicle (AUV) glider in order to measure the underwater noise. However, in this thesis, a TDOA algorithm has been developed and tested, which has been used to acoustically track sound sources using four smart hydrophones (A2).

2.3 TDOA algorithm

The algorithm used to localize the source of an underwater acoustic sound has been developed using the TDOA estimation method [75], which is commonly used in Long BaseLine (LBL) systems. As depicted in Fig. 2.3, the centre of the first hydrophone is considered as the origin of the Cartesian coordinate system arranged by the others 3 hydrophones. In this configuration, the 4 hydrophones are placed on the same plane, which is on the seabed.

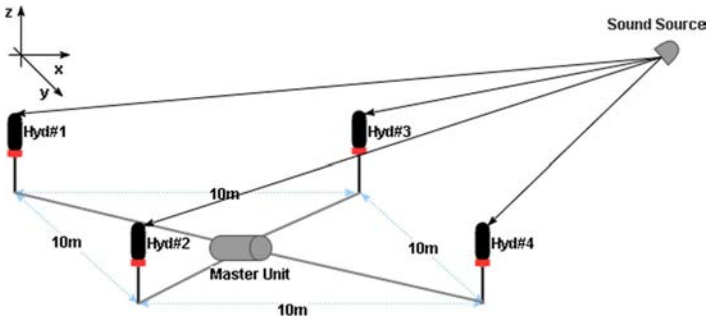

Figure 2.3: A2 array configuration for a 2D localization

The Difference Of Arrival (DOA) of a source sound is characterized by two angles, the azimuth (ϕ) and the elevation (θ). The DOA estimation deals with the case where the source is in the array's far field, which is equivalent to a plane wave at the sensor array [76]. With this assumption, the unit vector $\mathbf{a}_{\theta,\phi} \in \mathbb{R}^n$ (where n is the dimension state) at the sensor array pointing towards the source can be consider as

$$\mathbf{a}_{\theta,\phi} = \mathbf{a}_{DOA} = [-\sin\theta\cos\phi \quad -\sin\theta\sin\phi \quad -\cos\theta]^T. \tag{2.1}$$

The TDOA of the source signal from each hydrophone pair ij is defined as τ_{ij}, and corresponds to the estimated time required for the sound wave-front coming in the direction of $\mathbf{a}_{\theta,\phi}$ to travel a distance d_{ij} [76], given by

$$d_{ij} = \mathbf{a}_{\theta,\phi}^T(\mathbf{p}_i - \mathbf{p}_j), \tag{2.2}$$

where $\mathbf{p}_i \in \mathbb{R}^n$ and $\mathbf{p}_j \in \mathbb{R}^n$ are the position vectors of two sensor array elements, where $i, j \in \{0, \ldots, m-1\}$ and m equals to the number of hydrophones used. Moreover, the d_{ij} can be computed under far-field assumption as

$$d_{ij} \simeq \hat{\tau}_{ij} c, \tag{2.3}$$

where c is the sound speed in water. These equations, (2.1)-(2.3), can be written in a linear matrix form $\mathbf{Ax} = \mathbf{b}$ as

$$\mathbf{A} = \Delta\mathbf{p} = \begin{bmatrix} (p_{ix} - p_{jx}) & (p_{iy} - p_{jy}) & (p_{iz} - p_{jz}) \\ \vdots & \vdots & \vdots \\ (p_{mx} - p_{mx}) & (p_{my} - p_{my}) & (p_{mz} - p_{mz}) \end{bmatrix}, \tag{2.4}$$

$$\mathbf{x} = \mathbf{a}_{\theta,\phi} = \begin{bmatrix} a_x \\ a_y \\ a_z \end{bmatrix} = - \begin{bmatrix} \sin\theta\cos\phi \\ \sin\theta\sin\phi \\ \cos\theta \end{bmatrix}, \tag{2.5}$$

$$\mathbf{b} = \mathbf{d} = \begin{bmatrix} d_{ij} \\ \vdots \\ d_{mm} \end{bmatrix}, \tag{2.6}$$

Using a minimum of three sensors in a 2D scenario, and four or more sensors in a 3D scenario, knowing the TDOA, and the sensor array position, the $\mathbf{a}_{\theta,\phi}$ is uniquely determined, with full-rank matrix where all equations are linearly independent, and can be computed in a closed-form solution, directly or using a least squares method for overdetermined systems [77]. Finally, from (2.5) the azimuth angle estimation can be computed as $\hat{\phi} = \tan^{-1}(\hat{a}_y/\hat{a}_x)$ and the elevation angle is given by $\hat{\theta} = \cos^{-1}(-\hat{a}_z)$ as in [72].

A Maximum expected performance

Finally, the maximum expected performance which can be achievable with this system is computed, which will be used to compare both simulation and field test results.

In an estimation problem, where a set of noisy observations are used to estimate a certain parameter of interest, the Cramér-Rao Bound (CRB) sets the lowest bound on the covariance matrix that is asymptotically achievable by any unbiased estimation algorithm, and therefore, sets its maximum accuracy. The CRB is calculated using the inverse of the Fisher Information Matrix (FIM), represented as **FIM**, of the likelihood function of a system. Let the emitter location $\mathbf{q} \in \mathbb{R}^n$ be the parameter of interest obtained from a vector of TDOAs measurements $\mathbf{z} = h(\mathbf{p}) + \mathbf{w} \in \mathbb{R}^m$, where m is the number of measurements and w_m is a zero mean Gaussian error with covariance $\mathbf{R} \in \mathbb{R}^{m \times m}$. Each entry of the vector $h(\mathbf{p})$ has the form

$$h_{1j}(\mathbf{p}) = r_1(\mathbf{p}) - r_j(\mathbf{p}) = |\mathbf{q} - \mathbf{p}_1| - |\mathbf{q} - \mathbf{p}_j|, \tag{2.7}$$

where the TDOAs have been taken between the reference sensor $\mathbf{p}_1$ and the sensors $\mathbf{p}_j$ with $j \in \{2, \ldots, m\}$. Due to the Gaussian measurement noise, the likelihood function $p(z_{1j}|\mathbf{p})$ for a single TDOA measurement is given by

$$p(z_{1j}|\mathbf{p}) = \frac{1}{2\pi^{m/2}\mathbf{R}^{1/2}} \exp\Big\{ -\frac{1}{2}[z_{1j} - h_{1j}(\mathbf{p})]^T \mathbf{R}^{-1} [z_{1j} - h_{1j}(\mathbf{p})] \Big\}. \tag{2.8}$$

And the gradient of the log likelihood function $p(z_{1j}|\mathbf{p})$ with respect to $\mathbf{p}$ computed as [78] results in a FIM equal to

$$\mathbf{FIM} = \nabla h_{1j}(\mathbf{p})^T \mathbf{R}^{-1} \nabla h_{1j}(\mathbf{p}), \tag{2.9}$$

where

$$\nabla h_{1j}(\mathbf{p}) = \frac{h_{1j}(\partial \mathbf{p})}{\partial \mathbf{p}} = \frac{1}{r_1(\mathbf{p})}(\mathbf{q} - \mathbf{p}_1)^T - \frac{1}{r_j(\mathbf{p})}(\mathbf{q} - \mathbf{p}_j)^T, \tag{2.10}$$

which in matrix formulation can be described as

$$\begin{aligned} \nabla h(\mathbf{p}) = \begin{bmatrix} \nabla h_{1j}(\mathbf{p}) \\ \vdots \\ \nabla h_{1m}(\mathbf{p}) \end{bmatrix} &= \frac{1}{r_1(\mathbf{p})}(\mathbf{q} - \mathbf{p}_1)^T \mathbf{I} \\ &- \begin{bmatrix} \frac{1}{r_j(\mathbf{p})} & \cdots & 0 \\ \vdots & \ddots & \vdots \\ 0 & \cdots & \frac{1}{r_m(\mathbf{p})} \end{bmatrix} \begin{bmatrix} (\mathbf{q} - \mathbf{p}_j)^T \\ \vdots \\ (\mathbf{q} - \mathbf{p}_m)^T \end{bmatrix}, \end{aligned} \tag{2.11}$$

where $\mathbf{I} \in \mathbb{R}^{m \times m}$ is an identity matrix with size m by m.

Therefore, using (2.9) and (2.11) the CRB inequalities can be computed as follows. Suppose that $\hat{\mathbf{q}}$ is some unbiased estimation of the source of the sound position, which is computed using as observations some noisy TDOA measurements $\bar{\mathbf{z}}$ then

$$\text{var}\{\hat{\mathbf{q}}\} = \text{E}\{|\hat{\mathbf{q}}(\bar{\mathbf{z}}) - \mathbf{q}|^2\} \geq \text{tr}[\mathbf{FIM}(\mathbf{p})^{-1}] \tag{2.12}$$

Finally, a simulation using the **FIM** for a set of two TDOA measurements is calculated for a grid of possible emitter positions in the plane, which is shown in Fig. 2.4. A Standard Deviation (STD) of 1 μs has been used to compute the CRB, which yields in this typical pattern, where in some areas the accuracy of the source's localization is better than others (e.g. the error goes from 3 m to 30 m). This is due

to the source's position relative to the hydrophones' position. If the source's position is collinear with two or more hydrophones' positions, the resulting system will be undermined, and therefore, the estimated position using the computed TDOA will have less accuracy.

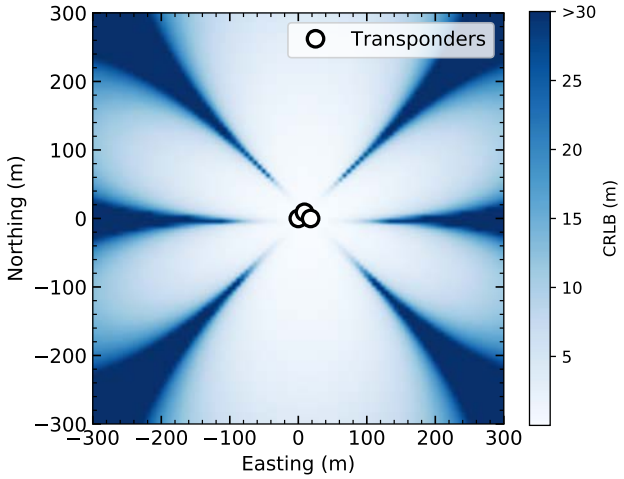

Figure 2.4: Simulation: The estimation of the expected accuracy using the CRB method for a set of two TDOA measurements.

2.4 NeXOS A2 software

All these equations are implemented in the algorithm shown in Fig. 2.5, which is used to estimate the DOA of an underwater acoustic signal source. This algorithm, which runs inside the master unit, has two main parts. The first part consists of four sub-processes, which run in parallel with the main process. These sub-processes are used to read the User Datagram Protocol (UDP) packets sent from the four hydrophones (Hyd♯1 ... Hyd♯4). In this step, a first synchronization is carried out using a zero crossing detector of a reference counter inside each UDP packet. After that, the acquisition is started. Each sub-process generates groups of N UDP packets, corresponding to the sampling windows defined previously by the user. Finally, these groups are saved as a valid data into a First-In First-Out (FIFO) queue which is used to share information between parallel processes.

The second part of this algorithm is the reading of one item from the four FIFO queues at each iteration. All of these signals have their own timestamp, and therefore, a second synchronization is carried out to obtain a common timestamp. After that, each signal is filtered using a Band-Pass Filter (BPF) and compared with a minimum threshold. When all channels have a signal greater than the threshold and

are centred in the sampling windows, the signal is processed to estimate the TDOA and the DOA.

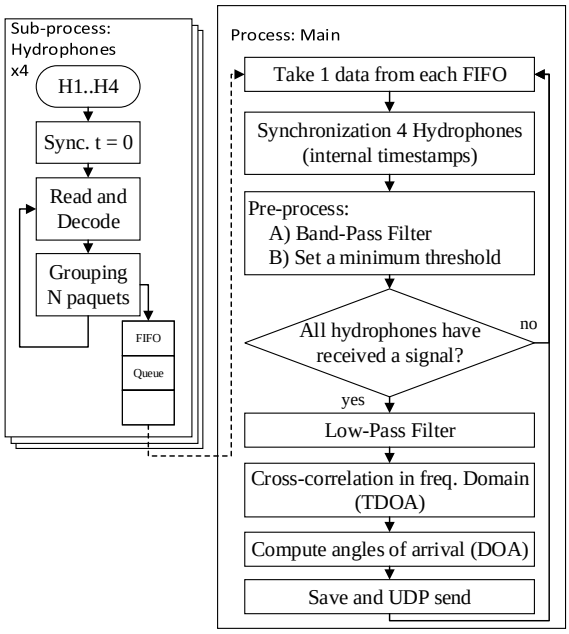

Figure 2.5: Block diagram of the algorithms used to compute the DOA of a sound's source using the NeXOS A2 sensor.

2.5 Simulation tests

The initial validation of the DOA algorithm has been carried out by performing four simulations with four different virtual locations of the sound's source (e.g. a boat) around the A2 array configuration, which is shown in Fig. 2.6. The TDOA is then calculated depending on the distance between the virtual sound source and the hydrophones. This delay is simulated by taking different audio signals with the corresponding delay in samples. Moreover, the signal's attenuation due to the spherical divergence is also calculated for each simulated signal. The output of the algorithm consists with the angle (ϕ) between x-axis and the vector which defines the DOA.

The result of these simulations are shown in Table 2.1, where the DOA estimation is compared with an ideal case (using the real positions). The result shows a great correlation, and therefore, corroborates the algorithm's performance as a good estimator. On the other hand the error computed is between the error predicted by CRB presented in Section A.

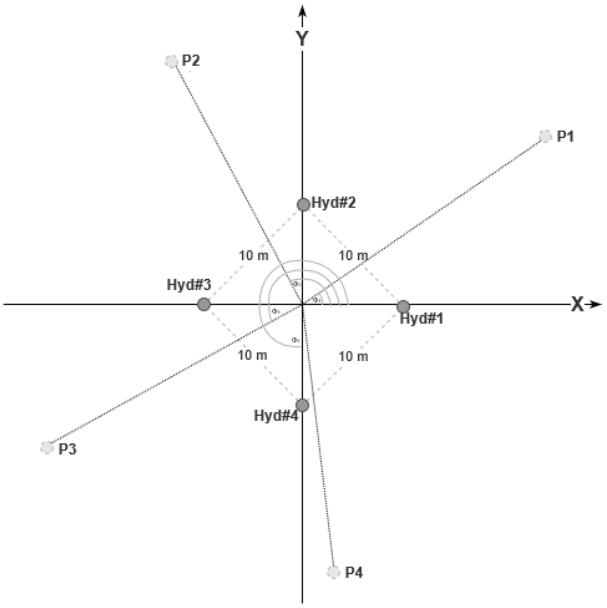

Figure 2.6: 2D representation of the hydrophones' positions and the 4 sources' locations during the simulations carried out to evaluate the algorithm proposed.

Table 2.1: Algorithm Difference Of Arrival (DOA) estimation compared with ideal case in 4 different source's positions.

Source	x-pos (m)	y-pos (m)	Ideal ϕ (deg)	Estimated ϕ (deg)	error (deg)
P1	52.1	27.9	28.5	25.5	3.0
P2	-21.0	56.9	110.6	109.2	1.4
P3	-45.0	-25.0	209.1	211.4	-2.3
P4	5.3	63.0	274.8	275.1	-0.3

2.6 Sea tests

The A2 sensor (configurated as a Short BaseLine (SBL)) was deployed on June 7, 2017 to observe its performance. The SBL is similar to the LBL, the main difference is the inter-baseline between hydrophones. Here, the SBL system was used because of its lower deployment complexity. The A2 sensor was connected into the OBSEA observatory (`www.obsea.es`), near Barcelona, Spain (Fig. 2.7) and [79]. The OBSEA can provide 12/24 V up to 3 A to power supply an external sensor, and Ethernet connection through their specific instrument ports. One of these ports was connected to the A2 sensor master unit using a wet-mate connector. Fig. 2.7 also shows one of the four A2 hydrophones deployed on the OBSEA observatory, and the final deployment scheme where the 4 hydrophones were positioned in the vertices of

a 10 x 10 m square shape.

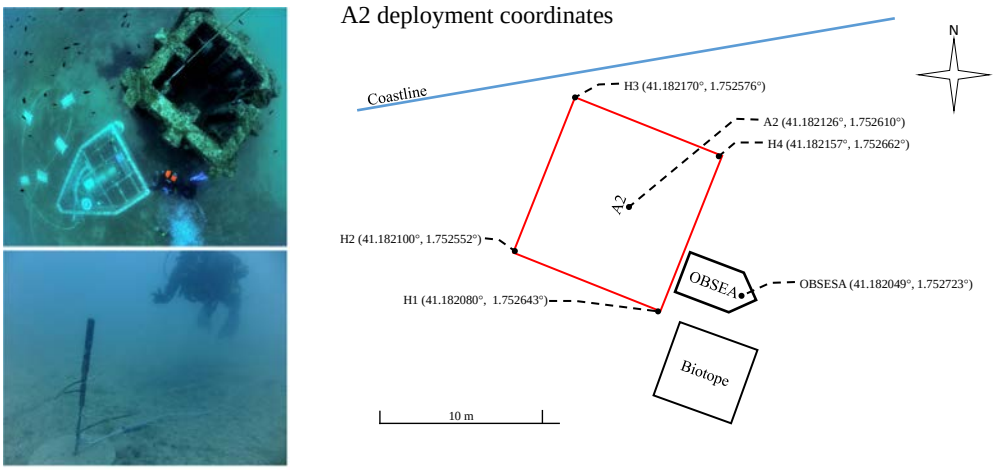

(a) (b)

Figure 2.7: The OBSEA observatory (a)-top and one of the A2 hydrophones deployed on the seabed (a)-bottom. Final deployment location of each component once connected to the OBSEA, hydrophones (H1,H2,H3,H4) and the A2 master unit (b).

In this test, an A2-centred 500 m radius circle path was performed using a boat equipped with a sound generator, allowing a 360 deg assessment of A2 DOA performance. The tone generated had the pattern presented in Fig. 2.8, and was used to facilitate the post-process carried out for calibration purposes.

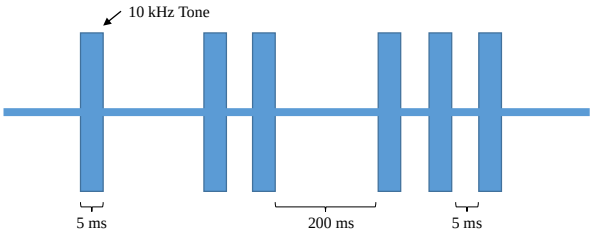

Figure 2.8: Sound pattern generated used to calibrate the system. Each tone was conducted with a 10 kHz sinusoidal signal during 5 ms, and the separation between tones was always 5 ms, and between tone's groups was 200 ms.

The raw signal received at each hydrophone is shown in Fig. 2.9, where the time delays between each device can be observed, which are also notated in Table 2.2. For example, in this acquisition can be observed that the first hydrophone which received the transmitted signal was H2, followed by H3 and finally H4. Therefore, the signal was arriving from the west side of the system, as can be noticed due to the array configuration (Fig. 2.7b). The angle between the boat and the A2 SBL

was 270 deg (based on GPS positions) whereas the angle computed using the A2 was 269 deg, which yields with an error of −1 deg.

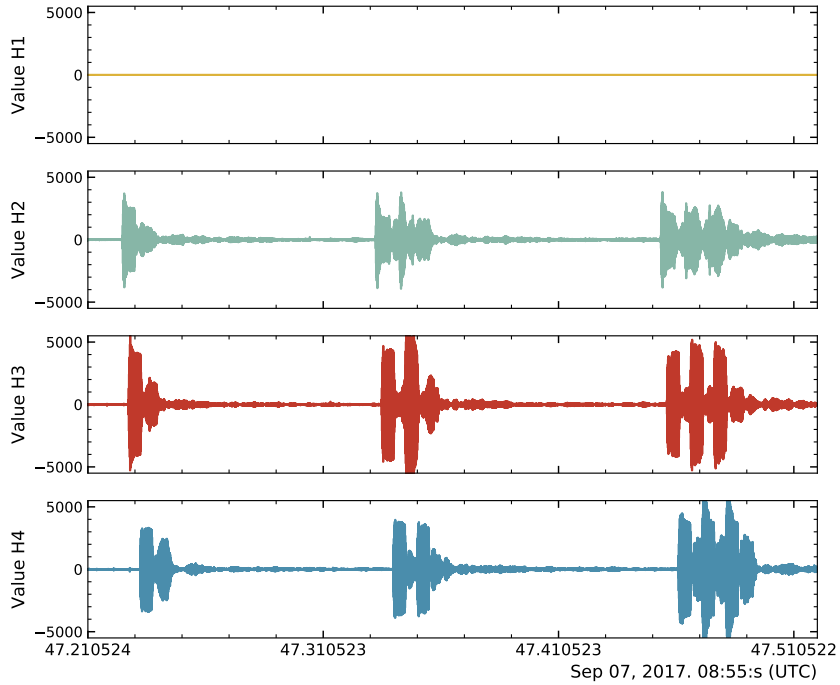

Figure 2.9: Field test: Raw signals received at each hydrophone during a field test.

During this test the hydrophone number 1 (H1) was not working properly due to some hardware failure. Therefore, the signal measured was always 0. Nevertheless, the boat could be detected in a 2D plane which was placed on the sea surface. In this scenario, a minimum of 3 hydrophones are mandatory to compute the source of sound, which allowed to carry out the test.

Table 2.2: Time Of Arrival (TOA) and TDOA obtained from a single transmission when the source of sound where on the west side of the A2 system.

Hydrophone	TOA (s)	TDOA (ms)	Pair
H4	47.233	–	–
H3	47.228	-4.9	H4-H3
H2	47.225	-7.4	H4-H2
H1	–	–	–

On the other hand, all the DOA estimations computed during the test were sent to the Sensor Observation Service (SOS) server, which also received the "true" angle between the A2 and the boat computed using the boat's GPS. These angles

can be observed in Fig. 2.10, where the computed DOA estimation is depicted in red whereas the "true" angle between the A2 and the boat is depicted in blue.

Figure 2.10: The A2 sensor DOA vs GPS-measured of boat's location delivered to NeXOS SOS server and viewed in the NeXOS Sensor Web Enablement (SWE) viewer. The blue line is the "true" angle between the A2 sensor and the boat, whereas the red line is the computed angle by the A2.

However, in order to improve the accuracy of the system, a python-based post processing was applied to the SOS-downloaded data. The results are shown below.

First the outliers generated by the A2 were eliminated, Fig. 2.11a and Fig. 2.11b. A derivative method was used to eliminate unnatural discontinuities. Then, a 0 to 360 deg segment was used and the A2 headings interpolated to correlate the timestamps and the values of both GPS-based and A2-estimated DOAs to perform a calibration Fig. 2.11c. Then, the values were divided in three segments to improve the calibration curve. Moreover, a high grade curve fitting on each of these three segments was used. The result is shown in Fig. 2.11d, where the heading value error of the A2 respect to the Boat is represented.

Finally, the error in a polar plot representation can be observed in Fig. 2.12. In some areas the error is much higher than others, this kind of pattern is typically expected as it is shown in [78], where the authors runs a simulation using the CRB, and also presented in Section A.

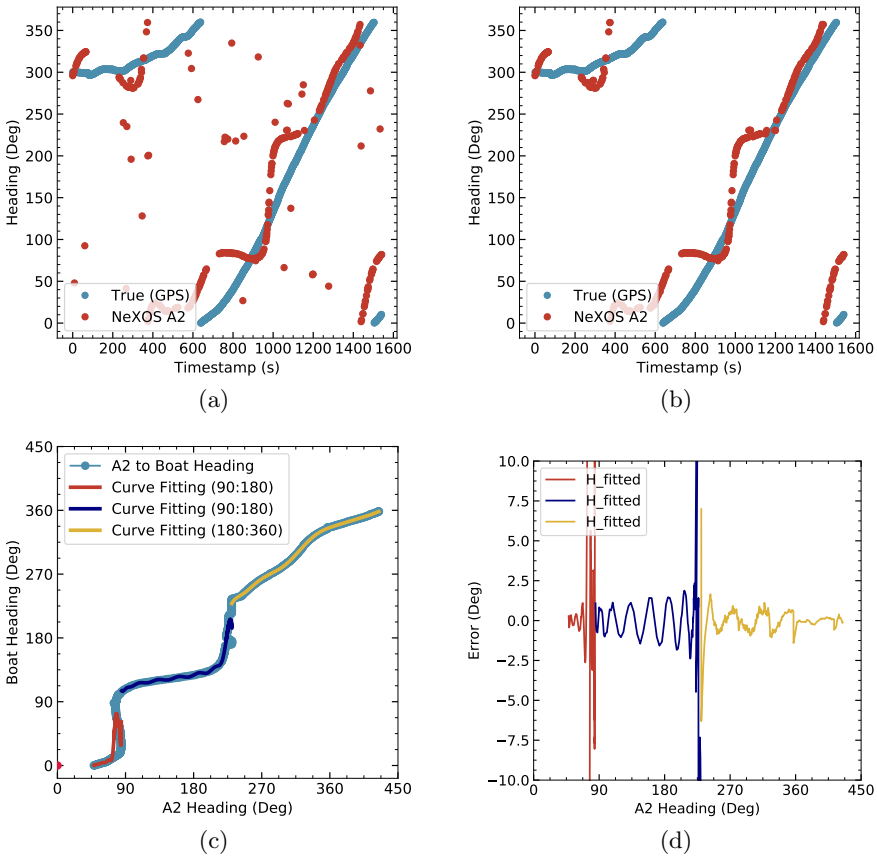

Figure 2.11: Field test: (a) Raw data obtained from the SOS server. (b) Data without the outliers using a derivative method. (c) Segment of data used to calibrate the system and the three curve fitting employed. And (d) the error obtained after the calibration.

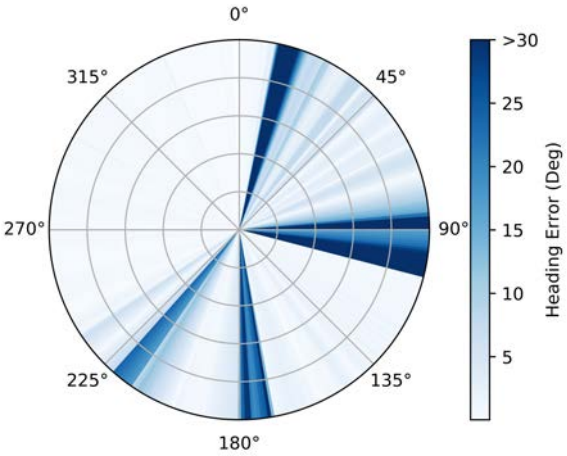

Figure 2.12: Field test: Polar representation of the heading error.

2.7 Conclusions

Finally, we can conclude that A2 estimates fit reasonably well with the actual sound generator location and therefore the result of this test was successful, partly validating/demonstrating, the capability of A2 to estimate. The DOA estimations with A2, tested at OBSEA observatory, have similar values to the simulation tests, presenting errors lower than 3 m on the good areas and errors around 30 m in the worst cases. Moreover, the differences between the field test estimations and the simulations can be due to the accuracy of the hydrophones position during their deployment. More experiments would be needed for further validation in different scenarios (e.g. changing landscape or robustness vs background noise).

Chapter 3

USBL systems on autonomous surface vehicles

Introducing a Ultra-Short BaseLine (USBL) system in an Autonomous Surface Vehicle (ASV), such as a Wave Glider, which is smaller than standard oceanographic vessels, will introduce more uncertainty in the prediction of the target's position due to the sea state (e.g. waves and surface wind).

3.1 Introduction

The Long BaseLine (LBL) and Short BaseLine (SBL) systems are usually installed on the seafloor, which increases their deployment costs and complexity. Whereas these methods offers a great target localisation accuracy, they can only be used to track devices which are inside an specific area, i.e. those targets which are too far away, and therefore not inside the system zone of influence, cannot be tracked. Moreover, the LBL needs a complex procedure to be calibrated, which has to be done after each deployment. For example, each transponder must be located accurately, where the difficulty is proportional to the transponder's depth. Consequently, if the required deployment's and the calibration's times are taken into account, it can be conclude that these systems are hardly mobile, and therefore, are only used to monitor specific areas (e.g. areas around an offshore oil platform or an underwater observatory).

To solve this problem, other target localisation methods have been developed. For example, the USBL system. This device has the four transducers, which are typically used in LBL systems, integrated into a single acoustic receiver, which can easily be installed in different observation platforms (e.g. oceanographic vessels). As a result, with this system the localisation is not restricted to the system coverage

zone (as happens with the LBL), because of the fact that the vessel can easily move to different areas of interest. Nevertheless, this system also has to be calibrated, but only the first time which is installed on the vessel.

Nowadays, with the size and power consumption reduction implemented in the modern USBL systems, these can be used in smaller platforms such as ASV or Autonomous Underwater Vehicle (AUV) [80] and [81]. However, the integration of these devices in such platforms rises different specific problems which have to be taken into consideration. For example, the calibration procedures and the maximum target localization accuracy that can be achievable. In general, the ASV can navigate in sallower waters and suffers more consequences in front of worse sea state conditions compared with bigger ships. Some of these specific problems will be addressed below.

3.1.1 Motivation

This study is motivated by the problem observed when an USBL system was used in one of the Monterey Bay Aquarium Research Institute (MBARI)'s Wave Glider (Liquid Robotics, USA). The USBL used was the Directional Acoustic Transponder (DAT) system (Benthos Teledyne, USA, `www.teledynemarine.com/benthos/`). This is an extension to the Teledyne Benthos ATM-900 Series modem, which automatically estimates the azimuthal and vertical arrival angles of a message sent by a remote modem [82].

It is known that the USBL must be calibrated after its installation in order to adjust some possible misalignment between the transducer, the Inertial Measurement Unit (IMU), and the vehicle itself. Furthermore, when these kind of systems are installed in a small mobile platform (e.g. a Wave Glider) the sea state can potentially have an important influence in their performance. Finally, due to the small profile of these vehicles, this instrument can also be used in shallow waters, where other problems may appear, such as acoustic multipath behaviour.

3.1.2 Related work

The calibration methods typically used in USBL systems can be divided in three groups [83]: the Linear Algebra Batch Methods (LA-BM), the Linear Algebra Online Methods (LA-OM), and the Geometric Algebra Batch Methods (GA-BM). From these methods, the constrained Least Square (LS) solution using Single Value Decomposition (SVD), known as Least Square Single Value Decomposition (LS-SVD) [84], is the present standard batch method for rotation identification, which guarantees a rigid body rotation, and therefore, it is a better approach than the previous LS methods such as [85]. On the other hand, in [83], Stanway focused

his research in the developing of a new method for GA-BM calibration procedures, which used a more compact and efficient encoding method for rotation matrix than the Linear Algebra (LA) methods. In addition, the Geometric Algebra (GA) formulations provides a greater meaningful and intuitive error measures than the LA approaches.

These methods can be used under different scenarios when the rotation and translation transformation matrix between two groups of points are desirable. For example, these methods are very common in computing vision. In underwater localisation and navigation environments using autonomous vehicles, these methods have been used to calibrate some misalignment between the Doppler Velocity Log (DVL) or USBL devices and the vehicle reference frame [86] and [87]. Here, the LS-SVD method is presented and used.

3.1.3 Contributions

In this chapter a complete study in order to identify and characterize the best accuracy achievable with an USBL installed on an ASV and working in a complex scenarios, such as shallow waters and adverse sea state conditions, is conducted. For this study, not only analytical procedures have been carried out, but also sea tests.

Whereas the present standard method LS-SVD has been used to calibrate the misalignment presented in the USBL systems, here the most important contribution has been the demonstration of the USBL performance when it is used on autonomous vehicles. Different localisation manoeuvres have been conducted in shallow waters, and the target prediction accuracy has been characterized.

3.2 Calibration method using LS-SVD

Following the first work carried out by Arun et al. and Umeyama, [88] and [84] respectively, the following procedure to identify the USBL's misalignment can be presented.

The LS-SVD needs more than two distinct points in 2D scenarios, and more than three non-collinear points in 3D scenarios. In such circumstances, the algorithm can determine uniquely the parameters of the transformation matrix. If the relationship between two set of points (X and Y) is restricted to the rigid body rotations, the solution is constrained into the special orthogonal group

$$y = \mathbf{R}x : \quad \mathbf{R} \in SO(3), \tag{3.1}$$

which has the orthogonality and normality constrains, where the columns of the

matrix are orthogonal (i.e. independent) and the scale and chirality are preserved. These constrains can be defined as

$$SO(3) \equiv \{\mathbf{R} : \mathbf{R} \in \mathbb{R}^{3\times 3}, \mathbf{R}^T\mathbf{R} = \mathbf{I}_{3\times 3}, \det(\mathbf{R}) = 1\}. \tag{3.2}$$

Using this rotation matrix in three dimensions, the misalignment between the instrument frame and the vehicle frame can be defined by

$$\mathbf{q}^w(t) = \mathbf{R}_b^w(t)\mathbf{R}_i^b\mathbf{q}^i(t), \tag{3.3}$$

where $\mathbf{q}^i(t)$ is the position of a target in the instrument reference frame (denoted by the superscript ^{i}), $\mathbf{R}_i^b$ constant is the unknown misalignment matrix which must be found, $\mathbf{R}_b^w(t)$ is the transformation matrix to rotate and translate the target position in the body frame (denoted by the superscript ^{b}) to the world coordinates (denoted by the superscript ^{w}), and finally, $\mathbf{q}^w(t)$ is the target position in world coordinates. In this formulation, the matrix $\mathbf{R}_b^w(t)$ is function of the Euler angles roll, pitch and yaw (denoted by ϕ, θ, and ψ respectively), and the Global Positioning System (GPS) positions.

In order to obtain (3.3) in parameters of (3.1), we can multiply both sides of (3.3) by $\mathbf{R}_w^b(t)$, which is equal to $\mathbf{R}_b^w(t)^T$.

$$\mathbf{R}_w^b(t)\mathbf{q}(t)^w = \mathbf{R}_w^b(t)\mathbf{R}_b^w(t)\mathbf{R}_i^b\mathbf{q}^i(t) = \mathbf{R}_i^b\mathbf{q}^i(t). \tag{3.4}$$

Then, considering a set of target positions measurements obtained at different discrete times k using the USBL, which can be denoted as $\mathbf{X} = \{\mathbf{q}^i(k+1), \ldots, \mathbf{q}^i(k+n)\}$, where n is the number of the measurements carried out. These measurements yields in a set of output points denoted by $\mathbf{Y} = \{\mathbf{q}^w(k+1), \ldots, \mathbf{q}^w(k+n)\}$. The following group of equations are used to define the mean $\boldsymbol{\mu}$, the variance σ^2, and the covariance matrix $\boldsymbol{\Sigma}_{XY}$ of these vectors

$$\boldsymbol{\mu}_X = \frac{1}{n}\sum_{k=1}^{n}\mathbf{q}_k^i, \tag{3.5}$$

$$\boldsymbol{\mu}_Y = \frac{1}{n}\sum_{k=1}^{n}\mathbf{q}_k^w, \tag{3.6}$$

$$\sigma_X^2 = \frac{1}{n}\sum_{k=1}^{n}||\mathbf{q}_k^i - \boldsymbol{\mu}_X||^2, \tag{3.7}$$

$$\sigma_Y^2 = \frac{1}{n}\sum_{k=1}^{n}||\mathbf{q}_k^w - \boldsymbol{\mu}_Y||^2, \tag{3.8}$$

$$\mathbf{\Sigma}_{XY}^2 = \frac{1}{n}\sum_{k=1}^{n}(\mathbf{q}_k^w - \boldsymbol{\mu}_Y)(\mathbf{q}_k^i - \boldsymbol{\mu}_X)^T. \tag{3.9}$$

Finally, the LS-SVD method can be solved to find $\mathbf{R}_i^b$, which will contain a rotation matrix $\mathbf{R}_{SVD}$, a translation matrix $\mathbf{T}_{SVD}$, and a scaling factor c_{SVD}. From [84], these parameters can be computed as

$$\mathbf{R}_{SVD} = \mathbf{U}\mathbf{S}\mathbf{V}^T, \tag{3.10}$$

$$\mathbf{T}_{SVD} = \boldsymbol{\mu}_Y - c_{SVD}\mathbf{R}\boldsymbol{\mu}_X, \tag{3.11}$$

$$c_{SVD} = \frac{1}{\sigma_X^2}\mathrm{tr}(\mathbf{D}\mathbf{S}), \tag{3.12}$$

where $\mathbf{U}$, $\mathbf{D}$, and $\mathbf{V}^T$ are the values of the SVD with the input matrix $\mathbf{\Sigma}_{XY}^2$, and $\mathbf{S}$ must be chosen as

$$\mathbf{S} = \begin{cases} \mathbf{I}, & \text{if } \det(\mathbf{U})\det(\mathbf{V}) = 1 \\ \mathrm{diag}(1,\ldots,1,-1), & \text{if } \det(\mathbf{U})\det(\mathbf{V}) = -1 \end{cases}. \tag{3.13}$$

With this method, the optimum transformation is determined uniquely when $\mathrm{rank}(\mathbf{\Sigma}_{XY}) \geq m - 1$.

3.3 Simulations

Different simulations have been conducted in order to validate the implemented algorithm, which has been used to calibrate the possible misalignment presented between the USBL installed on the Wave Glider and the others navigation instruments involved, such as the IMU and the GPS.

The main idea behind the calibration procedure is to conduct a set of maneuvers around a fixed transponder, usually deployed on the seabed. These maneuvers must enfatisace the possible misalignment presented. The general method used by most of the acoustic manufactures is known as the cardinal point scheme, where the vessel occupies four primary cardinal points around the transponder [89]. For example, moving the vessel systematically either side of the transponder and by reversing its heading at the static cardinal collection point. Nonetheless, in vehicles without Dynamic positioning (DP) systems this can be hard to achieve. In such cases, a constant movement around the transponder can be used.

On the other hand, the traditional ideal distance from each cardinal point to

the transponder was around three times the water depth. However, due to the nowadays deeper water scenarios, the distance used is typically limited at 500 m, which reduce the amount of ray bending that might occur, and maximise the signal to noise ratio [89].

Here, a square path has been used to calibrate the USBL, where two of its sides has been conducted twice, each one using an opposite direction (i.e. north/south and east/west). Each side of the square path is 400 m long, and a new measurement is conducted every 20 m. For example, Fig. 3.1 shows the two simulated paths conducted by the ASV (up-down left side, and up-down right side), the real target position and its estimation using the USBL, where some noise was added and a misalignment was introduced. In this case, 1 m and 1 deg of noise is added in the range, roll, pitch and yaw measurements respectively, and a misalignment of 45 deg in the roll, pitch and yaw angles.

In Fig. 3.2, a complete path is presented. Additionally, the target estimation position, before and after the calibration, is shown. The following parameters have been used in this example:

- Noise:
  - Range = 1 m
  - Roll = 1 deg
  - Pitch = 1 deg
  - Yaw = 1 deg
- Misalignment (angular):
  - Roll = 20 deg
  - Pitch = 20 deg
  - Yaw = 20 deg
- Misalignment variability (angular):
  - Roll = $\pm$5 deg
  - Pitch = $\pm$5 deg
  - Yaw = $\pm$5 deg
- Misalignment (distance):
  - x-axis = 2 m
  - y-axis = 0.5 m
  - z-axis = 0 m

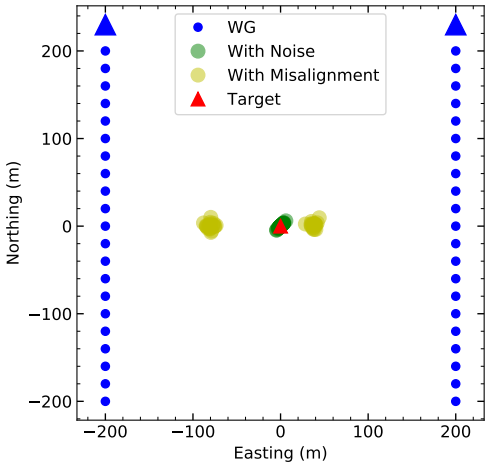

(a) Roll

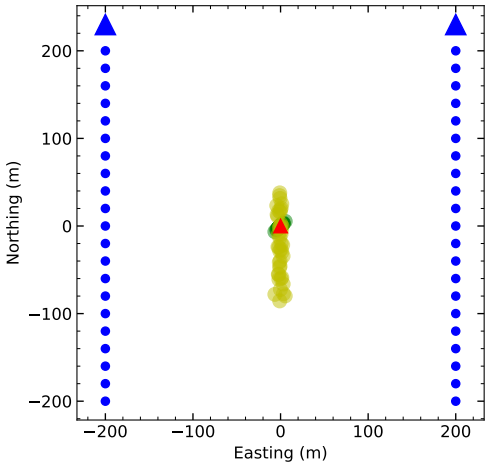

(b) Pitch

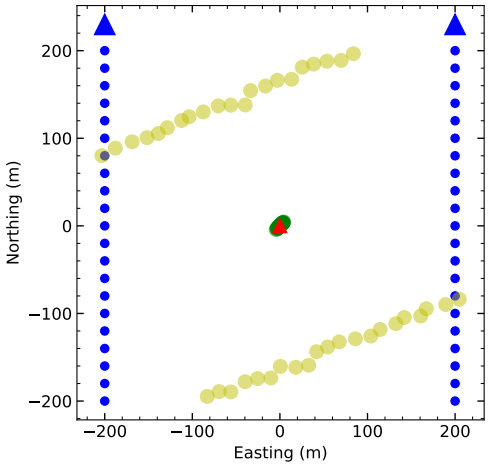

(c) Yaw

Figure 3.1: 45 deg of misalignment behaviour on the roll (a), pitch (b) and yaw (c) angles. Simulations conducted with 1 deg of noise on the angle's measurements and 1 m on the range's measurements.

with these parameters, the initial average error before the calibration was 96.45 m, which decrease down to 17.24 m after the calibration, see the circumferences of Fig. 3.2. The misalignment computed using the LS-SVD method were:

- Misalignment (angular):
  - Roll = 19.9 deg
  - Pitch = 19.7 deg
  - Yaw = 20.7 deg
- Misalignment (distance):
  - x-axis = 0.3 m
  - y-axis = 1.0 m
  - z-axis = 0.1 m

which are similar to the real parameters introduced. Hance, the great performance of the implemented LS-SVD method can be derived. In Fig. 3.3 the Root Mean Square Error (RMSE) of the target's estimation before and after the calibration procedure is represented.

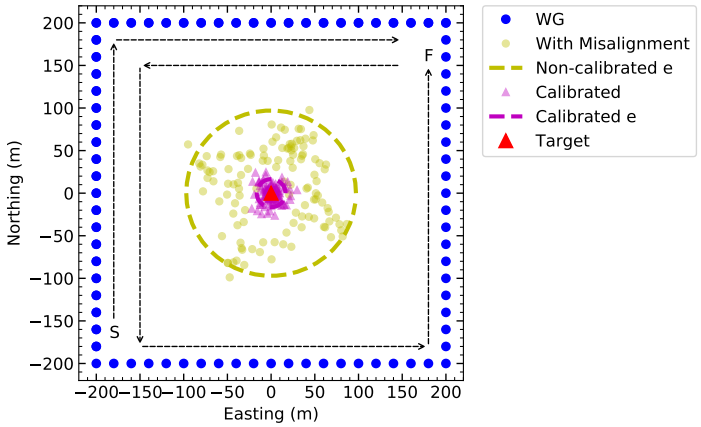

Figure 3.2: Simulation results after conducting a square path trajectory around the target with an ASV in order to calibrate its USBL. The arrows indicates the trajectory's direction of the ASV (WG), the yellow points are the target prediction without the calibration, and the magenta points are the estimations after the calibration. The circumferences indicate the RMSE after and before the calibration.

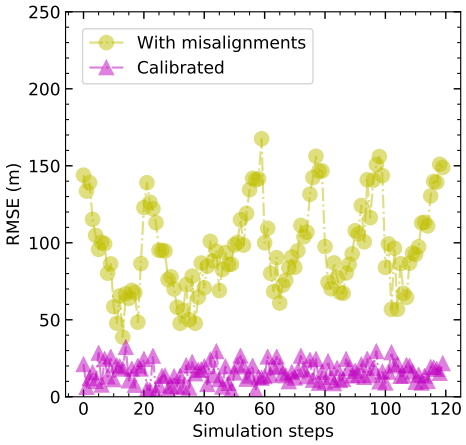

Figure 3.3: The RMSE of the target position result estimated with the USBL before and after its calibration.

3.4 Field tests

Finally, a set of tests have been conducted to calibrate and parameterise the Benthos DAT modem error. The DAT transponder is installed on a keel situated in the stern part of the Wave Glider, as can be observed in Fig. 3.4. Firstly, a detailed set of measurements were conducted to measure all the misalignments between the DAT transponder, the Inertial Navigation System (INS), and the GPS elements. These measurements are shown in Fig. 3.5 and Fig. 3.6.

Figure 3.4: The Wave Glider used during the tests, and a zoom of the DAT system installed in the keel (inset)

Mechanical Specifications
GPS, INS and DAT Overall Dimensions (cm)

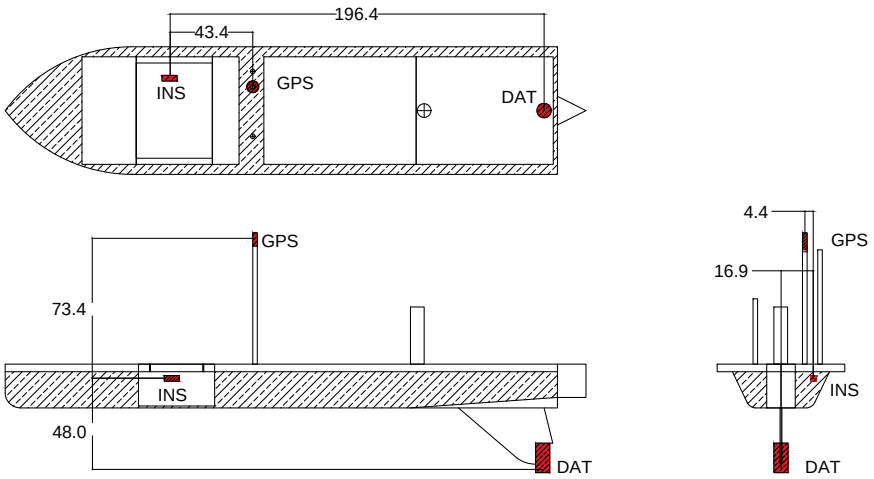

Figure 3.5: Distances in cm between each element installed on the Wave Glider, the DAT, the INS, and the GPS

Wave Glider-based Communications Hot Spot. Task ID 1: Improve DAT target location accuracy

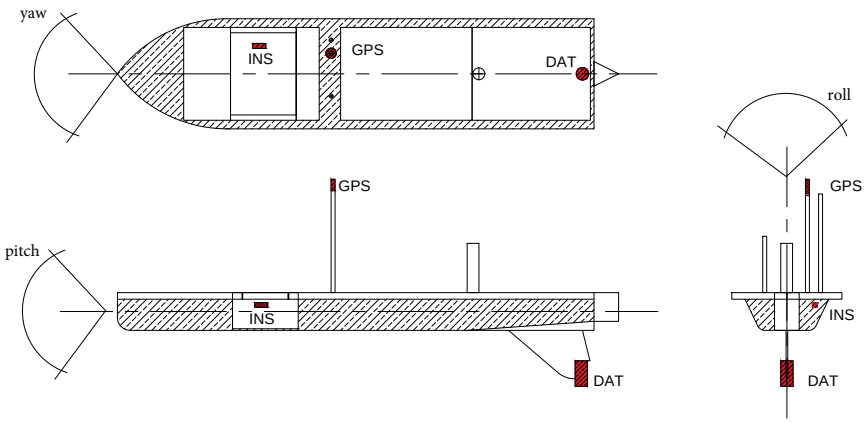

Figure 3.6: The roll, pitch and yaw angles representation using the Wave glider as a reference

On the other hand, these tests were conducted using an acoustic modem which was deployed in a moored line (used as a target), near to the Moss Landing harbour, at ~34 m depth on July 20, of 2016. The moored line had a surface buoy with a Stella GPS to know its position. This configuration is shown in Fig. 3.7, and a photography conducted after its deployment is shown in Fig. 3.8. The geographic coordinates of the target obtained using the Stella GPS were 36.81359 deg latitude

and -121.82074 deg longitude.

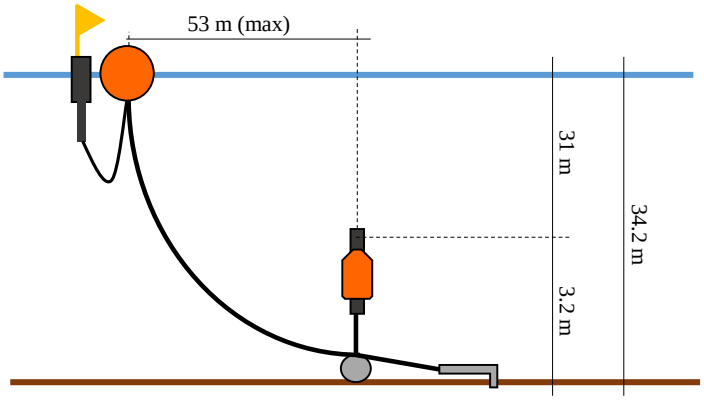

Figure 3.7: Configuration of the Benthos acoustic modem and the Stella GPS systems used to calibrate the USBL of the Wave Glider

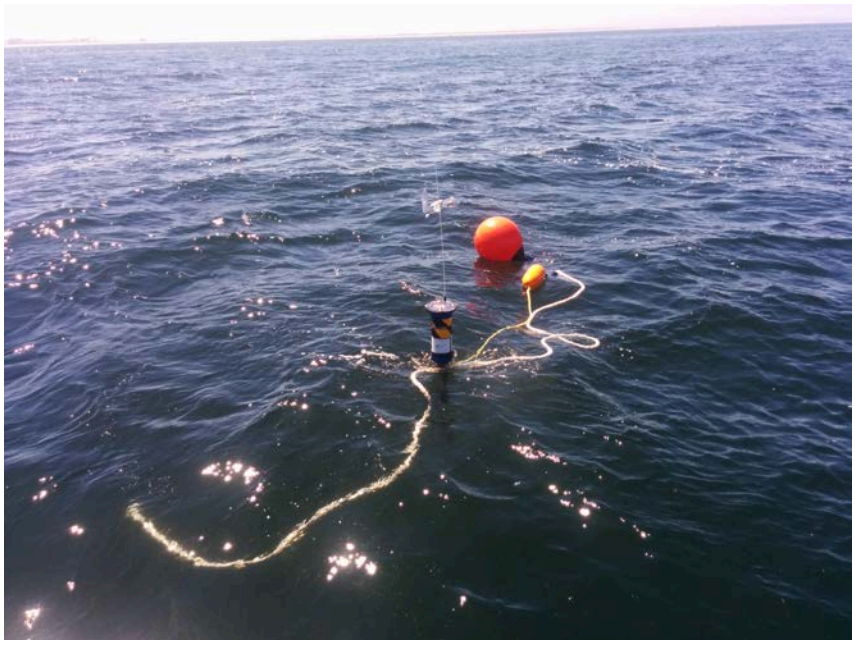

Figure 3.8: The moored line used as a target to calibrate the Wave Glider's DAT system

With this modem as a target to detect, different tests were conducted, each one with a different path configuration, the results obtained are presented in the following section.

3.5 DAT filter

In order to improve the data generated by the Benthos DAT system, a filter should be implemented. This is specially important in acoustically complicated scenarios such as shallow waters (e.g. due to the multipath propagation). Under this consideration, here the filter proposed by Bred Jones [90] was used. This filter was designed specifically for the same Wave Glider (with the DAT) used in these tests, which is used to remove the influence of the data outliers produced by multipath behaviour. The main idea is to use an error function weighted moving range average filter. This filter is combined with the bearing and elevation data to better estimate a real time position for an underwater target.

Firstly, the average of the target estimation position $\hat{\mathbf{q}}_k \in \mathbb{R}^n$ using the latest $N \in \mathbb{N}$ estimations is computed, where $k \in \mathbb{N}$ is the current discrete time, and $n \in \{2, 3\}$ is the space dimension of the problem. This is defined as

$$\hat{\mathbf{q}}_k = \frac{1}{N} \sum_{i=1}^{N} \hat{\mathbf{q}}_{k-i}. \tag{3.14}$$

Then, the difference between the estimated position $\hat{\mathbf{q}}$ and the new position $\mathbf{q}$ is computed for each new DAT measurement as

$$\Delta \mathbf{q}_k = \mathbf{q}_k - \hat{\mathbf{q}}_k, \tag{3.15}$$

which yields into a difference equal to

$$\Delta r_k = ||\hat{\mathbf{q}}_k|| = \sqrt{\hat{\mathbf{q}}_k^T \hat{\mathbf{q}}_k}. \tag{3.16}$$

The position difference is then *weighted* according to the following exponential decay function

$$\Delta \mathbf{q}_w = w \Delta \mathbf{q}_k, \tag{3.17}$$

where $w = \exp(-\Delta r/\tau)$, and τ is an empirically derived constant. Using (3.17), the new weighted position becomes

$$\hat{\mathbf{q}}_w = \mathbf{q}_k + \Delta \mathbf{q}_w, \tag{3.18}$$

which is used to compute the final target position by

$$\hat{\mathbf{q}}_k = \frac{1}{N} \Big[\Big(\sum_{i=1}^{N-1} \hat{\mathbf{q}}_{k-i} \Big) + \hat{\mathbf{q}}_w \Big] \tag{3.19}$$

3.6 Results

Different Wave Glider tracks were conducted on July 2016 to observe some possible misalignment and to characterize the target position estimation accuracy obtained using the Benthos DAT system.

3.6.1 Preliminary adjustments

A set of tests were carried out on July 21, 25 and 27, where a square path with 400 m at each side was used for the two first tests, and a square path with 800 m side was used for the third test. Different information could be obtained with the raw data registered during these tests, such as filtering performance, range error and compass misalignment.

In addition, the real target position was obtained using a range-only target localisation method based in the LS algorithm. This method is well explained in Section 4.3, here it has only been used to adjust the initial deployment position measured with the boat's GPS, and to correct the difference between the Stella GPS position on the sea surface and the modem deployed on the sea floor.

A Filtering performance

In Fig. 3.9 the data generated during the three tests is presented, where besides the Wave Glider's path and the real target position, the target estimated by the DAT before and after applying the filter explained in Section 3.5 are shown.

We can observe that the raw target position obtained with the DAT system presented some outliers, in those cases, the estimation had a significant error which was greater than 400 m. The error computed between the real target position and the measured one with the DAT before and after the filter are presented in Fig. 3.9 (right column).

Whith these figures, the necessity of a filter in order to eliminate outliers (probably produced by multipath behaviour due to the shallow water scenario) was demonstrated, where the good performance of the filter proposed in [90] was also validated, which proportionate a maximum error down to ~200 m.

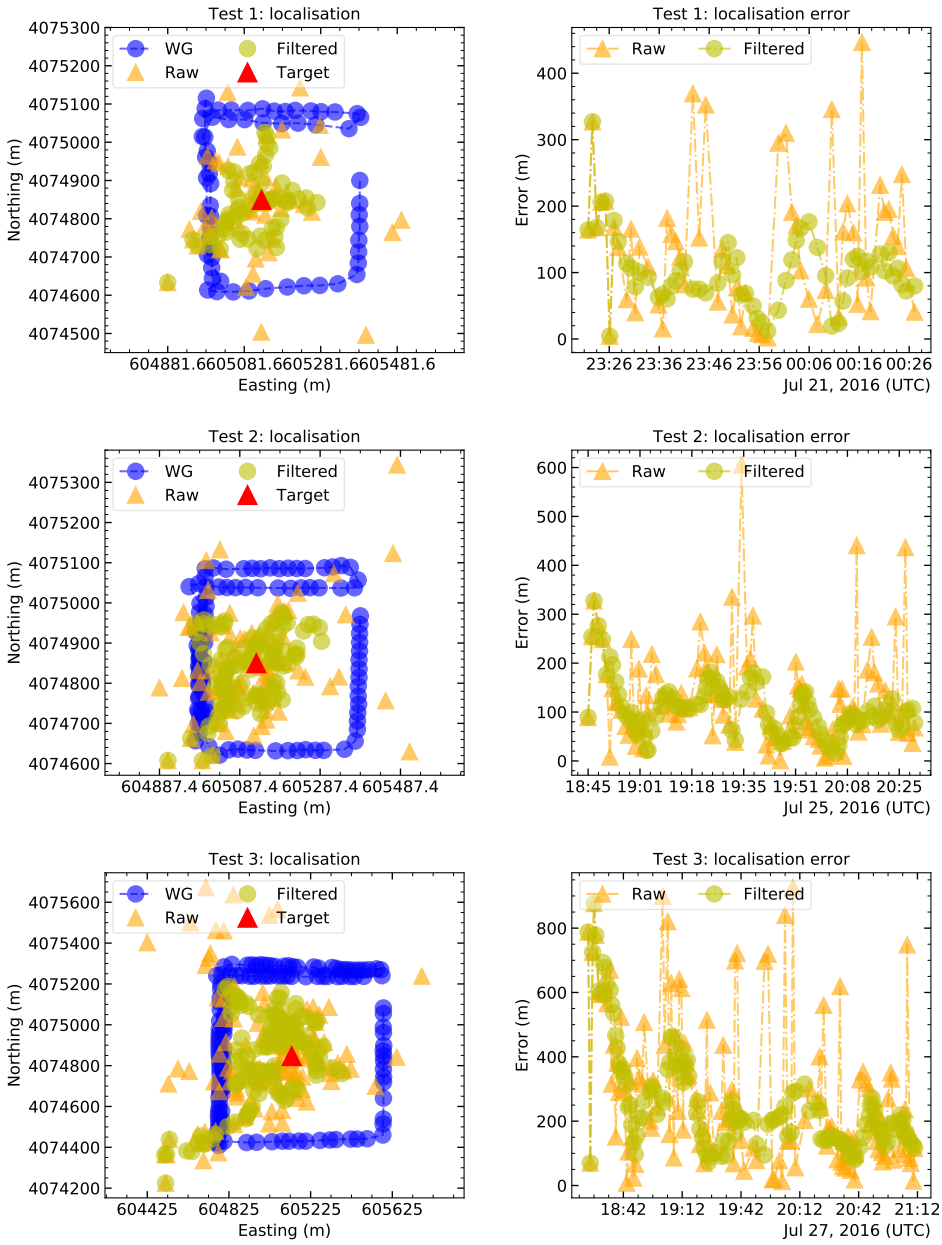

Figure 3.9: Left column: x-y representation of the target estimated position using the DAT system, before the filter (Raw) and after applying the filter (Filtered). Moreover, the Wave Glider's track and the real target position are represented as blue dots and a red triangle respectively. Right column: Error computed between the real target position and the measured one with the DAT, before and after applying the filter.

B Range adjustments

In the following subsection, the range measured between the Wave Glider and the acoustic modem deployed on the sea floor was studied, see Fig. 3.10. The main goal here was to compute the error which might appear due to the variation of the sound velocity in water, which is typically ~1500 m/s, which may vary depending on different parameters (e.g. due to the temperature or salinity). Then, a compensation parameter can be added to adjust the slant range measured with the DAT. It is known that, using the Time Of Flight (TOF), the range between two devices is defined by

$$r_{DAT} = \tau c + \tau w_c, \tag{3.20}$$

where τ is the time that a signal transmitted by the device A needs to reach the device B, c is the sound velocity in water (1500 m/s), and w_c is the unknown uncertainty about the sound velocity in water.

Then, using the real slant range $r_{GPS} = \tau c$ which was computed by the GPS positions of both devices, (3.20) can be rewritten as

$$r_{DAT} = r_{GPS} + \frac{r_{GPS}}{c} w_c = r_{GPS}\big(1 + \frac{w_c}{c}\big) = \mathrm{k} r_{GPS}, \tag{3.21}$$

where the constant ratio $\mathrm{k} = 1 + w_c/c$ can be easily computed dividing the slant range measured by the DAT and the one computed using the GPS's positions. This ratio is shown in Fig. 3.10 right column. We can see that the ratio is ~1, which demonstrates that the range measurement by (3.20) is very precise.

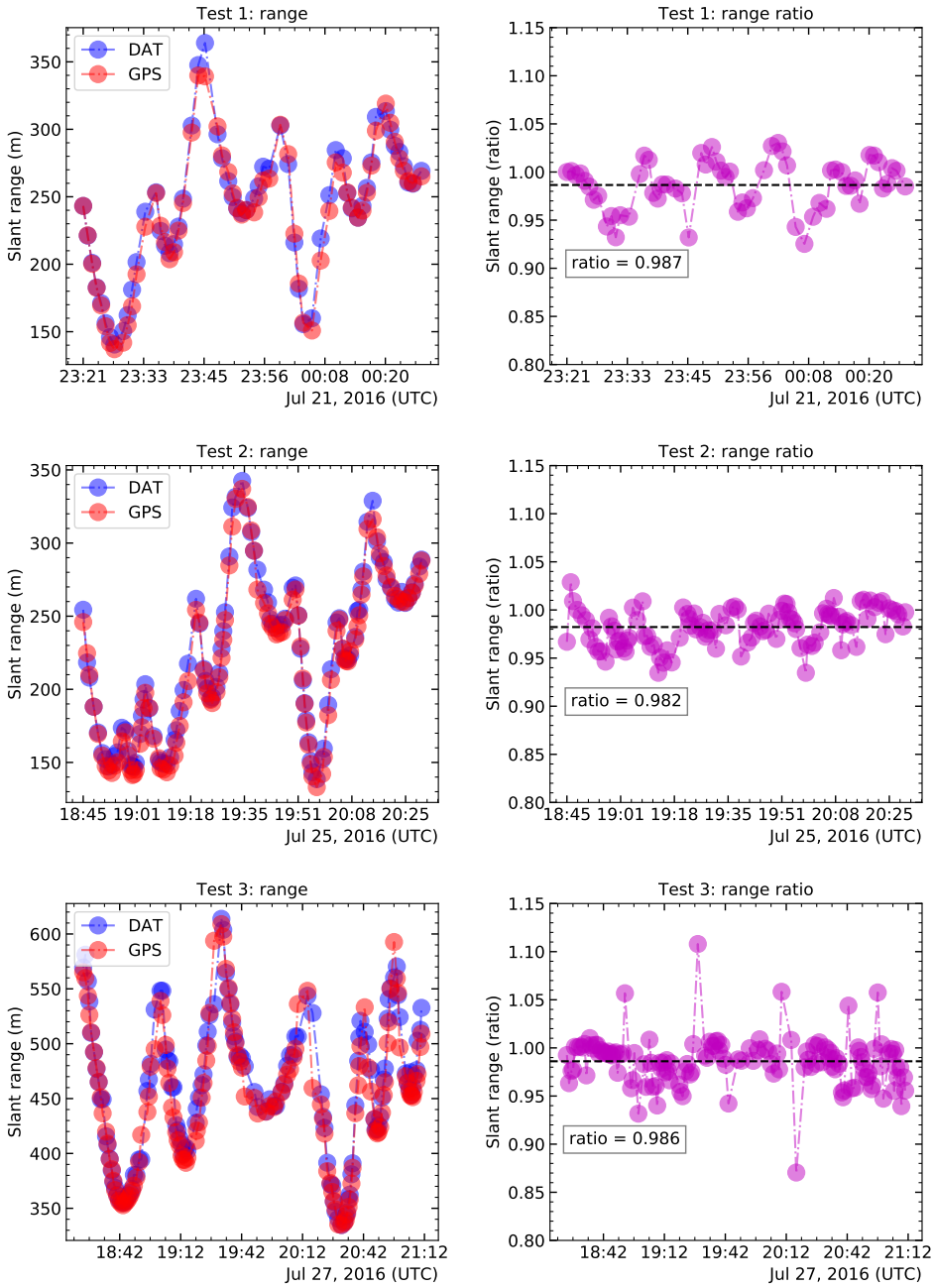

Figure 3.10: Left column: Slant range obtained using the DAT system, and the slant range computed using the Wave Glider's GPS. Right column: Range ratio used to adjust the slant range measured by the DAT

C Compass calibration

The compass is an important element which must be regularly calibrated. Usually, all manufacturers have their own dedicated software to accomplish that. Nonetheless, a good praxis is to check frequently if some bias is presented in situ. For this purpose, a theoretical *ideal* vehicle yaw was computed using the GPS positions, using the following assumption: The Wave Glider's yaw and its direction velocity were the same. Whereas this assumption can be wrong (e.g. due to strong sea currents), its the best estimation that we had. For that reason, only an approximation of the compass's performance is conducted in this section, and a detailed calibration should be conducted in a deck for a better result.

In Fig. 3.11 the *ideal* compass yaw (green colour), and the vehicle yaw (blue colour) and the easting position (red colour) are represented. On the other hand, in Fig. 3.11 (right column) the error between the compass and vehicle yaw with a curve fitting of 2^{nd} order is also represented. We can observe that some misalignment is presented in the yaw compass, especially for the angle values close to 0 deg.

D Bearing and elevation angles

Finally, a close look into the bearing and elevation angles measured by the DAT system are shown in Fig. 3.12 and Fig. 3.13 respectively. In these figures we can observe the large error presented in the measurements, specially in the elevation angles. This poor performance was probably due to the complicated scenario used to conduct these tests. In shallow waters, the multipath behaviour is a challenging aspect which must be faced by any acoustic localisation system, specially by the USBL system, which is less robust in front of this behaviour.

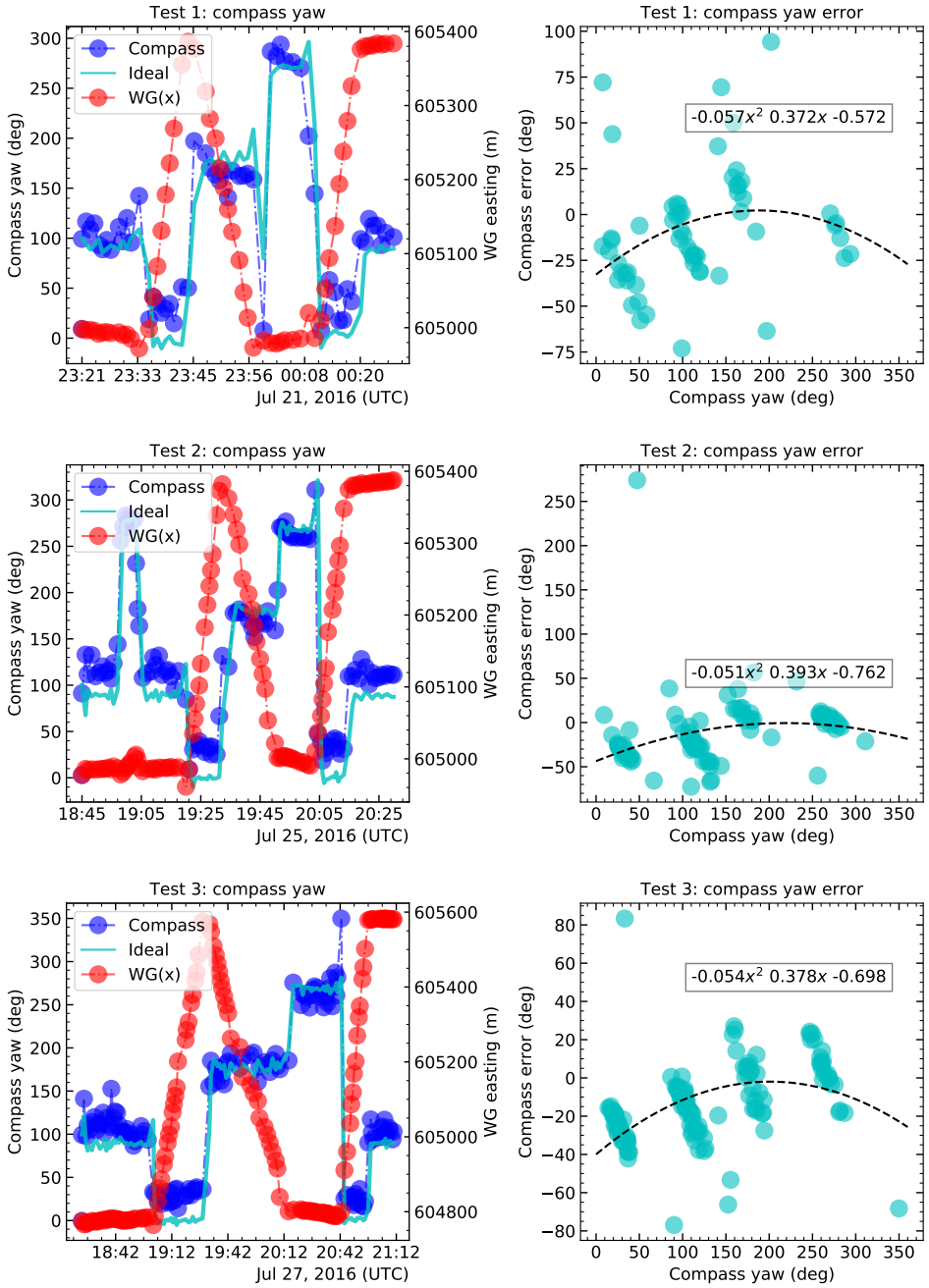

Figure 3.11: Left column: Comparison between the compass yaw (Compass) and the *real* yaw (Ideal) computed using the Wave Glider's velocity direction. The easting values of Wave Glider path are represented as WG(x). Right column: Compass error and its second degree polynomial curve fitting

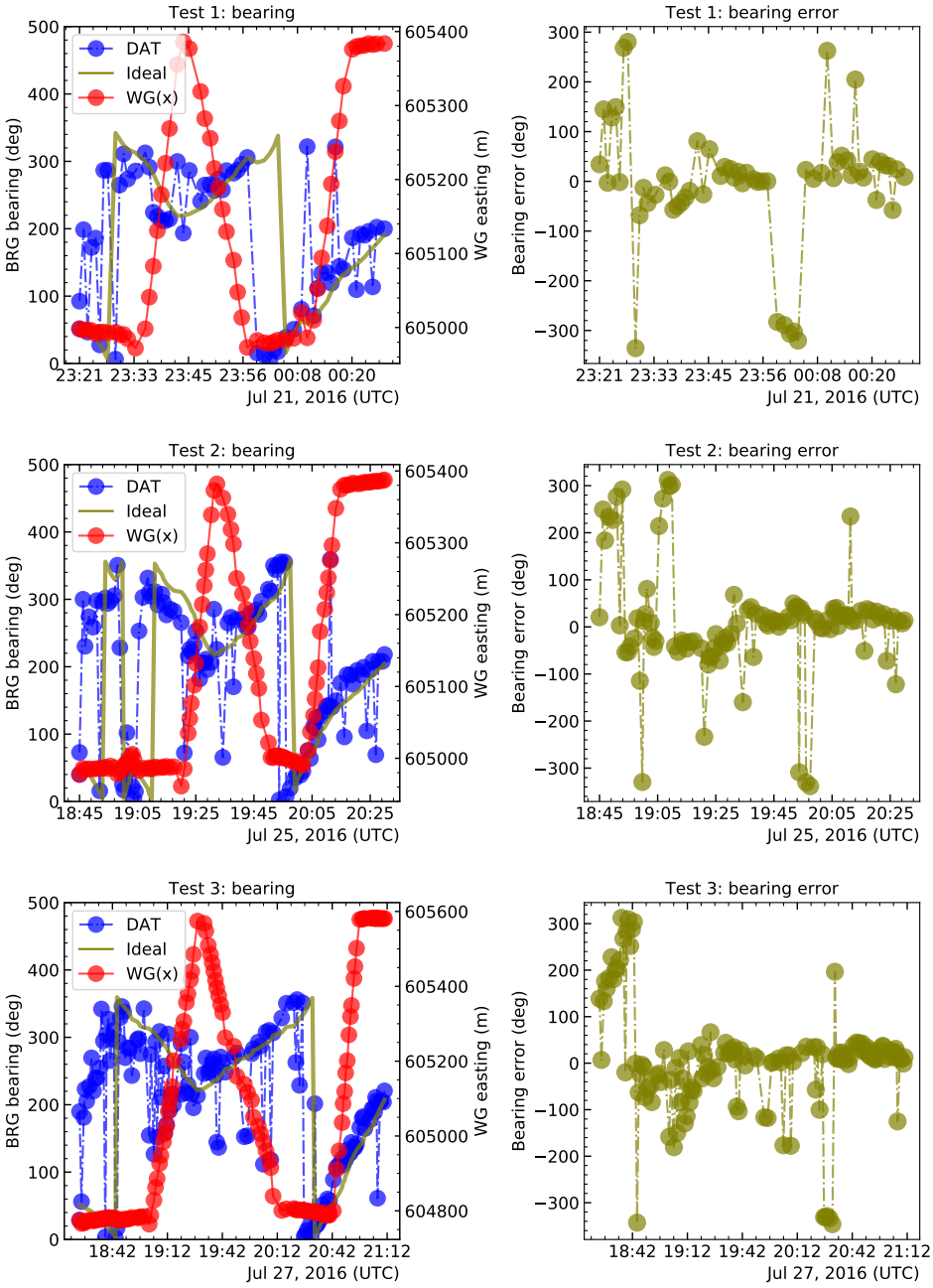

Figure 3.12: Left column: Comparison between the target bearing measured by the DAT, and the *real* bearing computed using the Wave Glider's and target's position. Right column: Bearing error

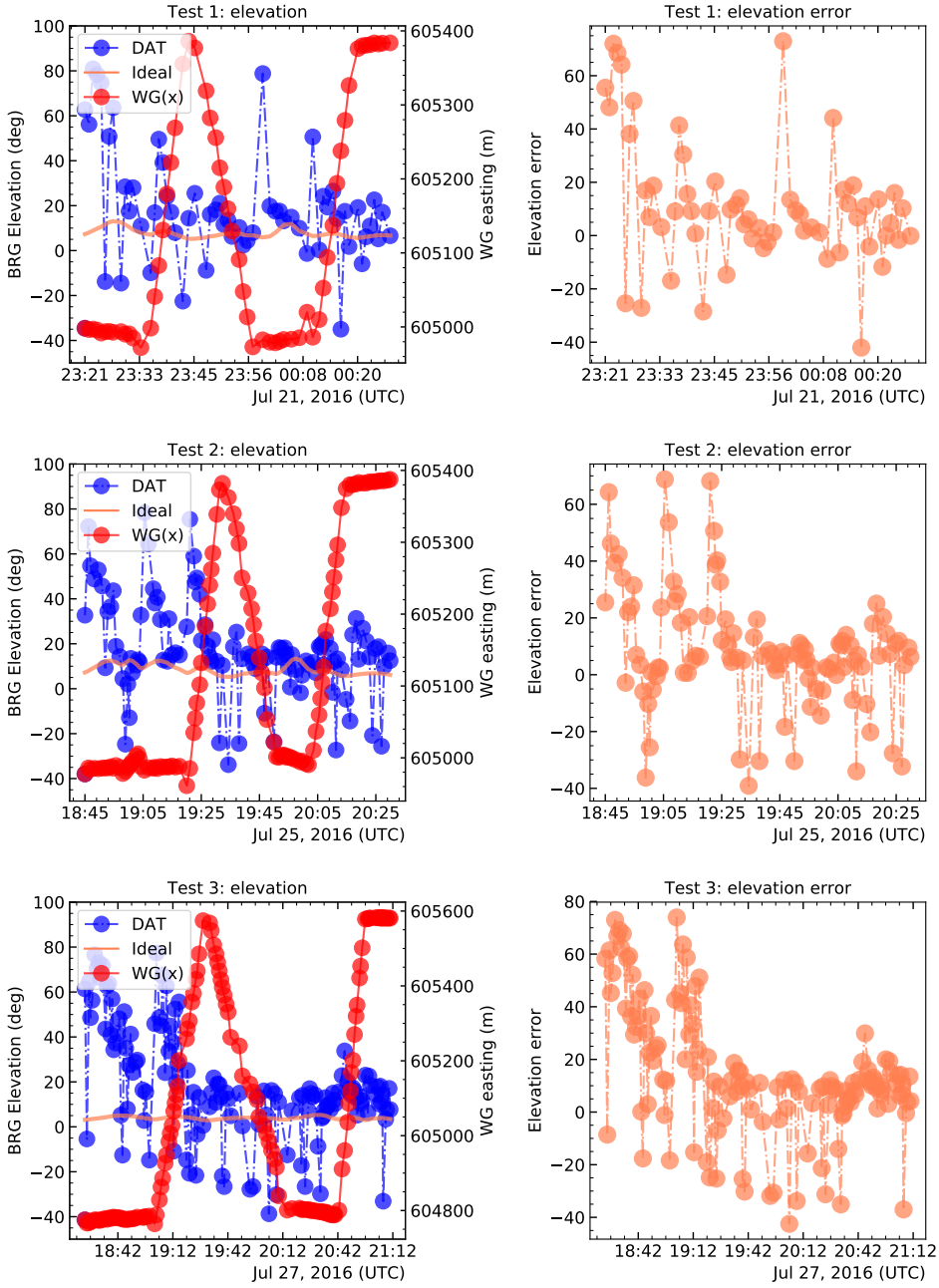

Figure 3.13: Left column: Comparison between the target elevation measured by the DAT, and the *real* elevation computed using the Wave Glider's and target's position. Right column: Elevation error

E Recapitulation

Finally the parameters obtained during the three tests presented above are summarized in Table 3.1.

Table 3.1: Preliminary parameters to adjust the Benthos Directional Acoustic Transponder (DAT) system.

Test number	Date	Range ratio	Compass coefficients
1	July 21	0.987	$-0.057x^2 + 0.371x - 0.552$
2	July 25	0.982	$-0.051x^2 + 0.393x - 0.762$
3	July 27	0.986	$-0.054x^2 + 0.378x - 0.698$

Taken into consideration the mean of the three tests, the range ratio was equal to 0.985, and the compass calibration coefficients were equal to $-0.054x^2 + 0.381x - 0.671$.

3.6.2 DAT calibration parameters

Now, with the information obtained during the three tests explained in the previous section, the LS-SVD algorithm explained in Section 3.2 was used to compute the possible misalignments presented between the Wave Glider and the different USBL elements. The results for all three tests are shown in Fig. 3.14, where the error before and after applying the misalignment correction is presented. We can see that in all cases the estimated final target position was better when the misalignment adjustment was conducted. The misalignment parameters for all the three tests are summarized in Table 3.2.

Finally, in Table 3.3 the target position error is presented. In this case, the final estimated target position was computed using the average values between the first two tests as a misalignment coefficients. With these parameters, the target estimated positions and their errors were computed again. In this table, the errors' reduction in percentage are also presented.

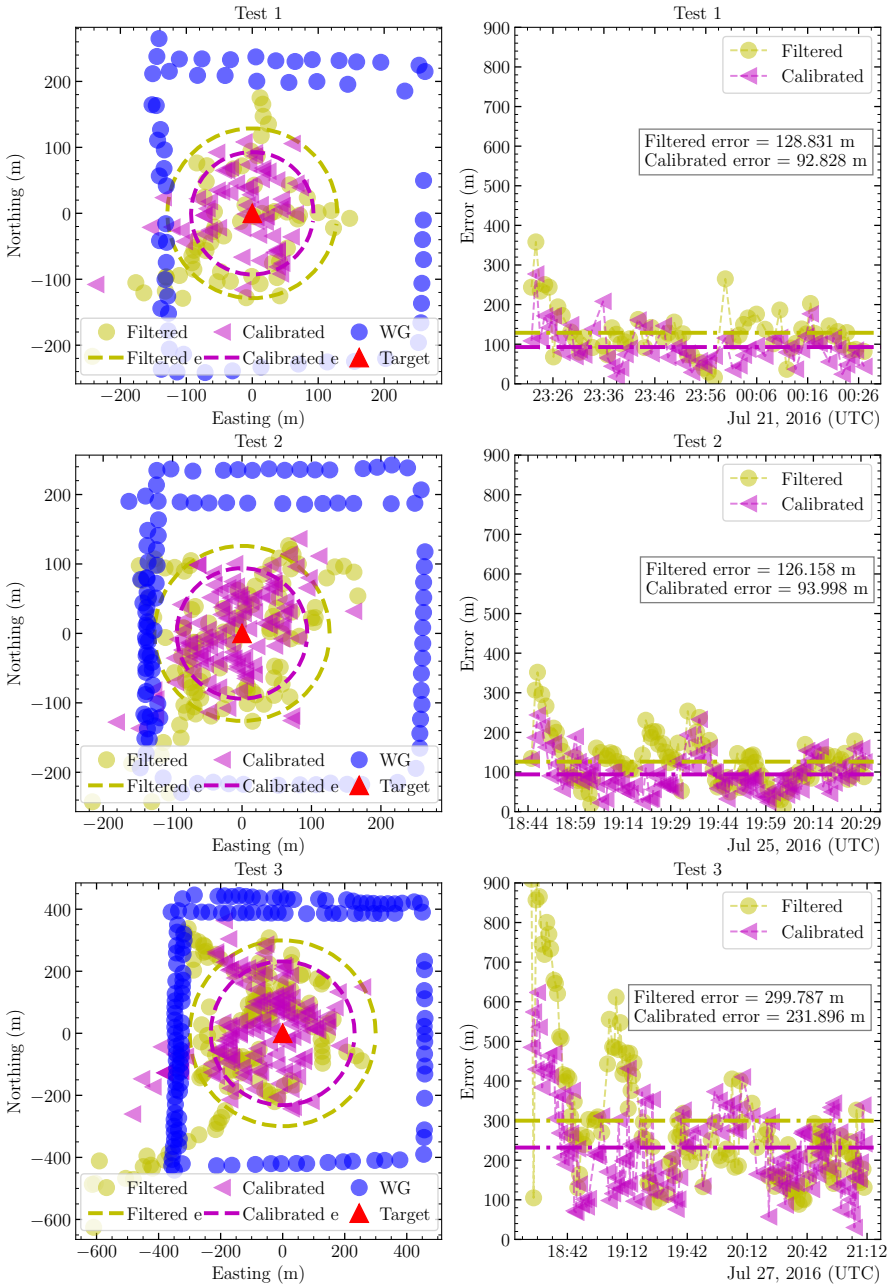

Figure 3.14: The left plots show the $x - y$ plane with the Wave Glider positions (blue dots), the true target position (red triangle), and the target estimations using the DAT before and after the misalignment's correction (yellow circles and violet triangles respectively). The right plots show the errors and their average values before and after the misalignment correction.

Table 3.2: Misalignment parameters: Rotation matrix, translation matrix and scaling factor

Test	$\mathbf{R}_{SVD}$	$\mathbf{T}_{SVD}$	c_{SVD}
1	$\begin{bmatrix} 0.962 & 0.087 & -0.258 \\ -0.037 & 0.98 & 0.194 \\ 0.27 & -0.177 & 0.947 \end{bmatrix}$	$\begin{bmatrix} 46.040 \\ -3.143 \\ 61.549 \end{bmatrix}$	0.986
2	$\begin{bmatrix} 0.944 & -0.032 & -0.329 \\ 0.152 & 0.925 & 0.348 \\ 0.293 & -0.378 & 0.878 \end{bmatrix}$	$\begin{bmatrix} 47.234 \\ 16.272 \\ 77.306 \end{bmatrix}$	1.046
3	$\begin{bmatrix} 0.822 & 0.127 & -0.556 \\ 0.13 & 0.907 & 0.4 \\ 0.555 & -0.401 & 0.729 \end{bmatrix}$	$\begin{bmatrix} 23.723 \\ 14.9 \\ 210.308 \end{bmatrix}$	1.053

Table 3.3: Target estimation errors before and after the misalignment's adjustment

	Error (m)				
Test	Initial	Compensated [a]	Reduction (%)	Compensated [b]	Reduction (%)
1	128.83	92.83	28	95.10	26
2	126.16	94.0	25	95.27	24
3	299.79	231.9	23	259.02	14

[a] using their own misalignment parameters

[b] using the average value of the two first tests

3.7 Conclusions

As observed in this section, the use of an USBL to localise an underwater target is a great tool, but has its limitations. For example, in complex scenarios, such as shallow waters, this system has important errors. Some of them provably due to the multipath propagation. Moreover, the Wave Glider is more vulnerable in front of adverse sea state than bigger vessels.

This behaviour can be observed specially in the elevation angles, which are really noisy and have lots of outliers during all the tests conducted. The error measured in this section is not unusual. For example, in posterior tests conducted by Brent Jones [90] the estimated target error obtained for a target's depth equal to 80 m was also around 100 m, and only was better when the target was tracked at 200 m depth, in that case the error was ~30 m.

On the other hand, the installation of a USBL in small platforms, such as a Wave Glider, yields in a complex configurations, where both the size and power consumption restrictions cause the use of better devices infeasible (e.g. Fibre Optic Gyro Compass (FOG) systems).

As a result, other acoustic underwater target localisation methods should be taken into considerations, for example the ones which lies on range measurements, which have been demonstrated much more reliable. These methods are extensively explained in the following sections.

Chapter 4

Range-only and single-beacon methods: A static scenario

The Range-Only and Single-Beacon (ROSB) target localisation using autonomous vehicles and acoustic modems will solve the limitations in the coverage zone and deployment costs presented by Long BaseLine (LBL) systems, and will solve the uncertainty presented by Ultra-Short BaseLine (USBL) systems when working in complex scenarios such as shallow waters.

4.1 Introduction

Underwater localisation using acoustic signals is one of the main components in a navigation system for an Autonomous Underwater Vehicle (AUV) as a more accurate alternative to dead-reckoning techniques. While different methods based on the idea of multiple beacons have been studied, other approaches use only one beacon, which reduces the system's costs and deployment complexity. The inverse approach for single-beacon navigation is to use this method for target localisation by an underwater or surface vehicle. In the previous chapters, we have observed some limitations of the traditional Short BaseLine (SBL) and USBL methods. For example, the SBL system require a complex deployment and calibration procedure, and the USBL system has important errors measuring the bearing and elevation angles, whereas the range error was quite low. Therefore, if a more dynamic system, capable of localising targets in different zones without previous interventions, and with high accuracy is needed, a system by the use of autonomous vehicles and range measurements is the most appropriate. Here, a method of ROSB target localisation using a Wave Glider is presented, for which simulations and sea tests have been conducted to determine optimal parameters to minimize acoustic energy use and search time, and

to maximize location accuracy and precision. Finally, a field mission is presented, where a benthic Rover (an autonomous seafloor vehicle) is localized and tracked using low human intervention. This mission shows, as an example, the power of using autonomous vehicles in collaboration for oceanographic research.

4.1.1 Motivation

One of the main challenges in oceanographic research lies in underwater positioning. Due to the large attenuation of radio waves in water, it is well known that Global Positioning System (GPS) signals are not suitable underwater. Consequently, different methods and architectures have been developed using acoustic signals, which have better a underwater performance, such as LBL, USBL and GPS Intelligent Buoy (GIB). Usually, the range between two transponders is computed knowing the Time Of Flight (TOF) of a transmitted signal (and the sound speed in water), then these ranges are used to calculate the position of the sound source. Each of these systems has its own application as a function of the project's necessities and constraints. For example, the LBL system offers the best precision and accuracy, but with high deployment and maintenance costs. These costs can be somewhat reduced by GIB systems, which use surface buoys instead of sea-floor nodes. If the main goal is to reduce the set up time, the best option is a USBL system, but with less accuracy than the other methods.

On other hand, some studies have focused on single beacon localisation methods to reduce the deployment costs (e.g. [63], [78], [91] and [92]). The main idea behind this architecture is to use an autonomous vehicle as a mobile landmark to compute the position of an underwater target, which, while moving in the area, takes some ranges between the target and itself to triangulate the target's position.

4.1.2 Related work

In general, the ROSB methods are based on an autonomous vehicle which is used as a tracker (or observer). This vehicle conducts a set of manoeuvres in order to track (or localise) some target(s). In this manoeuvre, the vehicle periodically performs new slant range measurements using the TOF of exchanged messages between the tracker and the target (e.g. [93]), whereas the LBL method uses the Time Difference Of Arrival (TDOA) between different well localized and synchronized transponders deployed previously on the seafloor (e.g. [94], [95], and [96]). The TOF method estimates the target's position by the use of different range measurements, and then, applying triangulation methods [97]. The interest in ROSB has increased in recent years as a consequence of the necessity to reduce localisation costs (e.g. transpon-

ders' deployment and clocks' synchronization) [58] [98], and to find new techniques to localize and track multiple nodes in Underwater Acoustic Networks (UWAN), [58], or in fleets of AUVs, where all the nodes have their own acoustic communication modem, which can be used to know the ranges from other nodes on the gird. For example, this methodology is used in the MORPH EC FP7 project [20] as explained in [59]. The authors present a system called Distributed Long Baseline (DLBL), where high synchronized modems from EvoLogics in 4-node network composed for AUVs were used.

In contrast, this technique is also used in single node architectures. For example, it is used in applications such as Simultaneous Localisation and Mapping (SLAM) and AUVs aid navigation, [60], [61], and [62], and AUV homing as well, [63] and [64]. Finally, single-beacon localisation using autonomous vehicles as a moving landmark can also be used for target positioning and tracking in large areas without the fixed beacons' constraints. As an example, in [65] a tracking and following method of a tagged Leopard shark was presented.

However, the ROSB has its particular challenges, such as path characterisation (path shape, number of points and maximum range) or performance evaluation (accuracy and reliability). All of these parameters must be evaluated under different circumstances and setup characteristics.

In the literature, different papers about observability (which introduces some restrictions in paths and maneuvers) can be found, for example in [99] the authors derive that the best trajectory is to do turning motions around the beacon, and in [91] a similar approach is used with a surface vehicle following three AUVs. On other hand, [98] shows a complete study to determine the optimal sensor placement for acoustic underwater target positioning with range-only measurements. Other works are focused on algorithms and their improvement under specific circumstances, such as in [100], where the authors improve a recursive algorithm for target localisation in an isogradient sound speed profile. Nevertheless, all these works are mathematical developments and only show some simulations.

[101] have studied cooperative AUV navigation using surface vehicles, which use acoustic ranges as navigation aids. They studied three filtering and smoothing techniques, the Extended Kalman Filter (EKF), the Particle Filter (PF), and the Nonlinear Least Squares (NLS), where the NLS yielded with a better accuracy. Experiments and field tests had been conducted in a shallow water environment. Posterior studies conducted by [102] show the performance of the Centralized Extended Kalman Filter (CEKF) to improve the dead-reckoning navigation systems, using acoustic ranges from a surface vehicle as a navigation aid. Moreover, they show different experiments in a deep water area. In both studies, they used the

Woods Hole Oceanographic Institution (WHOI) micro-modems, [103]. Nonetheless, whereas their studies are extended and completed in the use of acoustic range as navigation aids, more studies are needed to characterize the ROSB target localisation method; e.g. to find the best range distances or path shapes.

Finally, in other works such as [92] and [104] the authors present some field test results to localize an underwater target using range-only methods, but in their case, they do not present a general study to find the best parameters for target localisation.

4.1.3 Contributions

The work presented in this chapter shows how to determine the optimal parameters of the ROSB target localisation method for static targets. Additionally, results of simulations and sea tests to demonstrate the good performance of a Wave Glider used as a single-beacon LBL system for target localisation are presented. This method can be used in a wide range of applications using the long-duration, autonomous navigation, and computational characteristics of Wave Glider applications:

(i) Target localisation in a benthic zone:

- Instruments on seabed, which may be stationary or moving (e.g. slowly sliding down a submarine canyon, or on a benthic Rover)
- Low motion tagged benthic marine species

(ii) Target localisation in a Pelagic zone:

- Drifter buoys
- Autonomous Underwater Vehicle (AUV)
- Low motion tagged pelagic marine species

Preliminary studies were presented in [105], where both simulations and field test results were shown under different circumstances such as circular radius and offsets. However, the field results in the case of different offsets did not coincide with the simulations with the same accuracy as in the radius case. In this chapter, a more accurate random error model, which it was described in [106], and a systematic error is studied in order to increase the simulations' accuracy. Finally, more cases such as path shape, time and power consumption are presented to have a completed study.

4.2 Optimal path shape

The relationship between the sensor location and the accuracy that can be achieved in measurement estimation has been widely studied, see [107] and the references therein. The potential areas which are faced with the sensor-location problem can be for example environmental monitoring, surveillance, and meteorology.

In general, the computation of the optimal sensor configuration can be carried out by examining the Cramér-Rao Bound (CRB) or its Fisher Information Matrix (FIM) as is well known [108]. In an estimation problem, where a set of noisy observations are used to estimate a certain parameter of interest, the CRB sets the lowest bound on the covariance matrix that is asymptotically achievable by any unbiased estimation algorithm.

Therefore, because the CRB is calculated from the inverse of the FIM of the likelihood function, one can use both to find the optimal sensor configuration. At this point, the determinant of the FIM is used as a performance indicator, where maximizing this quantity yields the most appropriate sensor formation geometry. For example, [98] used this method to find the optimal sensors' locations of an underwater sensor network to find a target using their ranges, and [94] derived the target's localisation accuracy using TDOAs measurements on different sensor geometry scenarios. In this chapter, similar approaches are used, where the optimal path shape can be derived taken into consideration that each sensor's position is where the Wave Glider will obtain a new range measurement from the target. This method can be called: ROSB target localisation.

As a reslut, following standard procedures, the FIM corresponding to the problem of range-based target positioning can be computed from the likelihood function

$$p(\boldsymbol{z}|\boldsymbol{p}_T) = \frac{1}{(2\pi)^{m/2}|\boldsymbol{R}|^{1/2}} \exp\Big\{ -\frac{1}{2}\big(\boldsymbol{z} - \boldsymbol{r}(\boldsymbol{p}_T)\big)\boldsymbol{R}^{-1}\big(\boldsymbol{z} - \boldsymbol{r}(\boldsymbol{p}_T)\big)\Big\}, \tag{4.1}$$

where m is the number of measurements, $\boldsymbol{p}_T$ is the target's position, $\boldsymbol{z} = [z_1, ..., z_m]^T$ are the measured ranges, $\boldsymbol{r}(\boldsymbol{p}_T)$ are the true ranges between each position of the WG and target, and $\boldsymbol{R}$ are the covariance matrix. In the particular case that $\boldsymbol{R} = \sigma^2\boldsymbol{I}_m$ (where $\boldsymbol{I}_m$ is the identity matrix), taking the logarithm of (4.1), computing its derivative with respect to $\boldsymbol{p}_T$, and taking its expected value, the FIM can be expressed as

$$\text{FIM} = \frac{1}{\sigma^2}\nabla\boldsymbol{r}(\boldsymbol{p}_T)^T\nabla\boldsymbol{r}(\boldsymbol{p}_T). \tag{4.2}$$

For a notation simplicity, and without loss of generality, hereinafter the target is considered to be placed at the origin of the inertial coordinate frame. Consequently,

(4.2) can be rewritten as

$$\text{FIM} = \frac{1}{\sigma^2}\sum_{i=1}^{m}\begin{bmatrix} \left(\frac{\partial r_i(\boldsymbol{p}_T)}{\partial p_{Tx}}\right)^2 & \frac{\partial r_i(\boldsymbol{p}_T)}{\partial p_{Tx}}\frac{\partial r_i(\boldsymbol{p}_T)}{\partial p_{Ty}} & \frac{\partial r_i(\boldsymbol{p}_T)}{\partial p_{Tx}}\frac{\partial r_i(\boldsymbol{p}_T)}{\partial p_{Tz}} \\ \frac{\partial r_i(\boldsymbol{p}_T)}{\partial p_{Ty}}\frac{\partial r_i(\boldsymbol{p}_T)}{\partial p_{Tx}} & \left(\frac{\partial r_i(\boldsymbol{p}_T)}{\partial p_{Ty}}\right)^2 & \frac{\partial r_i(\boldsymbol{p}_T)}{\partial p_{Ty}}\frac{\partial r_i(\boldsymbol{p}_T)}{\partial p_{Tz}} \\ \frac{\partial r_i(\boldsymbol{p}_T)}{\partial p_{Tz}}\frac{\partial r_i(\boldsymbol{p}_T)}{\partial p_{Tx}} & \frac{\partial r_i(\boldsymbol{p}_T)}{\partial p_{Tz}}\frac{\partial r_i(\boldsymbol{p}_T)}{\partial p_{Ty}} & \left(\frac{\partial r_i(\boldsymbol{p}_T)}{\partial p_{Tz}}\right)^2 \end{bmatrix}, \tag{4.3}$$

$$\text{FIM} = \frac{1}{\sigma^2}\sum_{i=1}^{m}\frac{1}{r_i^2}\begin{bmatrix} p_{ix}^2 & p_{ix}p_{iy} & p_{ix}p_{iz} \\ p_{iy}p_{ix} & p_{iy}^2 & p_{iy}p_{iz} \\ p_{iz}p_{ix} & p_{iz}p_{iy} & p_{iz}^2 \end{bmatrix}, \tag{4.4}$$

where $\boldsymbol{p}_i = [p_{ix}, p_{iy}, p_{iz}]^T$ for $i \in \{1, ..., m\}$ is the position of the *i-th* ranging Wave Glider position, and r_i the actual distance between target $\boldsymbol{p}_T$ and the *i-th* WG position.

The $log|\,\text{FIM}\,|$ function is used to define the optimal FIM which provides the maximum FIM determinant for simplicity reasons. Then, its derivatives with respect to the norms of the vectors and with respect to the angles have to be computed and equalled to zero to find its maximum, and consequently, the optimal path configuration. All this process is derived in [98], and therefore, here the final result is only presented, that is

$$\text{FIM}_{opt} = \frac{1}{\sigma^2}\begin{bmatrix} \frac{m}{3} & 0 & 0 \\ 0 & \frac{m}{3} & 0 \\ 0 & 0 & \frac{m}{3} \end{bmatrix}. \tag{4.5}$$

Finally, the general conditions that must be satisfied by the Wave Glider path in order to be optimal can be derived comparing the optimal FIM in (4.5) with the generic one in (4.4) as follows

$$\sum_{i=1}^{m}\frac{p_{ix}^2}{r_i^2} = \sum_{i=1}^{m}\frac{p_{iy}^2}{r_i^2} = \sum_{i=1}^{m}\frac{p_{iz}^2}{r_i^2} = \frac{m}{3}, \tag{4.6}$$

$$\sum_{i=1}^{m}\frac{p_{ix}p_{iy}}{r_i^2} = \sum_{i=1}^{m}\frac{p_{ix}p_{iz}}{r_i^2} = \sum_{i=1}^{m}\frac{p_{iz}p_{iy}}{r_i^2} = 0. \tag{4.7}$$

The above equations can be rewritten in terms of the angles that each range vector makes with the unit vector of the inertial reference frame as $cos(\alpha_{ij}) = p_{ij}/r_i$ for $i \in \{1, ..., m\}$ and $j \in \{x, y, z\}$, obtaining

$$\sum_{i=1}^{m}\cos^2(\alpha_{ix}) = \sum_{i=1}^{m}\cos^2(\alpha_{iy}) = \sum_{i=1}^{m}\cos^2(\alpha_{iz}) = \frac{m}{3}, \tag{4.8}$$

$$\sum_{i=1}^{m} \cos(\alpha_{ix}) \cos(\alpha_{iy}) = \sum_{i=1}^{m} \cos(\alpha_{ix}) \cos(\alpha_{iz}) \\ = \sum_{i=1}^{m} \cos(\alpha_{iz}) \cos(\alpha_{iy}) = 0. \tag{4.9}$$

With this formulation, the optimal sensor configuration is described in terms of the angles between the range vectors and the inertial frame. Consequently, the ranges themselves are not an important factor in this 3D scenario, and it can be concluded that the optimal sensor configuration lies on a sphere centred on the target.

Finding a generic formulation for a 3D scenario that solves these equations to obtain the optimal geometry is not trivial, however, the scenario presented in this chapter is a surface vehicle trying to localize an underwater target, which in other words means that all the sensors are placed on a plane. This situation is derived in the following subsection.

4.2.1 Surface vehicle and underwater target scenario

Considering that all the measurements are taken from a plane, which in this case is the sea surface, the optimal geometry is the intersection between a sphere centred on the target and this plane, Fig. 4.1. The circumference obtained (which with radius r_c) presents a relation between the target's depth z_T and the ranges r_i between the target $\boldsymbol{p}_T$ and the Wave Glider $\boldsymbol{p}_i$, which will define the optimal path that the vehicle must follow in order to obtain the best accuracy on the target's localisation prediction problem.

Thus, using $p_{iz} = z_T$, assuming that all ranges are equal, and substituting that in (4.6) the following relation is derived

$$\sum_{i=1}^{m} \frac{p_{iz}^2}{r_i^2} = \frac{m z_T^2}{r^2} = \frac{m}{3} \rightarrow \frac{z_T}{r} = \frac{1}{\sqrt{3}}. \tag{4.10}$$

Using simply a trigonometric formulation ($r_c^2 + z_T^2 = r^2$) the optimal path can be found, which is a circumference centred over the target with a radius equal to

$$r_c = \sqrt{2} z_T. \tag{4.11}$$

In contrast, the difference between the optimal solution and a solution by using

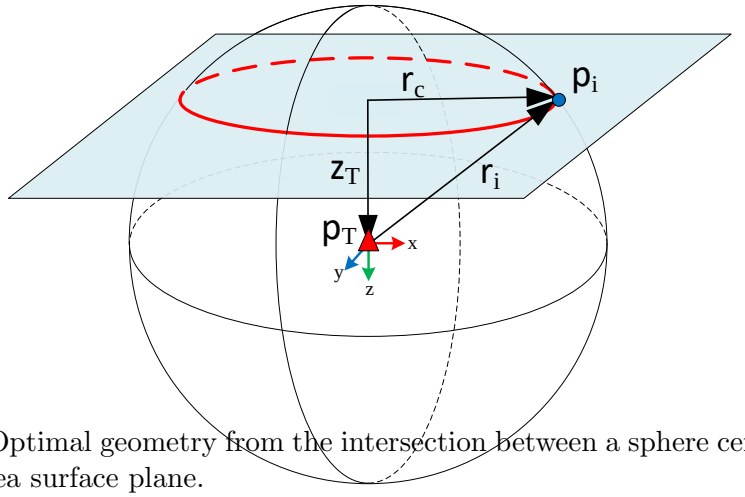

Figure 4.1: Optimal geometry from the intersection between a sphere centred on the target and sea surface plane.

different values of r_c can be derived using (4.10) as

$$\epsilon_1 = \frac{1}{3} - \frac{z_T^2}{r_c^2 + z_T^2}, \tag{4.12}$$

which can be used as an indicator of how the circumference radius affects the optimal solution, which is found when $\epsilon_1 = 0$. Fig. 4.2 shows a specific case for a target depth equal to 1800 m, the optimal circumference radius is equal to 2546 m can be observed.

Now, after the circumference geometry has been derived, it is necessary to find the optimal distribution of all measurements over this path. Consequently, rewriting (4.6) and (4.7) in polar coordinates, considering a unit sphere ($z_T = 1/\sqrt{3}$ and $r_c = \sqrt{2}/\sqrt{3}$), and $p_{ix} = r_c cos(\alpha_i)$, $p_{iy} = r_c sin(\alpha_i)$ (where α_i is the projected angle of the *i-th* range vector on the $\{x, y\}$ plane), and $p_{iz} = z_T$, the following notation is obtained

$$\sum_{i=1}^{m} \cos^2(\alpha_i) = \sum_{i=1}^{m} \sin^2(\alpha_i) = \frac{m}{2}, \tag{4.13}$$

$$\sum_{i=1}^{m} \cos(\alpha_i)\sin(\alpha_i) = \sum_{i=1}^{m} \cos(\alpha_i) = \sum_{i=1}^{m} \sin(\alpha_i) = 0. \tag{4.14}$$

A simple and elegant solution for α_i is obtained by noticing the orthogonality relationship for sines and cosines from Fourier's analysis, which yields with the solution

$$\alpha_i = \frac{2\pi}{m} i, \quad i \in \{0, ..., m-1\}. \tag{4.15}$$

This means that all the measurements have to be taken uniformly distributed

over the entire circumference in order to compute the target's most accurate position.

Finally, it can be pinpointed that a large number of measurements m yield with a better estimation because of $FIM_{opt} = m/(\sigma^6 3^3)$ increases proportionally to m.

4.2.2 With a known target depth

Commonly, the target's depth can be known easily using a small and affordable sensor, which implies simple computation methods for target localisation. The information of the target's depth can be sent to the Wave Glider at each range interrogation through the acoustic modems. On the other hand, if the target lies on the sea floor, the area's bathymetry can be used to compute its depth. In such situations, a 2D scenario can be derived from the 3D problem explained in the previous subsection knowing z_T, where instead of r_i, its projection r_{ci} to the $\{x, y\}$ plane is used. Then, the Fisher Information Matrix for the 2D scenario can be obtained rewriting (4.3) and (4.4) as

$$FIM = \frac{1}{\sigma^2} \sum_{i=1}^{m} \begin{bmatrix} \left(\frac{\partial r_i(\boldsymbol{p}_T)}{\partial p_{Tx}}\right)^2 & \frac{\partial r_i(\boldsymbol{p}_T)}{\partial p_{Tx}} \frac{\partial r_i(\boldsymbol{p}_T)}{\partial p_{Ty}} \\ \frac{\partial r_i(\boldsymbol{p}_T)}{\partial p_{Ty}} \frac{\partial r_i(\boldsymbol{p}_T)}{\partial p_{Tx}} & \left(\frac{\partial r_i(\boldsymbol{p}_T)}{\partial p_{Ty}}\right)^2 \end{bmatrix}, \tag{4.16}$$

$$\text{FIM} = \frac{1}{\sigma^2} \sum_{i=1}^{m} \frac{1}{r_{ci}^2} \begin{bmatrix} p_{ix}^2 & p_{ix}p_{iy} \\ p_{iy}p_{ix} & p_{iy}^2 \end{bmatrix}, \tag{4.17}$$

where $r_{ci}^2 = r_i^2(1 - z_T^2/r_i^2)$, which yields with a FIM_{opt} equal to

$$\text{FIM}_{opt} = \frac{1}{\sigma^2} \begin{bmatrix} \frac{m}{2}(1 - \frac{z_T^2}{r_i^2}) & 0 \\ 0 & \frac{m}{2}(1 - \frac{z_T^2}{r_i^2}) \end{bmatrix}. \tag{4.18}$$

In this scenario, the ratio between the slant range measurement and the target's depth plays a different role to the previous one. Here, the maximum FIM will be reached when r_i^2 tends to infinite, in such a case $FIM_{opt} \simeq m/(2\sigma^2)\boldsymbol{I}_2$, which is the maximum achievable value and it is equal to the 2D scenario ($z_T = 0$). Therefore, if the target's depth is different to zero and it is known, a bigger circumference's radius will proportion a better estimation on the target's position.

As done before, the difference between the optimal solution and a solution by using different values of the circumference's radius value can be derived using

$$\epsilon_2 = \frac{1}{2} - \frac{1}{2}\left(1 - \frac{z_T^2}{r_c^2 + z_T^2}\right), \tag{4.19}$$

which can be used as an indicator of how the circumference's radius effects the optimal solution, which is found when $\epsilon_2 = 0$. Fig. 4.2 shows a specific case for

a target depth equal to 1800 m, where the optimal circumference radius tends to infinite can be observed.

Until now, all the errors that have been used were assumed constant, range independent, and with mean equal to zero, $error \sim \mathcal{N}(0, \sigma^2)$. Whereas this is a good approximation, which yields with a tractable formulation to be analytically studied, in the reality the error is more complex. As a consequency, a set of different simulations with a more complex error have been carried out to study the performance, and the optimal path of the ROSB localisation algorithms. Nevertheless, the starting point for these simulations were the results obtained in this section.

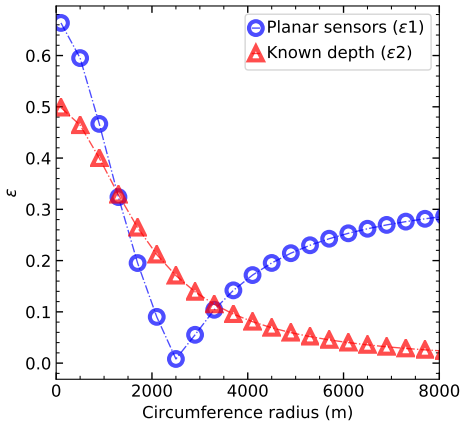

Figure 4.2: Error ϵ between the optimal solution and a solution by using different values of r_c. Results obtained for both scenarios: planar sensors (ϵ_1) and planar sensors with a known target's depth (ϵ_2). These graphs should be only used as an indicator of the localisation performance, they do not give the absolute accuracy reachable. Values computed for a target depth equal to 1800 m.

4.3 Static target localisation algorithms

The concept of single-beacon range-only positioning can be divided into two groups: as a navigational aid for a moving vehicle [62] (group 1), or to localize a stationary or moving target [63] (group 2). All these methods use a set of ranges between a target and different static nodes, known as anchor nodes or landmarks. Typically, these ranges can be obtained using TOF given the speed of sound in water. Then, the unknown underwater target position problem can be solved using trilateration, where in general, three or more points are needed in 2D dimensions and, at least, four points in 3D scenarios.

In general, the navigation aid problem has received more attention in the literature (group 1) where an AUV needs to be located using a set of known transponders,

as in [78]. Nonetheless, similar approaches can be used in the inverse case, where an autonomous vehicle is used to find an underwater target (group 2). The method used in this chapter can be seen in Fig. 4.3, where a range-only target localisation method based on single-beacon architecture is presented. The target's position is computed using a Wave Glider, which periodically measures the range to the underwater target, while it is moving on the surface.

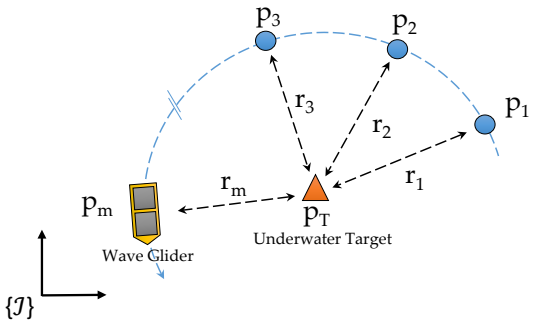

Figure 4.3: Range-only single-beacon underwater target localisation methodology representation, using a Wave Glider as a moving LBL.

Consequently, following the same notation as [78], the underwater target positioning vector can be defined as $\boldsymbol{p}_T \in \mathbb{R}^n$, where n can be either 2 or 3 and is the space dimension of the problem. All the Wave Glider positions used in the trilateration problem can be denoted as $\boldsymbol{p}_i \in \mathbb{R}^n$ where $i \in \{1, 2, \ldots, m\}$, where m indicates the number of measurements carried out. Then, the ranges measured with Wave Glider between itself and the target can be expressed as

$$\overline{r}_i = \|\boldsymbol{p}_T - \mathbf{p}_i\| + w_i, \quad i \in \{1, 2, \ldots, m\}, \tag{4.20}$$

where $\|\boldsymbol{p}_T - \boldsymbol{p}_i\| = r_i$ is the true range, and $w_i \sim \mathcal{N}(\varepsilon, \sigma^2)$ is some nonzero mean Gaussian measurement error where σ^2 is the variance and ε is the systematic error.

Thus, (4.20) can be written in matrix form as $\overline{\boldsymbol{r}} = \boldsymbol{r} + \boldsymbol{w}$. In general, this nonlinear, non-smooth and overdetermined (when $m > n + 1$) system does not have a straightforward solution. At this point, two different methodologies are used in the literature to solve the system and find the target's position through ranges, [109]: linearise the function and find a closed-form Least Square (LS) solution; or use an iterative minimisation algorithm to minimize a cost function related to the Maximum Likelihood (ML) estimate.

4.3.1 Closed-form Least Squares algorithm

As the main goal of this chapter is not to compare the performance of different algorithms, a simple Unconstrained Least Square (ULS) algorithm is used, which was introduced in [110]. However, as it will be shown, its performance is quite good.

The main idea on LS algorithms lies in a linearisation of the system by using the squared range measurements to obtain a linear equation as a function of the unknown target's position $\boldsymbol{p}_T$ and its norm,

$$\overline{\boldsymbol{d}} = \boldsymbol{d} + \boldsymbol{\xi}, \tag{4.21}$$

where $\boldsymbol{d}$ is equal to the squared range $\boldsymbol{r}^2$, and $\boldsymbol{\xi}$ is the new measurement error as a function of $\mathbf{w}$ and $\boldsymbol{r}$. In this case, it is not obvious that $\boldsymbol{\xi} \sim \mathcal{N}(\varepsilon, \boldsymbol{\sigma}^2)$ as before, and the new error is not independent to the range. Nevertheless, under some circumstances this assumption is possible, for example when $r_i \gg \sigma_i$, but this assumption is not true when the vehicle is close to the target. See [78] for more information. However, from hereafter it is assumed an error that is independent to the range and its square, which is true as the ranges used will be much bigger than the error itself.

On the other hand, when all the points used to compute the underwater target position are coplanar (e.g. in the same z-plane), which in this case is on the sea surface, a 2D formulation can be used. The square ranges are defined by

$$\begin{aligned} d_i =& \|\boldsymbol{p}_T - \boldsymbol{p}_i\|^2 \\ =& (p_{Tx} - p_{ix})^2 + (p_{Ty} - p_{iy})^2 + (p_{Tz} - p_{iz})^2 \\ =& \|\boldsymbol{p}'_T - \boldsymbol{p}'_i\|^2 + z_T^2 \\ =& \boldsymbol{p}_i'^T \boldsymbol{p}'_i - 2\boldsymbol{p}_i'^T \boldsymbol{p}'_T + \|\boldsymbol{p}'_T\|^2 + z_T^2, \end{aligned} \tag{4.22}$$

where $\boldsymbol{p}'$ represents the projection of $\boldsymbol{p}$ on the $\{x, y\}$ plane, and z_T is the target depth. This equation can be formulated in a matrix form as

$$\boldsymbol{d} = \delta(\boldsymbol{P}'^T \boldsymbol{P}') - 2P'\boldsymbol{p}'_T + (\|\boldsymbol{p}'_T\|^2 + z_T^2)1_m, \tag{4.23}$$

where $\boldsymbol{P} = [\boldsymbol{p}_1, ..., \boldsymbol{p}_m] \in \mathbb{R}^{nxm}$, and δ is defined as the diagonal of the matrix.

The unknown scalar terms $\|\boldsymbol{p}'_T\|^2 + \delta_z^2$ are multiplying the vector of ones 1_m. Therefore, this unknown term can be deleted multiplying both sides of the equation by matrix $\mathbf{M}$, which has 1_m in its null space, obtaining

$$\boldsymbol{M}\boldsymbol{d} = \boldsymbol{M}\delta(\boldsymbol{P}'^T \boldsymbol{P}') - 2\boldsymbol{M}P'^T \boldsymbol{p}'_T = \boldsymbol{M}\boldsymbol{d}'. \tag{4.24}$$

Consequently, the square range in 2D is the same as in 3D and the same algorithm can be used. In this situation, the depth of the target is not necessary to obtain its (x,y) position. Hence, the depth can be computed using Pythagoras' theorem. Finally, (4.23) can be written as a linear system with form $\boldsymbol{A\theta} = \boldsymbol{b} + \boldsymbol{\xi}$, which can be solved by minimizing as small as possible the length of the error, with solution $\boldsymbol{A}^T\boldsymbol{A}\widehat{\boldsymbol{\theta}} = \boldsymbol{A}^T\boldsymbol{b}$. Therefore, the target position estimation is

$$\widehat{\boldsymbol{p}}_T = \boldsymbol{N}(\boldsymbol{A}^T\boldsymbol{A})^{-1}\boldsymbol{A}^T\boldsymbol{b}, \tag{4.25}$$

where

$$\boldsymbol{N} = \begin{bmatrix} \boldsymbol{I}_n & 0 \end{bmatrix} \tag{4.26}$$

$$\boldsymbol{A} = \begin{bmatrix} 2\boldsymbol{p}_1^T & -1 \\ \vdots & \vdots \\ 2\boldsymbol{p}_m^T & -1 \end{bmatrix} \tag{4.27}$$

$$\boldsymbol{b} = \begin{bmatrix} \|\boldsymbol{p}_1\|^2 - \overline{d}_1 \\ \vdots \\ \|\boldsymbol{p}_m\|^2 - \overline{d}_m \end{bmatrix} \tag{4.28}$$

$$\boldsymbol{\theta} = \begin{bmatrix} \boldsymbol{p}_T \\ \|\boldsymbol{p}_T\|^2 \end{bmatrix}. \tag{4.29}$$

4.3.2 Iterative minimisation algorithm

The main goal of this method is to use the Maximum Likelihood Estimation (MLE), a statistical technique to compute the value that maximizes the similarity between selected values and observed data, which come with an unknown probability density function. For a normal distribution and using the log-likelihood function, which is a continuous strictly increasing function over the range of the likelihood, the log-likelihood can be written as

$$\begin{aligned} &\log \mathcal{L}(\boldsymbol{p}_T) = \\ &-\frac{m}{2}log2\pi - \frac{1}{2}log|\boldsymbol{R}| - \frac{1}{2}(\overline{\boldsymbol{r}} - \boldsymbol{r})^T\boldsymbol{R}^{-1}(\overline{\boldsymbol{r}} - \boldsymbol{r}) \\ &\quad = K - \frac{1}{2}(\overline{\boldsymbol{r}} - \boldsymbol{r})^T\boldsymbol{R}^{-1}(\overline{\boldsymbol{r}} - \boldsymbol{r}), \end{aligned} \tag{4.30}$$

where $\boldsymbol{R}$ is a diagonal matrix, the values of which are the measurement error covariance σ^2. Then the MLE can be found by solving the optimisation problem

$\widehat{\theta} = \arg\min_{p_T} f(\boldsymbol{p}_T)$, where the cost function is

$$f(\boldsymbol{p}_T) := \frac{1}{2}(\overline{\boldsymbol{r}} - \boldsymbol{r})^T \boldsymbol{R}^{-1}(\overline{\boldsymbol{r}} - \boldsymbol{r}). \tag{4.31}$$

In general, this cost function is non-linear because of the square root that defines the range measurements, therefore there is no closed form solution. Nonetheless, an iterative method can be used to solve this minimisation problem, such as negative gradient descent or Newton's methods. Only the final formulation is presented in this chapter to reduce its length, for detailed development see [78] and [61].

To use these two iterative minimisation methods the cost function gradient and its Hessian must be calculated, obtaining

$$\nabla f(\boldsymbol{p}_T) = -\boldsymbol{C}\delta(\boldsymbol{r})^{-1}\boldsymbol{R}^{-1}(\overline{\boldsymbol{r}} - \boldsymbol{r}), \tag{4.32}$$

and

$$\begin{aligned} &\nabla^2 f(\boldsymbol{p}_T) = \\ &-\boldsymbol{C}\delta(\boldsymbol{r})^{-2}\boldsymbol{R}^{-1}\delta(2\boldsymbol{r} - \overline{\boldsymbol{r}})\boldsymbol{C}^T + \boldsymbol{\alpha}^T\delta(\boldsymbol{r})^{-1}\mathbf{1}_m\boldsymbol{I}_n \end{aligned}, \tag{4.33}$$

where

$$\boldsymbol{R} = \begin{bmatrix} \sigma^2 & \cdots & 0 \\ \vdots & \ddots & \vdots \\ 0 & \cdots & \sigma^2 \end{bmatrix} \tag{4.34}$$

$$\boldsymbol{\alpha} = \boldsymbol{R}^{-1}(\overline{\boldsymbol{r}} - \boldsymbol{r}) \tag{4.35}$$

$$\boldsymbol{C} = \begin{bmatrix} \boldsymbol{p}_T - \boldsymbol{p}_1 & \cdots & \boldsymbol{p}_T - \boldsymbol{p}_m \end{bmatrix}. \tag{4.36}$$

Using the gradient of the cost function and its Hessian the iterative minimisation algorithm can be computed by Algorithm 1.

After these mathematical formulations, a set of different simulations and real tests can be conducted to characterize the performance of the system and identify the best parameters for underwater target localisation using a Wave Glider with single-range and single-beacon architecture.

if *_Init_* **then** Initialize:
| $\boldsymbol{p}_{T0}$, $k = 0$
end
while $\|\nabla f(\boldsymbol{p}_T)\| \leq \epsilon$ *or* $k \geq k_{max}$ **do**
| 1: Calculate a search direction using Gradient descent (4.32) or Newton descent (4.33):
| $h(\boldsymbol{p}_T) = -\nabla f(\boldsymbol{p}_T)$
| $h(\boldsymbol{p}_T) = -(\nabla^2 f(\boldsymbol{p}_T))^{-1} \nabla f(\boldsymbol{p}_T)$
|
| 2: Determine the step size (Armijo rule):
| $s_k = s\beta^{mi}$
| where $s > 0$, β, $\sigma \in (0, 1)$, and m_i is the first integer that satisfies:
| $f(\boldsymbol{p}_{Tk} + s\beta^{mi} h(\boldsymbol{p}_{Tk})) \leq f(\boldsymbol{p}_{Tk}) + \sigma s\beta^{mi} h(\boldsymbol{p}_{Tk})^T \nabla f(\boldsymbol{p}_{Tk})$
|
| 3: Update the estimation value:
| $\boldsymbol{p}_{Tk+1} = \boldsymbol{p}_{Tk} + s_k h(\boldsymbol{p}_T)$
| $k = k + 1$
end

Algorithm 1: Iterative Minimisation method.

4.4 Simulations

Different simulations were conducted to determine the best parameters to increase the capabilities of the acoustic positioning system. The scenario chosen is a Wave Glider on the surface conducting different paths and an underwater target at 1800 m of depth to be located. Four parameters were selected: path shape, number of points needed, radius around target, and offset from target. Moreover, the performance of the derived LS and MLE algorithms was compared to the CRB, which specifies the best possible performance attainable with any estimator [111].

The CRB theorem states that under some regular conditions of the probability density functions, the variance (4.37) represents the lower bound on the mean-square error of an unbiased estimator. Where, for a scalar unbiased case, the variance of estimator $\hat{\boldsymbol{p}}_T$ is bounded by the Fisher information $I(\hat{\boldsymbol{p}}_T)$ as

$$var(\hat{\boldsymbol{p}}_T) \geq \frac{1}{I(\hat{\boldsymbol{p}}_T)}, \tag{4.37}$$

where the Fisher information is defined by

$$I(\hat{\boldsymbol{p}}_T) = -E\left[\frac{\partial^2 \ell(r; \boldsymbol{p}_T)}{\partial \boldsymbol{p}_T^2}\right], \tag{4.38}$$

where $\ell(r; \boldsymbol{p}_T) = log\mathcal{L}(\boldsymbol{p}_T)$, which can be seen in (4.30), and E denotes the expected value. Computing the second derivative of the likelihood logarithm function and its

expected value, the CRB obtained is

$$var(\hat{\boldsymbol{p}}_T) \geq tr[(\boldsymbol{C}\delta(\boldsymbol{r})^{-1}\boldsymbol{R}^{-1}\delta(\boldsymbol{r})^{-1}\boldsymbol{C}^T)^{-1}] \tag{4.39}$$

which can be compared to the Root Mean Square Error (RMSE), which represents the sample standard deviation of the differences between predicted values and observed values, using the expression

$$RMSE = \sqrt{var(\hat{\boldsymbol{p}}_T)}. \tag{4.40}$$

Different scenarios can be computed using (4.39) to observe the theoretical performance of the system (a Wave Glider as a LBL system to find an underwater target at 1800 m of depth). For example, Fig. 4.4 shows the CRB using different points and configurations as landmarks to compute the target's location. This figure shows that the best accuracy and precision are obtained when the target is located in the path's centre and using distributed points around it (Fig. 4.4e and Fig. 4.4f).

Nevertheless, more scenarios have been simulated to obtain a better characterisation, such as path shape, radius around the target, number of points or offset from the target. All the simulations conducted for this chapter have been obtained through 1000 Monte Carlo iterations, with a normal noise probability distribution, with zero mean and variance equal to (4.41). For a better explanation of this mathematical error model and all of their parameters see [106].

$$\mathcal{U}_c^2(r) = \sum_{i=1}^{N} \left(\frac{\partial r}{\partial x_i}\right)^2 \mathcal{U}^2(x_i) = \frac{1}{2}\sum_{i=1}^{N} c_i \mathcal{U}^2(x_i). \tag{4.41}$$

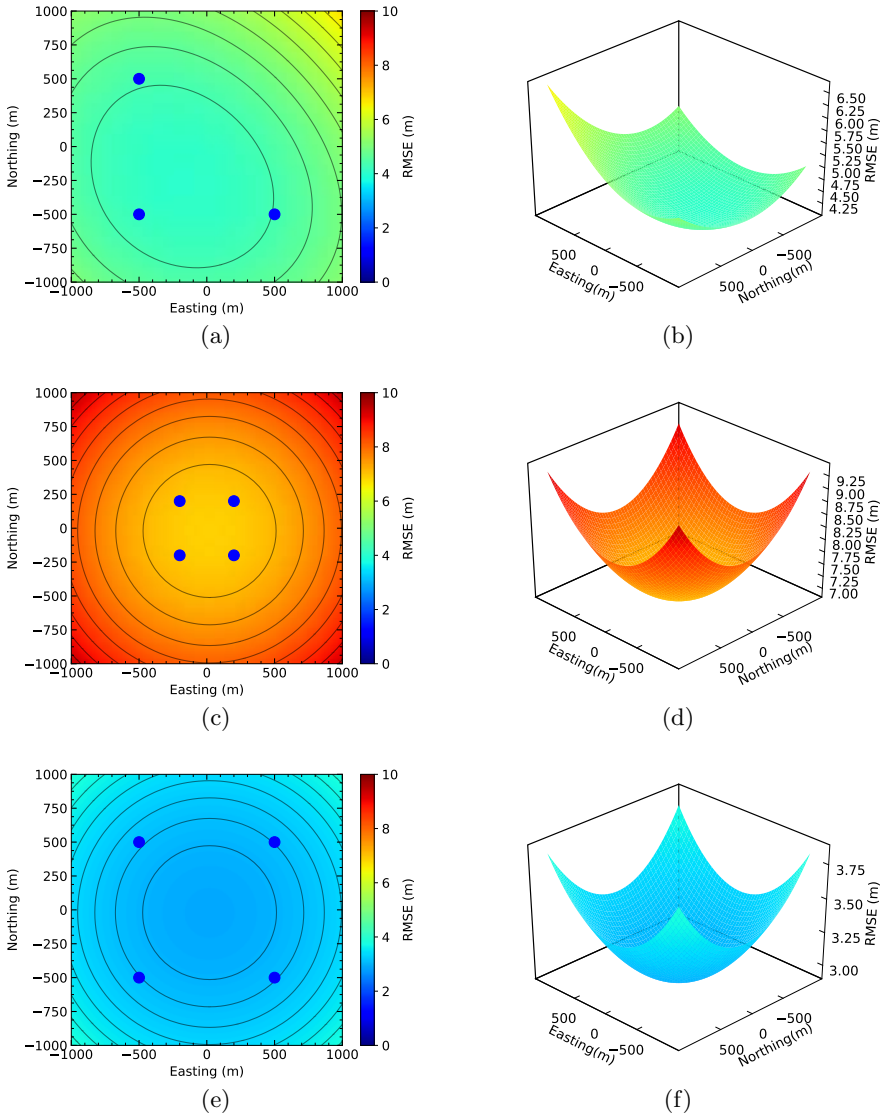

Figure 4.4: CRB representation for 3 landmarks with inter-baseline equal to 1000 m (a), 4 landmarks with inter-baseline equal to 500 m (c), and 4 landmarks with inter-baseline equal to 1000 m (e) (Blue dots). Planar representation and 3D representation are shown on left and right plots respectively.

4.4.1 Path Shape

One of the first aspects to be considered in range-only target localisation is the landmark's position, or in our case the Wave Glider path shape. It is well known that the non-collinear points are mandatory, where the circular path is the optimum one as was demonstrated in the previous section. However, the best landmark positions will be determined in each case for the specific mission requirements (e.g. vehicle's use, time required, or power consumption). In this situation, others than circle path shapes could be used, where any shape can be considered as a conjunction of multiple circles, and therefore, its optimum performance is guaranteed. Fig. 4.5 shows the RMSE evolution as a function of the path's completed ratio for four path shapes: a circle with 400 m of radius, and a square, a triangle and an L shape with 800 m for each side. They all use 17 points of landmarks, which are placed on the surface of the sea, due to the use of a Wave Glider. The dimension of these paths were chosen due to time constraints as it is exposed in the following subsection, where they had compared with real field tests.

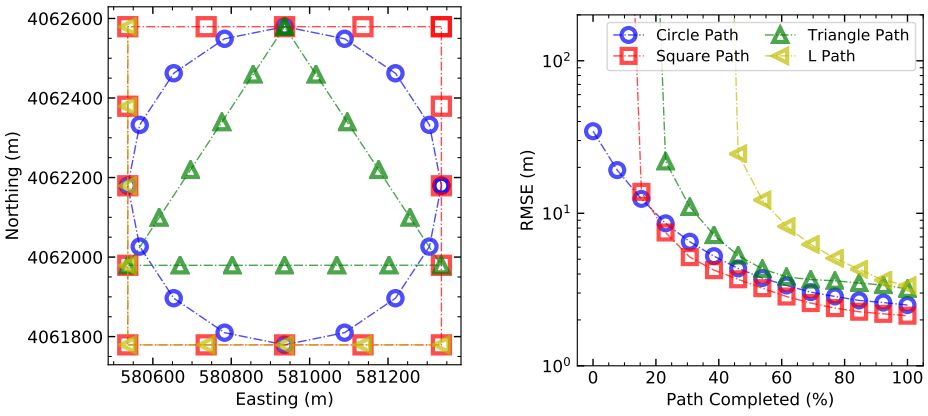

Figure 4.5: (a) Paths conducted to study the performance of range-only localisation methods under different observer's trajectories. (b) RMSE evolution as a function of path completed ratio. The Circle, Square, Triangle and L shape paths are represented.

The RMSE for the *square*, the *L* and the *triangle* paths is much bigger than the circle path at the beginning of the path, when the path's completed ratio is less than 20%, can be observed. This is because all the points in these cases are still coplanar. At the end of the path the best case obtained is the *square* path, while the worst cases are the *triangle* and *L* path. This difference is because of the ranges obtained between the Wave Glider and the target. Longer ranges are used in the *square* path, and have been demonstrated in the previous sections, longer ranges cause better

accuracy, where the *square* path can be considered as a combined set of multiple circle paths, [98]. For that reason, other aspects such as time to the path completed or power consumption should also be taken into account (for example, the Wave Glider will take more time to finish the *square* path than the *circle* path). Finally, if the path is not closed a worse performance is obtained (i.e. the *square* and *L* shape), and therefore a closed path is desired, which has been demonstrated in the previous section, where all the measurements should be made equally distributed over the whole path.

4.4.2 Radius around target

Another interesting test is to observe the behaviour under different circle path radii centered over the target, this parameter is shown in Fig. 4.6 where 50, 100, 200, 400, 600, 800, 1000, 5000, 10000 and 20000 metres path radii are simulated, where 6 points as landmarks have been used in each case. LS and ML algorithms have been compared to CRB. Nonetheless, it was observed that the performance of both algorithms was very similar and very close to the CRB. Thus, only the LS is represented for a better graph understanding. Furthermore, the depth error due to the systematic range measurement error has been treated separately (dash line). Lastly, the time necessary to finish the path has been plotted (PathTime), which can be helpful to decide the optimal circle radius.

On the other hand, a greater radius results in a lower RMSE until a specific distance where the Signal-to-Noise Ratio (SNR) error causes an important error increase can be observed. This behaviour can be derived computing the surface range r_s, which is

$$r_s = \sqrt{r^2 - depth^2} = \sqrt{r^2 - (r-\alpha)^2}, \tag{4.42}$$

where α is the difference between range and depth. The error can be defined as the true value and its estimation $\varepsilon = (r_s - \overline{r}_s)$, and is

$$\varepsilon = \sqrt{2r\alpha - \alpha^2} - \sqrt{2r(\alpha + w) - \alpha^2 + w^2} \tag{4.43}$$

where w is some non-zero mean Gaussian measurement error. With (4.43) if $\alpha \simeq 0$ (depth and range are very similar) the error is $\varepsilon \simeq \sqrt{2rw + w^2}$ and if $\alpha \simeq r$ (range is much bigger than depth) the error is $\varepsilon \simeq w$ can be observed.

If the error model described in [106], and is shown in (4.41), is used (blue dots line, *LS(Emod)*), the RMSE increases rapidly after a radius equal to 5000 m can be observed. As a result, the best radius will be between 1000 and 5000 metres. Novertheless, the time required to complete the path have to be considered, in this case the best radius can be less than 1000 metres, where the necessary time is less

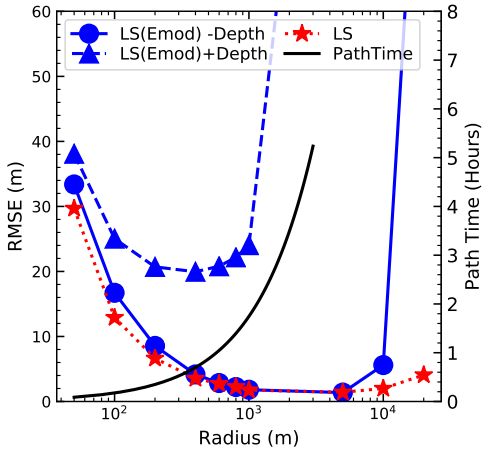

Figure 4.6: The RMSE evolution as a function of the circle radius for a target at 1800 m of depth, using LS algorithm. Where, *LS(Emod)+Depth* incorporates the range error model shown in (4.41). Also the RMSE, when depth error is not taken into account, is plotted as *LS(Emod)-Depth*. In both cases a 1% of systematic error is added to the range measurement. These two results can be compared to a simple $\sigma = 1$ error, which is used in section 4.2, where the optimal radius 4.30 is defined. Finally, the time to complete the path is also shown (black line).

than 1 hour (moreover, the depth error is the most reduced).

Another method such as increasing the number of points used as landmarks can be used to reduce the RMSE instead of lengthening the radius.

4.4.3 Number of points as landmarks

One of the main ways to increase the precision of the system is by using more points to compute the target's position. This is the most common method to reduce the variance of any measurement with random noise, and is given by

$$var(z_i) = \frac{1}{n-1}\sum_{i=1}^{n}(z_i - \overline{z})^2, \tag{4.44}$$

where z_i are n independent observations of z. This behaviour can be seen in Fig. 4.7, which shows the results for 4, 6, 12, 24 and 48 points. However, the optimal number of points will also be constrained by power consumption requirements, where more points will produce more power consumption.

Fig. 4.7 shows that if more points are used to compute the target's position, a better accuracy in x and y position is obtained, while the depth error is still equal. Therefore, the best solution is to use as many points as can be possible if the power consumption is not taken into account. This consumption can also be observed

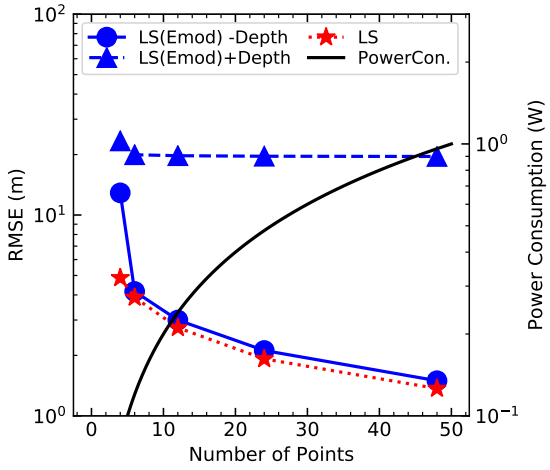

Figure 4.7: The RMSE evolution as a function of the number of points used to compute the target's position, for circles centred over the target (with 1800 m target depth and 400 m of radius). The red line is the simulation result using LS algorithm. The triangular blue dash line is the same algorithm but with the error model *LS(Emod)+Depth*, and the dotted blue dash line is the error without the depth error, *LS(Emod)-Depth*. In both cases, a 1% of systematic error is added to each range measurement. Finally, the black line is the normalized power consumption (PowerCon.).

(black line) as a normalized power consumption in Fig. 4.7, where if 50 points are used the maximum power "1" will be used, and otherwise, if zero points are used, the minimum power "0" will be used. An important difference between 20 and 50 points cannot be observed, whereas a great power consumption reduction can be obtained (note that y-axis is in logarithmic scale). As a result, around 20 points will be the desired number of landmarks to use for target locating.

4.4.4 Offset from target

Finally, a set of simulations have been conducted to observe the RMSE with different offsets between the centre of the circular path and the underwater target, with a 400 m radius and 12 landmarks (Fig. 4.8).

In this case, the introduction of a systematic error and error model *LS(Emod)* due to the uncertainty of water sound velocity knowledge lead to a significant difference between this and the previous work shown in [105], where a simple random error was used (LS). In addition, this is also different to what is derived in section 4.4.2, and also explained in [98], where the systematic error is not taken into account, and therefore, the error produced by circles not centred over the target is neglected. Finally, the worst effect produced by the offset is in the x and y RMSE can be

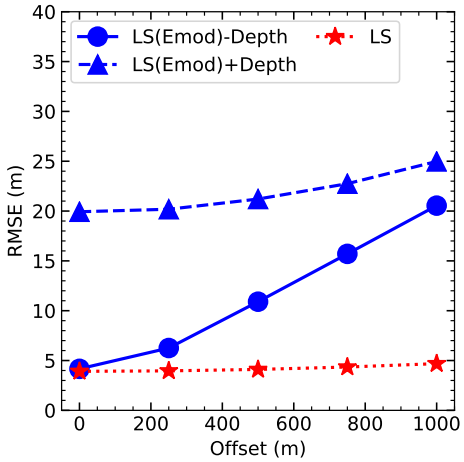

Figure 4.8: The RMSE evolution as a function of the offset between the circumference centre and the target, for a target at 1800 m of depth. The red line is the simulation result using the LS algorithm, the triangular blue dash line is the same algorithm but with the error model plus a systematic error of 1% *LS(Emod)+Depth*, and the dotted blue dash line is without the depth error, *LS(Emod)-Depth*.

observed in Fig. 4.8, which in the end will rise to the same error that it is obtained with the depth measurement (LS(Emod)+Depth). For that reason, a zero offset is mandatory if a good target accuracy is desired.

4.5 Field tests

Several sea tests have been conducted to compare and validate the algorithm's ability to locate a target, and to validate the optimal path, radius and number of points suggested by simulations. These tests have been conducted with the Benthic Instrument Node (BIN) target placed in Monterey Bay, California, which is at 1800 m of depth (in the middle of Monterey Canyon). Three groups of tests were conducted over the BIN instrument node, one to determine the best shape, another one to find the best radius, and finally a third one to characterize the offset effect.

4.5.1 Path shape

Firstly, three path shapes were made with the same dimensional characteristics in order to observe the main differences among them. These paths were a circle with 400 metres of radius, and a square and triangle with 800 metres of side. These values have been chosen to be able to compare them with simulations. Fig. 4.9 shows the paths obtained and Table 4.1 shows the main values: the target's position computed

using the LS algorithm (easting, northing and depth), the error versus the target's true position, the number of points used (Np), and the total of time to complete the path. The target's true position was obtained using the average value of three paths shapes with a total of 154 ranges.

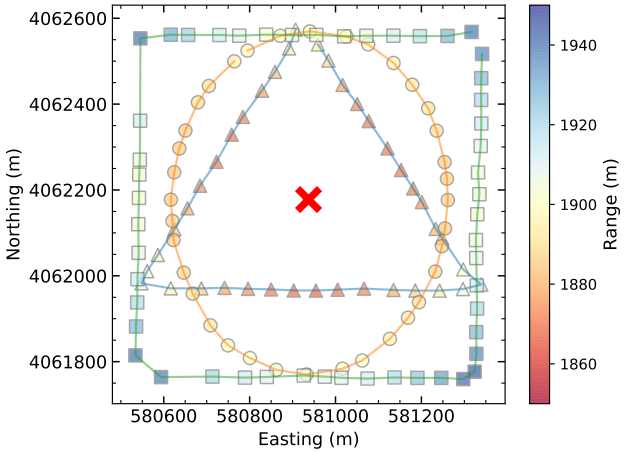

Figure 4.9: Field test: Wave Glider trajectories performed over the BIN target (X) with three different paths, a square, a triangle and a circle. The colour bar indicates the slant ranges obtained between both devices.

Table 4.1: Main results for field test 1

Path	**Easting**	**Error**[1]	**Northing**	**Error**[1]	**Depth**	**Error**[1]	**Np**	**Time**
Circle	580937.0	0.9	4062175.6	-3.8	1858.7	-5.1	36	56'
Square	580937.5	1.4	4062177.4	-2.0	1861.9	-1.9	51	1h50'
Triangle	580937.9	1.8	4062176.0	-3.4	1858.5	-5.3	39	55'

[1]Error from target's true position was obtained using the average value of three path shapes with a total of 154 ranges. Values in metres.

In Table 4.1 the main results obtained during the three different path shape tests can be observed. The target localisation RMSE (for x and y positions) obtained during these paths was approximately the same, 3.5 metres. However, a better accuracy for the square path was measured, this is due to twofold: firstly, the square path uses longer ranges, and this cause a better accuracy (section 4.4.2) as it has been pinpointed in section 4.4.1, where the square path can be considered as a combined set of multiple circle paths without loss of generality [98]; secondly, the square path used in this field test had more points to compute the target's localisation ($N_p = 51$), and increasing the number of points yields into the reduction of the variance of a

measured value as it is highlighted in section 4.4.3. Nevertheless, the square shape's time required to complete the path was around 1h more than the time required for the triangle and circle paths, this reduce the viability of using this path for scenarios where speed is an important factor, for example where multiple scientific tests have to be carried out or the weather prediction is not very good. Similar results were obtained with the simulations, therefore the circle is one of the best paths among these path shapes can be concluded, due to its speed and accuracy.

4.5.2 Radius around target

Fig. 4.10 shows the path shapes of the second group of tests, which consist of three circles of 100 m, 400 m and 800 m of radius, all of them centred over the BIN, where the main results are shown in Table 4.2. Note that an 800 m of maximum radius was selected during the field test to reduce the time consumption, which does not compromise the accuracy, as explained in section 4.4.2.

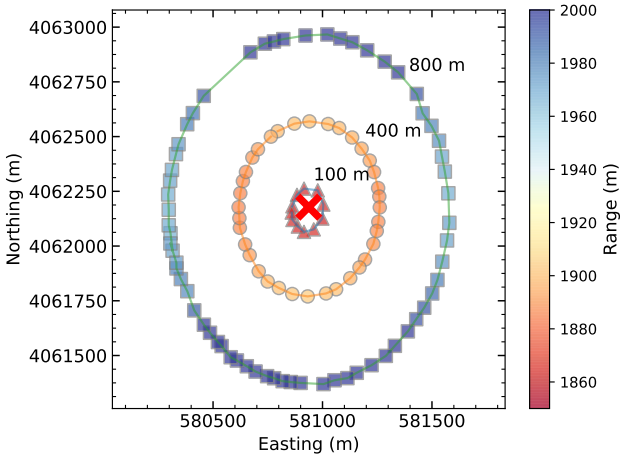

Figure 4.10: Field test: Wave Glider trajectories conducted over BIN target with three different radius, which were 100, 400 and 800 metres. The ranges are also plotted using the colour bar legend on the right.

In addition, the ranges obtained during the field tests can be observed in Fig. 4.10, which were around 2020 m, 1920 m and 1880 m for path circles with a radius equal to 800 m, 400 m and 100 m consecutively, and a target depth equal to 1800 m.

To compare field test results with the simulation results the target's position using only 6 equidistant points among all the ranges obtained in the field test during one circle path was computed, which allows us to choose different groups of 6 points and take the average value of the RMSE (represented by red circles and denoted

Table 4.2: Main results for field test 2

Path	Easting	Error[1]	Northing	Error[1]	Depth	Error[1]	Np	Time
r100	580922.1	15.1	4062178.8	-1.2	1860.7	0.7	11	13’
r400	580937.0	0.2	4062175.6	2.0	1858.7	2.7	36	56’
r800	580936.1	1.1	4062179.4	-1.8	1863.8	-2.4	64	1h57’

[1]Error from target’s true position was obtained using the average value of the three paths’ shapes from test 1 with a total of 154 ranges. Values in metres.

as *Real Data* in Fig. 4.11). Additionally, the power trend line (red dash line) is computed and represented to obtain a better performance’s representation. The target position was computed using the LS algorithm in both simulations and field test. The LS algorithm is accurate enough compared to MLE as is explained in section 4.4. Moreover, the error bars are plotted to show the standard deviation of uncertainty and the mean point *LS(Emod)*, during a 1000 run times simulation using the error model described in [106].

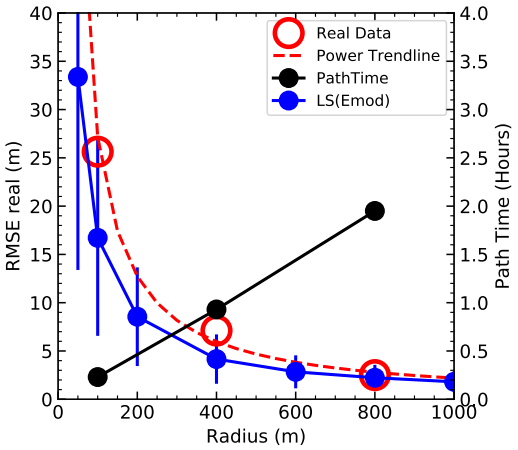

Figure 4.11: Comparison between simulation (with error model *LS(Emod)*) and real data results for different radii of circle paths centred over the BIN target. Using 6 equidistant points to compute the target’s localisation and the LS algorithm. The dash line is the power trend line computed using real data (red circles). Additionally, the time which was required to complete the path is also represented (black line).

In this graph the real data behaviour is similar to the results obtained with simulations can be observed. And with a radius equal or greater than 400 m a good performance was obtained, with a RMSE lower than 10 m. It can be obtained a RMSE lower than 5 m for a radius greater than 800 m. However, the time required (PathTime) by the Wave Glider to complete the path has to be taken into account,

which introduces an important limitation. For example, the Wave Glider needs practically 2 h to complete a circle of 800 m radius, while this time is reduced to 1 h for a radius equal to 400 m.

4.5.3 Offset from target

Finally, a third field test was conducted over the BIN target to observe the offset's influence in the accuracy. For this purpose three paths were conducted, with distances of 0 m, 500 m and 1000 m between the circumference centre and the target, and with a radius of 400 m. Fig. 4.12 shows the path shapes of this third test, where the ranges obtained are also represented using the colour bar on the right. Ranges between 2030 m and 1870 m were obtained for a target depth equal to 1800 m. Moreover, the main results are shown in Table 4.3.

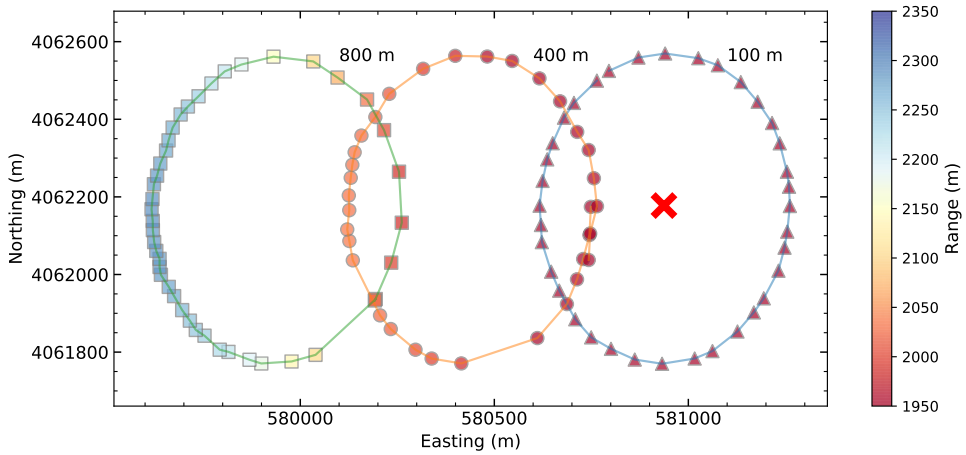

Figure 4.12: Field test: Wave Glider trajectories performed over BIN target with three different offsets between target and circle centre, which were 0, 500 and 1000 m. The ranges are also plotted using the colour bar legend on the right. Target depth equal to 1800 m.

Table 4.3: Main results for field test 3

Path	**Easting**	**Error**[1]	**Northing**	**Error**[1]	**Depth**	**Error**[1]	**Np**	**Time**
d0	580937.0	0.2	4062175.6	2.0	1858.7	2.7	36	56'
d500	580946.3	-9.1	4062187.1	-9.5	1860.3	1.1	34	59'
d1000	580956.8	-19.6	4062190.2	-12.6	1856.3	5.1	43	1h4'

[1]Error from the target's true position was obtained using the average value of the three paths' shapes from test 1 with a total of 154 ranges. Values in metres.

The RMSE using different groups of 6 equidistant ranges to compare the field results with simulations were computed, as it has done in the above subchapter. These results can be observed in Fig. 4.13, where the similarity between both the behaviour and the RMSE in real tests and simulations can be observed. Consequently, a better mathematical model than in our previous work [105] has been obtained, which consisted in taking into account the systematic error and a better random error model (4.41).

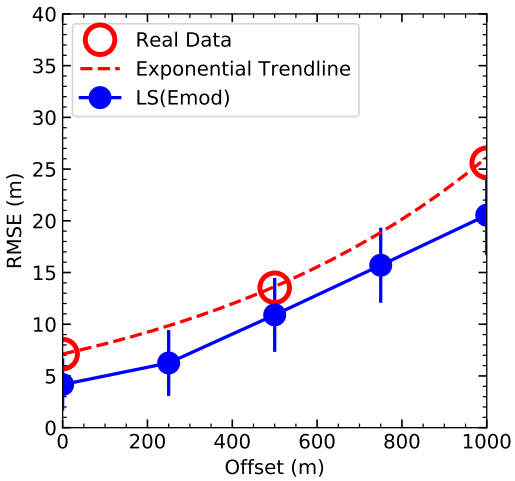

Figure 4.13: Comparison between simulation (with error model *LS(Emod)*) and real data results for different offsets of circle paths over the BIN target. Using 6 equidistant points to compute the target's localisation. The dash line is the exponential trend line computed using real data.

4.6 Benthic Rover mission

Finally, a mission performed to find a benthic Rover [112], and to know its trajectory is explained in this section. This is a final demonstration to show some of the uses of a Wave Glider as a moving LBL system. The benthic Rover is a mobile physiology laboratory designed by Dr. Ken Smith at Monterey Bay Aquarium Research Institute (MBARI), which slowly crawls along the seafloor. The Rover and its deployment localisation can be observed in Fig. 4.14, which also shows the Monterey Bay and the MBARI laboratories' localisation.

Figure 4.14: The initial benthic Rover deployment at "Station M" in the north eastern Pacific ocean, at $34^o50'N$ and $123^o00'W$, a region with 4000 m of depth, situated at 220 km west of central California coast. Also, the MBARI localisation is represented at the centre of Monterey Bay, California.

The main goal of this mission was to observe if the moving benthic instrument was working correctly. The rover was moving forward very slowly on the seafloor following a straight line. The initial parameters were set to a velocity equal to 5 metres/day, following a line of 45^o in inclination with respect to the magnetic north. As a result, its position's estimation could be computed. As a consequence, the rover's position estimated using its initial parameters and the position founded using the Wave Glider could be compared, and used to observe if the trajectory followed by the rover was the programmed one.

To accomplish this objective, an initial position and two localisation missions were used (as is shown in Fig. 4.15):

(a) **Initial position**: The benthic Rover was deployed at geographic coordinates $35^o\ 7'\ 59.988''N$ and 123^oW, on August 11, 2015.

(b) **Test 1**: First localisation mission conducted on April 14, 2016. In this case the Rover was localized at $35^o\ 8'\ 22.0668''N$ and $122^o\ 59'\ 39.3''W$, which means that it had travelled 858 metres in 158 days, with an angle of 52^o. The parameters used are summarized below:

- Circle's radius = 200 m
- Number of points = 39
- Test duration = 1h 8.15'

(c) **Test 2**: Finally, a last mission conducted on July 11, 2016, localized the Rover at $35^o8'30.5736''N$ and $122^o59'31.9236''W$. In this case, it had travelled 322 metres in 88 days, with an angle of 55^o, from the last known point. The parameters used are summarized below:

- Circle's radius = 800 m
- Number of points = 81
- Test duration = 1h 22'

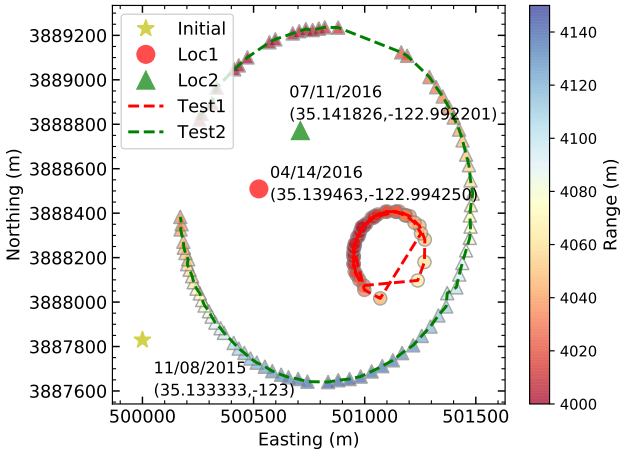

Figure 4.15: Field test: This figure shows the benthic Rover's deployment position (yellow star), and the two missions conducted to find it (red dot and green triangle).

Therefore, the benthic Rover travelled 1180 metres in total for 246 days. This indicates a velocity of 4.8 metres/day, which is highly close to the programmed one, obtaining an error of 40 metres between the final estimated position and the position obtained using the Wave Glider. On the other hand, the inclination followed by the

Rover was around 53.5^o in respect to the geodetic north. If the magnetic declination is taken into consideration, which was 13.15^o east in this area, the trajectory of the rover was 40.35^o in respect to the magnetic north, which yields an error less than 5^o compared to the programmed one.

The missions performed to find and track the benthic Rover, using a Wave Glider, shows an example of collaboration between two autonomous vehicles, with low human intervention. Furthermore, using the ROSB methods for target localisation, we are not limited to work in a specific area (like in traditional LBL systems), and we do not need to introduce more instruments (like a USBL), instead of that, standard acoustic modems can be used, which are also used to communicate and download information from underwater instruments. For these reasons, this method is interesting in terms of cost, flexibility and consumption.

Finally, the reasons to choose the paths selected to perform this mission were twofold, the time required to complete the path and the desirable accuracy. The first test was carried out using a 200 metres radius circle. In this case, a first inaccurate estimation of the Rover's position was required. Moreover, due to other tests that had to be carried out, the time constraint was a key factor. Then, a more accurate localisation was desirable during the second test, and therefore, more time was designated for the localisation mission. In this case, an 800 metre radii circle was used, which is one of the best radius in terms of accuracy and time consumption, as can be observed in the previous study explained above.

4.7 Discussion

The aim of this work was to study and develop new procedures for underwater target localisation using a Wave Glider, Autonomous Surface Vehicle (ASV), which could be used as a platform in support of applications in marine, geoscientific, ecology and archaeology, which have been increasingly used over the past 30 years [113]. Here, a complete study about the best practices for underwater target localisation using range-only techniques has been carried out, which includes different areas such as analytical studies, simulations, and field tests. At the same time, a real mission to find an underwater rover has been presented, where the successful collaboration between both autonomous vehicles was shown. From a methodology point of view, this work advanced the understanding of accuracy that can be achievable by using both the ROSB localisation methods and an autonomous vehicle, which has been demonstrated not only numerically, but also in real tests. In this context, those advancements would contribute to expanding the use of surface vehicles, and in concrete Wave Gliders, as multi-purpose platforms, which have been used widely around the world [114].

Most of the works about optimal sensor placement for underwater target localisation are centred on analytical studies, [98] and [94]. Whereas this is an important area of study, real tests have a great impact on the final users, which demonstrates not only in simulations but also in real missions the operability of this kind of systems. As far as the authors know, such complete study, where both theoretical and practical work is addressed, has not been conducted previously.

The initial point of this chapter is the work performed by [98], which studied the optimal sensor placement for target localisation. However, whereas they work with multiple sensors, the work presented here is focused on a single sensor (which is the Wave Glider), therefore a different point of view is used. In addition, due to the mission's limitations, such as time and power consumption, new different limitations have been studied. One has to take into consideration such limits before planning each missions, these are a key factor, which are really important for vehicle operators. As shown, finally a relationship between accuracy and time/power consumption is obtained, and the mission planner must deal with that.

As a summary, the below indications should be in general followed before planning a mission in order to find the optimal path:

a) The optimal path is a circle centred over the target's position

b) The optimal circle's radius is:

- $r_c = \sqrt{2} z_T$ if the target's depth is unknown

- As large as possible if the target's depth is known

c) The optimal measurements distribution is equally distributed over the circle's path

d) The optimal number of measurements is as large as possible

Nevertheless, as demonstrated, in some scenarios it is not possible to use these indications (e.g. when the time to complete the mission is not enough), and therefore, a smaller radius has to be used. Nevertheless, in the field test (for a target depth equal to 1800 m) a RMSE less than 5 m had been obtained using a radius of 800 m instead of $1800\sqrt{2}$ m, which is in general good enough for many missions.

In contrast, a Gaussian noise with zero mean and variance equal to σ as range error has been used during the analytical derivation of the optimal path's shape. It was assumed that this error was range independent and equal for all range values. This procedure enables the analityical interpretation of the mathematical equations. However, the variance of the range error can be much more complex, which is determined by different parameters such as SNR, transmission frequency, weather conditions and sea state. All of these factors were discussed in [106]. Moreover, the range error suffers from a systematic error, which is due to underwater sound speed uncertainty, which is usually difficult to measure qualitatively in-situ. As a consequence, this error introduces a constant error in the range measured. This is also dependent to the range. Concequently, in the simulations that have been conducted, the range error introduced in [106], plus a 1% of systematic error have been used in order to increase the similarity between simulations and the real world. It has been observed that to reduce the range error consequences, a path centred over the target is desired. Nonetheless, while the error in x and y can be solved easily using this recommendation, with the depth error one has to be more careful. The common way to solve the depth error is by using a depth sensor, since it is easy to find a small and cheaper one on the market with a good performance. In addition, other methodologies can be used such as pre-calibration or path techniques in order to find the exact underwater speed sound or depth position [104].

Finally, the similarity among the performance of the analytical methodology used, the simulations using LS and MLE, and the field tests can be highlighted. For example, if Fig. 4.2 and Fig. 4.6 are compared, in both cases a minimum error is obtained at a similar radius, which is when the ϵ_1 and *LS* graphics are minimum. Nevertheless, if the error model plus a systematic error is used, the minimum error that is achievable is obtained much earlier, *LS(Emod)+Depth*. This performance is also observed in the field tests, Fig. 4.11. Similar situations can be derived in the other cases under study, such as path shape and target offset.

To conclude, the main benefit of the simulations in respect to the analytical studies is that they can give the final users the expected RMSE, instead of a simple indication of their performance. Consequently, the simulations can be used to find the accuracy that can be achievable under different conditions, such as the path shape, but also the range error estimated.

4.8 Conclusions

This work extends the study conducted in [105] and shows the Wave Glider's performance as a moving LBL with simulations and real sea tests. Mathematical algorithms and performance have been compared with sea tests, showing a good similarity, which corroborates the simulations conducted in this chapter.

Two different algorithms have been implemented, the LS and the MLE, which have been compared through 1000 Monte Carlo iteration simulations. The scenario implemented was a static target at 1800 m depth. In this case, both algorithms show a similar performance, which is close to the CRB, used as a reference.

Furthermore, three types of field tests have been conducted to observe the system's performance under different conditions: the path shape, the path radius and the offset from the target. For each test three different paths have been conducted, which result in 9 Wave Glider missions, more than 300 ranges, and around 10 hours of tests.

With this study the best path and its characteristics can be determined, such as the number of points, the radius or offset, to obtain the desired target localisation performance, which are a minimum number of points equal to 12, a radius between 400 m and 800 m, and an offset as low as possible. With these parameters a RMSE less than 4 metres can be obtained, while maintaining both low time and power consumption requirements.

Finally, it can be concluded that the Wave Glider can be used as a moving LBL to find underwater targets with a good accuracy, as demonstrated in the experimental tests and the benthic Rover mission explained in this chapter. This system has been mathematically modeled and tested in real conditions, obtaining a good performance. Therefore, this will be a new powerful tool among MBARI's equipment for future missions.

Chapter 5

Range-only and single-beacon methods: A dynamic scenario

Range-only and single-beacon underwater target localisation methods using an autonomous vehicle and acoustic modems can also be used to track mobile targets. In such case, the previous target state and its propagation model must be taken into consideration.

5.1 Introduction

Underwater localisation is one of the main problems which has to be addressed in ocean exploration, as it has been observed in the previous Chapters, where no Global Positioning System (GPS) is available due to the high attenuation that electromagnetic waves suffer in seawater [30]. Therefore, most underwater positioning systems have to be conducted with acoustic communications, despite the channel limitations, such as frequency dependent attenuation, Doppler spread and multipath propagation [34].

5.1.1 Motivation

In addition to the traditional Long BaseLine (LBL) and Ultra-Short BaseLine (USBL) methods for target localisation (Chapter 2 and Chapter 3), new methods are being developed (e.g. moving long baseline or cooperative range-only tracking methods, Chapter 4) using improvements in autonomous vehicles' performance, and their capabilities to work in more complex scenarios (e.g. [20]). Here we present different approaches which have been conducted to solve the Range-Only and Single-Beacon (ROSB) strategy for underwater target tracking in a moving target scenario, describing the algorithms and characterizing their performance.

5.1.2 Related work

In the previous Chapter, the optimal path for static target localisation was not only demonstrated analytically and using simulations, but also in real field tests. In both cases a Least Square (LS) and a Maximum Likelihood (ML) estimator where used, and a circumference path was determined as optimal. However, to track moving targets, another approximation is required using filtering and estimation techniques. For example, in [115], the authors derived the same idea but for cooperative range-based underwater moving target localisation. In that case an Extended Kalman Filter (EKF) estimator was used.

As previously observed, the ROSB methods are based on an autonomous vehicle which is used as a tracker. This vehicle conducts a set of manoeuvres in order to track some target(s). However, in a dynamic scenario, where both tracker and targets are mobile, the ROSB target tracking method can also be seen as a Hidden Markov Model (HMM) problem. Usually, the HMM is defined as a sequence of states, known as a Markov chain, and a set of observations for each state [116]. Using Bayes' rule

$$p(\mathbf{x}_k|\mathbf{z}) = \frac{p(\mathbf{z}|\mathbf{x}_k)p(\mathbf{x}_{k-1})}{p(\mathbf{z})}, \tag{5.1}$$

the probability distribution function of the HMM states can be derived given a set of observations $\mathbf{z} \in \mathbb{R}^m$, and therefore, the current state $\mathbf{x} \in \mathbb{R}^{2n}$ can be estimated. Where m indicates the number of observations carried out, and n can be either 2 or 3, which is the space dimension of the problem. And $p(\mathbf{x}_k|\mathbf{z})$ is the posterior probability distribution, expressed also as $p(\mathbf{x}_k|\mathbf{z}_{:k})$; $_{:k}$ subscript denotes all observations up to k. The $p(\mathbf{x}_{k-1})$ is the prior probability distribution expressed also as $p(\mathbf{x}_k|\mathbf{z}_{:k-1})$. And finally, $p(\mathbf{z})$ is the total probability of $\mathbf{z}$ [117], expressed also as $\int_{\mathbf{x}_k} p(\mathbf{z}|\mathbf{x}_k)p(\mathbf{x}_{k-1})d\mathbf{x}_k$, which is used as a normalized factor. However, to compute the predicted state $\mathbf{x}_k$, the total probability $p(\mathbf{z})$ can be ignored, which yields in the optimal solution of the following maximization problem

$$\mathbf{x}_k^{OPT} = \underset{\mathbf{x}_k}{\operatorname{argmax}}\ p(\mathbf{x}_k|\mathbf{z}_{:k}). \tag{5.2}$$

In prediction theory and filtering, the posterior distribution can be computed recursively from the prior distribution using a prediction step $p(\mathbf{x}_k|\mathbf{z}_{:k-1})$ and an update step $p(\mathbf{x}_k|\mathbf{z}_{:k})$.

In general, the existing filtering methodologies compute either the predictions with respect to the conditional probability distribution $p(\mathbf{x}_k|\mathbf{z}_{:k})$, such as Particle Filter (PF), or with respect to the probability joint distribution $p(\mathbf{x}_k, \mathbf{z}_k|\mathbf{z}_{:k-1})$,

such as EKF, see [118] and the references therein. One of the differences between these methods is the computational cost. Whereas the computational cost of the first methodology increases exponentially with the state dimension, the second one increases linearly with the state dimensions. Consequently, in areas with either great state dimensions or computational restrictions, this performance should be taken into consideration, see Table 5.6.

Hereinafter, the following considerations and parameters will be considered in all filtering methodologies which have been studied. In order to simplify the notation, a 2D scenario is used, where the tracker conducts manoeuvres on the sea surface to predict the target's position. This is a common procedure due to the facility of knowing the target's depth with high accuracy using cheap devices (e.g. used in GPS Intelligent Buoys [119, Chapter 3]), and therefore, a 3D scenario can be projected into a 2D plane. Consequently, the state vector used for both tracker and target is defined as

$$\mathbf{x} = [x \quad \dot{x} \quad y \quad \dot{y}]^T, \tag{5.3}$$

where x and y are the positions in the 2D plane, and $\dot{x}$ and $\dot{y}$ are their associated velocities. Finally, the observation measurement vector is defined as

$$\mathbf{z} = [z_1, \ \ldots, \ z_m]^T, \tag{5.4}$$

where m denotes the number of observations conducted. In ROSB methods, those are the ranges between the tracker and the target, which will be computed using the slant range measured by acoustic modems and the target's depth provided by a pressure sensor during the exchange message procedure conducted to measure the range between both devices or by the prior knowledge of the target's depth.

5.1.3 Contributions

Our data may be useful in developing autonomous networks to monitor and quantify human impacts, as described by the Marine Strategy Framework Directive of the European Commission [120]. The spatial scaling of data gathered at fixed observatories, could be complemented by the use of flexible and adaptive networks of monitors and autonomous underwater vehicles. Our data could help toward the implementation of multi-parametric coordinated monitoring.

The ROSB target tracking methods can be studied from different points of view. For example, the tracker's optimal path, where [98] and [121] developed a complete analytical study for an optimal sensor placement in an underwater target localisation scenario. In Chapter 4 the optimal path for static target localisation was not only

demonstrated analytically and using simulations, but also in real field tests. In both cases a LS and a ML estimator where used, and a circumference path was determined as optimal. Later, in [115], the authors derived the same idea but for cooperative range-based underwater moving target localisation. In that case an EKF estimator was used.

5.2 Range-Only and Single-Beacon Methods

In Chapter 4 we studied the optimal path shape which should be performed by an autonomous vehicle to increase the accuracy of a static target localisation using a ROSB method. The LS and the ML estimators were compared to Cramér-Rao Bound (CRB) and different field tests. These two methods are commonly used when no straightforward solution is possible [109]. For example, for either non-linear, non-smooth, or overdetermined systems (when $m > n + 1$).

Nevertheless, when the target to be localised is not static, but moving, and active tracking is desired, the LS and ML estimators are not suitable. These dynamic scenarios are typically modelled in a state-space representation of HMM, where the next state only depends on the current state, and the current measurement depends only on the current state.

In this Chapter, different filters and methods have been studied and compared, presenting main aspects and some implementation. These methods are:

- Extended Kalman Filter (EKF)
- Unscented Kalman Filter (UKF)
- Maximum A Posteriori (MAP)
- Particle Filter (PF)

The main aspects of these filters are presented below with a description for their implementation. We have conducted a study of the performance of different ROSB methods through simulations, and validated them through field tests. This extended study has been carried out focusing on performance comparison among different algorithms (EKF, Unscented Kalman Filter (UKF), Maximum A Posteriori (MAP), and PF), specifically designed for 3 typical underwater scenarios: localising a static target, tracking a dynamic target, and multi-target tracking. For a methodology point of view, this work advanced the understanding of accuracy that can be achievable using ROSB localisation methods and an autonomous vehicle.

The notation employed to develop these algorithms is summarized in Table 5.1.

Table 5.1: Nomenclature

List of symbols	
$\mathbf{x} \in \mathbb{R}^{2n}$	State vector
$\hat{\mathbf{x}}_k \in \mathbb{R}^{2n}$	Target state vector estimated at time k
$\mathbf{q} \in \mathbb{R}^n$	Target position
$\mathbf{p} \in \mathbb{R}^n$	Tracker position
$\mathbf{z} \in \mathbb{R}^m$	Vector of ranges
$\mathbf{F} \in \mathbb{R}^{n \times n}$	State transition matrix
$\mathbf{Q} \in \mathbb{R}^{n \times n}$	Process noise matrix
$\mathbf{R} \in \mathbb{R}^{n \times n}$	Range measurement error covariance matrix
$\mathbf{P} \in \mathbb{R}^{n \times n}$	State covariance matrix
$h(\cdot)$	Measurement model function
$\mathbf{H} \in \mathbb{R}^n$	Jacobian matrix of $h(\cdot)$
$n \in \{2, 3\}$	Dimension of estimation problem
$m \in \mathbb{N}$	Number of measurements

5.2.1 Extended Kalman Filter

The EKF is the classical inference method for non-linear dynamic systems, which is based on the linearisation of the state and measurement equations along the trajectory [122] and [123]. This deterministic and parametric method estimates the target position based on the probability joint distribution. First of all, the state vector of the target at time-step k is defined by $\mathbf{x}_k = [x_{Tk} \;\; \dot{x}_{Tk} \;\; y_{Tk} \;\; \dot{y}_{Tk}]^T$. Then, assuming a constant target velocity, which is a general consideration, the motion model of the target is

$$\mathbf{x}_k = \mathbf{F}_{k-1}\mathbf{x}_{k-1} + \mathbf{Q}_{k-1}, \tag{5.5}$$

where $\mathbf{F}$ is the state transition matrix, and $\mathbf{Q}$ is the process noise, which has variance σ_v^2. Both are related to time-step Δt, and are described as

$$\mathbf{F} = \begin{bmatrix} 1 & \Delta t & 0 & 0 \\ 0 & 1 & 0 & 0 \\ 0 & 0 & 1 & \Delta t \\ 0 & 0 & 0 & 1 \end{bmatrix} \tag{5.6}$$

and

$$\mathbf{Q} = \begin{bmatrix} \frac{1}{4}\Delta t^4 & \frac{1}{2}\Delta t^3 & 0 & 0 \\ \frac{1}{2}\Delta t^3 & \Delta t^2 & 0 & 0 \\ 0 & 0 & \frac{1}{4}\Delta t^4 & \frac{1}{2}\Delta t^3 \\ 0 & 0 & \frac{1}{2}\Delta t^3 & \Delta t^2 \end{bmatrix} \sigma_v^2. \tag{5.7}$$

On the other hand, the measurement model used at time-step k can be described by

$$\begin{aligned} h(\mathbf{x}_k) &= \| \mathbf{q}_k - \mathbf{p}_k \| + w_k \\ &= \sqrt{(x_{qk} - x_{pk})^2 + (y_{qk} - y_{pk})^2} + w_k, \end{aligned} \tag{5.8}$$

where $\mathbf{q}_k \in \mathbb{R}^2$ and $\mathbf{p}_k \in \mathbb{R}^2$ are the target and observer positions respectively in a 2D scenario, and $w_k \sim \mathcal{N}(0, \sigma_{wk}^2)$ is a zero-mean Gaussian noise, leading to a covariance matrix equal to $\mathbf{R} = \text{diag}[\sigma_{wk}^2]$. Finally, the Jacobian matrix of $h(\mathbf{x}_k)$ is computed as

$$\mathbf{H} = \left.\frac{\partial h(\mathbf{x}_k)}{\partial \mathbf{x}}\right|_{\mathbf{x}_k} = \begin{bmatrix} \frac{(x_{qk} - x_{pk})}{\sqrt{(x_{qk} - x_{pk})^2 + (y_{qk} - y_{pk})^2}} \\ 0 \\ \frac{(y_{qk} - y_{pk})}{\sqrt{(x_{qk} - x_{pk})^2 + (y_{qk} - y_{pk})^2}} \\ 0 \end{bmatrix}^T. \tag{5.9}$$

Algorithm 2 has been designed to track an underwater target using the ROSB method and the EKF, which has been derived using the equations explained above, where the target state estimation $\hat{\mathbf{x}}_k$ and its associated covariance $\mathbf{P}_k = \mathbf{F}\mathbf{P}_{k-1}\mathbf{F}^T + \mathbf{Q}$ at each step k are given.

5.2.2 Unscented Kalman Filter

The UKF was proposed in [124] as a derivative-free alternative to the EKF. Whereas the EKF's linearisation process incorporates inherent flaws (i.e. the expressions are approximated using a firs-order Taylor series), the UKF addresses them by utilizing a deterministic *sampling* strategy [125], where essentially, a set of points are propagated through the true nonlinearity, without approximation. i.e. the unscented transformation uses a set of appropriately chosen weighted points to parameterise the means and covariances of probability distributions. These points, called sigma points $\boldsymbol{\chi}$, are propagated through the system using the state transition matrix $\mathbf{F}$ presented in (5.6).

Input: $\Delta t, z_i$, New_range
Output: Next target state estimation $\hat{\mathbf{x}}_k$
if *_Init_* **then** Initialize:
  $\mathbf{F}, \mathbf{R}, \mathbf{Q}, \mathbf{P}_0, \hat{\mathbf{x}}_0$
end
Predict step:
$\hat{\mathbf{x}}_k = \mathbf{F}\hat{\mathbf{x}}_{k-1}$
$\mathbf{P}_k = \mathbf{F}\mathbf{P}_{k-1}\mathbf{F}^T + \mathbf{Q}$
if *New_range* **then** Update step:
  $\mathbf{H}_x = \mathbf{H}(\hat{\mathbf{x}}_k)$
  $\mathbf{S} = \mathbf{H}_x\mathbf{P}\mathbf{H}_x^T + \mathbf{R}$
  $k = \mathbf{P}\mathbf{H}_x^T\mathbf{S}^{-1}$
  $h_x = h(\hat{\mathbf{x}}_k)$
  $y = z_k - h_x$
  $\hat{\mathbf{x}}_k = \hat{\mathbf{x}}_k + ky$
  $\mathbf{I}_k = \mathbf{I}_{k-1} - k\mathbf{H}_x$
  $\mathbf{P}_k = \mathbf{I}\mathbf{P}_k\mathbf{I}^T + k\mathbf{R}k^T$
end

Algorithm 2: EKF method for Range-Only and Single-Beacon target tracking.

Different methods can be used to choose the sigma points (e.g. [126] and [127]). Here, the method presented in [127] has been used, where $\boldsymbol{\chi} \in \mathbb{R}^{(n \times 2n+1)}$ is defined as

$$\boldsymbol{\chi} = \begin{bmatrix} \hat{\mathbf{x}}^T \\ \hat{\mathbf{x}} + \gamma\sqrt{\mathbf{P}} \\ \hat{\mathbf{x}} - \gamma\sqrt{\mathbf{P}} \end{bmatrix}, \tag{5.10}$$

where $\gamma = \sqrt{n+\lambda}$, with $\lambda = \alpha^2(n+\mathsf{k}) - n$. These constant values are usually set as follows: α is chosen between $1e^{-4}$ and 1, which determines the spread of the sigma points; k is set to 0 for state estimation; and $\beta = 2$ for Gaussian distributions.

Finally, these sigma points are weighted as follows,

$$W_0^{(\mathbf{x})} = \frac{\lambda}{n+\lambda}, \tag{5.11}$$

$$W_0^{(\mathbf{P})} = \frac{\lambda}{n+\lambda} + 1 - \alpha^2 + \beta, \tag{5.12}$$

$$W_i^{(\mathbf{x})} = W_i^{(\mathbf{P})} = \frac{1}{2(n+\lambda)}, i \in \{1, \ldots, 2n\}. \tag{5.13}$$

The equations (5.5)-(5.9) presented in the previous section are also used in the UKF. Following the notation of [124] and [127] the UKF for ROSB tracking is described in Algorithm 3.

Input: $\Delta t, z_i$, New_range
Output: Next target state estimation $\hat{\mathbf{x}}_k$
if *_Init_* **then** Initialize:
| $\mathbf{F}, \mathbf{R}, \mathbf{Q}, \mathbf{P}_0, \hat{\mathbf{x}}_0$
end
Predict step:
$\boldsymbol{\chi} = [\ \hat{\mathbf{x}}_{k-1},\ \hat{\mathbf{x}}_{k-1} + \gamma\sqrt{\mathbf{P}_{k-1}},\ \hat{\mathbf{x}}_{k-1} - \gamma\sqrt{\mathbf{P}_{k-1}}\ ]$
$\boldsymbol{\chi}_{\mathbf{F}} = \mathbf{F}\boldsymbol{\chi}$
$\hat{\mathbf{x}}_k = \sum_{i=0}^{2n} W_i^{(\mathbf{x})} \boldsymbol{\chi}_{\mathbf{F}}$
$\mathbf{P}_k = \sum_{i=0}^{2n} W_i^{(\mathbf{P})} [\boldsymbol{\chi}_{\mathbf{F}} - \hat{\mathbf{x}}_k][\boldsymbol{\chi}_{\mathbf{F}} - \hat{\mathbf{x}}_k]^T + \mathbf{Q}$
if *New_range* **then** Update step:
| $\boldsymbol{\chi} = [\ \hat{\mathbf{x}}_k,\ \hat{\mathbf{x}}_k + \gamma\sqrt{\mathbf{P}_k},\ \hat{\mathbf{x}}_k - \gamma\sqrt{\mathbf{P}_k}\ ]$
| $\boldsymbol{h}_{\boldsymbol{\chi}} = h(\boldsymbol{\chi})$
| $\hat{\mathrm{y}}_k = \sum_{i=0}^{2n} W_i^{(\mathbf{x})} h_{\boldsymbol{\chi},i}$
| $\mathbf{P}_{\boldsymbol{h}_{\boldsymbol{\chi}}\hat{\mathrm{y}}} = \sum_{i=0}^{2n} W_i^{(\mathbf{P})} [h_{\boldsymbol{\chi},i} - \hat{\mathrm{y}}_k][h_{\boldsymbol{\chi},i} - \hat{\mathrm{y}}_k]^T + \mathbf{R}$
| $\mathbf{P}_{\hat{\mathbf{x}}\hat{\mathrm{y}}} = \sum_{i=0}^{2n} W_i^{(\mathbf{P})} [\boldsymbol{\chi}_i - \hat{\mathbf{x}}_k][h_{\boldsymbol{\chi},i} - \hat{\mathrm{y}}_k]^T$
| $k = \mathbf{P}_{\hat{\mathbf{x}}\hat{y}} \mathbf{P}^{-1}_{\boldsymbol{h}_{\boldsymbol{\chi}}\hat{y}}$
| $y = z_k - \hat{\mathrm{y}}_k$
| $\hat{\mathbf{x}}_k = \hat{\mathbf{x}}_k + ky$
| $\mathbf{P}_k = \mathbf{P}_k - k\mathbf{P}_{\boldsymbol{h}_{\boldsymbol{\chi}}\hat{\mathrm{y}}} k^T$
end

Algorithm 3: UKF for Range-Only and Single-Beacon target tracking.

5.2.3 Maximum a Posteriori Estimation

The MAP estimation [116] is a well-known method for target tracking problems. Although, the MAP estimator had long been considered to be too computationally intensive for real-time applications [128], it is becoming more commonly used thanks to processor improvements (e.g. [129] and the references therein).

The EKF addresses the non-linear estimation problems by applying linearisation methods, which introduce inherent errors. While UKF has been developed as an alternative strategy to address these errors, it only refines the current state, being unable to refine past linearized points (see the previous Section. In contrast, the MAP estimator computes the estimations of all states at all time steps, by using all available measurements.

The main equations of the MAP estimator are described below (adapted from [116] and [129]). Firstly, as mentioned, all available information is used to estimate

the entire target trajectory by stacking all states in the time interval $[0, \ldots, k]$,

$$\mathbf{x}_{0:k} = [\mathbf{x}_0^T \ \mathbf{x}_1^T \ \cdots \ \mathbf{x}_k^T]^T. \tag{5.14}$$

Then, the entire state vector is estimated by maximising the posterior probability density function as follows

$$p(\mathbf{x}_{0:k}|\mathbf{z}_{0:k}) \propto p(\mathbf{x}_0) \prod_{k=1}^{k} p(\mathbf{x}_k|\mathbf{x}_{k-1}) p(\mathrm{z}_k|\mathbf{x}_k), \tag{5.15}$$

where $p(\mathbf{x}_0) \sim \mathcal{N}(\hat{\mathbf{x}}_0, \mathbf{P}_0)$ is the prior distribution. By applying Bayes' rule, and assuming a Gaussian and independent noise in both measurement and state functions, plus using the target motion model (5.5) and the range measurement model (5.8) explained above, (5.15) can be rewritten as

$$\begin{aligned} &p(\mathbf{x}_{0:k}|\mathbf{z}_{0:k}) \propto \\ &\underbrace{\frac{1}{\sqrt{(2\pi)^{2n}|\mathbf{P}_0|}} \exp\left(-\frac{1}{2}||\mathbf{x}_0 - \hat{\mathbf{x}}_0||^2_{\mathbf{P}_0} \right) \times}_{\text{Initial state constraint}} \\ &\underbrace{\prod_{k=1}^{k} \frac{1}{\sqrt{(2\pi)^{2n}|\mathbf{Q}_{k-1}|}} \exp\left(-\frac{1}{2}||\mathbf{x}_k - \mathbf{F}\mathbf{x}_{k-1}||^2_{\mathbf{Q}_{k-1}} \right) \times}_{\text{State transition constraint}} \\ &\underbrace{\prod_{k=1}^{k} \frac{1}{\sqrt{2\pi\sigma_{wk}^2}} \exp\left(-\frac{1}{2}||z_k - h(\mathbf{x}_k)||^2_{\sigma_{wk}^2} \right),}_{\text{Measurement constraint}} \end{aligned} \tag{5.16}$$

where $||\mathbf{a}||_{\mathbf{M}} \triangleq \mathbf{a}^T\mathbf{M}^{-1}\mathbf{a}$.

Using the monotonicity of the negative logarithm, the maximisation of (5.16) is equivalent to the minimisation of the following cost function

$$\begin{aligned} c(\mathbf{x}_{0:k}) = &\frac{1}{2}||\mathbf{x}_0 - \hat{\mathbf{x}}_0||^2_{\mathbf{P}_0} + \sum_{k=1}^{k} \frac{1}{2}||\mathbf{x}_k - \mathbf{F}\mathbf{x}_{k-1}||^2_{\mathbf{Q}_{k-1}} \\ &+ \sum_{k=1}^{k} \frac{1}{2}||z_k - h(\mathbf{x}_k)||^2_{\sigma_{wk}^2} \end{aligned}, \tag{5.17}$$

Due to the non-linearity of the measurement model (5.8), there is no straightforward solution. A standard approach for its optimisation is to employ iterative algorithms, which can find the solution from an initial estimation $\hat{\mathbf{x}}_0$ based on the

recursion of

$$\hat{\mathbf{x}}_{0:k}^{i+1} = \hat{\mathbf{x}}_{0:k}^{i} + \delta\mathbf{x}_{0:k}^{i}, \tag{5.18}$$

where the parameter $\delta\mathbf{x}_{0:k}^{i}$ is a correction factor, which indicates the step size and its direction. Employing the Newton-Raphson iterative minimisation method [130], as in previous works (e.g. [119]), and following [129], $\delta\mathbf{x}_{0:k}^{i}$ can be found solving the linear system

$$\delta\mathbf{x}_{0:k}^{i} = -\boldsymbol{A}^{i^{-1}}\boldsymbol{b}^{i}, \tag{5.19}$$

where $\boldsymbol{A}$ and $\boldsymbol{b}$ are the Jacobian (∇) and Hessian (∇^2) of the cost function (5.17) with respect to all stacked states (5.14), evaluated at the latest state estimation, which can be obtained as

$$\begin{aligned}\boldsymbol{b}^{i} = &\boldsymbol{\Pi}^{T}\mathbf{P}_{0}^{-1}(\hat{\mathbf{x}}_{0:k}^{i} - \hat{\mathbf{x}}_{0}) \\ &+ \sum_{k=1}^{k} \mathbf{F}_{k-1}^{i\,T}\mathbf{Q}_{k-1}^{-1}(\hat{\mathbf{x}}_{k}^{i} - \mathbf{F}_{k-1}\hat{\mathbf{x}}_{k-1}^{i}), \\ &+ \sum_{k=1}^{k} \mathbf{H}_{k}^{i\,T}\mathbf{R}_{k}^{-1}(z_k - h(\hat{\mathbf{x}}_{k}^{i}))\end{aligned} \tag{5.20}$$

and

$$\begin{aligned}\boldsymbol{A}^{i} \simeq &\boldsymbol{\Pi}^{T}\mathbf{P}_{0}^{-1}\boldsymbol{\Pi} \\ &+ \sum_{k=1}^{k} \mathbf{F}_{k-1}^{i\,T}\mathbf{Q}_{k-1}^{-1}\mathbf{F}_{k-1}^{i}, \\ &+ \sum_{k=1}^{k} \mathbf{H}_{k}^{i\,T}\mathbf{R}_{k}^{-1}\mathbf{H}_{k}^{i}\end{aligned} \tag{5.21}$$

where $\boldsymbol{\Pi}$, $\mathbf{H}$, and $\mathbf{F}$ are used to adjust the dimension of a single state estimation to the entire stacked state, which have the following structure

$$\boldsymbol{\Pi} = [\mathbf{I}_{2n}\ \mathbf{0}\ \cdots\ \mathbf{0}], \tag{5.22}$$

$$\mathbf{H} = [\mathbf{0}_{1\times 2n}\ \cdots\ -\mathbf{H}\ \cdots\ \mathbf{0}_{1\times 2n}], \tag{5.23}$$

$$\mathbf{F} = [\mathbf{0}_{2n\times 2n}\ \cdots\ -\mathbf{F}\ \mathbf{I}_{2n}\ \cdots\ \mathbf{0}_{2n\times 2n}]. \tag{5.24}$$

Hence, the MAP algorithm can be formulated using these equations as shown in Algorithm 4.

Finally, a marginalisation method can be used to reduce the computational cost of stacking all the states, which at a certain point can be computationally intractable. Different marginalisation methods have been developed to discard old states, which are not affected significantly by a new measurement available at the current target

Input: $\Delta t, z_i$, New_range
Output: Next target state estimation $\hat{\mathbf{x}}_k$
if *_Init_* **then** Initialize:
| $\mathbf{F}, \mathbf{R}, \mathbf{Q}, \mathbf{P}_0, \hat{\mathbf{x}}_0$
end
Predict step:
$\hat{\mathbf{x}}_k = \mathbf{F}_{k-1}\hat{\mathbf{x}}_{k-1}$
$\mathbf{P}_k = \mathbf{F}_{k-1}\mathbf{P}_{k-1}\mathbf{F}_{k-1}^T + \mathbf{Q}_{k-1}$
if *New_range* **then** Update step:
| $\mathbf{x}_{0:k} = [\mathbf{x}_0^T \ \mathbf{x}_1^T \ \cdots \ \mathbf{x}_k^T]^T$
| Refine all the states using Newton-Raphson iterative minimisation algorithm:
| **while** $i < max$ ***or*** $\nabla c(\mathbf{x}_{0:k}) > min$ **do**
| | Find $\boldsymbol{b}^i$ and $\boldsymbol{A}^i$ using (5.20) and (5.21)
| | $\delta\mathbf{x}^i_{0:k} = -\boldsymbol{A}^{i^{-1}}\boldsymbol{b}^i$
| | $\hat{\mathbf{x}}^{i+1}_{0:k} = \hat{\mathbf{x}}^i_{0:k} + \delta\mathbf{x}^i_{0:k}$,
| **end**
end

Algorithm 4: MAP for Range-Only and Single-Beacon target tracking.

position. For example, in [129] the Schur complement is used. Nonetheless, as will be shown, a simple sliding window can also be applied with good results, where at each time-step k the state vector is updated with a new state, while the oldest one is discarded. As a result, the stacked state vector always has the same size, and therefore, the computational cost does not change.

5.2.4 Particle Filter

Despite the benefits of the above algorithms, the EKF, the UKF or the MAP all have difficulties in tracking multi-modal probability density functions, which is a usual problem in ROSB tracking methods [131]. Only a few estimators are specifically designed to treat multi-modal distributions. Nowadays, the PF is one of the most commonly used [132] and [133].

The PF solves, in a non-parametric way, the probability distribution problem of the HMM using the Bayes' rule (5.1) with the recursion of

$$p(\mathbf{x}_k|\mathbf{z}_{:k-1}) = \sum_{\mathbf{x}_{k-1}} \underbrace{p(\mathbf{x}_k|\mathbf{x}_{k-1})}_{\substack{\text{Motion}\\ \text{model}}} \underbrace{p(\mathbf{x}_{k-1}|\mathbf{z}_{:k-1})}_{\text{Particles}}, \tag{5.25}$$

and

$$p(\mathbf{x}_k|\mathbf{z}_{:k}) \propto \underbrace{p(\mathbf{z}_k|\mathbf{x}_k)}_{\substack{\text{Importance}\\ \text{weights}}} \underbrace{p(\mathbf{x}_k|\mathbf{z}_{:k-1})}_{\text{Particles}}, \tag{5.26}$$

where a bunch of particles $\mathbf{x} \in \mathbb{R}^{2n}$ are spread on a 2D area, and are used to represent different possible states. Equation (5.25) represents the prediction step, which uses the motion model presented in (5.5) to move each particle with some random noise. In this case, the mean of all these particles represents the prior probability distribution. Then, using (5.26), each particle is weighted with a likelihood ratio based on the measurement probability function

$$W_k^n = \frac{1}{\sqrt{2\pi\sigma_{wk}^2}} \exp\left(- \frac{(h(\mathbf{x}_k^n) - z_k)^2}{2\sigma_{wk}^2} \right), \tag{5.27}$$

which calculates the probability of the state $\mathbf{x}_k^n$ for one dimensional Gaussian function with mean equal to the distance between the observer and the particle $h(\mathbf{x}_k^n)$, which is the measurement model described in (5.8), and variance equal to σ_{wk}^2. In this case, the index $n \in \{0, \ldots, N\}$ indicates the particle number up to N.

Finally, all the particles are resampled according to their weight in order to obtain the posterior probability distribution and to estimate the target's position. Different resampling methods have been developed [134], where the Systematic method offers a good performance in terms of computational complexity and resampling quality. However, [135], demonstrated that other methods, such as the Compound strategy, have better performance under fast target manoeuvre circumstances.

The Compound method consists of a twofold strategy: a standard Systematic resampling method for $(N - \ell)$ particles; and a Random resampling method for the last (ℓ) particles, which are dropped randomly inside a circular area around the previous target position that has been estimated as $\hat{\mathbf{x}}_{k-1}$. This strategy maintains particles near the target in all directions, improving the PF's time response in front of unexpected target position variations. Moreover, it maintains the particles' spatial variability, which helps to reduce the common degeneracy problem in the PF.

Using all these considerations, Algorithm 5 can be used to track underwater targets using the PF.

Input: $\Delta t, z_i$, New_range
Output: Next target state estimation $\hat{\mathbf{x}}_k$
if *_Init_* **then** Initialize:
  $\mathbf{F}, \mathbf{Q}, \hat{\mathbf{x}}_0$
  The state vector for each particle and its weight associated are also initialised:
  $\{\mathbf{x}_0^n\}_{n=1}^N \sim p(\mathbf{x}_0)$
  $\{W_0^n\}_{n=1}^N = 1/N_p$
end
Predict step (5.25):
$\{\hat{\mathbf{x}}_k^n\}_{n=1}^N = \mathbf{F}_{k-1}\{\hat{\mathbf{x}}_{k-1}^n\}_{n=1}^N + \mathbf{Q}_{k-1}$
if *New_range* **then** update step (5.26):
  Importance weight update using (5.27)
  $\{W_k^n\}_{n=1}^N$
  Normalize the importance weights
  $\{W_k^n\}_{n=1}^N = \{W_k^n\}_{n=1}^N / \sum_{j=1}^N W_k^j$
  Resampling:
  $c = [W_k^0, W_k^{i-1} + W_k^i, \ldots, W_k^{N-1} + W_k^N]$ for
  $i = \{1, \ldots, N-1\}$
  $u = random()/(N-\ell)$
  $i = 0$
  for j ***in*** *range*$(N-\ell)$ **do**
    while $u > c^i$ **do**
      $i \mathrel{+}= 1$
    end
    $\mathbf{aux}^j = \mathbf{x}_k^i$
    $u \mathrel{+}= 1/(N-\ell)$
  end
  for i ***in*** *range*(ℓ) **do**
    $\mathbf{aux}^{j+i+1} = random(\mathbf{x})$
  end
  $\{\mathbf{x}_k^n\}_{n=1}^N = \mathbf{aux}$
  $\hat{\mathbf{x}}_k = \frac{1}{N}\sum_{n=1}^N \mathbf{x}_k^n W_k^n$
end

Algorithm 5: PF for Range-Only and Single-Beacon target tracking.

5.3 Optimal path

One of the first problems to solve in underwater target tracking is to determine the path that should be followed by the observer in order to increase the accuracy of the target estimations. The ROSB methods suffers from the multi-modal distribution estimation, which is difficult to solve using standard algorithms such as the EKF. Different solutions have been found to solve this problem. For example, EKF or MAP filters have been used in parallel, where each filter tracks one possible trajectory, and a cost function is derived to find the most probable target path. One example of

this is the RP-EKF [136], where each EKF uses a different initial range estimation to track a target using bearings-only, and the bank-MAP in [129], where the authors used different MAP estimators for Range-Only target tracking.

Other authors (e.g. [98], [93], [99], and [91]) have solved the multimodal problem from the system's observability perspective: i.e. by driving specific paths to maximise the amount of information or quality of the measurements conducted, affecting the accuracy of the estimated target position. Using an optimum path, the multimodal problem can be avoided, and consequently, the tracking algorithms can compute the correct target position. These studies, which are based on the Fisher Information Matrix [108], determined that a circular trajectory centred over the target maximises the system's observability. In Chapter 4, the optimal circumference for target tracking using a surface vehicle was derived not only analytically, but with field tests. Whereas the ideal circumference is one with a radius as large as possible, in real scenarios the maximum radius is typically a few hundred metres due to time constraints. For example, for a typical velocity of 1 m/s, an boat will need more than 50 min to conducts one trajectory with 500 m of radius, and Furthermore, the power consumption and battery limitations should also be taken into consideration. This circumference can be written as follows

$$\mathbf{p}_k^* = \mathbf{q}_k + d_k^* \mathbf{g}(\beta_k), \tag{5.28}$$

where $\mathbf{p}_k^*$ is the optimal position of the tracker, $\mathbf{q}_k$ is the target's position, $\mathbf{g}(\beta_k) = [\cos\beta_k \;\; \sin\beta_k]^T$ with $\beta_k = 2m^{-1}\pi k$, where m is the number of range measurements per circle, and d_k^* is the optimal circumference's radius.

On the other hand, in [115] the optimal radius was estimated when the tracker's velocity was taken into account according to the larger magnitude of

$$d_k = |-||\mathbf{q}_k - \mathbf{p}_{k-1}^*||\cos\theta_k \pm \sqrt{\alpha_k^2 - (||\mathbf{q}_k - \mathbf{p}_{k-1}^*||\sin\theta_k)}|, \tag{5.29}$$

where α_k is the tracker's displacement at time k, defined by the time elapsed ΔT and the tracker's velocity $\bar{v}$ as $\alpha_k = \Delta T \bar{v}_k$, and θ_k is the angle between the vectors $(\mathbf{q}_k - \mathbf{p}_{k-1}^*)$ and $\mathbf{g}(\beta_k)$.

The maximum radius in (5.29) has two main boundaries: the tracker's maximum velocity $\bar{v}$; and the number of range measurements m to be conducted for each circumference, both implicitly defined in α_k and θ_k. As the tracker's velocity is constrained by the specifications of the vehicle being used, the only parameter that can be adjusted is the number of measurements. If a small number of measurements is used, a small circular radius will be obtained, otherwise the number of measurements must be increased. Nevertheless, another option is to introduce

additional time steps $M \in \{1, ..., M\}$ between measurements to increase the circumference's radius while respecting the vehicle's maximum velocity. In this case the circumference is defined by $\beta_k = 2(Mm)^{-1}\pi k$.

As a result, considering all these factors, a circular tracker path with a constant radius of 100 m (~10 min per circle) and range measurements every 40 s have been used in our study, in order to evaluate the performance of each ROSB method.

5.4 Simulations

A set of simulations have been conducted for the following scenarios: (a) Static Target Tracking; (b) Mobile Target Tracking; and (c) Multi-Target Tracking. These simulations have been performed in order to characterize the performance of each method described above, and tested them under different noise levels.

In general, Gaussian noise with zero mean and unit variance during the process of measurement is typically assumed [118] in analytical developments, whereas it has been observed that in some cases this is not accurate [93]. A Gaussian noise with non-zero mean and non-unit variance errors, $w \sim \mathcal{N}(\epsilon_w, \sigma_w^2)$, introduces a systematic error and a random uncertainty respectively in field measurements. Moreover, some measurements can differ substantially from the true range (i.e. outliers), with a potentially strong influence on the estimations. During simulations, different outlier measurements were randomly introduced by multiplying the real range by four. The total number of outlier measurements did not exceed the 1% of the total number of measurements. Consequently, each scenario has been studied using Monte Carlo Simulation (MCS) methods [137], where different noise levels have been added to each range measurement to evaluate the tracking method's robustness in the face of them, and to obtain a more realistic simulation.

To characterise the tracking filters' performance, the step response criteria has been used. The step response concept is generally used in control system analysis to characterise the time evolution of a dynamic system [138, Fig. 5-2]. It is known that the system's response has two components: transient response and steady state response. The transient response is present in the short period of time immediately after the system is turned on or a change is conducted on the input control. If the system is asymptotically stable, then the transient disappears and the system is determined by its steady state component only. Under this assumption, the ROSB methods presented in this Chapter can be characterised by

- Settling Time (T_S): Time required to reach and stay below a threshold error
- Recovery Time (T_R): Time required to reach and stay below a threshold error

after a step response

- Steady State Error (ε_{SS}): The error between the real target position and its estimation in the limit as time goes to infinity
- Root Mean Square Error (RMSE): The X-Y error between the true target position and its estimation computed as

$$\text{RMSE} = \sqrt{\mathbb{E}\left\{\left\|\mathbf{x}_k - \hat{\mathbf{x}}_k\right\|^2\right\}} \tag{5.30}$$

Finally, with all these considerations, the main parameters used to conduct the simulations are described below:

- Observer velocity: 1 m/s
- Observer circumference radius: 100 m
- Target velocity: 0 or 0.2 m/s (variable among tests)
- Random range noise: 1 or 4 m (variable among tests)
- Systematic range noise: up to 1%
- Range measurement outliers: up to 1%
- Time between iterations: 20 s
- Time between range measurements: 40 s
- Simulation steps: 200
- MCS iterations: 100
- Number of particles (PF): 3000

5.4.1 Static target localisation

The target localisation algorithms explained in the previous section were first tested in a static scenario. This scenario is used as an initial test to evaluate the performance of the ROSB methods. Moreover, we were able to compare them against standard target localisation methods such as the LS [93], which is a good estimator to localise targets in static scenarios.

Fig. 5.1a shows the simulated RMSE average value and its Standard Deviation (STD) after 100 MCS iterations, showing the filters' time response, and Fig. 5.1b shows the filters covariance matrix response. This test was conducted with a range

noise equal to $\epsilon_w = 1\%$ and $\sigma_w = 4$ m. The fastest algorithm to reach an RMSE lower than 15 m is the LS (2.0 min), which is also the algorithm with the lowest ε_{SS} (0.8 m). On the other hand, the EKF provided the worst performance with an ε_{SS} of 9.5 m, and a T_S of 30 min, i.e. it did not estimate the target's position with very high accuracy.

Table 5.2 shows the simulated filters' performance under other range noise parameters. The LS method is the best one in many scenarios. However, the most robust filter in the face of outliers is the PF, which has an average $T_S = 11$ min and $\varepsilon_{SS} = 8.8$ m. In contrast, the inclusion of a systematic error was not relevant to the filters' performance. It is known that concentric circumferences around a target constitute the most robust path in the face of systematic errors, as explained in Chapter 4.

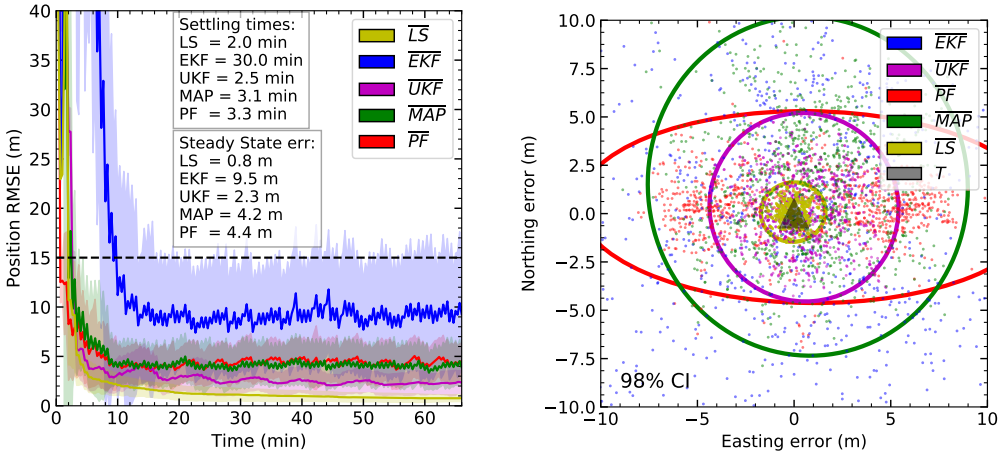

(a) (b)

Figure 5.1: (a) algorithms' time response for static target localisation. The settling time and the steady state error have been derived for the EKF, UKF, PF, MAP and LS algorithms. Results obtained through 100 MCS iterations with $\epsilon_w = 1\%$ and $\sigma_w = 4$ m. The dark colours represent the average whereas the light colours represent their standard deviation. (b) indicates the covariance matrix response, where a confidence interval of 98 % has been used to draw each circumference.

Table 5.2: Filters' performance for different range measurement errors: Static scenario.

Parameter	Filter	Mean (STD)[a]	Mean (STD)[b]	Mean (STD)[c]	Mean (STD)[d]
T_S (min)	LS	1.7 (0.0)	**2.0 (0.5)**	**2.0 (0.5)**	26.5 (31.0)
	EKF	9.0 (0.4)	33.5 (16.7)	30.0 (14.5)	38.5 (19.6)
	UKF	2.3 (0.0)	2.4 (0.2)	2.5 (0.3)	15.8 (21.3)
	MAP	1.7 (0.3)	2.8 (2.4)	3.1 (3.0)	16.7 (22.9)
	PF	**0.3 (0.4)**	2.3 (3.5)	3.3 (7.5)	**11.0 (15.5)**
ε_{SS} (m)	LS	**0.2 (0.1)**	**0.7 (0.4)**	**0.8 (0.4)**	13.0 (2.6)
	EKF	2.1 (1.3)	10.0 (6.3)	9.5 (6.2)	36.2 (74.2)
	UKF	0.6 (0.3)	2.3 (1.2)	2.3 (1.2)	**8.8 (15.2)**
	MAP	1.0 (0.5)	4.0 (2.1)	4.2 (2.2)	25.6 (49.5)
	PF	3.1 (1.4)	4.2 (2.1)	4.4 (2.0)	8.8 (17.0)

The range error introduced at each range measurement was as follows:

[a] ($\sigma_w^2 = 1$m)

[b] ($\sigma_w^2 = 4$m)

[c] ($\sigma_w^2 = 4$ m, $\epsilon_w = 1$ %)

[d] ($\sigma_w^2 = 4$ m, $\epsilon_w = 1$ %, plus 1% of outliers)

5.4.2 Mobile target tracking

In this section we discuss the results of simulations, where a mobile target with constant velocity of 0.2 m/s plus a 90° right turn after the 100$^{\text{th}}$ step (i.e. at 35 min from starting) was used as the second testing scenario. Besides the T_S and the ε_{SS}, the T_R was also computed as the filter's time response after the right turn, when the accuracy of the target's trajectory is lost, see Fig. 5.2a. Moreover, Fig. 5.2b shows the filters covariance matrix response.

The result of these indicators (T_S, T_R, and ε_{SS}) after 100 MCS and for different configurations of range noise are shown in Table 5.3. In general, the PF algorithm out-performed all the other methods, followed by the MAP algorithm. On the other hand, the LS was unable to track the mobile target as expected. The same performance is observed in all the noise cases, and for all the indicators studied.

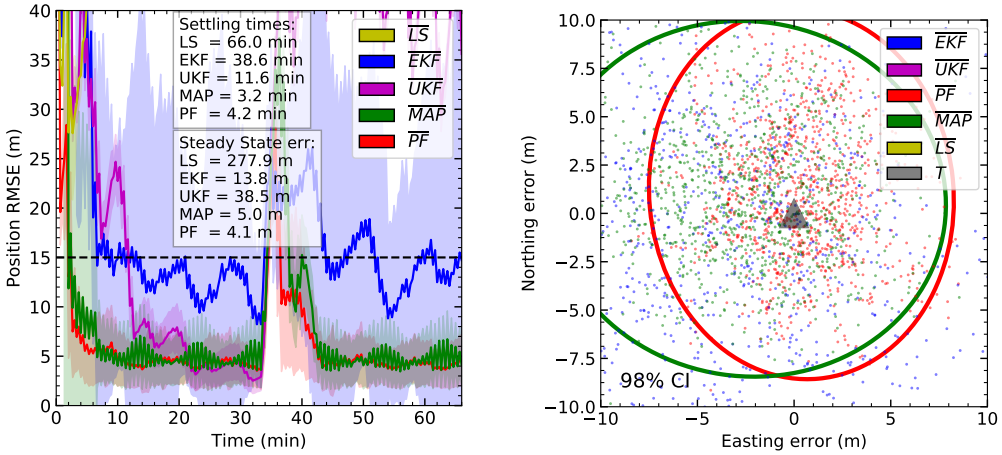

(a) (b)

Figure 5.2: (a) agorithms' time response for dynamic target tracking. The settling time and the steady state error are derived for the EKF, UKF, PF, MAP and LS algorithms. Moreover, the increase of the RMSE due to the target's right turn can also be observed. Results obtained through 100 MCS iterations with $\epsilon_w = 1\%$ and $\sigma_w = 4$ m. The dark colours represent the mean whereas the light colours represent their standard deviation. (b) indicates the covariance matrix response, where a confidence interval of 98 % has been used to draw each circumference.

Table 5.3: Filters' performance for different range measurement errors: Dynamic scenario.

Parameter	Filter	Mean (STD)[a]	Mean (STD)[b]	Mean (STD)[c]	Mean (STD)[d]
T_S (min)	LS	66.0 (0.0)	66.0 (0.0)	66.0 (0.0)	66.0 (0.0)
	EKF	6.2 (0.3)	45.8 (19.4)	38.6 (19.0)	46.9 (20.1)
	UKF	11.7 (0.1)	11.5 (0.4)	11.6 (0.4)	26.1 (22.3)
	MAP	1.9 (0.5)	5.1 (9.6)	**3.2 (2.7)**	21.2 (24.5)
	PF	**1.7 (0.3)**	**4.0 (7.4)**	4.2 (5.0)	**17.0 (20.8)**
T_R (min)	LS	30.0 (0.0)	30.0 (0.0)	30.0 (0.0)	30.0 (0.0)
	EKF	8.1 (1.3)	28.1 (4.0)	28.6 (3.4)	29.7 (4.6)
	UKF	34.6 (0.1)	34.5 (0.2)	34.5 (0.2)	18.7 (25.2)
	MAP	6.0 (0.1)	7.8 (3.6)	**8.8 (3.8)**	19.8 (25.6)
	PF	**5.8 (1.5)**	**7.4 (3.2)**	8.8 (5.1)	**15.1 (25.3)**
ε_{SS} (m)	LS	272.6 (0.1)	272.6 (0.3)	277.8 (0.2)	405.4 (2.5)
	EKF	4.3 (1.5)	12.7 (18.8)	13.8 (6.3)	37.0 (94.2)
	UKF	38.7 (0.4)	38.6 (1.8)	38.5 (1.7)	**8.0 (15.9)**
	MAP	2.5 (0.6)	4.8 (2.3)	5.0 (2.3)	16.7 (38.9)
	PF	**1.0 (0.5)**	**3.8 (2.1)**	**4.1 (2.2)**	10.3 (22.8)

The range error introduced at each range measurement was as follows:

[a] ($\sigma_w^2 = 1$m)

[b] ($\sigma_w^2 = 4$m)

[c] ($\sigma_w^2 = 4$ m, $\epsilon_w = 1$ %)

[d] ($\sigma_w^2 = 4$ m, $\epsilon_w = 1$ %, plus 1% of outliers)

We now discuss the performance of the PF using different configurations, e.g. the contribution of different resampling methods, the number of particles used, and the computational time required.

A PF: Resampling Method

The Compound (C) method has the advantage of sudden response in case of fast changes in the target's direction (see Section 5.2.4), by combining Systematic and Random resampling algorithms. Therefore, it can be adjusted by modifying the ratio between the number of particles used for the Systematic method (N_{sys}) and for the Random method (N_{rand}) respectively.

We conducted a set of simulations using different resampling methods as: (1) Multimodal, (2) Systematic, and (3) Compound. The results obtained in the time domain are presented in Table 5.4. After different iterations, we observed that the best ratio ($r(\%) = N_{rand}/N_{sys} * 100$) for the Compound resampling method was ~6.7 (i.e. only 6.7% of particles are resampled using the Random method).

Table 5.4: Particle Filter (PF)'s performance for different resampling strategies: Dynamic scenario.

	T_R(min)	T_S(min)	ε_{SS}(m)
Resampling[a]	Mean (STD)[b]	Mean (STD)[b]	Mean (STD)[b]
Multimodal	24.7 (5.0)	3.7 (1.9)	5.7 (9.8)
Systematic	21.2 (4.6)	4.4 (2.9)	2.6 (2.9)
C($r = 0.3$)	13.3 (8.2)	4.4 (2.7)	3.1 (6.2)
C($r = 1.7$)	9.6 (5.9)	3.3 (1.2)	1.3 (0.6)
C($r = 3.3$)	5.8 (2.5)	**3.2 (0.4)**	1.3 (0.7)
C($r = 6.7$)	**5.6 (2.2)**	3.3 (0.5)	**1.2 (0.7)**
C($r = 10.0$)	5.9 (1.9)	3.5 (0.9)	1.4 (0.6)
C($r = 16.7$)	5.6 (2.9)	3.4 (1.0)	1.3 (0.7)
C($r = 33.3$)	12.6 (8.2)	5.2 (4.2)	2.8 (0.9)
C($r = 66.7$)	29 (0.0)	29 (0.0)	14.5 (2.2)

[a] see [134] and [135] for a detailed description of these methods

[b] ($\sigma_w^2 = 1$m)

B PF: Number of Particles

The number of particles also has an important impact on the PF's performance. The more particles used to represent the target's position, the more accurate its estimation will be. In Table 5.5 the results for 1000, 3000, 6000, and 10000 particles are shown. In all these simulations, the Compound method with ratio 6.7 was used.

Table 5.5: PF's performance for different number of particles: Dynamic scenario.

	T_R(min)	T_S(min)	ε_{SS}(m)
# particles	Mean (STD)[a]	Mean (STD)[a]	Mean (STD)[a]
1000	13.2 (3.9)	6.1 (3.4)	1.4 (0.7)
3000	9.6 (5.9)	3.3 (1.2)	1.3 (0.6)
6000	7.3 (3.1)	2.8 (0.7)	1.1 (0.5)
10000	**6.1 (2.4)**	**2.5 (0.4)**	**1.1 (0.5)**

[a] ($\sigma_w^2 = 1$m)

C Processing Time Required

Finally, the processing time can be an important constraint and a decisive factor to choose one or another method. While processing time may not be a limiting factor in some underwater scenarios due to slow dynamic processes involved, in some cases this may not be true. For example, in centralised multi-target tracking situations, the total time required to compute all the targets' positions could increase significantly with the number of targets, and therefore, the processing time must be taken into consideration.

The algorithms' runtime performance is shown in Table 5.6, where clearly the PF is the most expensive method from the computational time point of view, whereas the MAP algorithm appears as good compromise between performance and computation time. Nonetheless, both methods are suitable for this application due to the slow dynamics in most underwater scenarios.

Table 5.6: Filter's average runtime required at each step.

Filter	Runtime[a] (ms)
EKF	0.2
LS	0.4
UKF	0.6
MAP	10.6
PF (1000)	34.4
PF (3000)	98.4
PF (6000)	181.9
PF (10000)	276.7

[a] Processor Intel(R) Core(TM) i7-4760HQ CPU @ 2.10 GHz with 8 GB of RAM memory

5.4.3 Multi-Target Tracking

Multi-target Monte Carlo simulations using both static and dynamic target were used to characterise the filters' performance, in order to determine: (1) the filter's response when the tracker is not conducting its manoeuvres directly over the target, but with some offset; and (2) the feasibility of tracking multiple targets simultaneously.

Firstly, 49 targets were spread on a grid of 7x7, each one separated 100 m from its immediate neighbour. Then, a tracker conducted circular manoeuvres over the centre of the grid with a radius of 100 m and a velocity of 1 m/s. Every 40 seconds a new range measurement was computed between the tracker and each of the 49 targets, updating an individual filter for each target in order to estimate its position. This procedure was repeated 5 times, one for each tracking algorithm.

A Multiple Static Targets

The filter's performance in a multi-static target localisation scenario is represented through coloured maps (Fig. 5.3). Those maps indicate the RMSE between the true target position (black triangles) and its estimation. This test was conducted 50 times using MCS iterations with a range noise equal to $\epsilon_w = 1\%$ and $\sigma_w = 4$ m. The average value among all RMSE is presented in Fig. 5.3a. This style of X-Y representation is commonly used [119], which indicates the target's estimation error obtained as a function of its position with respect to the tracker's path centre. For example, the best performance achievable using the LS algorithm for static target localisation was presented in [93, Fig. 4], where the CRB was used, and then verified through real field tests. Here, not only the LS but also the MAP and PF algorithms followed a similar performance.

The simulations show that the LS, MAP, and PF have a superior performance, where the targets close to the centre were better estimated. This behaviour is due to the observability of the system (see Section 5.3). On the other hand, both the EKF and UKF have the poorest performance, with more accurate estimated positions close to the centre of the tracker's path. This behaviour can be explained by the state's initialisation, where the first tracker position is used as an initial target estimation. As a result, the targets which are close to the tracker have the best initial estimation.

Finally, the average values of the 49 target estimations for the T_S and the ε_{SS} are shown in Fig. 5.3 (top left) and in Table 5.7. The LS algorithm exhibited the best performance with a $T_S = 4.2$ min and a $\varepsilon_{SS} = 6$ m. This result is similar to the result obtained in the previous section. However, here we also showed what could

be expected in the case of tracking only one target which is not directly below the tracker's path centre.

Table 5.7: Target tracking algorithms' performance in a multi-target scenario. Average results obtained from 49 targets: Static scenario.

	T_S(min)	ε_{SS}(m)
Filter	Mean (STD)[a]	Mean (STD)[a]
LS	**4.2 (1.3)**	**6.0 (0.1)**
EKF	29.3 (2.8)	64.5 (6.8)
UKF	25.1 (9.0)	55.0 (7.4)
MAP	15.4 (7.4)	9.7 (1.1)
PF	8.9 (4.0)	7.3 (0.4)

[a] ($\sigma_w^2 = 4$ m, $\epsilon_w = 1$ %)

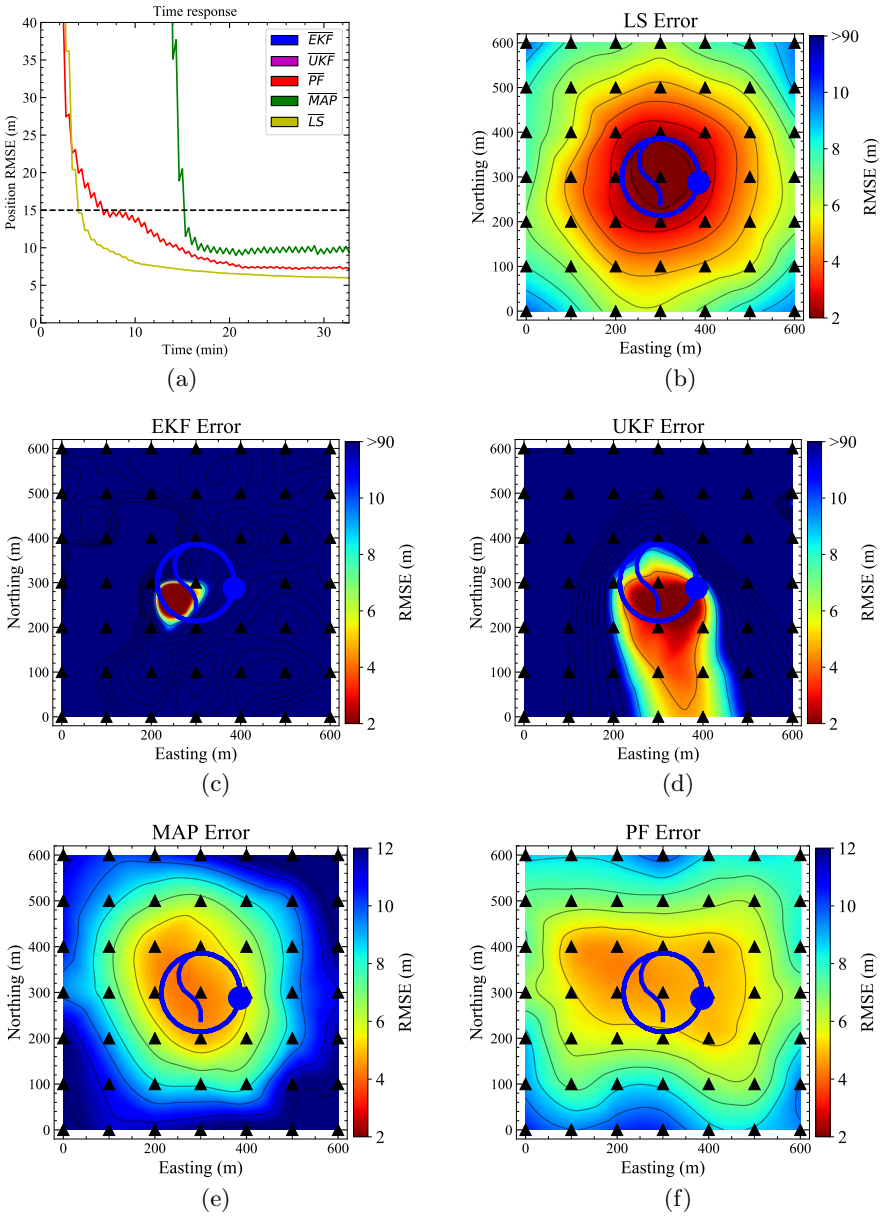

Figure 5.3: Algorithms' performance for static multi-target tracking scenario. A Gaussian error of 4 m plus a systematic error of 1% at each range measurement have been added. Each triangle represents the targets' position. The blue line and the circle represents the tracker's trajectory and its last position respectively. The colour map indicates the interpolation of the RMSE between the real target position and its estimation (the average of the last value over all the MCS iteration). Subplot (a) indicates the average of the time response over all the targets' RMSE, where the methods not depicted had an error greater than 40 m, and the dashed line represents the threshold used to compute the T_S.

B Multiple Mobile Targets

The performance of each tracking method using mobile targets is presented in Fig. 5.4. The EKF and the UKF had difficulties to track the targets when these were not directly below the centre of the tracker's path. Obviously, the LS algorithm cannot accurately estimate their position either.

In Table 5.8, the values of T_R, T_S, and ε_{SS} are shown, where a Gaussian noise of 4 m with 1% of systematic error has been added in all range measurements. The results show that only the PF and the MAP algorithms were able to track all the targets with an acceptable accuracy, where the PF had the best performance, also when they conduct a right turn (~30 min after the simulation's beginning).

Table 5.8: Target tracking algorithms' performance in a multi-target scenario. Average results obtained from 49 targets: Dynamic scenario.

	T_R(min)	T_S(min)	ε_{SS}(m)
Filter	Mean (STD)[a]	Mean (STD)[a]	Mean (STD)[a]
LS	29.7 (0.0)	65.0 (0.0)	313.6 (9.1)
EKF	29.7 (0.0)	65.0 (0.0)	51.4 (5.6)
UKF	26.2 (5.7)	65.0 (0.0)	114.7 (9.7)
MAP	18.0 (9.0)	**11.3 (5.4)**	10.1 (1.5)
PF	**13.4 (5.8)**	12.3 (7.4)	**7.8 (0.6)**

[a] ($\sigma_w^2 = 4$ m, $\epsilon_w = 1$ %)

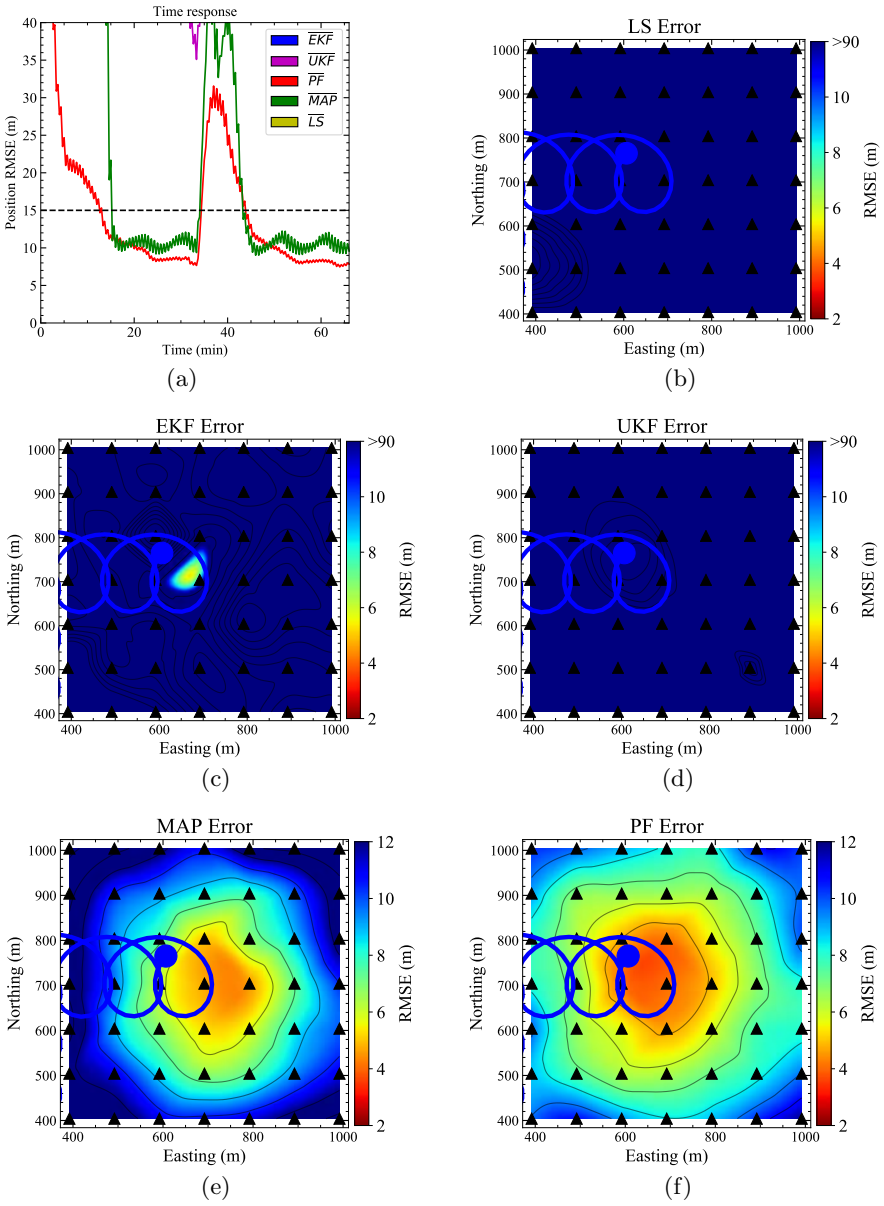

Figure 5.4: Algorithms' performance for dynamic multi-target tracking scenario. A Gaussian error of 4 m plus a systematic error of 1% at each range measurement have been added. Each triangle represents the targets' last position. The blue line and the circle represent the tracker's trajectory and its last position respectively. The colour map indicates the interpolation of the RMSE obtained at each target (the average of the last value over all the MCS iterations. Subplot (a) indicates the average of the time response over all the targets' RMSE, where the methods not depicted had an error greater than 40 m, and the dashed line represents the threshold used to compute the T_S.

5.5 Field Tests

After the study conducted using the MCS methods, different field tests were conducted in order to validate the results and conclusions derived. These tests were divided into two groups:

1. Tests carried out in the OBSEA underwater observatory (www.obsea.es) of the *Universitat Politècnica de Catalunya* (UPC)
   (a) Static test
   (b) Dynamic test
2. Dynamic tests conducted in Monterey Bay with the support of the Monterey Bay Aquarium Research Institute (MBARI) (www.mbari.org)

During those tests, the main parameters were the same ones used in Section 5.4 to be able to perform the appropriate comparisons (e.g. number of particles (PF) = 3000).

5.5.1 OBSEA Tests

These tests consisted in localizing three static targets and tracking a mobile one located at the coastal cabled observatory OBSEA. In both cases, S2C-18/34 acoustic modems from the EvoLogics company were used to measure ranges between observer and targets. These modems use the Sweep-Spread Carrier (S2C) technology, delivering an excellent performance, and working at 18 - 34 kHz. For these tests, a small boat was employed as observer, which computes the target position using the different methods studied. Fig. 5.5 shows one of the modems deployed in the seafloor used in the static test (left picture), and the drifter buoy used in the dynamic test (right picture).

A Static test at OBSEA

The first experiment carried out at OBSEA was designed to localise three acoustic modems previously deployed. One was attached to the observatory's buoy (M3) at 5 m depth, and two other modems deployed on the seafloor (M1 and M2), near the observatory's junction box at 20 m depth. Moreover, one of the seafloor modems had USBL capabilities (M1).

The slant range between the boat and each modem is represented in Fig. 5.6, where only one outlier (out of more than 300 measurements) between the boat and the USBL was obtained. However, this outlier must be taken into consideration,

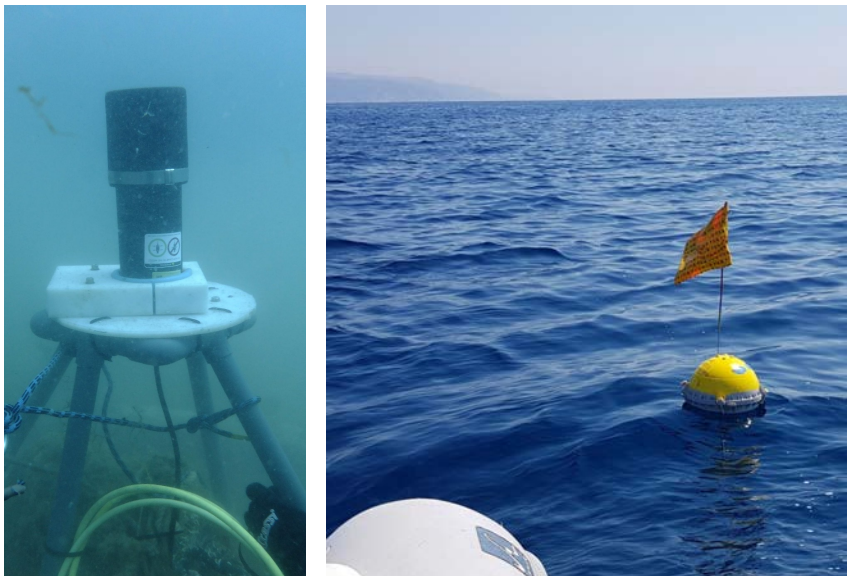

Figure 5.5: Underwater photography of the USBL (left) used as a target to localise during the static test, and the drifter buoy (right) used as a target to track during the dynamic test conducted in the OBSEA observatory.

which has an important implication in the performance of the localisation algorithms, especially for the LS method as observed in Table 5.2. Thus, it has to be removed in order to obtain an accurate estimation, whereas the PF is more robust even with the outlier included.

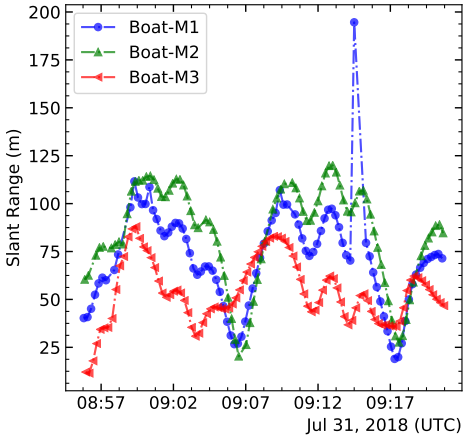

Figure 5.6: Slant ranges obtained between the boat and the underwater modems deployed at OBSEA.

Fig. 5.7 shows a geographic Cartesian coordinate map, where the target position estimations using the LS, MAP and PF, and the boat path conducted are represented. The PF algorithm has been executed 10 times in order to observe the

prediction's variability due to the inherent random processes involved. The estimation of the second modem (M2) using the MAP algorithm has an important error, which can be caused by the lack of observability in the system. The M2 was the farther modem from the centre of the boat path, and as observed in Section 5.4.3, not only the steady state error is worse, but also the settling time, which is important in such situations. Under these circumstances the MAP algorithm needs more time to obtain an accurate estimation of the target's position.

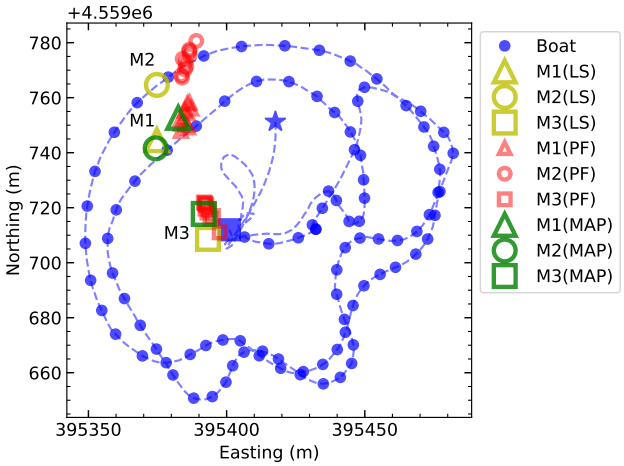

Figure 5.7: Static target localisation results obtained in the OBSEA observatory. The small blue dots represent the X-Y coordinates where a range measurement between the boat and each underwater target were carried out. The dotted blue line represents the boat's trajectory, where the start and square dots are the start and end positions respectively. Finally, the estimated positions for M1, M2 and M3 modems using LS, PF, and MAP algorithms are also represented.

Finally, the results obtained during this experiment can be compared against the results obtained through simulations as depicted in Table 5.9. Unfortunately, the true deployment position was not available, and therefore, the RMSE could not be computed. In this case, the error between the slant range measured with the modems and the theoretical slant range computed using the targets' prediction was used, denoted as Real ε_{SS}(Mean). On the other hand, the STD variation of the latest 10 estimations of each filter were used to obtain an indicator of its variability, denoted as Real ε_{SS}(STD). Therefore, the values are not equal, even so, the error's proportion is the same. On the other hand, both the EKF and the UKF were not taken into consideration during the field tests because of their lower performance, especially for targets not centred below the tracker's path (Table 5.7).

Table 5.9: Target tracking algorithms' performance for multi-target localisation purposes. Simulations vs real field tests: Static scenario. Test conducted on July 8, 2018.

	Sim ε_{SS}(m)		Real ε_{SS}(m)
# Filter	Mean (STD)[a]	Mean (STD)[b]	Mean (STD)
LS	0.8 (0.4)	6.0 (0.1)	8.2 (0.0)
EKF	9.5 (6.2)	64.5 (6.8)	– (–)
UKF	2.3 (1.2)	55.0 (7.4)	– (–)
MAP	4.2 (2.2)	9.7 (1.1)	29.3 (5.9)
PF	4.4 (2.0)	7.3 (0.4)	10.7 (3.3)

[a] ($\sigma_w^2 = 4$ m, $\epsilon_w = 1$ %) from static scenario (Table 5.2)

[b] ($\sigma_w^2 = 4$ m, $\epsilon_w = 1$ %) from static multi-target scenario (Table 5.7)

B Dynamic test at OBSEA

The second experiment carried out in the OBSEA was designed to track a dynamic target, which was a drifting buoy with an acoustic modem. The results obtained are presented in Fig. 5.8a, where the boat path (blue dotted line), the range measurements (blue dots), the real target position (black dotted line), the PF estimation (red dots), and the MAP estimation (green dots) are represented. On the other hand, the inset graphic (in the bottom-right corner) shows the RMSE between the estimated target position and its real position. Whereas the communication with the drifter was lost around 10:10 h UTC, the boat was able to track the drifter as soon as the communication was available again.

Nevertheless, it has to be taken into consideration that the real target position was interpolated using its initial deployment and recovery positions, and the sea currents present during the test, where the GPS position was not available during this experiment. For that reason, the mean error computed during this test should not be taken strictly into consideration, but as an indicator of the filter's performance. For example, as demonstrated in simulations, the MAP algorithm has a Recovery Time greater than the PF algorithm, and such performance is also observed in this field test, see Fig. 5.8b.

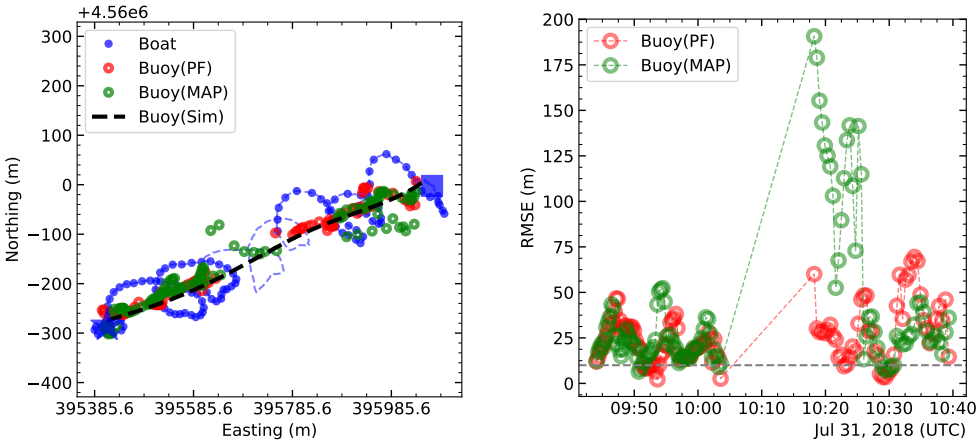

(a) (b)

Figure 5.8: (a) Dynamic target tracking results obtained in the OBSEA observatory. The small blue dots represents the X-Y coordinates where a range measurement between the boat and drifter was carried out. The dotted blue line represents the boat trajectory. The red dots represent the target's estimation using the PF algorithm, whereas the green dots represent the target's estimation using the MAP algorithm. The black slashed line is the drifter trajectory. Finally, (b) represents the RMSE between the real and the estimated target's position.

5.5.2 MBARI tests

Finally, a last test in Monterey Bay California in collaboration with the Monterey Bay Aquarium Research Institute (MBARI) was conducted in order to validate the algorithms and observe their performance under real conditions. This test was performed using a Wave Glider (WG) from the Liquid Robotics company, which tracked a Coastal Profiling Float (CPF) [139] for more than 15 hours, Fig. 5.9.

Figure 5.9: Coastal Profile Float (left) and Wave Glider (right) during sea tests conducted at Monterey Bay, California.

The CPF is a device which spends the majority of its time static, resting on the seabed. It periodically goes to the surface to fix a GPS position, then it drifts with the sea currents a few metres until it conducts another immersion to return to the seabed. During the test, the CPF conducted three immersions to ~60 m depth, as depicted in Fig. 5.10 (red line).

In order to know the CPF's position, the WG conducted circular paths around the area while periodically measuring the slant range to the CPF. An acoustic modem (ATM-900) from the Teledyne Benthos company was installed in the CPF and a Benthos DAT modem installed in the WG to measure the ranges. Both devices work at 16-21 kHz, and use a phase shift keying modulation technique. The Benthos DAT modem is a standard acoustic modem which also has USBL capabilities. Because of that, a comparative study between the target's position obtained with the USBL and the position estimated using the ROSB tracking algorithms explained above could be performed.

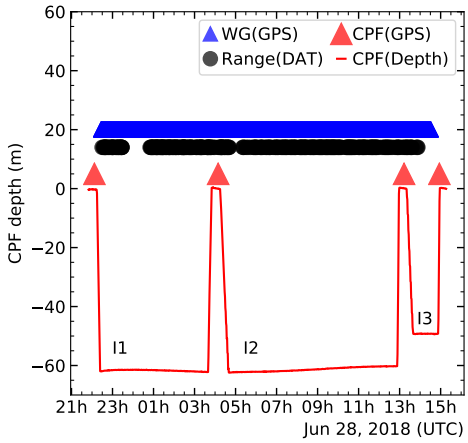

Figure 5.10: The CPF's depth profile (red line), when a CPF (red triangles) and a Wave Glider (blue triangles) positions were fixed, and when a slant range measurement was conducted between both devices (black dots) are presented in this graph.

Fig. 5.11 shows the path conducted by the Wave Glider and the CPF, both obtained using their own GPS. Moreover, the CPF estimated path computed using the PF (red dots) and the MAP (green dots) algorithms are also shown.

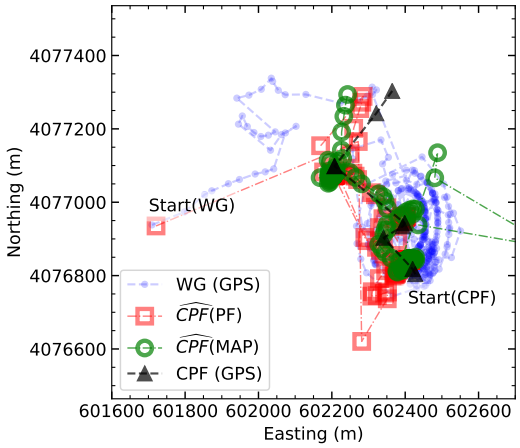

Figure 5.11: The Wave Glider trajectory during the field test WG(GPS), the CPF path CPF(GPS), and the CPF estimated position using PF $\widehat{CPF}$(PF) and MAP estimation $\widehat{CPF}$(MAP), are shown in this figure.

In addition, Fig. 5.12a shows the RMSE between the real CPF position and its estimations provided by the USBL system, and the PF and the MAP algorithms. The real CPF position has been computed by using the GPS positions while on the surface. However, it should be taken into consideration that no "true" CPF position while on the seabed was available. Therefore, this can cause an increase in

the average error. For example, the CPF's displacement produced by sea currents during the immersion has not been taken into consideration to compute the real CPF position.

On the other hand, the error obtained from USBL is much greater than the error obtained from the PF or MAP algorithms. In general, a USBL system has to be calibrated in advance, especially to eliminate the attitude misalignment between the acoustic transducer and the Inertial Measurement Unit (IMU), and also to adjust their internal clocks. However, despite the calibrations, large errors can be expected due to the sea state when a USBL instrument is installed on small platforms, such as a Wave Glider. Nonetheless, the error measured during this test is something unexpected, and therefore, indicates a poor calibration or some undetected misalignment.

Finally, the inset of Fig. 5.12b shows a zoom of PF' and MAP' RMSE results, where a mean of 21.9 m (PF) and 22.4 m (MAP) with an STD of 0.8 (PF) and 2.3 (MAP) have been obtained, which can be compared to the results obtained through the simulations as shown in Table 5.10.

Table 5.10: Target tracking algorithm's performance for target tracking. Simulations vs real field tests: Dynamic scenario. Test conducted on July 31, 2018.

	Sim ε_{SS}(m)		Real ε_{SS}(m)
# Filter	Mean (STD)[a]	Mean (STD)[b]	Mean (STD)
LS	277.8 (0.2)	313.6 (9.1)	– (–)
EKF	9.3 (6.3)	51.4 (5.6)	– (–)
UKF	38.3 (1.7)	114.7 (9.7)	– (–)
MAP	4.8 (2.3)	10.1 (1.5)	22.4 (2.3)
PF	4.0 (2.2)	7.8 (0.6)	21.9 (0.8)

[a] ($\sigma_w^2 = 4$ m, $\epsilon_w = 1$ %) from dynamic scenario (Table 5.3)

[b] ($\sigma_w^2 = 4$ m, $\epsilon_w = 1$ %) from dynamic multi-target scenario (Table 5.8)

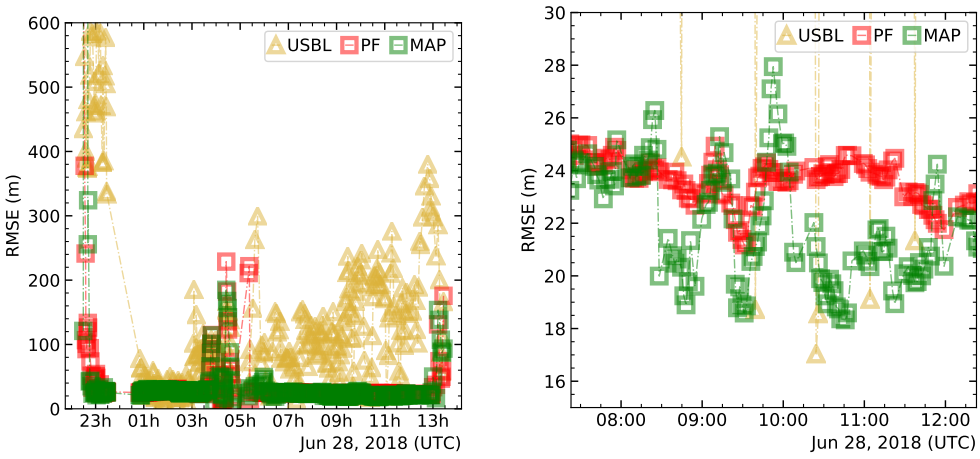

(a) (b)

Figure 5.12: (a) RMSE between the real CPF position and its estimation. Comparison between USBL (purple triangles), PF algorithm (red dots), and MAP algorithm (green dots). Inset shows a close look of the RMSE between 8:00 and 12:00 hours. Finally, (b) shows a closed view of the error.

5.6 Discussion

The aim of this Chapter is the study and development of different algorithms to track targets with autonomous marine vehicles moving along an horizontal plane by using range-only methods, such approach reduces the cost, power requirements, and complexity over other methods (e.g. using a USBL system which also requires an IMU). The methods presented in this Chapter may improve autonomous target tracking as a key factor for maritime and industries activities. For example, in the framework of fishery management (i.e. producing ancillary data for fishery management of relevant commercial items, as the Norway lobster (*Nephrops norvegicus*), as well as snow crabs [140]), where multiple platforms intercommunication protocols and autonomous navigation capabilities should be developed (i.e. the acoustic tracking of emitters placed on freely moving animals, spreading out from repopulating marine reserves).

Our data may also be useful in developing autonomous networks to monitor and quantify human impacts, as described by the Marine Strategy Framework Directive of the European Commission [120]. The spatial scaling of data gathered at fixed observatories, could be complemented by the use of flexible and adaptive networks of monitors and autonomous underwater vehicles. Our data could help toward the implementation of multi-parametric coordinated monitoring.

In this work, an extended study has been carried out focusing on performance comparisons among different ROSB algorithms (LS, EKF, UKF, MAP, and PF),

specifically designed for 3 typical underwater scenarios: localising a static target, tracking a dynamic target, and multi-target tracking. The MCS method provides a close comparison between the simulations and real field tests conducted. Simulations are powerful tools which allow a close study of more complex and noisy/real scenarios, compared to strictly deterministic analytical studies.

For example, Table 5.9 summarises the field test results conducted in the cabled observatory station OBSEA (`www.obsea.es`) to localise multiple targets, which have been compared with the Steady State Error (ε_{SS}) among 100 MCS for single target localisation (with 4 m of Gaussian error and 1% of systematic error), and 100 MCS for multi-target localisation (with 4 m of Gaussian error and 1% of systematic error). The results show that the target which is in the centre of the tracker path is estimated better. Finally, the real results show a greater error than the simulations, however, the error's proportion is the same, where the LS is the best algorithms whereas the MAP is the worst method. One can observe that neither the EKF nor UKF algorithms have been considered for real field tests. Moreover, the variability of these filters (STD) also follows the same trend presented in the simulations. It should also be noted that the real position of each modem was not available, and the mean error presented has been obtained using the slant range measured with the acoustic modems, and the slant range computed using their estimated positions. Furthermore, the greatest error presented in the field tests may be due to the lower number of ranges used, since the more measurements used, the greater the accuracy can be achieved.

The dynamic target tracking test conducted in the OBSEA, where a drifter buoy was used as a target, and presented in Fig. 5.8, shows the performance of PF and MAP algorithms in real field tests. The inset shows the evolution of the RMSE over time, where one can clearly observe that the PF has a settling time faster than that of the MAP. This behaviour has been observed previously using MCS (e.g. Fig. 5.4).

Finally, the test conducted in Monterey Bay with the PF and the MAP algorithms can be compared as before with simulations, see Table 5.10. The field test performance is shown to be quite similar to that of the simulations. However, in this case one should take into consideration that the real position of the CPF was only obtained when it was on the surface, using a GPS. As a consequence, its displacement while it conducted the immersion and before it settled down on the seafloor could not be computed. This means that the RMSE presented in Fig. 5.12b may have an inherent error, although the general performance was demonstrated.

5.7 Conclusion

This work shows the performance of different algorithms under different scenarios with the objective of tracking underwater target by using autonomous vehicles. The main mathematical notation of each algorithm, and their performance under simulations and field tests have been conducted, and the best practice has been derived. From a methodological point of view, this work advances the understanding of accuracy that can be achieved by using ROSB target tracking methods with autonomous vehicles.

The algorithms considered in this study are LS, EKF, UKF, MAP, and PF. All these algorithms have been compared with each other. Simulations and experimental results suggest that that an accuracy of a few metres can be achieved using the PF, which we demonstrated to be the fastest and the most accurate algorithm with respect to other studied approaches to estimate an underwater target position especially when this target is moving. For example, in a simulated dynamic scenario with a quasi ideal noise measurement of 1m, the PF achieves a settling time equal to 1.7 min, a recovery time equal to 5.8 min, and a steady state error of 1 m, but it also has more accurate values than the other algorithms in noisier cases.

Chapter 6

A novel Area-Only biologging method

The area-only underwater target localisation and tracking algorithm using acoustic tags will allow the study at the behaviour of small marine species and their movements in a way which has not been possible until the present day.

6.1 Introduction

One of the main challenges in oceanographic research is underwater localisation. It is well known that Global Positioning System (GPS) signals suffer large attenuation underwater. Therefore, different methods have been developed using acoustic signals, which have better underwater performance. Besides the traditional Long Base-Line (LBL) and Ultra-Short BaseLine (USBL), new strategies are being developed (e.g. moving long baseline) which leverage the higher performance of autonomous vehicles and their capabilities to work in increasingly complex scenarios, as it has been explained in the previous Chapters.

6.1.1 Motivation

However, the size and power requirements of current modems that provide range measurement capabilities are not negligible, and therefore, are not viable to track small targets, such as some marine species (e.g. jellyfishes). For example, the standard modem S2C-M-18/34 (Evologics) has a total length of 310 mm and a weight of 1265 g.

In this framework, we present a novel Area-Only Target Tracking (AOTT) method using an autonomous vehicles, such as a Wave Glider from the Liquid Robotics company, which detects and tracks a tagged underwater target while mov-

ing on the surface. Using the detection/no-detection information provided by an acoustic receiver, the algorithm is able to compute the target position and the vehicle follows it. The main algorithm used in this method is based on the Particle Filter (PF), which has been used successfully in the Range-Only Target Tracking (ROTT) method [135].

6.1.2 Related work

In ROTT methods, the information used to track the target is the slant range measured using acoustic modems. However, the size and power requirements of current modems that provide such capability are not negligible, whereas the AOTT method can be implemented to track smaller animals due to the small size of acoustic tags [37]. Nonetheless, the only information available in AOTT is the presence/absence of tag detection, which requires a more complex method.

The AOTT method is a passive, "listen-only" approach where there is no interrogation between the tracker and the target. This distinction contrasts with the ROTT method, which uses two-way communication to compute the slant range between two devices.

Current tracking methods for marine species use acoustic tags, which enable two kind of studies [37]: (a) study their long-range migrations through receivers spread in specific points, which only provides general information about their movements; and (b) study their small movements in a reduced area using different receivers nearby, which has the same limitations of the traditional LBL systems (e.g. deployment cost or synchronisation between devices). In addition, animals that emerge periodically on the surface can send their position by satellite communications [141]. Other studies have focused in the development of new tags to study the animal behaviour [42]. Whereas these tags can be used to measure different behavioural and environmental parameters, they do not transmit any acoustic signal, and therefore, can not be tracked. Finally, the Woods Hole Oceanographic Institution (WHOI) has developed a new method to track tagged animals (e.g. sharks or turtles) using an Autonomous Underwater Vehicle (AUV) and custom build USBL and transponders [142] and [143]. In this case however, whereas the results are impressive, the USBL uses more energy than a simple hydrophone (i.e. the USBL needs to communicate with the transponder to measure the range) and is necessary to tagged the marine animal with a "big" tag with bidirectional communication capabilities, and therefore, could not be optimum in some applications such as the use of glider vehicles, where the power consumption is an important constraint. Others, such as Clark C.M. et al [65] and [133], have used two passive hydrophones (mounted in a ~2 m frame) to find the angle of arrival of a signal transmitted by a tagged leopard

shark.

6.1.3 Contributions

The method presented in this Chapter can be used in a wide range of applications using the long-duration, autonomous navigation and on-board processing characteristics of Wave Glider vehicles, which can geolocate stationary or slowly moving tagged targets on the seabed or in the water column (e.g. benthic vehicles [93] or marine animals [144]). However, the AOTT method is especially an important step forward to track spatiotemporal changes in animal behaviour, which is not feasible using the current state-of-the-art.

6.2 Area-only target tracking method

In the following, the main idea behind the AOTT method and its mathematical formulation are presented.

6.2.1 AOTT idea

Given the acoustic receiver and tag used for this effort, the only information that can be determined is presence or absence of tag transmissions in the area of the receiver. In other words, the receiver only "knows" whether the tag is inside the area of reception, but has no-information about the tag's direction or range. The AOTT method infers the target position by taking the area determined by the maximum reception range as the only filter input (illustrated in Fig. 6.1).

Two types of areas can be observed: one where the tag is detected (blue circles), and one where the tag is not detected (white circles). The estimation of the target's localisation can then be computed by overlapping all of these areas, where the zone with a main coincidence is where the target should be, thereby representing its probability distribution.

The AOTT is implemented using a PF algorithm, where initially all the particles are placed in a specific area. Then, each particle is moved accordingly to a motion model, and each particle's weight is updated for each new detection (or no-detection) until all of them converge into the target position estimation.

6.2.2 Mathematical formulation

The AOTT target tracking method can also be seen as a Hidden Markov Model (HMM) problem. Generally, the HMM is defined as a sequence of states, known as

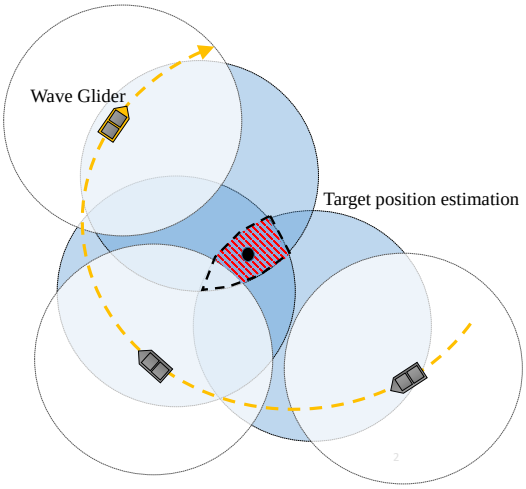

Figure 6.1: Area-Only Target Tracking (AOTT) problem representation. Blue circles represent the area around the Wave Glider where a tag transmission was detected. White circles represent the area around the Wave Glider where a tag transmission was missing. The centre point of the overlapping area among all these detection/no-detection is the target estimated position.

a Markov chain, and a set of observations for each state [116]. Using Bayes' rule

$$p(\mathbf{x}_k|\mathbf{z}) = \frac{p(\mathbf{z}|\mathbf{x}_k)p(\mathbf{x}_{k-1})}{p(\mathbf{z})}, \tag{6.1}$$

the probability distribution function of the HMM states can be derived given a set of observations $\mathbf{z} \in \mathbb{R}^m$, and therefore, the current state $\mathbf{x} \in \mathbb{R}^{2n}$ can be estimated. Where m indicates the number of observations carried out, and n can be either 2 or 3, which is the space dimension of the problem. And $p(\mathbf{x}_k|\mathbf{z})$ is the posterior probability distribution, expressed also as $p(\mathbf{x}_k|\mathbf{z}_{:k})$; $_{:k}$ subscript denotes all observations up to k. The $p(\mathbf{x}_{k-1})$ is the prior probability distribution expressed also as $p(\mathbf{x}_k|\mathbf{z}_{:k-1})$. And finally, $p(\mathbf{z})$ is the total probability of $\mathbf{z}$ [117], expressed also as $\int_{\mathbf{x}_k} p(\mathbf{z}|\mathbf{x}_k)p(\mathbf{x}_{k-1})d\mathbf{x}_k$, which is used as a normalized factor. However, to compute the predicted state $\mathbf{x}_k$, the total probability $p(\mathbf{z})$ can be ignored, which yields in the optimal solution of the following maximization problem

$$\mathbf{x}_k^{OPT} = \underset{\mathbf{x}_k}{\operatorname{argmax}}\ p(\mathbf{x}_k|\mathbf{z}_{:k}). \tag{6.2}$$

In prediction theory and filtering, the posterior distribution can be computed recursively from the prior distribution using a prediction step $p(\mathbf{x}_k|\mathbf{z}_{:k-1})$ and an update step $p(\mathbf{x}_k|\mathbf{z}_{:k})$.

In general, the existing filtering methodologies compute either the predictions

with reference to the conditional probability distribution $p(\mathbf{x}_k|\mathbf{z}_{:k})$, such as the PF, or with reference to the probability joint distribution $p(\mathbf{x}_k, \mathbf{z}_k|\mathbf{z}_{:k-1})$, such as the Extended Kalman Filter (EKF), see [118] and the references therein.

On the other hand, in order to simplify the notation, a 2D scenario has been used, where the tracker conducts manoeuvres on the sea surface to predict the target's position. This is a common procedure due to the facility of knowing the target's depth with high accuracy using cheap devices (e.g. used in GPS Intelligent Buoys [119, Chapter 3]), and therefore, a 3D scenario can be projected into a 2D plane. Consequently, and hereinafter, the following considerations and parameters will be considered. Firstly, the state vector used for both tracker and target is defined as

$$\mathbf{x} = [x \quad \dot{x} \quad y \quad \dot{y}]^T, \tag{6.3}$$

where x and y are the positions in the 2D plane, and $\dot{x}$ and $\dot{y}$ are their associated velocities. The observation measurement vector is defined as

$$\mathbf{z} = [z_1, \ \ldots, \ z_m]^T, \tag{6.4}$$

where m denotes the number of observations conducted. In the ROTT methods, those are the ranges between the tracker and the target, whereas in the AOTT the measurement will be

$$z_m = \begin{cases} 1 & \text{if tag detection} = True \\ 0 & \text{if tag detection} = False \end{cases}, \tag{6.5}$$

which is used in the filter update step to indicate if a tag's transmission was or was not detected.

Finally, assuming that the target state vector at time-step k is defined by $\mathbf{x}_k$, and a constant target velocity, which is a general consideration, the target motion model is

$$\mathbf{x}_k = \mathbf{F}_{k-1}\mathbf{x}_{k-1} + \mathbf{Q}_{k-1}, \tag{6.6}$$

where $\mathbf{F}$ is the state transition matrix, and $\mathbf{Q}$ is the process noise, which has variance σ_v^2. Both are related to time-step Δt, and are described as

$$\mathbf{F} = \begin{bmatrix} 1 & \Delta t & 0 & 0 \\ 0 & 1 & 0 & 0 \\ 0 & 0 & 1 & \Delta t \\ 0 & 0 & 0 & 1 \end{bmatrix} \tag{6.7}$$

and

$$\mathbf{Q} = \begin{bmatrix} \frac{1}{4}\Delta t^4 & \frac{1}{2}\Delta t^3 & 0 & 0 \\ \frac{1}{2}\Delta t^3 & \Delta t^2 & 0 & 0 \\ 0 & 0 & \frac{1}{4}\Delta t^4 & \frac{1}{2}\Delta t^3 \\ 0 & 0 & \frac{1}{2}\Delta t^3 & \Delta t^2 \end{bmatrix} \sigma_v^2. \tag{6.8}$$

6.2.3 Algorithm designed using PF

Nowadays, the PF is one of the most used method in target tracking [132] [133], especially for its robustness in front of multi-modal probability density functions. The PF solves, in a non-parametric way, the probability distribution problem of the HMM using the Bayes' rule (6.1) with the recursion of

$$p(\mathbf{x}_k|\mathbf{z}_{:k-1}) = \sum_{\mathbf{x}_{k-1}} \underbrace{p(\mathbf{x}_k|\mathbf{x}_{k-1})}_{\substack{\text{Motion} \\ \text{model}}} \underbrace{p(\mathbf{x}_{k-1}|\mathbf{z}_{:k-1})}_{\text{Particles}}, \tag{6.9}$$

and

$$p(\mathbf{x}_k|\mathbf{z}_{:k}) \propto \underbrace{p(\mathbf{z}_k|\mathbf{x}_k)}_{\substack{\text{Importance} \\ \text{weights}}} \underbrace{p(\mathbf{x}_k|\mathbf{z}_{:k-1})}_{\text{Particles}}, \tag{6.10}$$

where a bunch of particles $\mathbf{x} \in \mathbb{R}^{2n}$ are spread on a 2D area, which are used to represent different possible states. Equation (6.10) represents the prediction step, which uses the motion model presented in (6.6) to move each particle with some random noise. In this case, the mean of all these particles represents the prior probability distribution.

Then, using (6.10), each particle is weighted with a likelihood ratio based on a measurement probability function. Here, an important difference with reference to ROTT methods is introduced as follows:

Range-only In the ROTT methods, this function is based on the error between the real range measurement z_k and the range that each particle have between each other and the observer, expressed as

$$W_k^n = \frac{1}{\sqrt{2\pi\sigma_W^2}} \exp\left(- \frac{(h(\mathbf{x}_k^n) - z_k)^2}{2\sigma_W^2} \right), \tag{6.11}$$

which calculates the probability of the state $\mathbf{x}_k^n$ for one dimension Gaussian function with mean equal to the distance between the observer and the particle, and variance equal to σ_W^2. In this case, the index $n \in \{0, \ldots, N\}$ indicates the particle number

up to N. Where the measurement model can be described by

$$\begin{aligned} h(\mathbf{x}_k^n) =& \parallel \mathbf{x}_k^n - \mathbf{p}_k \parallel + w_k \\ =& \sqrt{(x_{xk}^n - x_{pk})^2 + (y_{xk}^n - y_{pk})^2} + w_k, \end{aligned} \tag{6.12}$$

where $\mathbf{p}_k \in \mathbb{R}^2$ is the observer position, and $w_k \sim \mathcal{N}(0, \sigma_{wk}^2)$ is a zero-mean Gaussian noise.

Equation (6.11) is known as Probability Density Function (PDF), and its representation is presented in Fig. 6.2a, where a $\sigma_W^2 = 40$ was used.

Area-only However, in the AOTT method the measurement probability function is based on the distance that each particle has between each other and the observer, where the particles which are inside an area defined by the maximum range that a tag can be detected will be more weighted than the particles which are outside of this area. On the other hand, if a tag detection is missed, the particles inside the area will be less weighted than the particles which are outside. This behaviour can be represented using the Cumulative Distribution Function (CDF) [145] and its complementary Survival Function (SF) (known also as Q-function [146]), which can be expressed as

$$W_k^n = \begin{cases} \frac{1}{\sqrt{2\pi\sigma_W^2}} \int_{-\infty}^{r} \exp\left(-\frac{(\mathrm{x}-\mu)^2}{2\sigma_W^2} \right) \mathrm{dx} & \text{if } z_m = 1 \\ 1 - \frac{1}{\sqrt{2\pi\sigma_W^2}} \int_{-\infty}^{r} \exp\left(-\frac{(\mathrm{x}-\mu)^2}{2\sigma_W^2} \right) \mathrm{dx} & \text{if } z_m = 0 \end{cases}, \tag{6.13}$$

where r is the distance between each particle and the observer, μ is the maximum range that a tag can be detected, and σ_W^2 is the variance, which is used to modify the slope of the function.

The 3D representation of (6.13) is shown in Fig. 6.2b and Fig. 6.2c. Where the weight's distribution used in the area-only method is computed using a $\sigma_W^2 = 20$ for the SF, and a $\sigma_W^2 = 80$ for the CDF functions, which are detection and no-detection scenarios respectively.

Finally, all the particles are resampled accordingly to their weight in order to obtain the posterior probability distribution and to estimate the target's position.

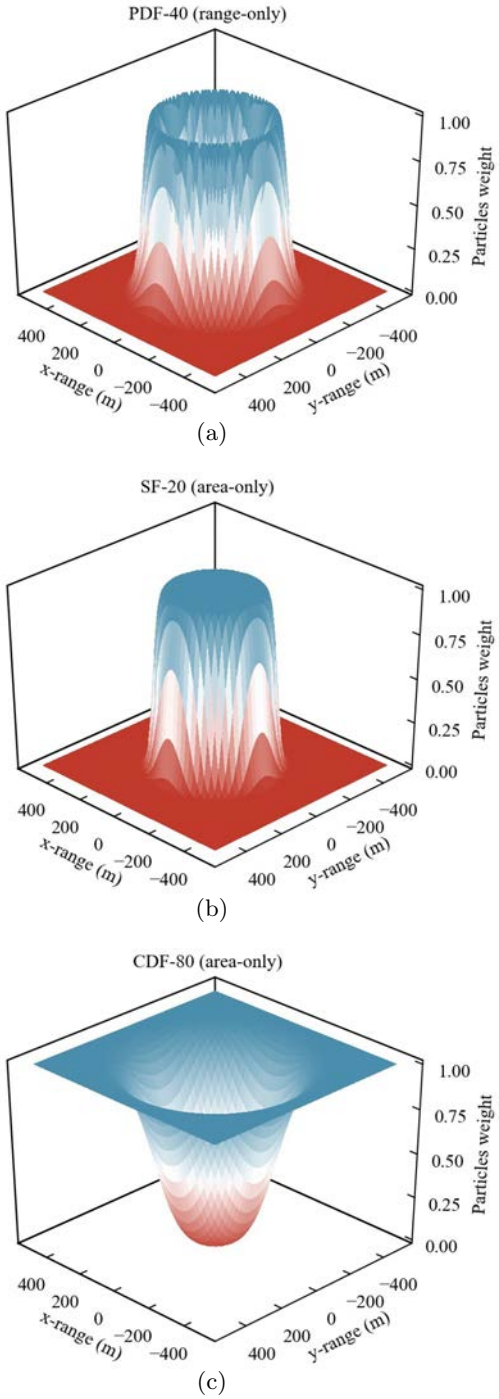

Figure 6.2: (a) weight's distribution used in the range-only method, for a $\sigma_W^2 = 40$. (b) weight's distribution used in the area-only method when a tag is detected (SF), for a $\sigma_W^2 = 20$. And (c) weight's distribution used in the area-only method when a tag transmission is missed CDF, for a $\sigma_W^2 = 80$.

Resampling method Different resampling methods have been developed over the past years [134], where the Systematic method offers a good performance in terms of computational complexity and resampling quality. However, in [135], we demonstrated that other methods, such as the Compound strategy, have a greater performance under fast target manoeuvre circumstances.

The Compound method consists of twofold strategies: a standard Systematic resampling method for $(N - \ell)$ particles; and a Random resampling method for the last (ℓ) particles, which are drooped randomly inside a circular area around the latest Wave Glider position. This strategy is carried out to always maintain some particles nearby the last tag's detection, which improves the PF time response in front of unexpected target position variations. Moreover, it maintains the particles' diversity, which helps to reduce the common degeneracy problem presented in the PF [134].

Using all these considerations, the following algorithm can be used to track underwater targets using autonomous vehicles by the use of PFs, Algorithm 6.

Input: $\Delta t, z_i$, New_range
Output: Next target state estimation $\hat{\mathbf{x}}_k$
if *_Init_* **then** Initialize:
  $\mathbf{F}, \mathbf{Q}, \hat{\mathbf{x}}_0$
  The state vector for each particle and its weight associated are also initialised:
  $\{\mathbf{x}_0^n\}_{n=1}^N \sim p(\mathbf{x}_0)$
  $\{W_0^n\}_{n=1}^N = 1/N_p$
end
Predict step (6.9):
$\{\hat{\mathbf{x}}_k^n\}_{n=1}^N = \mathbf{F}_{k-1}\{\hat{\mathbf{x}}_{k-1}^n\}_{n=1}^N + \mathbf{Q}_{k-1}$
if *Time_has_elapsed* **then** update step (6.10):
  Importance weight update using (6.13)
  $\{W_k^n\}_{n=1}^N$
  Normalize the importance weights
  $\{W_k^n\}_{n=1}^N = \{W_k^n\}_{n=1}^N / \sum_{j=1}^N W_k^j$
  Resampling:
  $c = [W_k^0, W_k^{i-1} + W_k^i, \ldots, W_k^{N-1} + W_k^N]$ for
  $i = \{1, \ldots, N-1\}$
  $u = random()/(N-\ell)$
  $i = 0$
  for j ***in*** *range*$(N-\ell)$ **do**
    while $u > c^i$ **do**
      $i \mathrel{+}= 1$
    end
    $\mathbf{a}^j = \mathbf{x}_k^i$
    $u \mathrel{+}= 1/(N-\ell)$
  end
  for i ***in*** *range*(ℓ) **do**
    $\mathbf{a}^{j+i+1} = random(\mathbf{x})$
  end
  $\{\mathbf{x}_k^n\}_{n=1}^N = \mathbf{a}$
  $\hat{\mathbf{x}}_k = \frac{1}{N}\sum_{n=1}^N \mathbf{x}_k^n W_k^n$
end

Algorithm 6: PF for Area-Only tagged target tracking.

6.3 Optimal parameters

In this section different simulations have been conducted in order to characterize the AOTT algorithm under different parameters and scenarios. These simulations have been carried out using the Monte Carlo Simulation (MCS) method. For all the simulations, the mean and the average result after 30 iterations are presented. The other parameters, which are not involved in the current simulation, have been considered ideal. Two different scenarios have been studied in each case: (a) localising a static target, and (b) tracking a moving target which had a velocity equal to 0.2 m/s.

6.3.1 Optimal path

The optimal path that should be conducted by an observer in order to maximise the accuracy of the estimated target position is a common problem of the target tracking methods, which has been addressed exhaustively over the past years. For example, Moreno-Salinas et al. [98] conducted a study to find the optimal sensor placement in an underwater range-only target localisation scenario. In the previous Chapters, we presented a complete study to derive the optimal path to conduct by a surface vehicle in a range-only and single-beacon static target localisation scenario. Further in [115], Crasta et al. extended the path optimisation problem for underwater target tracking using multiple trackers. Whereas all these works have been conducted for the ROTT methods, some of the results derived can also be applied in the AOTT.

These studies pinpointed two basic rules to follow: (a) all the measurements must be performed uniformly distributed on a circumference centred over the target, and (b) the circumference's radius must be greater than the target depth and in some cases as large as possible:

Measurements' distribution We can derived intuitively that the measurements have to be uniformly distributed to maximise the system observability, and therefore, the target's estimation. The algorithms used in the ROTT methods find the intersection between circumferences to estimate the target position, if the measurements' positions are not well distributed, the possibility of errors due to noisy measurements increase (i.e. measurements too close between each other and obtained in a small region, provide circumferences too difficult to differentiate between them). This idea can also be applied in the AOTT method, if the tag's receptions are uniformly distributed around itself, the area that results by overlapping all those receptions is smaller, and therefore, the tag's uncertainty is reduced.

Circumference's radius The ROTT optimal circumference radius to follow by a tracker can be derived analytically which results in $r_c = \sqrt{2}Z_q$, where z_q is the target's depth. However, this basic rule has the limitation defined by the maximum tracker time required to perform the path. In real scenarios a circumference with $r_c < 800$ m is desired. On the other hand, the only information available in the AOTT method is the tag's detection/no-detection, which is specified by the Maximum Transmission Range (MTR) achievable by an acoustic tag. Therefore, seems logical that the maximum range to conduct by a tracker should be less than the maximum transmission range, but closer to it in order to reduce the area that results by overlapping all the tag receptions circles.

Following these two ideas, a set of simulations has been conducted. Fig. 6.3a shows the relation between the Tracker Circumference Radius (TCR) and the target estimation error, where the ratio expressed as Γ_{range} = TCR/MTR was used. We can see that the best circumference's radius is the closest one to the tag's MTR but lower than that. In contrast, radius too small or larger than the MTR produce a poor target's estimation. Therefore, these values are not recommended, which some times can cause the target's lost. Here, it is also interesting to observe that radius close to zero (TCR $\mapsto$ 0) yielded to an error equal to 50 m (on static target scenario). In this case, the target's prediction was equal to the tracker's position, and the error was equal to the initial separation between them, which was 50 m. In real situations this will not be accurate, and therefore, this value must be discarded to determine the optimal value.

6.3.2 Maximum transmission range

The MTR achievable by an acoustic tag is hard to known a priori, where different in situ field tests are recommended to be conducted to estimate its value. The transmission range performance can be affected by different factors such as the sea state, the acoustic noise, the sea temperature, or the battery charge. All these factors introduce an uncertainty in the MTR which is difficult to known and to study analytically. Here a set of different simulations with different relations between the MTR and the Maximum Particles Range (MPR) have been conducted, where the MPR is a key element used to spread the particles in the zone, expressed as μ in (6.13). These simulations allow to identify the relation between the ratio Γ_{range} = MPR/MTR and the AOTT's performance, and therefore, indicates the best MPR which should be used when the accurate real value of the MTR is unknown.

Fig. 6.3b shows that the optimum Γ_{range} was 1.4 for static targets, and 1.2 for moving targets. When the MPR was too low or high, the observer was not able to localise and track the target. Therefore, the best maximum particles range that

should be used to spread all the particles and compute their weight at each new tag detection is bounded by $0.8\text{MTR} \leqslant \text{MPR} \leqslant 1.4\text{MTR}$.

6.3.3 Reception ratio

The power transmission capability of standard tags is strongly limited by their size, which is restricted by the size of the marine specie under study. Moreover, if the different sources of noise that exist in the environment (e.g. sea waves [147]) are taken into consideration, it is obvious to think that the transmission will not always reach the observer, i.e. some tag's transmission will be missed, even though the tracker stays inside the tag's MTR.

The $Time\_has\_elapsed$ variable in Algorithm 6 is used to update the PF. However, only after four missing tag receptions it starts a no-reception cycle by applying the CDF, which weights all the particles accordingly to (6.13). This procedure is carried out to improve the algorithm performance, and to increase its robustness in front of missing receptions.

Nonetheless, if the number of transmissions carried out by the tag and successfully received by the observer is very low, the algorithm will be unable to localise the target. This behaviour can be observed in Fig. 6.3c, where the Successful Reception (SR) over the Total Transmissions (TT) ratio defined by $\Gamma_{reception} = \text{SR}/\text{TT}$ is presented. Here, a $\Gamma_{reception} \leqslant 0.5$ yielded in a poor AOTT performance, and therefore, the target could not be localised and followed.

6.3.4 Resampling method

As was pinpointed in [135], a Compound resampling method for the PF can increase the target tracking performance. The main idea of the Compound method is to spread a certain number of particles in a zone nearby the target, which helps the algorithm to track sudden changes in the direction of the target.

Here, the particles are deployed around the tracker instead of spreading them around the latest estimated target position. This action helps to increase the particles diversity, and emphasise the latest time that the tag was detected. The results obtained are shown in Fig. 6.3d. Whereas the influence of the resampling method to localise static targets is minimum, the Compound method overperforms the Systematic method in moving target scenarios.

Finally, all the optimum parameters obtained in this section are summarized in Table 6.1.

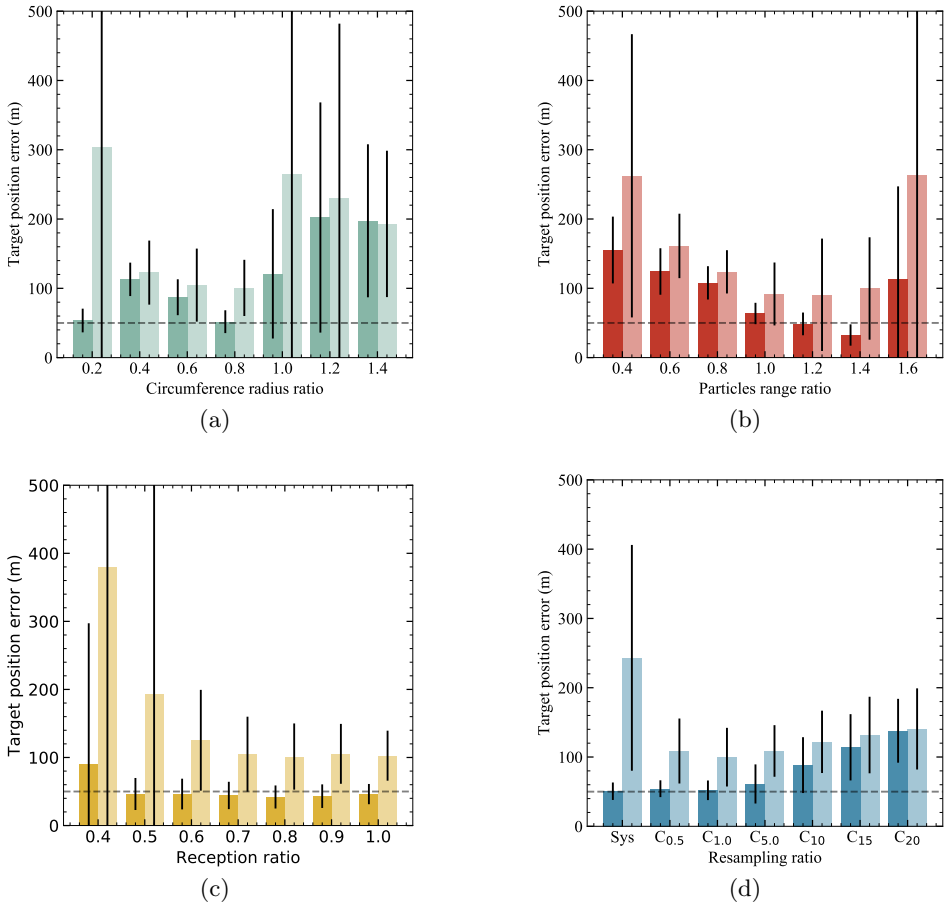

Figure 6.3: Estimated target position error as a function of the tracker circumference ratio (a), the maximum particles range ratio (b), the tag reception ratio (c), and the resampling method (d): Systematic (Sys), and Compound (C_{xx}) with different ratios. The dotted line indicates a 50 m of error. Simulations conducted for static target (dark color) and moving target (light color) cases. The mean and the Standard Deviation (STD) after 50 iterations are represented.

Table 6.1: Optimal parameters for Area-Only Target Tracking (AOTT) method.

	Parameter	Ratio definition	Optimal	Limits
Static and moving targets	Tracker Circumference Radius (TCR)	$\Gamma_{radius} = \text{TCR}/\text{MTR}$	$\Gamma_{radius} \mapsto 1$	$0.4\text{MTR} \leqslant \text{TCR} < \text{MTR}$
	Maximum Particles Range (MPR)	$\Gamma_{range} = \text{MPR}/\text{MTR}$	$\Gamma_{range} = 1.2$	$0.6\text{MTR} < \text{MPR} \leqslant 1.4\text{MTR}$
	Successful Reception (SR)	$\Gamma_{reception} = \text{SR}/\text{TT}$	$\Gamma_{reception} \mapsto 1$	$\text{SR} > 0.5\text{TT}$
	Compound resampling particles (ℓ)	$\Gamma_{resampling} = 100\ell/N$	$\Gamma_{resampling} = 1.5$	$\ell < 2.5N/100$

6.4 Simulated scenario

The next simulation has been conducted to observe the AOTT's performance using all the recommendations derived from the previous section. In this case, the target was moving at 0.2 m/s and performed a 90° right turn after 67 min, the rest of the parameters were:

- Tag transmission delay = 60 s
- Maximum tag transmission range = 250 m
- Tracker radius = 200 m
- Tracker velocity = 1 m/s
- Number of particles = 10000
- Resampling method = Compound with ratio 1.5%
- Maximum particles range = 300 m
- Number of iterations = 50

The result obtained in this simulation is shown in Fig. 6.4a, where the tracker and target trajectories are represented. In addition, at each time that a tag's transmission was received or missed is also visible with a black and a grey start consecutively. The estimated target position is shown in red.

Fig. 6.4b shows the error obtained between the estimated and the real target position, where the dark color represents the average value and the light color represents its STD, both after 50 iterations. Two set of simulations with different $\Gamma_{reception}$ were conducted, using ratios equal to 100% and 60%. Before and after the target right turn (at 67 min), the error was ~50 m using the ideal reception ratio, and ~100 m using the 60% ratio. In this situation, the AOTT had more problems to find and track the real target position, which lose the target position about ~2% of the iterations. Despite that, the tracker in general did not loss the target's position, and therefore, the great capabilities of the AOTT method were demonstrated.

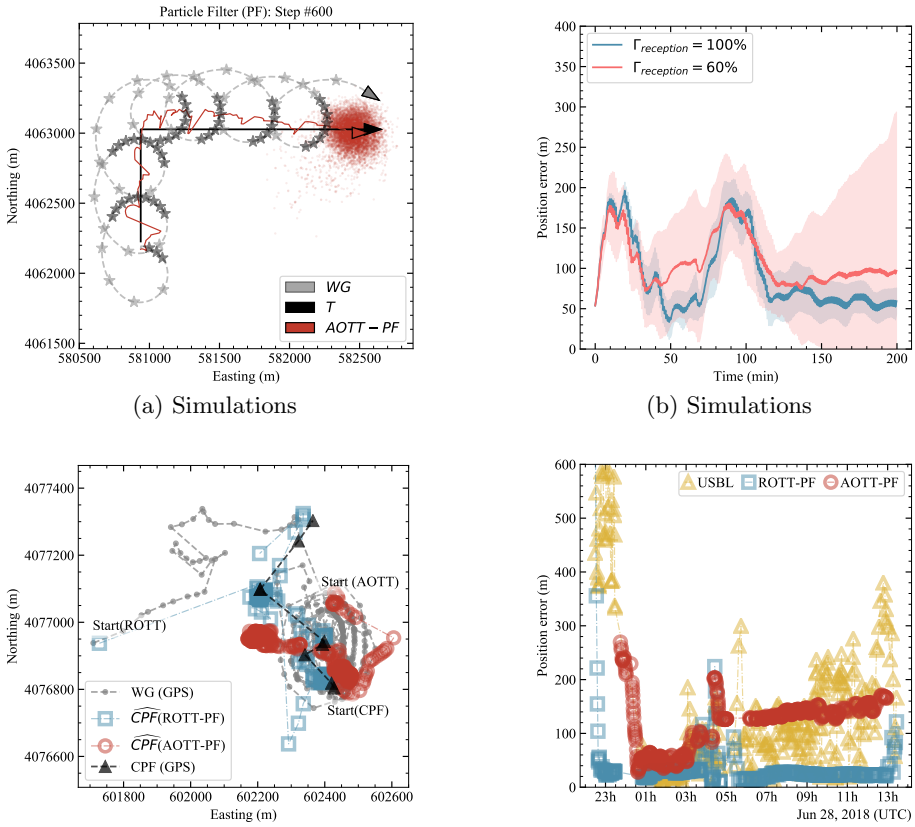

(a) Simulations (b) Simulations

(c) Field test (d) Field test

Figure 6.4: Simulations: (a) x-y map where the tracker (WG), the target (T), and the estimated target position using the PF ($AOTT - PF$) are presented. Black stars represent tag transmission receptions, whereas grey stars represent a missing tag detection; (b) Evolution of the estimated target position error over time. Mean (dark color) and STD (light color) limits after 50 iterations, for a $\Gamma_{reception} = 100\%$ and 60%. Field tests: (c) Wave Glider and Coastal Profiling Float (CPF) positions, and the estimated CPF position using both the ROTT and the AOTT algorithms; (d) Estimated target position error comparison among USBL, ROTT, and AOTT methods.

6.5 Field tests

Different field tests were conducted on June 27-28, 2018 using a Wave Glider as a tracker and the MBARI's CPF [139] as a target. The Wave Glider was equipped with a Vemco receiver (VR2C), and two Vemco tags (V7P-69k) were installed to the CPF. Additionally, the CPF was equipped with a Benthos acoustic modem (ATM-900), and the Wave Glider with a Benthos DAT (Direction Acoustic Transponder) modem, which is a type of USBL, both from the Teledyne company. Fig. 6.5 shows the CPF's deployment moment, and one of the acoustic tags affixed with a 3D

printed housing (inset). This target does not required the use of small tags due to its size. Nonetheless, it was used to compere the performance between different methods.

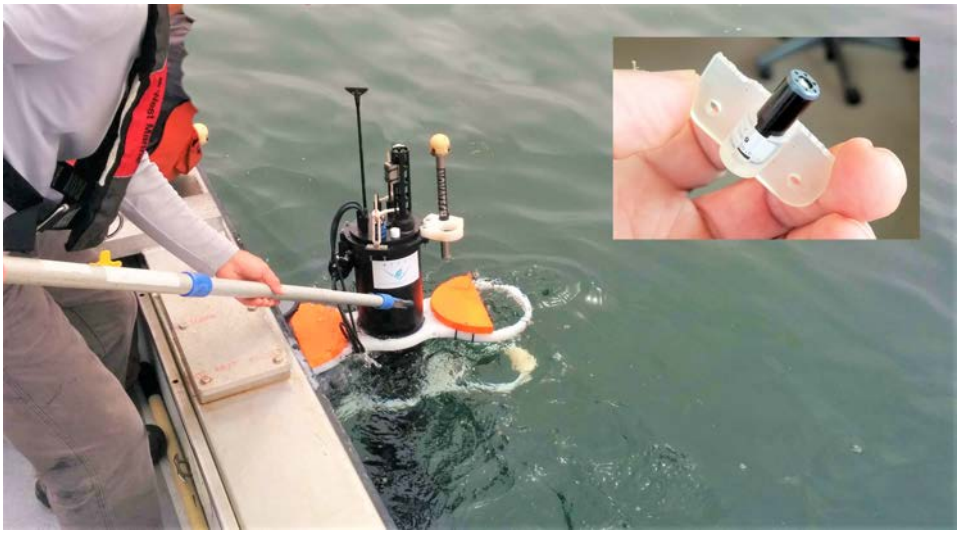

Figure 6.5: The CPF's deployment during the test, with the Vemco tags affixed to the float (inset) via a 3D printed housing.

This test lasted more than 15 h, where the CPF conducted 3 immersions at ~60 m depth. During all the test, the Wave Glider carried out different circumferences around the area which were used in twofold purposes: (a) to perform a tag detection ratio versus range test, finding the maximum range where the tags could be detected; and (b) to compare the accuracy of the USBL, the ROTT, and the AOTT methods.

6.5.1 Reception ratio

As we explained in Section 6.3.3, the maximum range that an acoustic tag can be detected is unknown a priori, and it is strongly dependent on the sea state. Moreover, the $\Gamma_{reception}$ decrease dramatically with the distance between the tag and the receiver due to the attenuation that acoustic waves suffers in water [147]. Therefore, in situ tests before each mission are recommended to know the MTR. Fig. 6.6 shows the results obtained after two days of tests, where a huge variation in $\Gamma_{reception}$ at different days can be observed, probably due to different sea conditions.

Here, the TT value was computed as $\mathrm{TT} = T_{tag}\Delta t$, where T_{tag} is the tag transmission period, and Δt is the elapsed time. And the SR where grouped in ranges of 25 m between the target and the tracker. The result shows that a $\Gamma_{reception}$ close to 80% for distances up to 75 m, and then it lows to ~30% until 400 m range.

Therefore, a tracker trajectory close enough to the target is mandatory in order

to maintain an acceptable reception ratio. Conducting not too large circumferences was also derived in Section 6.3.1 as a good practice.

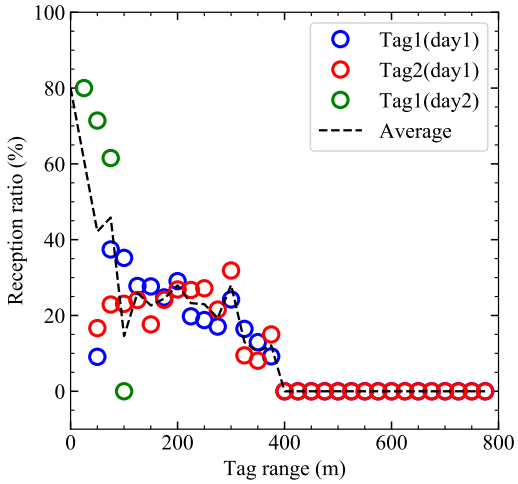

Figure 6.6: Reception ratio versus distance between devices. Results obtained during field trials in Monterey Bay, California.

6.5.2 Area-only vs range-only and traditional tracking methods

The second test was carried out to compare the performance of the AOTT method to others. These methods where the ROTT using the slant range measurements conducted by the acoustic modems, and the estimated target position obtained by the USBL. Both methods are widely used in the target localisation and tracking field.

Fig. 6.4c shows the paths conducted by the Wave Glider and the CPF, and their initial positions. Moreover, the estimated target position using both the ROTT and the AOTT methods are presented. On the other hand, Fig. 6.4d shows the estimated target position error of the AOTT, ROTT, and USBL methods.

From the AOTT's error we can pinpointed three elements: (a) the algorithm was notably stable, where the target was mostly all the time correctly localised; (b) during the first CPF's immersion, the error was lower than 100 m, and then it increased up to ¡200 m. If we compare this performance with the study conducted previously, and if we take into consideration that the Wave Glider's path was not optimal, the error's values were inside the expected boundaries; and (c) when the CPF was in the surface (at 05h) the error obtained was greater, probably due to a poorest tag reception.

On the other hand, we also can see from Fig. 6.4d that the USBL's error was bigger than 200 m, specially at the end of the test. This poor performance can be

produced by threefold causes: (a) due to a poor weather and sea state condition, which could increase the acoustic multi-path behaviour, and could make the vehicle more unstable; (b) due to the presence of some misalignment error in the USBL device (e.g. an offset between the transducer and the Inertial Measurement Unit (IMU)); and (c) the strong multi-path behaviour that existed due to the shallow water area where the test was conducted. The USBL range measurements are typically more robust than the bearing and elevation measurements. Therefore, the use of a filter to increase the system's performance is a good practice, e.g. in [90] the authors used a simple weighted filter to increase the estimated target position accuracy. In addition, the USBL should be calibrated in advance to reduce those possible misalignments. However, here the raw (i.e. without post processing) data is presented, which can explain the poor behaviour presented by the USBL.

Finally, we can see that the ROTT method was the best one to estimate the target position, which had an error lower than 20 m during almost all the test. The range-only methods can be used when two-way communication between the target and the tracker is possible. However, this functionality is not available in current commercial acoustic tags, at least to the best knowledge of the authors and until nowadays.

6.6 Conclusions

This work has described the basis of a novel method for target tracking using marine autonomous vehicles, which has been called AOTT. This technique can be used to track tagged marine species that could not be tracked otherwise due to their size.

Here, an extended study to find the optimal parameters for the AOTT method has been carried out, and its results are presented. With this study, best practices under different scenarios have been derived, which sets the basis of future tests and applications.

Moreover, different field tests have also been performed. For example, a target has been localised and tracked using a Wave Glider. This field test has been used to validate the simulations conducted and the hypothesis derived, and to evaluate its performance in a real scenario. In addition, a comparison between the AOTT's performance among other methods has been conducted. Whereas the error of AOTT is greater than the error of ROTT (as expected), the AOTT method overperforms other localisation techniques due to the use of small tags instead of bigger, more complex, and more expensive acoustic modems.

Chapter 7

Smart tag development

A new smart acoustic tag with bidirectional communications and range capabilities will allow the increase of the estimated target's position accuracy and will allow the transmission of important environmental measures. Both aspects could be used to increase the knowledge of biologging marine animals behaviour.

7.1 Introduction

The Range-Only and Single-Beacon (ROSB) method can be used when the range between the target and the tracker is known, as shown in Chapter 4 and 5. Those range measurements are usually conducted by acoustic modems which have bidirectional communication capabilities, and therefore, the range can be computed through the Time Of Flight (TOF) of exchanged messages. Nonetheless, the commercially available acoustic modems have important dimensions, and cannot be fitted in small objectives (e.g. marine animals such as jellyfish or Norway lobsters). One alternative to track small targets could be the method developed in Chapter 6 which uses small acoustic tags instead of modems. However, these tags do not have bidirectional communication capabilities, and therefore, the range between the target and the tracker cannot be measured.

7.1.1 Motivation

Nowadays, one of the most important tag's manufacturer is Vemco (`www.vemco.com`), which develops different tag's sizes and their correspondent receptors. However, those are only transmitters, and therefore, cannot be used for target tracking using the ROSB methods presented above, which have better performance than the Area-Only Target Tracking (AOTT) method developed in this thesis.

In this framework, the development of a new smart tag will allow the use of better

monitoring techniques for marine animals monitoring by the use of Autonomous Underwater Vehicle (AUV). That could be used for fishery management (i.e. producing ancillary data for fishery management of the relevant commercial items, as *Nephrops*, as well as the Ocean Tracking Network (OTN) tracking of snow crabs [140]), and in scenarios of multiple platforms intercommunicated.

7.1.2 Related work

Different new tags have been developed during the last years with new sensors, and improved capabilities (e.g. in size, power, and communication protocols). Those developments have utilized the expansion of miniature sensors and devices used in the boom which consumer electronics have suffered over last decades, such as smart phones and wearable fitness devices [148]. Nonetheless, in land environments, the animal tracking is relatively easier compared with underwater scenarios, where the Global Positioning System (GPS) and standard satellite communications are not available. Consequently, other tag strategies have been used (e.g. acoustic communication or stand-alone data-loggers), some of them are summarized in Table 7.1.

On the one hand, the size of the marine tags is determined by different factors, such as, the size and power of their batteries, or the number of sensors included. On the other hand, the size of those tags should not exceed the commonly used tag-to-body-mass rule of 2% [29]. This rule is used to not disturb the normal behaviour of the host marine specie. For that reason, the tag performance/size ratio is a key limiting factor which must be taken into consideration for each new development.

The typical available sensors are depth and temperature, where accelerometers or light sensors are also possible (see [37] and references therein). These sensors are used to study the behaviour of the marine specie (e.g. maximum depth or day/night activity). Moreover, these information can also be used to track the animal, where the temperature and depth information are correlated with global maps to estimate the path followed by the tagged animal [149].

Finally, some of these tags have acoustic communication, which can be used to detect their position when they are close to a receiver while underwater. These acoustic receivers are generally spread on specific spots of interest and are used to detect the presence of the tagged animals. Others tags have satellite communication, which is used to send their position and some telemetry. Nevertheless, these can only be used when they are on the sea surface. Also tags which non-communication capabilities can be found, in those cases, the tags must be recovered in order to download all the sensor's information recorded. However, in all these cases, the communication is one-way between the tag and the receiver (i.e. the user cannot send

information or commands to the tag). This is an important constraint, for example two-way communication (i.e. communication from the tag to the receiver, and from the receiver to the tag) will allow the conduction of range measurements between the tag and the receiver, which will be useful to track the tag using the Range-Only Target Tracking (ROTT) methods. In addition, two-way communication will allow the modification of different measurement parameters in-situ, such as the sampling frequency.

7.1.3 Contributions

In this chapter, the basis of a new smart tag is developed. This device will have bidirectional capabilities to communicate to/from a master device. This will enable the measure of the slant range between them, and therefore, the range-only tracking algorithms explained above could be used. Furthermore, this smart tag will also have different sensors to measure important surrounding parameters. As a result, the combination of both communication and measuring capabilities will allow new studies which are not possible nowadays.

Table 7.1: Specifications of some marine animal tags.

Company	Model	Freq. (kHz)	Battery (days)	Depth (m)	Size (mm)	Weight in air (g)	Communication	Depth	Temperature	Light	Magnetic field	Acceleration	Salinity
Vemco	V9AP	69	165	204	9x43	6.6	PPT-acoustic	•	–	–	–	•	–
	V9TP	69	405	290	9x29	4.6	PPT-acoustic	•	•	–	–	–	–
Wildlife computers	MiniPat	n/a	730	1700	38x124	60	Argos	•	•	•	–	–	–
	Daily Diary	n/a						•	•	•	•	•	–
Little Leonardo	Splash10	n/a		2000	105x56x30	217	Argos	•	•	•	–	–	–
	ORI400-D3GT			400	12x45	9		•	•	–	–	•	–
Lotek Wireless	M-48-T	200	161		9x23	2.7	CDMA-acoustic	–	•	–	–	–	–
	MM-XX-M8-SO	76	291		8.5x42	5.5	CDMA-acoustic	○	○	–	–	○	–
	MM-MC-8-SO	79	179		8.5x43	6.5	Acoustic-RF	○	○	–	–	○	–
Sirtrack	K2G173A	n/a	305	500	60x27x17	34	Argos	•	•	–	–	–	–
WHOI[a]	ITAG	n/a		1000	108x64x29	102.5	VHF	•	•	•	•	•	–
KAUST[b]	Marine Skin	n/a	28	2000	20x20x0.3	6	Bluetooth	•	–	–	–	–	•

[a] under development at Woods Hole Oceanographic Institution (WHOI) [42]

[b] under development at King Abdullah University of Science and Technology (KAUST) [150]

Unaddressed cells reflect the information was not found online

•, ○, and – reflect the sensor parameter is available, optional, or not possible consecutively

7.2 Common tags

In this section, the study of a Vemco tag is conducted using a Naxys hydrophone (Bjørge ASA, Norway), model Ethernet 02345. As it has been explained, these are one of the most used tags, and therefore, will be used as a reference.

7.2.1 Modulation

The Vemco's tags utilize a simple pulse position modulation [151], which uses the separation between eight pulses to encode the Identifier (ID) of each tag. These pulses are generated with a 69 kHz sinusoidal signal, each one with 5 ms of duration.

For example, the tag model V16-4x with an ID number equals to A69-1601-2687 has 8 pulses separated 300 ms, 420 ms, 350 ms, 380 ms, 400 ms, and 340 ms respectively.

7.2.2 Field tests

These tags have been tested in the OBSEA underwater observatory, using its hydrophone. Thanks to this instrument, we could observe in a real environment the signal generated by the tag, as well as all the interferences and noise presented in the area. As an example, Fig. 7.1 shows a single tag's transmission received by the hydrophone. The top plots show the raw signal received, whereas the bottom ones show the signal after the application of a 69 kHz Band-Pass Filter (BPF). In addition, the right plots are a zoom of the initial left plots.

In these plots, we can observe the kind of noise that must be faced in a real environment. The noise and interferences can be even worst in more adverse scenarios. For example, near a harbour or with the presence of boats or scuba divers nearby. In such circumstances the signal transmitted by the tag can be intractable, and therefore, the communication lost.

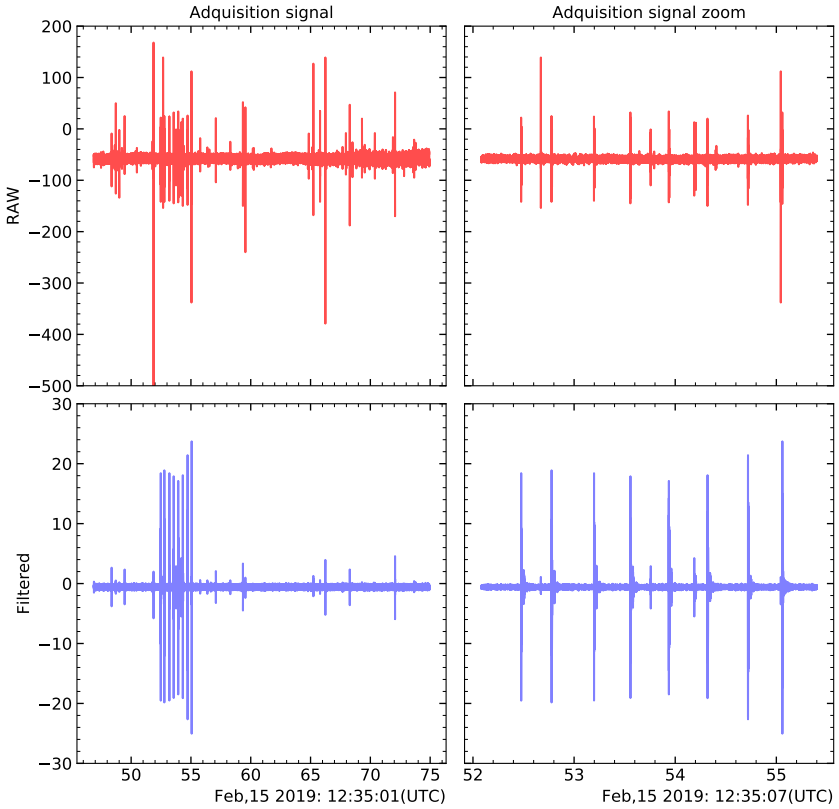

Figure 7.1: Representation of a single tag transmission received by the hydrophone. The top plots show the raw signal received, whereas the bottom ones show the signal after the application of a 69 kHz BPF. Additonally, the right plots are a zoom of the initial left plots.

7.3 Proposed smart tag

Here, we propose the development of a new tag with bidirectional acoustic and measuring capabilities, which is called smart tag. For this purpose, different simulations were conducted using Python, and a first implementation was realized using the CompactRIO (cRIO) platform from the National Instruments company.

7.3.1 Python implementation

The first approach to develop the smart tag was its implementation using the Python software, which allows a rapid implementation and modification scheme. Here, the main idea was to study the behaviour of a simple bidirectional communication in a simulated environment. For this purpose, a signal was generated, then it was transmission through a simulated channel, and finally it was de-codified and its TOF calculated. This was conducted twice, master-to-slave and slave-to-master. The main parts of the developed program are summarized below.

A TX waveform (master)

Firstly, a base band chirp signal is generated as

$$\mathbf{xc} = e^{j2\pi\mathbf{t}(\frac{-B}{2}+\frac{B}{2T}\mathbf{t})}, \tag{7.1}$$

where B is the chirp bandwidth, T is the chirp length, and $\mathbf{t} \in \{0, \ldots, T-1\}$ is the time scale. Then, the pass-band chirp signal is computed as

$$\mathbf{x} = e^{j2\pi F_0 \mathbf{t}}\mathbf{xc}, \tag{7.2}$$

where F_0 is the waveform center frequency.

B Master to slave channel

To simulate the channel, a simple low pass filter response is used. The filter response is also shifted to the right to represent the channel range delay using a zero array defined by $\mathbf{Z}_{delay} = zeros\{0, \ldots, |range/(vF_s)|\}$, where v is the speed of sound in water, and F_s is the sampling frequency. Thus, the channel response can be computed as

$$\mathbf{h}_{M2S} = \mathbf{Z}_{delay} \frown e^{-100\boldsymbol{\tau}}, \tag{7.3}$$

where $\boldsymbol{\tau} \in \{0, \ldots, ds\}$, where ds is the channel delay spread, is the exponential decay values.

C Applying the channel

Then, the channel response is applied to the chirp signal using a Finite Impulse Response (FIR) filter. Moreover, the response is normalized by

$$h_{norm} = \frac{1}{\sqrt{\sum |\mathbf{h}_{M2S}|^2}}, \tag{7.4}$$

and some random noise is added using

$$Aw = \frac{1}{2} 10^{\frac{-\text{SNR}}{10}}, \tag{7.5}$$

where the SNR is the signal to noise ratio. The final signal after applying the channel response is

$$\mathbf{y}_S = h_{norm}\text{FIR}(\mathbf{h}_{M2S}, \mathbf{x}) + Aw, \tag{7.6}$$

D RX decoding (slave)

The first step to decoding the signal is to convert the $\mathbf{y}_S$ into a base band by

$$\mathbf{y}_{Sdown} = \mathbf{y}_S e^{-j2\pi F_0 \mathbf{t}}, \tag{7.7}$$

and then it is filtered with a low pass filter. Finally, a correlation between the received $\mathbf{y}_{Sdown}$ signal with the generated **xc** signal is conducted to find the exact time of arrival.

E Slave to Master

A similar procedure is conducted to send a chirp signal from the slave modem to the master. This is conducted each time that a "good" correlation is observed, where a simple threshold is used.

F Range computation

Finally, the range between both modems is computed using the TOF of the exchanged messages, which is the sound velocity in water multiplied by the TOF.

7.3.2 Simulations

With the model of the modem explained above, a set of simulations was conducted. These simulations were used to know the behaviour of the proposed modem under a quasi-ideal scenario. For example, we could test two kind of signals: a simple sinusoidal tone of 5 ms, such as the one used by Vemco, and a chirp pulse of 5 ms.

The chirp signal had better detection accuracy than the simple tone, as it can be observed in Fig. 7.2. Therefore, if the TOF is wanted to be accurately detected, which then will be used to measure the slant range between two devices, the chirp signal should be used.

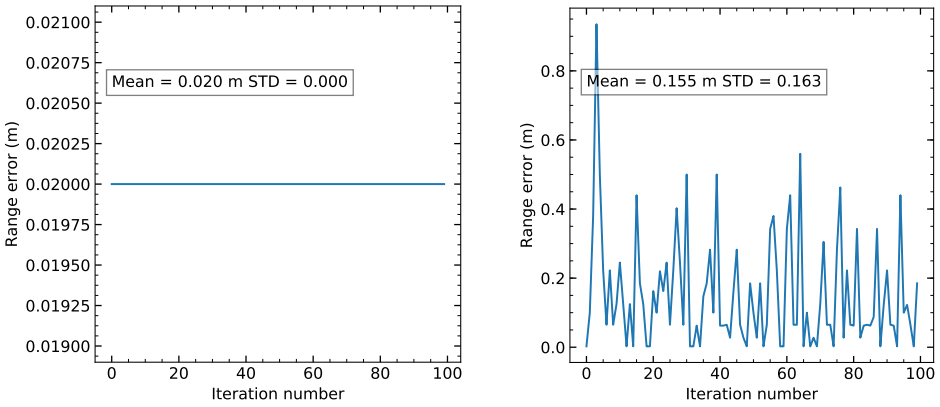

(a) Chirp signal (b) Sinusoidal signal

Figure 7.2: (a) range error computed using a chirp signal. And (b) the range error computed using a simple tone. In both cases 100 iterations have been conducted.

7.3.3 cRIO design

The platform used to design and test the acoustic modem was the CompactRIO (cRIO) (National Instruments, USA), which is programmed through the LabView language, also from the National Instruments company. The main parts of the cRIO system are: a real-time computer, a Field-Programmable Gate Array (FPGA) module, and a slots' bus to connect either analog or digital modules. Consequently, this versatile platform is useful to implement and test different parts of the designed acoustic modem. The system implemented is shown in Fig. 7.3. In this case, two cRIO model NI cRIO-9024 were used. Both equipped with a Digital-to-Analog Converter (DAC) and Analog-to-Digital Converter (ADC) modules, the NI-9263 and the NI-9215 respectively. These cRIO were controlled with a Personal Computer (PC) and the corresponding LabView software. The signals generated were amplified with a power amplifier and then transmitted using an acoustic transducer into a test tank. Then, the signal received with another transducer was conditioned and processed with a second cRIO.

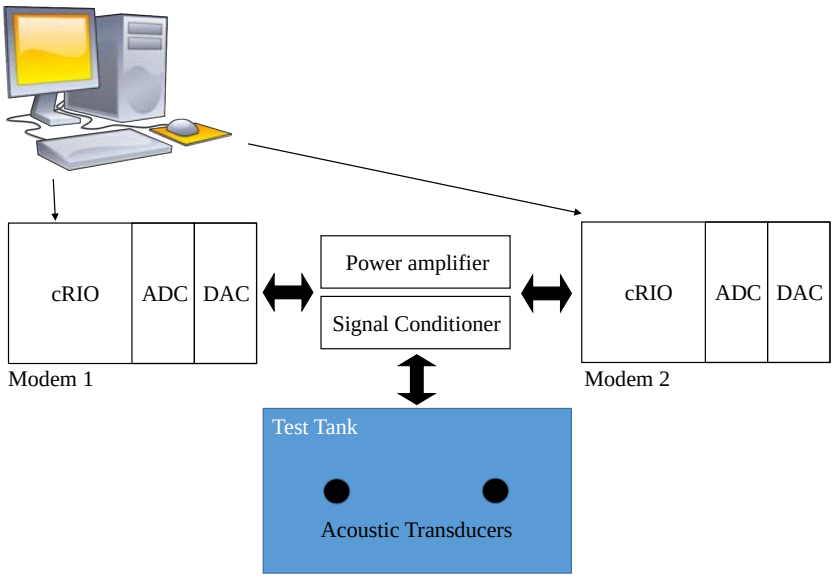

Figure 7.3: Bloc diagram of the two cRIO used to test the algorithms designed for slant range measurements in the laboratory. Each cRIO represents one acoustic modem/smart-tag

A Block diagram

The main parts of the software developed, which has been used to implement all the aspects of an acoustic communication between two devices, are represented in Fig. 7.4. In this case, one modem was used as a master and a second modem was used as a slave. The master started the communication sending a waveform signal through the channel (in this case, the channel could be real or simulated). Then, the signal was received by the slave modem.

The signal generated had two main parts: a wake up tone and a chirp signal. The slave modem was waiting for a wake up tone. When this was detected, it started the decoding and correlation procedure. Each time a correlated signal was detected, the slave computed the time between the start acquisition time and the correlated signal detection. Then this time was used to compute a constant time between the slave signal detection and the acknowledgement signal transmitted by the slave. This is an important step, because the master cannot know a priory the time required by the slave to process the signal, and therefore, this time must always be the same.

Finally, the master computed the range between both modems using the TOF elapsed.

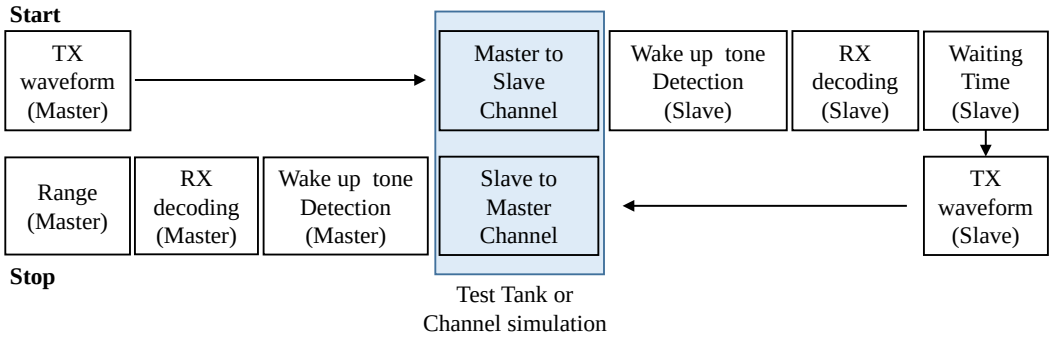

Figure 7.4: Bloc diagram of the communication scheme used to measure the slant range between two acoustic devices.

TX waveform The signal transmitted by both the master and the slave modems were composed by a wake up tone of 30 kHz and 5 ms of duration, and a chirp signal of 20 ms of duration. These had 100 ms of separation.

Wake-up tone In this case, a simple threshold method was used to set if the wake-up tone was detected or not.

RX decoding The decoding method used had two steps. Firstly, the received signal was converted into base band, multiplying it by the waveform centre frequency and then applying a low pass filter. Then, a correlation and a peak detection method were used to find the exact detection time.

Waiting time Using the cRIO's FPGA, the acquisition start time can be known. In addition, the chirp time detection can be known with the RX Decoding. Consequently, with both times, we could set a constant time between the chirp detection and the acknowledgement transmission. This constant time was indispensable to accurately compute the range between both modems.

Range Then the TOF was used to compute the range. The cRIO's FPGA module was also used to obtain a hardware time-stamp, which was used to known with precision both the transmission and the reception time. This time-stamp is needed to compute the TOF with high accuracy. Finally, knowing the TOF and the sound speed in water, the range between both modems can be computed.

B Software implementation

Each cRIO was programmed using its real-time processor and its FPGA module. The FPGA was used to obtain a high accuracy hardware time-stamp of both transmission and reception times. Additionally, the FPGA was also used to control the DAC and the ADC modules. On the other hand, the real-time processor was used to implement the rest of the code, which was in charge to conduct the wake up detection, the signal's decoding, and measure the slant range.

Real-time unit Fig. 7.5 shows the code implemented in LabView which runs inside of each cRIO. On the left, the project directory with all subVI developed is presented, an the two right images show the front panels of the acoustic modems of both slave and master units.

On the other hand, Fig. 7.6 shows the block diagram of the main software developed for the master and the slave units. In this picture, the different modules explained above are represented (e.g. wake up system, decoding, and ranging).

FPGA unit Fig. 7.7 shows the code implemented in LabView which was compiled for the FPGA module. The main purpose of this code was to have an accurate and reliable time of when a signal was either transmitted or received, which was crucial to measure the TOF, and therefore, to compute the range between the two acoustic modems.

7.3.4 Accurately computing the timestamp

To obtain an accurate and precise signal reception time, two methods have been used: (a) an exact and reliable hardware control, and (b) a robust signal detection procedure. Both strategies are explained below.

A Timestamp by hardware

A fundamental condition to obtain an accurate and reliable timestamp, either when the signal is transmitted or received, is be able control precisely the execution time of each instruction. Nonetheless, in some processors or microcontrollers this is not possible due to the Operating System (OS), which introduce some uncertainty. In general, the user does not have the control of the execution process of an OS, which can stop some current execution to attend to external interruptions. For this reason, is essential to have physical timers and direct access to them, which have to control the transmission and reception times.

The physic timers required to have a good timestamp have been implemented directly in the FPGA, which give to the upper software layers the requested time of when a signal has been received or when a signal has been transmitted. These timers are very reliable and does not have any kind of maladjustment produced by the OS.

B Signal detection algorithm

The second important aspect which must be addressed to obtain a good signal reception timestamp is the signal detection algorithm. The most used method is a simple correlation between the received signal with the known *ideal* one. This technique gives a maximum peak when both signals are equal, and therefore, the exact time when the signal was received. However, if the received signal is very noisy, or the reception is conducted in an important multipath scenario, the correlation might ends into false detections or inaccuracies.

To design a more robust detection algorithm, the correlation signal is computed using the following steps:

- Peak-scale related to noise
- Normalisation
- Envelope detection
- Center of gravity detection

Peak-scale related to noise The first step conducted when a correlation is performed is adjust the resultant correlated signal **C** with the noise level, using a predefined windows size L, where each correlation value is divided by the average values inside the windows as follows

$$\mathbf{CP} = \frac{|C_k|^2}{\sum_{n=0}^{2L-1} |C_{k+(n-L)}|^2}. \tag{7.8}$$

Normalisation After the peak-scale related to noise (7.8) adjustment, a normalisation step is conducted which adjust the values between 0 and 1.

$$\mathbf{CN} = \frac{CP_k}{\max(\mathbf{CP})}. \tag{7.9}$$

Envelope detection Then, an envelope detection algorithm is applied using a Butterworth low pass filter of order 5 and low cutoff frequency equal to 800 Hz, which yields in a normalized impulse response $h(k)$. As a consequence, the envelope of the correlation **CP** can be written as

$$\mathbf{CE} = CN(k) * h(k), \tag{7.10}$$

where $*$ is the convolution product.

Center of gravity detection Finally, the center of gravity around the first peak greater than a prefixed threshold is computed using a windows size L as

$$CG = \frac{\sum_{n=0}^{2L-1} [k + (n-L)] CE_{k+(n-L)}}{\sum_{n=0}^{2L-1} CE_{k+(n-L)}}. \tag{7.11}$$

As a result, after each correlation, the final timestamp obtained indicating when a signal has been received is $timestamp = CG/f_s$, where f_s is the sampling frequency used.

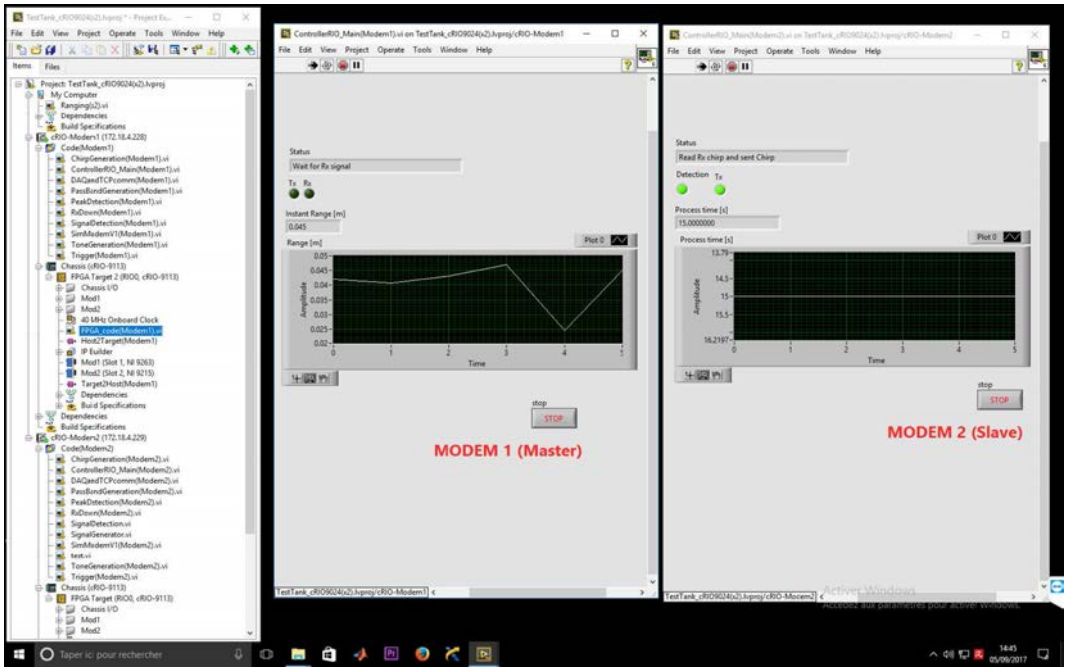

Figure 7.5: Project directory and front panel of the main program designed to acoustically communicate two cRIO and measure the range between them using the TOF. Real-time unit.

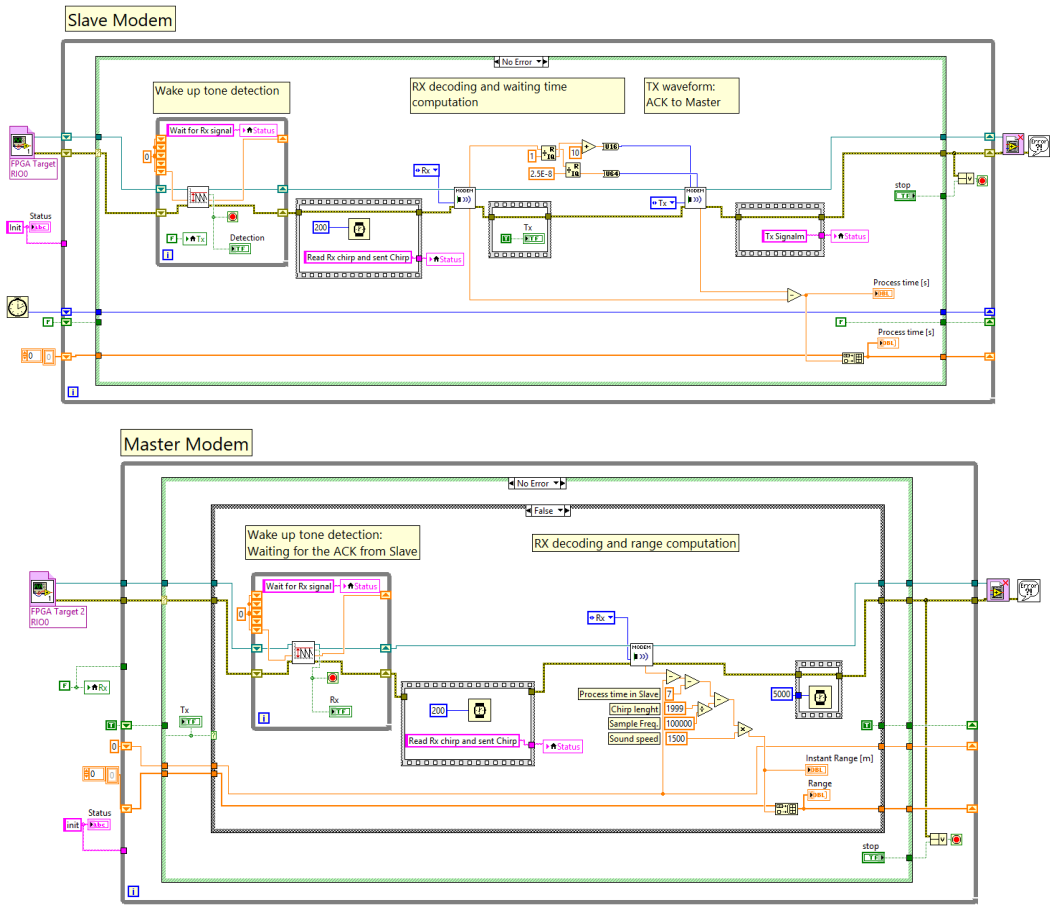

Figure 7.6: Bloc diagram of the main program designed to acoustically communicate two cRIO and measure the range between them using the TOF. Real-time unit.

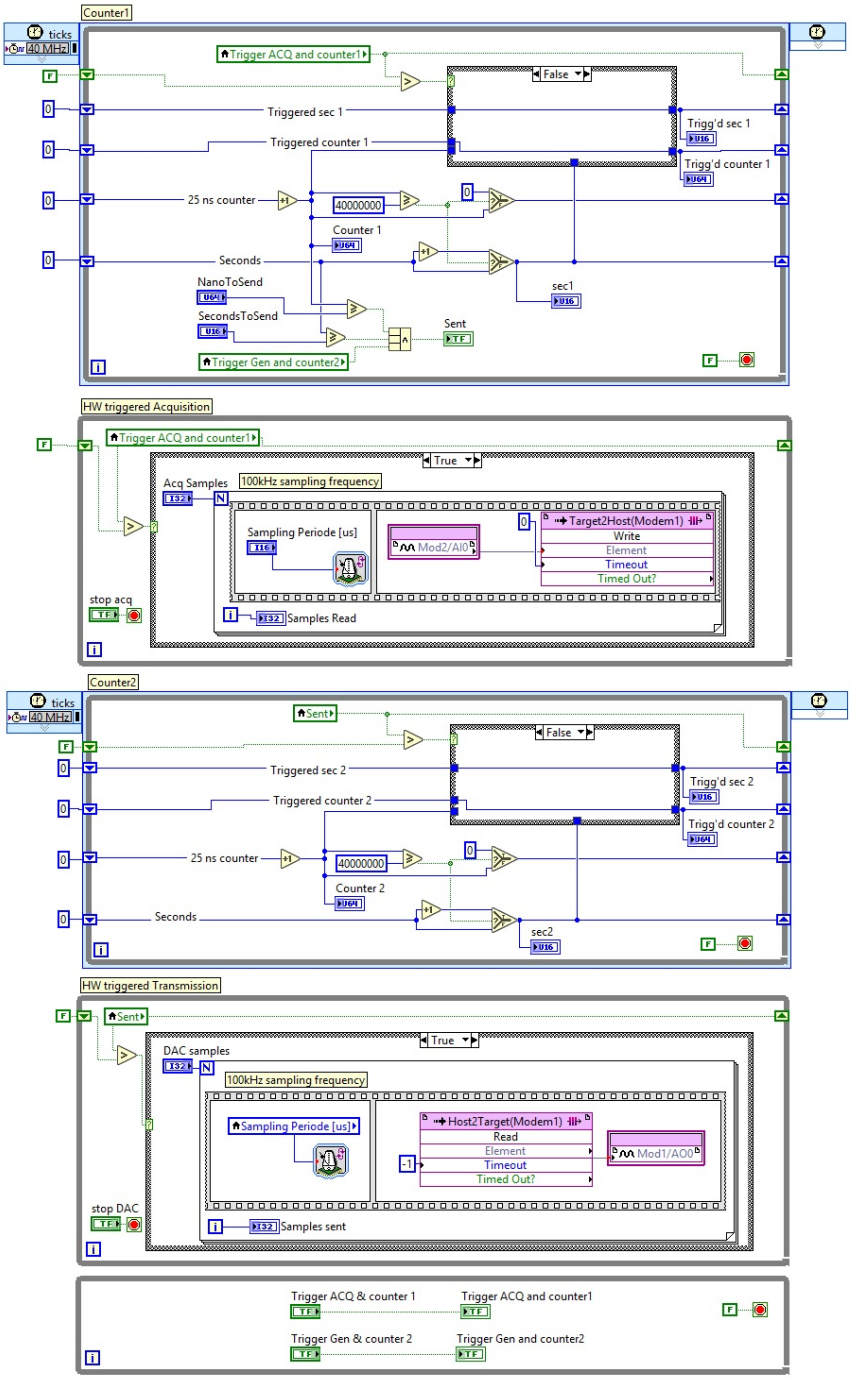

Figure 7.7: Bloc diagram of the main program designed to have a hardware timestamp of both reception signal and transmitted signal. FPGA unit.

7.3.5 Experimental results

The experimental results were conducted at *Institut Supérieur De L'electronique Et Du Numérique* (ISEN) - Brest (France) (`isen-brest.fr`), using the Seacom research group testing facilities. There, they have a water tank for underwater acoustics with all the required acoustic instrumentation. The photographs presented in Fig. 7.8 show the water tank used as a test-tank, the cRIO modules, and all the set used.

Figure 7.8: Images taken during a laboratory experiment, where the test-tank used and the cRIO modules can be observed.

Some of the results obtained are shown in Fig. 7.9. On the top left side the correlation signal between the received and the transmitted signal obtained after its normalisation is presented. This figure shows a non-clear peak. This behaviour is due to the test conditions. This test was conducted inside a water tank, and whereas it is prepared for acoustic tests, the acoustic waves still have rebounds and multi-path effects. Therefore, a simple peak-detection algorithm have occasionally difficulties to compute the correct time-stamp. This behaviour can be observed in the range measured using this technique (Fig. 7.9c), where the range measured between two acoustic modems had a large variation, sometimes the ranges measured

were ~2 m whereas others were ~5 m.

On the other hand, the right plots presented in Fig. 7.9 show the correlation and the range measurement results applying a more robust method (explained in Section B), which was used to avoid the poor performance experimented above. With this method, the range measured was ~2 m with a Standard Deviation (STD) of 0.068 m, which is a variability less than 7 cm. If we take into account the challenging environment (i.e. strong multipath effects), the result obtained validates the methodology proposed.

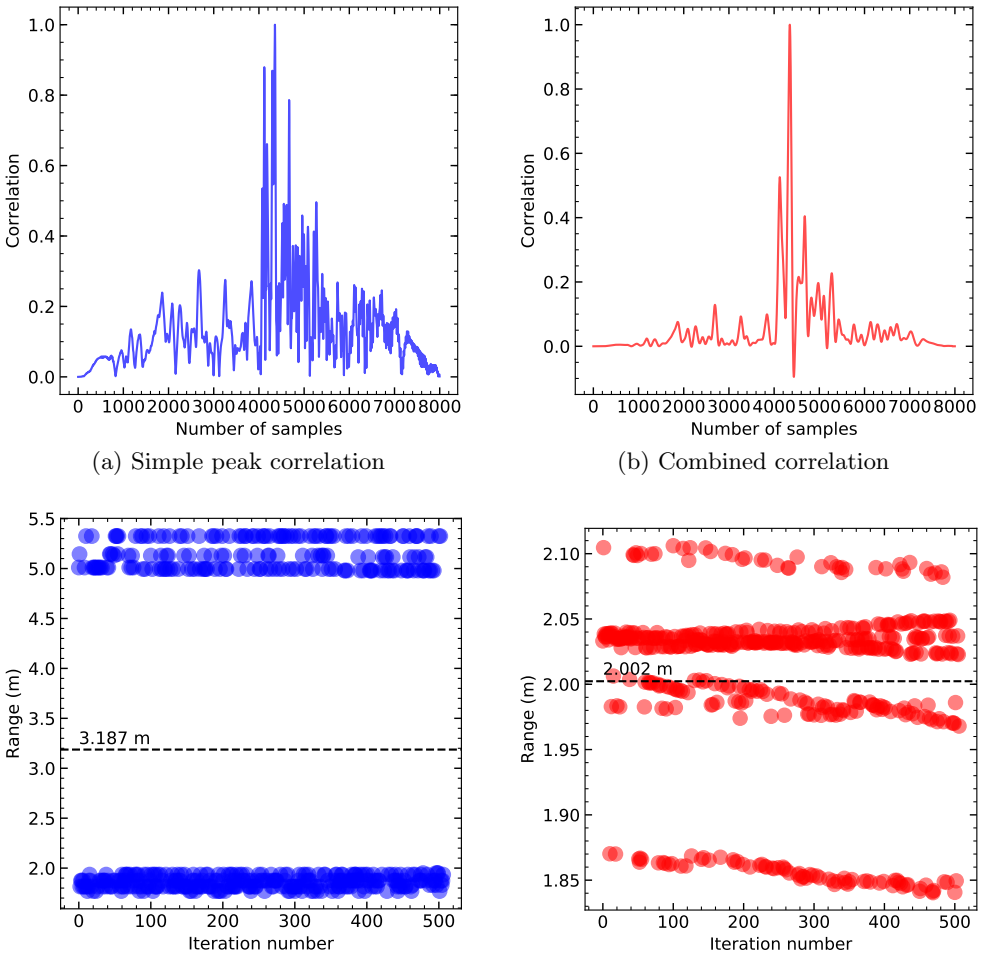

(a) Simple peak correlation

(b) Combined correlation

(c) Simple peak detection algorithm

(d) Combined detection algorithm

Figure 7.9: (a) result obtained after the received signal was correlated with the transmitted signal, and normalized. (b) correlation obtained after the the peak-scale related to noise plus the envelope detection was applied. (c) 500 distances measured between the two modems using a simple peak detection algorithm from the normalized correlation. (d) 500 distances measured between the two modems using a combined detection algorithm, where the peak-scale related to noise plus envelope detection correlation was used and the center of gravity was measured.

7.4 Conclusions

The current commercial tags are not suitable for range-only tracking purposes. As a result, here the basis of a new smart tag is proposed, which is designed with the goal to be able to track small marine animals using range-only methods by the use of autonomous underwater vehicles.

A set of simulations and an implementation using the cRIO architecture have been presented. Furthermore, initial laboratory experiments have been conducted to demonstrate the great capabilities of the methodology proposed and the algorithms designed. In these laboratory tests, different range measurements between two transponders with an error less than 10 cm were obtained.

Chapter 8

Conclusions and future work

This chapter contains the conclusions of the work presented throughout this thesis, which has been focused on the study and development of new acoustic target tracking methods.

Firstly, the study of classic acoustic tracking methods (e.g. Short BaseLine (SBL) and Ultra-Short BaseLine (USBL)) has been conducted, where the main constrains and problems have been observed. For example, the SBL deployment complexity, or the errors presented in the USBL due to the multipath or the sea state.

Then, a complete study about the best practices (e.g. optimal path or best tracker radius) for underwater target localisation and tracking using the Range-Only and Single-Beacon (ROSB) techniques has been carried out, which has included different areas such as analytical studies, simulations, and field tests. At the same time, real missions have been presented (e.g. finding a benthic Rover using a Wave Glider, situated at 220 km west of central California coast and 4000 m depth), where the successful collaboration between autonomous vehicles was conducted. From a methodology point of view, this work advanced the understanding of accuracy that can be achievable by using both range-only and single-beacon localisation and tracking methods by an autonomous vehicles, which has been demonstrated not only numerically but also in real tests. In this context, those advancements would contribute to expand the use of such autonomous vehicles as a multi-purpose platforms, which have been used widely around the world. From this study we could conclude that the ROSB methods is an interesting option, which can offer target position estimations with an accuracy lower than 5 m in many scenarios.

On the other hand, a novel method to track commercially available acoustic tags has been presented, which has been called Area-Only Target Tracking (AOTT). This technique can be used to track tagged marine species that could not be tracked otherwise due to their size. These acoustic tags do not have bidirectional commu-

nication capabilities, and therefore, the ROSB techniques are not applicable. Here, an extended study to find the optimal parameters as well as the results obtained through simulations are presented. With this study, best practices under different scenarios have been derived, which sets the basis of future tests and applications. Additionally, not only analytical studies and simulations have been conducted, but also many field tests. For example, tracking a Coastal Profiling Float (CPF) with a Wave Glider, where a comparison among the AOTT, the ROSB, and the USBL was carried out. In this study, we could observe that whereas the AOTT error (~100) is greater than the other methods (as expected), the AOTT method overperforms other localisation and tracking techniques due to the use of small tags instead of bigger, more complex, and more expensive acoustic modems. Consequently, this method is optimum to track tagged marine animals.

Finally, the basis of a new acoustic tag with bidirectional communications capabilities have been presented. This tag aims to improve the current standard tags, which can only be detected in a passive "listen-only" approach where there is no interrogation between the tracker an the target. Here, its implementation using the CompactRIO (cRIO) architecture form National Instruments, and different laboratory tests are presented, which sets the main ideas to consider in further developments.

8.1 Future work

The development of a research project always brings about the discovery of new problems, as well as new interesting research projects. As future work, here we can pinpoint four areas of interest. The first, and more obvious one, could be the development of an acoustic tag with bidirectional communication capabilities and small size; a second area of research could be the development of new strategies to obtain the optimal path which should be conducted by a tracker in order to optimize and increase the accuracy of the estimation of the target's position; moreover, the target tracking algorithms could be used in collaboration with other methods such as visual tracking; finally, the last area of interest as a future research could be the use of the tracking methods studied in this thesis in a multi-vehicle collaboration environment.

A Acoustic tag

In this thesis the basis of an acoustic tag with bidirectional communications capabilities have been presented. This device will allow new methods to study the behaviour of the marine species and their habitats. For this purpose, the *Sistemas*

Acusticos Submarinos para la monitorizacion del comportamiento especial de ESpecies (SASES) project has been financed this year (*Proyectos I+D+i "Retos Investigación" del Ministerio de Ciencia, Innovacón y universidades* ref. RTI2018-095112-B-I00), which will conclude with the development of a prototype. Therefore, the SASES project can be seen as a natural continuation of this thesis, which will finish the development of the acoustic tag using the study conducted here.

B Path optimization

In this thesis the optimization of the tracker's path has been conducted using the Fisher Information Matrix (FIM) method. However, other methods could be developed in the future where aspects such as the velocity of the target and the tracker, the presence of sea currents, or the power consumption could be taken into consideration. For example, the advances conducted in Artificial Intelligence (AI) in areas such as the Deep Reinforcement Learning (DRL) could bring new strategies to find the optimal path. The DRL refers to a goal-oriented algorithms, which learns how to attain a complex objective or maximize along a particular function. In this case, the key factor is to chose the correct rewarding function, which is not a priori obvious.

C Merge tracking methods

One of the main goal of this thesis has been the study and development of acoustic tracking methods to study the behaviour of marine species. This topic is very important for many scientists, who study not only the species, but also the impact that these have in the ecosystem and in our society. For example, a recent project has been announced which uses a new Autonomous Underwater Vehicle (AUV) called *Mesobot* to autonomously track marine animals using a stereo cameras. This vehicle has been developed in collaboration by the Woods Hole Oceanographic Institution (WHOI) and the Monterey Bay Aquarium Research Institute (MBARI), among others. In the future, will be interesting to merge the acoustic tracking methods with visual methods, where the best aspects of both worlds could be combined. For example, the acoustic methods can be used on longer distances between the tracker and the target. And the visual methods can offer more information about the animal's movements.

D Multi-vehicle scenario

Finally, all the tracking algorithms studied and developed in this thesis have focused in the use of a single tracker vehicle. However, as a future work, these methods

can be modified to be used in a multi-vehicle scenario, where multiple vehicles in collaboration could be used to track a target.

8.2 Publications associated to the thesis

8.2.1 Journals

(ACCESS'19) I. Masmitja, S. Gomáriz, J. Del Rio, B. Kieft, T. O'Reilly, P. J. Bouvet, J. Aguzzi. "Range-only single-beacon tracking of underwater targets from an autonomous vehicle: from theory to practice". IEEE Access, pp.1 - 18. ISSN 2169-3536. 2019. IF 4.098.

(IJRR'18) I. Masmitja, S. Gomáriz, J. Del Rio, B. Kieft, T. O'Reilly, P. J. Bouvet, J. Aguzzi. "Optimal path shape for range-only underwater target localization using a Wave Glider". International journal of robotics research (IJRR), pp. 1 16. ISSN 0278-3649. 2018. IF 6.134.

(MEASUREMENT'18) D. M. Toma, **I. Masmitja**, J. Del Rio, E. Martinez, C. Artero, A. Casale, A. Figoli, D. Pinzani, P. Cervantes, P. Ruiz, S. Memè, E. Delory. "Smart embedded passive acoustic devices for real-time hydroacoustic surveys". Measurement. 125, pp. 592 605. ISSN 0263-2241. 2018. IF 2.791.

8.2.2 Conferences

(OCEANS'19) I. Masmitja, S. Gomáriz, J. Del Rio, J. Aguzzi, P. J. Bouvet, C. Fannjiang, K. Katija. "Area-only method for underwater object tracking using autonomous vehicles". OCEANS - MTS / IEEE. Marseille, France. June 2019.

(OCEANS'18) I. Masmitja, S. Gomáriz, J. Del Rio, P. J. Bouvet, J. Aguzzi. "Underwater multi-target tracking with particle filters". OCEANS - MTS / IEEE Kobe Techno-Oceans (OTO). Kobe, Japan. May 2018.

(IMEKO'18) I. Masmitja, M. Carandell, P. J. Bouvet, J. Aguzzi, S. Gomáriz, J. Del Rio. "Underwater acoustic slant range measurements related to weather and sea state". XXII World Congress of the International Measurement Confederation. Belfast, United Kingdom. 2018.

(MARTECH'18) I. Masmitja, S. Gomáriz, J. Del Rio, B. Kieft, T. O'Reilly, J. Aguzzi, P. J. Bouvet. "Acoustic TAG tracking: First experiments". 8th International Workshop on Marine Technology - MARTECH. Porto, Portugal. 2018.

(SEATECKWEEK'18) J. Del Rio, J. Aguzzi, S. Gomariz, L. Thomsen, J. B. Company, **I. Masmitja**, S. Marini, E. Fanelli, C. Costa, J. Olive, S. Floeghel, T. Torkelsen, J. Schwendner, O. Pfannkuche, G. Rune. "Underwater sensor

networks applied to remote monitoring of biological indicators". 2018 International marine science and technology week - Sea Teck Week. Brest, France. 2018.

(ECCWO'18) J. Aguzzi, L. Thomsen, J. Del Rio, S. Gomariz, J. B. Company, **I. Masmitja**, S. Marini, E. Fanelli, C. Costa, J. Olive, S. Floeghel, T. Torkelsen, J. Schwendner, O. Pfannkuche, G. Rune, N. Lebris. "Fluid and adaptive networks of fixed and mobile robotic platforms for the monitoring of deep-sea ecosystems".4th International symposium on the effects of climate change on the worlds oceans. Washington DC, United States of America. 2018.

(OCEANS'17) I. Masmitja, P. J. Bouvet, S. Gomáriz, J. Aguzzi, J. Del Rio. "Underwater mobile target tracking with particle filter using an autonomous vehicle". OCEANS - MTS / IEEE. Aberdeen, United Kingdom. June 2017.

(IMEKO'17) I. Masmitja, P. J. Bouvet, S. Gomáriz, J. Aguzzi, J. Del Rio, D. M. Toma. "Accuracy and precision studies for range-only underwater target tracking in shallow waters". 22nd IMEKO TC4 International Symposium and 20th International Workshop on ADC Modelling and Testing. Iasi, Romania. September 2017.

(METROLOGIA'17) I. Masmitja, A. Garcia-Benadí, S. Gomariz, J. Del Rio. "Caracterización de posicionamiento en el medio marino mediante métodos acústicos". 6th Congreso Español de Metrologia. Cádiz, Spain. 2017.

(OCEANS'16) I. Masmitja, S. Gomáriz, J. Del Rio, B. Kieft, T. O'Reilly. "Range-only underwater target localization: path characterization". OCEANS - MTS / IEEE. Monterey, United States of America. September 2016.

(IMEKO'16) I. Masmitja, O. Pallares, S. Gomáriz, J. Del Rio, T. O'Reilly, B. Kieft. "Accuracy and precision studies for range-only underwater target tracking in shallow waters". 21st IMEKO TC4 International Symposium and 19th International Workshop on ADC Modelling and Testing Understanding the World through Electrical and Electronic Measurement. Budapest, Hungary. 2016.

(MARTECH'16) I. Masmitja, S. Gomáriz, J. Del Rio, B. Kieft, T. O'Reilly. "Range-only benthic rover localization off the central California coast". 7th International Workshop on Marine Technology - MARTECH. Barcelona, Spain. 2016.

8.3 Publications indirectly associated to the thesis

8.3.1 Journals

(ASTROBIOLOGY'19) J. Aguzzi, M.M. Flexas, S. Flgel, C. Lo Iacono, M. Tangherlini, C. Costa, S. Marini, N. Bahamon, S. Martini, E. Fanelli, R. Danovaro, S. Stefanni, L. Thomsen, G. Riccobene, M. Hildebrandt, **I. Masmitja**, J. Del Rio, E.B. Clark, P. Weiss, A.T. Klesh, M.P. Schodlok, "Exo-oceans exploration with deep-sea sensor- and platform technologies". Astrobiology, Submitted 2019. IF 3.768.

(SENSORS'18) **I. Masmitja**, J. Gonzalez , C. Galarza, S. Gomariz , J. Aguzzi , J. del-Rio, "New vectorial propulsion system and trajectory control designs for improved AUV mission autonomy". SENSORS, 18(4), 1241. 2018. IF 3.031.

8.3.2 Conferences

(EGU'18) J. Del Rio, J. Aguzzi, S. Gomariz, L. Thomsen, J.B. Company Claret, **I. Masmitja**, S. Marini, E. Fanelli, C. Costa, J. Olive, S. Floeghel, T. Torkeldsen, O. Pfannkuche, G.O. Rune, "Autonomous and cabled underwater sensor networks applied to remote monitoring of biological indicators". European Geosciences Union General Assembly (EGU). Vienna, Austria. April 2018.

(ECCWO'18) J. Aguzzi, L. Thomsen, J. Del Rio, S. Gomariz, J.B. Company, **I. Masmitja**, S. Marini, E. Fanelli, C. Costa, J. Olive, S. Floeghel, T. Torkelsen, J. Schwendner, O. Pfannkuche, G.O. Rune, N. Lebris, "Fluid and adaptive networks of fixed and mobile robotic platforms for the monitoring of deep-sea ecosystems". ECCWO-2018 - 4th International symposium on the effects of climate change on the worlds oceans. Washington D.C., USA. 2018.

(OCEANS'17) M. Nogueras, J. Antonijuan, **I. Masmitja**, J. Del Rio, "Evaluation of AUV-borne ADCP measurements in different navigation modes". IEEE/MTS OCEANS. Aberdeen, United Kingdom. 2017.

(OCEANS'17b) C.M. Galarza, **I. Masmitja**, J. Prat, S. Gomariz, "Design a vectorial propulsion system for Guanay II AUV". IEEE/MTS OCEANS. Aberdeen, United Kingdom. 2017.

(IMEKO'16) C.M. Galarza, X. Grimau, **I. Masmitja**, J. Prat, J. Del Rio, S. Gomariz, "Design of the obstacle detection system with the SONAR MK3 on Guanay II AUV". 21st IMEKO TC-4. Budapest, Hongria. 2016.

Bibliography

[1] E. K. Pikitch, K. J. Rountos, T. E. Essington, C. Santora, D. Pauly, R. Watson, U. R. Sumaila, P. D. Boersma, I. L. Boyd, D. O. Conover, P. Cury, S. S. Heppell, E. D. Houde, M. Mangel, . Plagnyi, K. Sainsbury, R. S. Steneck, T. M. Geers, N. Gownaris, and S. B. Munch, "The global contribution of forage fish to marine fisheries and ecosystems," *Fish and Fisheries*, vol. 15, no. 1, pp. 43–64, 2014.

[2] A. Lillebø, C. Pita, J. G. Rodrigues, S. Ramos, and S. Villasante, "How can marine ecosystem services support the blue growth agenda?," *Marine Policy*, vol. 81, pp. 132 – 142, 2017.

[3] G. Wst, "The major deep-sea expeditions and research vessels 18731960: A contribution to the history of oceanography," *Progress in Oceanography*, vol. 2, pp. 1 – 52, 1964.

[4] G. E. R. Deacon, "Progress in oceanographic research and technology," *Proceedings of the Institution of Mechanical Engineers*, vol. 182, no. 1, pp. 846–856, 1967.

[5] M. A. Danchenkov, V. B. Lobanov, S. C. Riser, K. Kim, M. Takematsu, and J.-H. Yoon, "A history of physical oceanographic research in the japan/east sea," *Oceanography*, vol. 19, March 2006.

[6] N. N. Soreide, C. E. Woody, and S. M. Holt, "Overview of ocean based buoys and drifters: present applications and future needs," in *MTS/IEEE Oceans 2001. An Ocean Odyssey. Conference Proceedings (IEEE Cat. No.01CH37295)*, vol. 4, pp. 2470–2472 vol.4, Nov 2001.

[7] S. Turchetti, "Sword, shield and buoys: A history of the nato sub-committee on oceanographic research, 195919731," *Centaurus*, vol. 54, no. 3, pp. 205–231, 2012.

[8] A. P. Santos, "Fisheries oceanography using satellite and airborne remote sensing methods: a review," *Fisheries Research*, vol. 49, no. 1, pp. 1 – 20, 2000.

[9] L.-L. Fu and E. Rodriguez, *High-Resolution Measurement of Ocean Surface Topography by Radar Interferometry for Oceanographic and Geophysical Applications*, pp. 209–224. American Geophysical Union (AGU), 2013.

[10] A. Chatterjee, M. M. Gierach, A. J. Sutton, R. A. Feely, D. Crisp, A. Eldering, M. R. Gunson, C. W. O'Dell, B. B. Stephens, and D. S. Schimel, "Influence of el niño on atmospheric co2 over the tropical pacific ocean: Findings from nasa's oco-2 mission," *Science*, vol. 358, no. 6360, 2017.

[11] B. Griffiths, *Technology and Applications of Autonomous Underwater Vehicles*. Taylor and Francis Group, London and New York, 2002.

[12] K. Fulton-Bennett, "Testing an undersea robot that can detect and map oil spills," 2019.

[13] L. Whitcomb, D. R. Yoerger, H. Singh, and J. Howland, "Advances in underwater robot vehicles for deep ocean exploration: Navigation, control, and survey operations," in *Robotics Research* (J. M. Hollerbach and D. E. Koditschek, eds.), (London), pp. 439–448, Springer London, 2000.

[14] R. L. Wernli, "Auvs-a technology whose time has come," in *Proceedings of the 2002 Interntional Symposium on Underwater Technology (Cat. No.02EX556)*, pp. 309–314, April 2002.

[15] L. L. Whitcomb, "Underwater robotics: out of the research laboratory and into the field," in *Proceedings 2000 ICRA. Millennium Conference. IEEE International Conference on Robotics and Automation. Symposia Proceedings (Cat. No.00CH37065)*, vol. 1, pp. 709–716 vol.1, April 2000.

[16] X. Xiang, B. Jouvencel, and O. Parodi, "Coordinated formation control of multiple autonomous underwater vehicles for pipeline inspection," *International Journal of Advanced Robotic Systems*, vol. 7, no. 1, p. 3, 2010.

[17] J. González, I. Masmitja, S. Gomáriza, E. Molino, J. del Río, A. Mànuel, J. Busquets, A. Guerrero, F. López, M. Carreras, D. Ribas, A. Carrera, C. Candela, P. Ridao, J. Sousa, P. Calado, J. Pinto, A. Sousa, R. Martins, D. Borrajo, A. Olaya, B. Garau, I. González, S. Torres, K. Rajan, M. McCann, and J. Gilabert, "Auv based multi-vehicle collaboration: Salinity studies in mar menor coastal lagoon," *IFAC Proceedings Volumes*, vol. 45, no. 5, pp. 287

– 292, 2012. 3rd IFAC Workshop on Navigation, Guidance and Control of Underwater Vehicles.

[18] H. Matsumoto, T. Hyakudome, Y. Nakano, Y. Watanabe, T. Fukuda, R. Suga, K. Meguro, and H. Yoshida, "Operational test of multiple auvs with an asv," in *2018 OCEANS - MTS/IEEE Kobe Techno-Oceans (OTO)*, pp. 1–4, May 2018.

[19] J. Melo and A. C. Matos, "Tracking multiple autonomous underwater vehicles," *Autonomous Robots*, vol. 43, pp. 1–20, Jan 2019.

[20] J. Kalwa, D. Tietjen, M. Carreiro-Silva, J. Fontes, L. Brignone, N. Gracias, P. Ridao, M. Pfingsthorn, A. Birk, T. Glotzbach, S. Eckstein, M. Caccia, J. Alves, T. Furfaro, J. Ribeiro, and A. Pascoal, "The european project morph: Distributed uuv systems for multimodal, 3d underwater surveys," *Marine Technology Society Journal*, vol. 50, no. 4, pp. 26–41, 2016.

[21] F. Sardà, "Symptoms of overexploitation in the stock of the norway lobster (nephrops norvegicus) on the 'serola bank' (western mediterranean sea off barcelona)," *Scientia Marina*, vol. 62, pp. 295–299, 1998.

[22] S. Lester, B. Halpern, K. Grorud-Colvert, J. Lubchenco, B. Ruttenberg, S. Gaines, S. Airamé, and R. Warner, "Biological effects within no-take marine reserves: a global synthesis," *Marine Ecology Progress Series*, vol. 384, pp. 33–46, 2009.

[23] M. D. Lorenzo, J. Claudet, and P. Guidetti, "Spillover from marine protected areas to adjacent fisheries has an ecological and a fishery component," *Journal for Nature Conservation*, vol. 32, pp. 62 – 66, 2016.

[24] F. Maynou and F. Sard, "Nephrops norvegicus population and morphometrical characteristics in relation to substrate heterogeneity," *Fisheries Research*, vol. 30, no. 1, pp. 139 – 149, 1997.

[25] M. P. Johnson, C. Lordan, and A. M. Power, "Chapter two - habitat and ecology of nephrops norvegicus," in *The Ecology and Biology of Nephrops norvegicus* (M. L. Johnson and M. P. Johnson, eds.), vol. 64 of *Advances in Marine Biology*, pp. 27 – 63, Academic Press, 2013.

[26] B. A. Block, I. D. Jonsen, S. J. Jorgensen, A. J. Winship, S. A. Shaffer, S. J. Bograd, E. L. Hazen, D. G. Foley, G. A. Breed, A.-L. Harrison, J. E. Ganong, A. Swithenbank, M. Castleton, H. Dewar, B. R. Mate, G. L. Shillinger, K. M.

Schaefer, S. R. Benson, M. J. Weise, R. W. Henry, and D. P. Costa, "Tracking apex marine predator movements in a dynamic ocean," *Nature*, vol. 475, 2011.

[27] R. Kays, M. C. Crofoot, W. Jetz, and M. Wikelski, "Terrestrial animal tracking as an eye on life and planet," *Science*, vol. 348, no. 6240, 2015.

[28] R. Harcourt, A. M. M. Sequeira, X. Zhang, F. Roquet, K. Komatsu, M. Heupel, C. McMahon, F. Whoriskey, M. Meekan, G. Carroll, S. Brodie, C. Simpfendorfer, M. Hindell, I. Jonsen, D. P. Costa, B. Block, M. Muelbert, B. Woodward, M. Weise, K. Aarestrup, M. Biuw, L. Boehme, S. J. Bograd, D. Cazau, J.-B. Charrassin, S. J. Cooke, P. Cowley, P. J. N. de Bruyn, T. Jeanniard du Dot, C. Duarte, V. M. Eguluz, L. C. Ferreira, J. Fernndez-Gracia, K. Goetz, Y. Goto, C. Guinet, M. Hammill, G. C. Hays, E. L. Hazen, L. A. Hckstdt, C. Huveneers, S. Iverson, S. A. Jaaman, K. Kittiwattanawong, K. M. Kovacs, C. Lydersen, T. Moltmann, M. Naruoka, L. Phillips, B. Picard, N. Queiroz, G. Reverdin, K. Sato, D. W. Sims, E. B. Thorstad, M. Thums, A. M. Treasure, A. W. Trites, G. D. Williams, Y. Yonehara, and M. A. Fedak, "Animal-borne telemetry: An integral component of the ocean observing toolkit," *Frontiers in Marine Science*, vol. 6, p. 326, 2019.

[29] N. Jepsen, C. Schreck, S. Clements, and E. Thorstad, "A brief discussion on the 2% tag/bodymass rule of thumb," in *Aquatic telemetry: advances and applications* (M. Spedicato, G. Lembo, and G. Marmulla, eds.), pp. 255–259, Food and Agriculture Organization of the United Nations, 2005.

[30] W. S. Burdic, *Underwater Acoustic System Analysis*. US: Peninsula Publishing, 2003.

[31] P. Milne, "Underwater acoustic positioning systems," 1 1983.

[32] K. Vickery, "Acoustic positioning systems. a practical overview of current systems," in *Proceedings of the 1998 Workshop on Autonomous Underwater Vehicles (Cat. No.98CH36290)*, pp. 5–17, Aug 1998.

[33] M. Erol-Kantarci, H. T. Mouftah, and S. Oktug, "Localization techniques for underwater acoustic sensor networks," *IEEE Communications Magazine*, vol. 48, pp. 152–158, December 2010.

[34] I. F. Akyildiz, D. Pompili, and T. Melodia, "Underwater acoustic sensor networks: research challenges," *Ad Hoc Networks*, vol. 3, no. 3, pp. 257 – 279, 2005.

[35] Bridger, Booth, McKinley, Scruton, and Lindstrom, "Monitoring fish behaviour with a remote, combined acoustic/radio biotelemetry system," *Journal of Applied Ichthyology*, vol. 17, no. 3, pp. 126–129, 2001.

[36] G. Rotllant, J. Aguzzi, D. Sarria, E. Gisbert, V. Sbragaglia, J. D. Río, C. G. Simeó, A. Mànuel, E. Molino, C. Costa, and F. Sardà, "Pilot acoustic tracking study on adult spiny lobsters (palinurus mauritanicus) and spider crabs (maja squinado) within an artificial reef," *Hydrobiologia*, vol. 742, pp. 27–38, Jan 2015.

[37] D. J. Skerritt, C. Fitzsimmons, and N. Polunin, "Fine scale acoustic telemetry as an offshore monitoring and research tool recommended practice," *Marine Biology, Ecosystems and Governance Research Group, NERC*, 2015.

[38] H.-P. Tan, R. Diamant, W. K. Seah, and M. Waldmeyer, "A survey of techniques and challenges in underwater localization," *Ocean Engineering*, vol. 38, no. 14, pp. 1663 – 1676, 2011.

[39] Y. T. Chan and K. C. Ho, "A simple and efficient estimator for hyperbolic location," *IEEE Transactions on Signal Processing*, vol. 42, pp. 1905–1915, Aug 1994.

[40] K. S. Andrews, N. Tolimieri, G. D. Williams, J. F. Samhouri, C. J. Harvey, and P. S. Levin, "Comparison of fine-scale acoustic monitoring systems using home range size of a demersal fish," *Marine Biology*, vol. 158, pp. 2377–2387, Oct 2011.

[41] V. Lauria, A. Power, C. Lordan, A. Weetman, and M. Johnson, "Spatial transferability of habitat suitability models of nephrops norvegicus among fished areas in the northeast atlantic: sufficiently stable for marine resource conservation?," *PLoS One*, 2015.

[42] T. A. Mooney, K. Katija, K. A. Shorter, T. Hurst, J. Fontes, and P. Afonso, "Itag: an eco-sensor for fine-scale behavioral measurements of soft-bodied marine invertebrates," *Animal Biotelemetry*, vol. 3, p. 31, Sep 2015.

[43] O. Pallarés Valls, *Time synchronization in underwater acoustic sensor networks.* PhD thesis, Universitat Politècnica de Catalunya. Departament d'Enginyeria Electrònica, 2016.

[44] D. Sarriá Gandul, *Sistemas inalámbricos para la monitorización continua del comportamiento de especies marinas.* PhD thesis, Universitat Politècnica de Catalunya. Departament d'Enginyeria Electrònica, 2014.

[45] J. González Agudelo, *Contribution to the model and navigation control of an autonomous underwater vehicle*. PhD thesis, Universitat Politècnica de Catalunya. Departament d'Enginyeria Electrònica, 2015.

[46] C. M. Galarza Bogotá, *Diseño del sistema de navegación en inmersión del vehículo Guanay II para aplicaciones de detección y seguimiento de vertidos de hidrocarburos en zonas costeras*. PhD thesis, Universitat Politècnica de Catalunya. Departament d'Enginyeria Electrònica, 2018.

[47] M. M. Hunt, W. M. Marquet, D. A. Moller, K. R. Peal, W. K. Smith, and R. C. Spindel, "An acoustic navigation system," *Technical Report WHOI-74-6*, vol. 74, no. 6, pp. 1–65, 1974.

[48] J. C. Kinsey, R. M. Eustice, and L. L. Whitcomb, "A survey of underwater vehicle navigation: recent advances and new challenges," vol. 88, 2006.

[49] L. Paull, S. Saeedi, M. Seto, and H. Li, "Auv navigation and localization: A review," *IEEE Journal of Oceanic Engineering*, vol. 39, pp. 131–149, Jan 2014.

[50] N. H. Kussat, C. D. Chadwell, and R. Zimmerman, "Absolute positioning of an autonomous underwater vehicle using gps and acoustic measurements," *IEEE Journal of Oceanic Engineering*, vol. 30, pp. 153–164, Jan 2005.

[51] M. V. Jakuba, C. N. Roman, H. Singh, C. Murphy, C. Kunz, C. Willis, T. Sato, and R. A. Sohn, "Long-baseline acoustic navigation for under-ice autonomous underwater vehicle operations," *Journal of Field Robotics*, vol. 25, no. 1112, pp. 861–879, 2008.

[52] D. Carta, "Optimal estimation of undersea acoustic transponder locations," in *OCEANS '78*, pp. 466–471, Sep. 1978.

[53] M. Morgado, P. Oliveira, and C. Silvestre, "Tightly coupled ultrashort baseline and inertial navigation system for underwater vehicles: An experimental validation," *Journal of Field Robotics*, vol. 30, no. 1, pp. 142–170, 2013.

[54] J. C. Kinsey, D. A. Smallwood, and L. L. Whitcomb, "A new hydrodynamics test facility for uuv dynamics and control research," in *Oceans 2003. Celebrating the Past ... Teaming Toward the Future (IEEE Cat. No.03CH37492)*, vol. 1, pp. 356–361 Vol.1, Sep. 2003.

[55] M. Audric, "Gaps, a new concept for usbl [global acoustic positioning system for ultra short base line positioning]," in *Oceans '04 MTS/IEEE Techno-Ocean '04 (IEEE Cat. No.04CH37600)*, vol. 2, pp. 786–788 Vol.2, Nov 2004.

[56] J. Opderbecke, "At-sea calibration of a usbl underwater vehicle positioning system," in *Oceans '97. MTS/IEEE Conference Proceedings*, vol. 1, pp. 721–726 vol.1, Oct 1997.

[57] H. G. Thomas, "Gib buoys: an interface between space and depths of the oceans," in *Proceedings of the 1998 Workshop on Autonomous Underwater Vehicles (Cat. No.98CH36290)*, pp. 181–184, Aug 1998.

[58] G. Han, H. Xu, T. Q. Duong, J. Jiang, and T. Hara, "Localization algorithms of wireless sensor networks: a survey," *Telecommunication Systems*, vol. 52, pp. 2419–2436, Apr 2013.

[59] T. C. Furfaro and J. Alves, "An application of distributed long baseline - node ranging in an underwater network," in *2014 Underwater Communications and Networking (UComms)*, pp. 1–5, Sept 2014.

[60] P. Newman and J. J. Leonard, "Pure range-only sub-sea SLAM," in *icra*, vol. 2, pp. 1921–1926, 2003.

[61] M. Bayat and A. P. Aguiar, "Auv range-only localization and mapping: Observer design and experimental results," in *2013 European Control Conference (ECC)*, pp. 4394–4399, July 2013.

[62] Y. T. Tan, R. Gao, and M. Chitre, "Cooperative path planning for range-only localization using a single moving beacon," *IEEE Journal of Oceanic Engineering*, vol. 39, pp. 371–385, April 2014.

[63] G. Vallicrosa, P. Ridao, D. Ribas, and A. Palomer, "Active range-only beacon localization for auv homing," in *2014 IEEE/RSJ International Conference on Intelligent Robots and Systems*, pp. 2286–2291, Sept 2014.

[64] J. Vaganay, P. Baccou, and B. Jouvencel, "Homing by acoustic ranging to a single beacon," in *OCEANS 2000 MTS/IEEE Conference and Exhibition. Conference Proceedings (Cat. No.00CH37158)*, vol. 2, pp. 1457–1462 vol.2, 2000.

[65] C. M. Clark, C. Forney, E. Manii, D. Shinzaki, C. Gage, M. Farris, C. G. Lowe, and M. Moline, "Tracking and following a tagged leopard shark with an autonomous underwater vehicle," *Journal of Field Robotics*, vol. 30, no. 3, pp. 309–322, 2013.

[66] E. Delory, A. Castro, C. Waldmann, J. . Rolin, P. Woerther, J. Gille, J. Del Rio, O. Zielinski, L. Golmen, N. R. Hareide, J. Pearlman, and R. Garello,

"Objectives of the nexos project in developing next generation ocean sensor systems for a more cost-efficient assessment of ocean waters and ecosystems, and fisheries management," in *OCEANS 2014 - TAIPEI*, pp. 1–6, April 2014.

[67] J. Pearlman, S. Jirka, J. d. Rio, E. Delory, L. Frommhold, S. Martinez, and T. O'Reilly, "Oceans of tomorrow sensor interoperability for in-situ ocean monitoring," in *OCEANS 2016 MTS/IEEE Monterey*, pp. 1–8, Sep. 2016.

[68] S. Memè, E. Delory, M. Felgines, J. Pearlman, F. Pearlman, J. del Rio, E. Martinez, I. Masmitja, J. Gille, J. Rolin, L. Golmen, N. R. Hareide, C. Waldmann, and O. Zielinski, "Nexos next generation, cost-effective, compact, multifunctional web enabled ocean sensor systems," in *OCEANS 2017 - Anchorage*, pp. 1–10, Sep. 2017.

[69] E. Martinez, D. Toma, E. Trullols, J. Del Rio, D. Pinzanin, E. Delory, S. Jirka, and J. Pearlman, "Smart hydrophone integration into the sensor web enablement framework," in *IEEE Sensors Applications Symposium - Catania, Italy*, pp. 20–22, 2016.

[70] D. M. Toma, J. del Ro, N. Carreras, L. Corradino, P. Braulte, E. Delory, A. Castro, and P. Ruiz, "Multi-platform underwater passive acoustics instrument for a more cost-efficient assessment of ocean ecosystems," in *2015 IEEE International Instrumentation and Measurement Technology Conference (I2MTC) Proceedings*, pp. 969–974, May 2015.

[71] B. Friedlander, "A passive localization algorithm and its accuracy analysis," *IEEE Journal of Oceanic Engineering*, vol. 12, pp. 234–245, January 1987.

[72] A. M. C. R. Borzino, J. A. Apolinário, and M. L. R. de Campos, "Consistent doa estimation of heavily noisy gunshot signals using a microphone array," *IET Radar, Sonar Navigation*, vol. 10, no. 9, pp. 1519–1527, 2016.

[73] D. M. Toma, I. Masmitja, J. del Ro, E. Martinez, C. Artero-Delgado, A. Casale, A. Figoli, D. Pinzani, P. Cervantes, P. Ruiz, S. Mem, and E. Delory, "Smart embedded passive acoustic devices for real-time hydroacoustic surveys," *Measurement*, vol. 125, pp. 592 – 605, 2018.

[74] J. E. and, "Ieee 1588 standard for a precision clock synchronization protocol for networked measurement and control systems," in *2nd ISA/IEEE Sensors for Industry Conference*, pp. 98–105, Nov 2002.

[75] J. Valin, F. Michaud, J. Rouat, and D. Letourneau, "Robust sound source localization using a microphone array on a mobile robot," in *Proceedings 2003*

IEEE/RSJ International Conference on Intelligent Robots and Systems (IROS 2003) (Cat. No.03CH37453), vol. 2, pp. 1228–1233 vol.2, Oct 2003.

[76] A. Nehorai and E. Paldi, "Acoustic vector-sensor array processing," *IEEE Transactions on Signal Processing*, vol. 42, pp. 2481–2491, Sep. 1994.

[77] J. Benesty, J. Chen, and Y. Huang, *Direction-of-Arrival and Time-Difference-of-Arrival Estimation*, pp. 181–215. Berlin, Heidelberg: Springer Berlin Heidelberg, 2008.

[78] A. Alcocer, *Positioning and Navigation Systems for Robotic Underwater Vehicles*. PhD thesis, Instituto Superior Tecnico, Universidade Tecnica de Lisboa, January 2010.

[79] M. Nogueras, J. del Rio, J. Cadena, J. Sorribas, C. Artero, J. Daobeitia, and A. Mnuel, "Obsea an oceanographic seafloor observatory," in *2010 IEEE International Symposium on Industrial Electronics*, pp. 488–492, July 2010.

[80] R. Costanzi, N. Monnini, A. Ridolfi, B. Allotta, and A. Caiti, "On field experience on underwater acoustic localization through usbl modems," in *OCEANS 2017 - Aberdeen*, pp. 1–5, June 2017.

[81] N. R. Rypkema, E. M. Fischell, and H. Schmidt, "One-way travel-time inverted ultra-short baseline localization for low-cost autonomous underwater vehicles," in *2017 IEEE International Conference on Robotics and Automation (ICRA)*, pp. 4920–4926, May 2017.

[82] S. J. McManus, "A method of navigation using a modified ultra short base line directional acoustic transponder," in *OCEANS 2007 - Europe*, pp. 1–5, June 2007.

[83] M. J. Stanway, *Contributions to automated realtime underwater navigation*. PhD thesis, Joint Program in Applied Ocean Science and Engineering (Massachusetts Institute of Technology, Dept. of Mechanical Engineering; and the Woods Hole Oceanographic Institution), 2012.

[84] S. Umeyama, "Least-squares estimation of transformation parameters between two point patterns," *IEEE Transactions on Pattern Analysis and Machine Intelligence*, vol. 13, pp. 376–380, April 1991.

[85] H. Strobel, "Strang, g., introduction to applied mathematics. wellesley, mass. wellesley-cambridge press 1986. ix, 758 pp. isbn 0-9614088-0-4," *ZAMM - Journal of Applied Mathematics and Mechanics / Zeitschrift fr Angewandte Mathematik und Mechanik*, vol. 69, no. 9, pp. 311–312, 1989.

[86] P. A. Miller, J. A. Farrell, Y. Zhao, and V. Djapic, "Autonomous underwater vehicle navigation," *IEEE Journal of Oceanic Engineering*, vol. 35, pp. 663–678, July 2010.

[87] A. Rossi, M. Pasquali, and M. Pastore, "Performance analysis of an inertial navigation algorithm with dvl auto-calibration for underwater vehicle," in *2014 DGON Inertial Sensors and Systems (ISS)*, pp. 1–19, Sep. 2014.

[88] K. S. Arun, T. S. Huang, and S. D. Blostein, "Least-squares fitting of two 3-d point sets," *IEEE Transactions on Pattern Analysis and Machine Intelligence*, vol. PAMI-9, pp. 698–700, Sep. 1987.

[89] D. R. C. Philip, "An evaluation of usbl and sbl acoustic systems and the optimisation of methods of calibration - part 1," *The Hydrographic Journal*, April 2003.

[90] B. Jones, "Field results from point to point real-time underwater acoustic tracking using a simple mathematical filter," *IEEE OES Autonomous Underwater Vehicle Symposium*, November 2018.

[91] J. D. Quenzer and K. A. Morgansen, "Observability based control in range-only underwater vehicle localization," in *2014 American Control Conference*, pp. 4702–4707, June 2014.

[92] E. Olson, J. J. Leonard, and S. Teller, "Robust range-only beacon localization," *IEEE Journal of Oceanic Engineering*, vol. 31, pp. 949–958, Oct 2006.

[93] I. Masmitja, S. Gomariz, J. Del-Rio, B. Kieft, T. O'Reilly, P.-J. Bouvet, and J. Aguzzi, "Optimal path shape for range-only underwater target localization using a wave glider," *The International Journal of Robotics Research*, vol. 37, no. 12, pp. 1447–1462, 2018.

[94] R. Kaune, J. Hrst, and W. Koch, "Accuracy analysis for tdoa localization in sensor networks," in *14th International Conference on Information Fusion*, pp. 1–8, July 2011.

[95] B. Zhang, Y. Hu, H. Wang, and Z. Zhuang, "Underwater source localization using tdoa and fdoa measurements with unknown propagation speed and sensor parameter errors," *IEEE Access*, vol. 6, pp. 36645–36661, 2018.

[96] C. Zheng, D. Sun, L. Cai, and X. Li, "Mobile node localization in underwater wireless networks," *IEEE Access*, vol. 6, pp. 17232–17244, 2018.

[97] H. Ramezani, H. Jamali-Rad, and G. Leus, "Target localization and tracking for an isogradient sound speed profile," *IEEE Transactions on Signal Processing*, vol. 61, pp. 1434–1446, March 2013.

[98] D. Moreno-Salinas, A. Pascoal, and J. Aranda, "Optimal sensor placement for acoustic underwater target positioning with range-only measurements," *IEEE Journal of Oceanic Engineering*, vol. 41, pp. 620–643, July 2016.

[99] B. T. Hinson, M. K. Binder, and K. A. Morgansen, "Path planning to optimize observability in a planar uniform flow field," in *2013 American Control Conference*, pp. 1392–1399, June 2013.

[100] H. Ramezani, H. Jamali-Rad, and G. Leus, "Target localization and tracking for an isogradient sound speed profile," *IEEE Transactions on Signal Processing*, vol. 61, pp. 1434–1446, March 2013.

[101] M. F. Fallon, G. Papadopoulos, J. J. Leonard, and N. M. Patrikalakis, "Cooperative auv navigation using a single maneuvering surface craft," *The International Journal of Robotics Research*, vol. 29, no. 12, pp. 1461–1474, 2010.

[102] S. E. Webster, R. M. Eustice, H. Singh, and L. L. Whitcomb, "Advances in single-beacon one-way-travel-time acoustic navigation for underwater vehicles," *The International Journal of Robotics Research*, vol. 31, no. 8, pp. 935–950, 2012.

[103] L. Freitag, M. Grund, S. Singh, J. Partan, P. Koski, and K. Ball, "The whoi micro-modem: an acoustic communications and navigation system for multiple platforms," in *Proceedings of OCEANS 2005 MTS/IEEE*, pp. 1086–1092 Vol. 2, Sept 2005.

[104] S. D. McPhail and M. Pebody, "Range-only positioning of a deep-diving autonomous underwater vehicle from a surface ship," *IEEE Journal of Oceanic Engineering*, vol. 34, pp. 669–677, Oct 2009.

[105] I. Masmitja, S. Gomariz, J. D. Rio, B. Kieft, and T. O'Reilly, "Range-only underwater target localization: Path characterization," in *OCEANS 2016 MTS/IEEE Monterey*, pp. 1–7, Sept 2016.

[106] I. Masmitja, O. Pallares, S. Gomariz, J. D. Rio, B. Kieft, and T. O'Reilly, "Range-only underwater target localization : error characterization," in *21st IMEKO TC4 International Symposium, Budapest*, pp. 267–271, Sept 2016.

[107] D. Ucinski, *Optimal Measurement Methods for Distributed Parameter System Identification*. Boca Raton: CRC Press, 2004.

[108] H. L. V. Trees, K. L. Bell, and Z. Tian, *Detection Estimation and Modulation Theory, Part I: Detection, Estimation, and Filtering Theory, 2nd Edition.* John Wiley & Sons, Inc., 2013.

[109] D. Bertsekas, *Nonlinear Programming.* Athena Scientific, 2nd edition, Belmont, MA, 1995.

[110] K. W. Cheung, H. C. So, W. K. Ma, and Y. T. Chan, "Least squares algorithms for time-of-arrival-based mobile location," *IEEE Transactions on Signal Processing*, vol. 52, pp. 1121–1130, April 2004.

[111] C. R. Rao, *Frontmatter.* John Wiley & Sons, Inc., 2008.

[112] P. R. McGill, A. D. Sherman, B. W. Hobson, R. G. Henthorn, A. C. Chase, and K. L. Smith, "Initial deployments of the rover, an autonomous bottom-transecting instrument platform for long-term measurements in deep benthic environments," in *OCEANS 2007*, pp. 1–7, Sept 2007.

[113] S. B. Williams, O. Pizarro, D. M. Steinberg, A. Friedman, and M. Bryson, "Reflections on a decade of autonomous underwater vehicles operations for marine survey at the australian centre for field robotics," *Annual Reviews in Control*, vol. 42, pp. 158 – 165, 2016.

[114] J. E. Manley, R. Carlon, and G. Hine, "Ten years of wave glider operations: A persistent effort," in *OCEANS 2017 - Anchorage*, pp. 1–5, Sept 2017.

[115] N. Crasta, D. Moreno-Salinas, A. Pascoal, and J. Aranda, "Multiple autonomous surface vehicle motion planning for cooperative range-based underwater target localization," *Annual Reviews in Control*, vol. 46, pp. 326 – 342, 2018.

[116] J. Gauvain and C. H. Lee, "Maximum a posteriori estimation for multivariate gaussian mixture observations of markov chains," *IEEE Transactions on Speech and Audio Processing*, vol. 2, pp. 291–298, April 1994.

[117] D. P. Bertsekas and J. N. Tsitsiklis, *Introduction to Probability.* Athena Scientific; Edition: 2nd, 2008.

[118] M. Wüthrich, S. Trimpe, C. G. Cifuentes, D. Kappler, and S. Schaal, "A new perspective and extension of the gaussian filter," *The International Journal of Robotics Research*, vol. 35, no. 14, pp. 1731–1749, 2016.

[119] A. Alcocer, *Positioning and Navigation Systems for Robotic Underwater Vehicles*. PhD dissertation, Universidade Técnica de Lisboa Instituto superior Técnico, 2009.

[120] "MSFD (Marine Strategy Framework Directive) 2008. Directive 2008/56/EC of the European Parliament and of the Council of 17 June 2008 establishing a framework for community action in the field of marine environmental policy,"

[121] N. Crasta, D. Moreno-Salinas, B. Bayat, A. M. Pascoal, and J. Aranda, "Range-based underwater target localization using an autonomous surface vehicle: Observability analysis," in *2018 IEEE/ION Position, Location and Navigation Symposium (PLANS)*, pp. 487–496, April 2018.

[122] O. Cappe, S. J. Godsill, and E. Moulines, "An overview of existing methods and recent advances in sequential monte carlo," *Proceedings of the IEEE*, vol. 95, pp. 899–924, May 2007.

[123] A. H. Jazwinski, *Stochastic processes and filtering theory*. Analytical Mechanics Associates, Inc. Academic Press., 1970.

[124] S. J. Julier and J. K. Uhlmann, "New extension of the kalman filter to nonlinear systems," *Proc.SPIE*, vol. 3068, pp. 3068 – 3068 – 12, 1997.

[125] S. J. Julier and J. K. Uhlmann, "Unscented filtering and nonlinear estimation," *Proceedings of the IEEE*, vol. 92, pp. 401–422, March 2004.

[126] S. Julier, J. Uhlmann, and H. F. Durrant-Whyte, "A new method for the nonlinear transformation of means and covariances in filters and estimators," *IEEE Transactions on Automatic Control*, vol. 45, pp. 477–482, March 2000.

[127] R. V. der Merwe and E. A. Wan, "The square-root unscented kalman filter for state and parameter-estimation," in *2001 IEEE International Conference on Acoustics, Speech, and Signal Processing. Proceedings (Cat. No.01CH37221)*, vol. 6, pp. 3461–3464 vol.6, May 2001.

[128] *Batch maximum likelihood (ML) and maximum a posteriori (MAP) estimation with process noise for tracking applications*, vol. 5204, 2004.

[129] G. Huang, K. Zhou, N. Trawny, and S. I. Roumeliotis, "A bank of maximuma posteriori(map) estimators for target tracking," *IEEE Transactions on Robotics*, vol. 31, pp. 85–103, Feb 2015.

[130] B. Triggs, P. F. McLauchlan, R. I. Hartley, and A. W. Fitzgibbon, "Bundle adjustment — a modern synthesis," in *Vision Algorithms: Theory and Practice*

(B. Triggs, A. Zisserman, and R. Szeliski, eds.), (Berlin, Heidelberg), pp. 298–372, Springer Berlin Heidelberg, 2000.

[131] G. P. M. Rozál and J. A. Hartigan, "The map test for multimodality," *Journal of Classification*, vol. 11, pp. 5–36, Mar 1994.

[132] F. Meyer, O. Hlinka, H. Wymeersch, E. Riegler, and F. Hlawatsch, "Distributed localization and tracking of mobile networks including noncooperative objects," *IEEE Transactions on Signal and Information Processing over Networks*, vol. 2, pp. 57–71, March 2016.

[133] C. Forney, E. Manii, M. Farris, M. A. Moline, C. G. Lowe, and C. M. Clark, "Tracking of a tagged leopard shark with an auv: Sensor calibration and state estimation," in *2012 IEEE International Conference on Robotics and Automation*, pp. 5315–5321, May 2012.

[134] T. Li, M. Bolic, and P. M. Djuric, "Resampling methods for particle filtering: Classification, implementation, and strategies," *IEEE Signal Processing Magazine*, vol. 32, pp. 70–86, May 2015.

[135] I. Masmitja, S. Gomariz, J. Del-Rio, , P.-J. Bouvet, and J. Aguzzi, "Underwater multi-target tracking with particle filters," in *OCEANS 2018 MTS/IEEE Kobe*, pp. 1–5, May 2018.

[136] P. D. Pradeep, D. A. Kumar, and G. Sahu, "Estimating the target tracking using a set of range-parameters for gain modification using kalman filters," *International Journal of Microwave Engineering (JMICRO)*, vol. 1, January 2016.

[137] D. W. Heermann, *Computer Simulation Methods in Theoretical Physics*. Springer-Verlag, Berlin, Germany, 1990.

[138] B. C. K. Farid Golnaraghi, *Automatic Control Systems 9th*. John Wiley and Sons Ltd; Edition: 9th Revised edition, 2009.

[139] B. Ha, "Coastal profiling float depth control," *MBARI Intern Report*, 2018.

[140] P. Elliman, "Snow crab tracking using wave gliders," *Hydro international*, 2017.

[141] S. M. Tomkiewicz, M. R. Fuller, J. G. Kie, and K. K. Bates, "Global positioning system and associated technologies in animal behaviour and ecological research," *Philosophical transactions of the Royal Society of London. Series B, Biological sciences*, vol. 365, pp. 2163–2176, Sep 2010.

[142] A. L. Kukulya, R. Stokey, C. Fiester, E. M. H. Padilla, and G. Skomal, "Multi-vehicle autonomous tracking and filming of white sharks carcharodon carcharias," in *2016 IEEE/OES Autonomous Underwater Vehicles (AUV)*, pp. 423–430, Nov 2016.

[143] A. L. Kukulya, R. Stokey, R. Littlefield, F. Jaffre, E. M. H. Padilla, and G. Skomal, "3d real-time tracking, following and imaging of white sharks with an autonomous underwater vehicle," in *OCEANS 2015 - Genova*, pp. 1–6, May 2015.

[144] D. Haulsee, M. Breece, D. Miller, B. Wetherbee, D. Fox, and M. Oliver, "Habitat selection of a coastal shark species estimated from an autonomous underwater vehicle," *Marine Ecology Progress Series*, vol. 528, pp. 277–288, may 2015.

[145] J. Zhang and D. Berleant, "Envelopes around cumulative distribution functions from interval parameters of standard continuous distributions," in *22nd International Conference of the North American Fuzzy Information Processing Society, NAFIPS 2003*, pp. 407–412, July 2003.

[146] G. K. Karagiannidis and A. S. Lioumpas, "An improved approximation for the gaussian q-function," *IEEE Communications Letters*, vol. 11, pp. 644–646, August 2007.

[147] M. Stojanovic and J. Preisig, "Underwater acoustic communication channels: Propagation models and statistical characterization," *IEEE Communications Magazine*, vol. 47, pp. 84–89, January 2009.

[148] C. C. Wilmers, B. Nickel, C. M. Bryce, J. A. Smith, R. E. Wheat, and V. Yovovich, "The golden age of bio-logging: how animal-borne sensors are advancing the frontiers of ecology," *Ecology*, vol. 96, no. 7, pp. 1741–1753, 2015.

[149] B. S. Graham, P. L. Koch, S. D. Newsome, K. W. McMahon, and D. Aurioles, *Using Isoscapes to Trace the Movements and Foraging Behavior of Top Predators in Oceanic Ecosystems*, pp. 299–318. Dordrecht: Springer Netherlands, 2010.

[150] S. F. Shaikh, H. F. Mazo-Mantilla, N. Qaiser, S. M. Khan, J. M. Nassar, N. R. Geraldi, C. M. Duarte, and M. M. Hussain, "Noninvasive featherlight wearable compliant marine skin: Standalone multisensory system for deep-sea environmental monitoring," *Small*, vol. 15, no. 10, p. 1804385, 2019.

[151] Y. Fujiwara, "Self-synchronizing pulse position modulation with error tolerance," *IEEE Transactions on Information Theory*, vol. 59, pp. 5352–5362, Sep. 2013.

"As areas of knowledge grow, so too do the perimeters of ignorance."

— Neil deGrasse Tyson

UNIVERSITAT POLITÈCNICA DE CATALUNYA
BARCELONATECH
Departament d'Enginyeria Electrònica